

# Journal of Environmental & Earth Sciences

---

Volume 5 • Issue 1 • April 2023 ISSN 2661-3190(Online)



## **Editor-in-Chief**

**Prof. Shuanggen Jin**

Henan Polytechnic University; Shanghai Astronomical Observatory, China

## **Editorial Board Members**

Fengtai Zhang, China	Nimal Shantha Abeysingha, Sri Lanka
Junfeng Wang, China	Mahmoud Taghavi, Iran
Chin H. Wu, United States	Bing Xu, China
Bingqi Zhu, China	Shaoliang Zhang, China
Carmine Apollaro, Italy	Kebede Wolka Wolancho, Ethiopia
Yu Jiang, China	Carla Patrícia Silva, Portugal
Lampros Vasiliades, Greece	Jixiang Yang, China
Karoly Nemeth, Hungary	Marco Kondracki Alcântara, Brazil
Wei Ju, China	Senthil Kumar Ramalinghm, Sultanate of Oman
Vincenzo Convertito, Italy	Gino Dardanelli, Italy
Shaoyong Lu, China	Ronglin Tang, China
Souhila Ait Hamoudi, Algeria	Masoud Masoudi, Iran
Maria Barbara Zygadlo, Poland	Jingying Fu, China
Abdeltif Amrane, France	Miklas Scholz, South Africa
Aqil Tariq, United States	Ayad M. Fadhil Al-Quraishi, Iraq
Rossana Sanfilippo, Italy	Ramayah Thurasamy, Malaysia
Astrida Miceikiene, Lithuania	Bahram Malekmohammadi, Iran
Yazan Mohammad Taamneh, Jordan	Ram Kishor Fagodiya, India
Teodosio Lacava, Italy	Dillip Kumar Swain, India

Volume 5 Issue 1 • April 2023 • ISSN 2661-3190 (Online)

# Journal of Environmental & Earth Sciences

**Editor-in-Chief**

Prof. Shuanggen Jin



## Contents

### Articles

- 1      **Impact of River Water Quality on Public Health in Perspective of Asian Rivers: A Case Study of Buriganga River, Bangladesh**  
A.B.M. Kamal Pasha, Mustafe Said Nur, Sagar Mozumder, Mahfuza Parveen
- 17     **Quantum Atmospheric Biophysics: A Comparison of Four Weather Stations in India on Average Monthly Temperatures Since 1892 and Forecasts to 2150**  
Mazurkin Peter Matveevich
- 65     **Source, Contamination Assessment and Risk Evaluation of Heavy Metals in the Stream Sediments of Rivers around Olode Area SW, Nigeria**  
Stellamaris Isioma Okonkwo, Sunday Ojochogwu Idakwo, Mofolorunsho Samuel Kolawole, Olufemi Faloye, Anthony Azubuike Elueze
- 85     **Statistical Characteristics of the Temporal Spectrum of Scattered Radiation in the Equatorial Ionosphere**  
George Jandieri , Nika Tugushi
- 95     **Landfill Site Suitability Assessment Using Geographic Information System (GIS) and Analytic Hierarchy Process (AHP) in Butuan City, Philippines**  
Francis Jhun T. Macalam, Kaleb P. Arreza, Angelica T. Magpantay, Kristine Y. Rabaño
- 108    **Domestic Wastewater Treatment through the Application of *Corchuros oltorius L.* as Bio-Coagulant in Cagayan de Oro City, Philippines**  
Gina C. Lacang, Corazon V. Ligaray

### Review

- 33     **Deep Learning Methods Used in Remote Sensing Images: A Review**  
Ekram M. Rewhel, Jianqiang Li, Amal A. Hamed, Hatem M. Keshk, Amira S. Mahmoud, Sayed A. Sayed, Ehab Samir, Hind H. Zeyada, Sayed A. Mohamed, Marwa S. Moustafa, Ayman H. Nasr, Ashraf K. Helmy

ARTICLE

## Impact of River Water Quality on Public Health in Perspective of Asian Rivers: A Case Study of Buriganga River, Bangladesh

A.B.M. Kamal Pasha<sup>1</sup>, Mustafe Said Nur<sup>2</sup>, Sagar Mozumder<sup>1</sup>, Mahfuza Parveen<sup>1\*</sup> 

<sup>1</sup> Department of Environmental Science and Disaster Management, Daffodil International University, Dhaka, 1216, Bangladesh

<sup>2</sup> Nkumba University, P.O. Box 237, Lyamutundwe, Uganda

### ABSTRACT

Water pollution is one of the current global problems. So many countries are suffering from this problem specifically most South Asian and Southeast Asian countries, and Bangladesh is one of those countries that are suffering from water pollution. Furthermore, the city of Bangladesh, Dhaka is one of the most densely populated cities in the world and overpopulation is showing a negative impact on the water quality now. Most of the rivers are very polluted around Dhaka city because of anthropogenic causes. This study focused on Buriganga river pollution and its impact on public health. This study intended to find out the major cause of Buriganga river pollution and the health status of the community living beside the Buriganga river. Also the study identified all the common diseases which people are suffering from around the Buriganga river area. Then the study compared the results with other southeast Asian countries so that it can make the relationship and can make it easier to understand the current situation of water pollution on public health in East Asia and Southeast Asia regions. During the research work, it was noticed that the Buriganga river is very polluted due to human activities. The transportation system, fishing, and waste canals from industries become the primary reasons behind Buriganga's current condition. Also irresponsibility of both the environmental department and civil society is the major factor in Buriganga river pollution. The hygienic level was also not in a good condition because so many wastes like plastic materials and other daily use materials were thrown out into the river. That's why public health conditions around the Buriganga river become vulnerable nowadays. So policies have to be implemented from the right perspective and the institutions have to be strong enough to handle all the issues regarding the Buriganga River.

**Keywords:** Buriganga; Water quality; River pollution; Public health; Dhaka city

#### \*CORRESPONDING AUTHOR:

Mahfuza Parveen, Department of Environmental Science and Disaster Management, Daffodil International University, Dhaka, 1216, Bangladesh; Email: mahfuza.esdm@diu.edu.bd; mahfuza\_parveen@yahoo.com

#### ARTICLE INFO

Received: 10 October 2022 | Revised: 5 January 2023 | Accepted: 6 January 2023 | Published Online: 20 February 2023

DOI: <https://doi.org/10.30564/jees.v5i1.5132>

#### CITATION

Kamal Pasha, A.B.M., Nur, M.S., Mozumder, S., et al., 2023. Impact of River Water Quality on Public Health in Perspective of Asian Rivers: A Case Study of Buriganga River, Bangladesh. Journal of Environmental & Earth Sciences. 5(1): 1-16. DOI: <https://doi.org/10.30564/jees.v5i1.5132>

#### COPYRIGHT

Copyright © 2023 by the author(s). Published by Bilingual Publishing Group. This is an open access article under the Creative Commons Attribution-NonCommercial 4.0 International (CC BY-NC 4.0) License. (<https://creativecommons.org/licenses/by-nc/4.0/>).

## 1. Introduction

Bangladesh is situated in the southern part of Asia which is one of the low-lying riverine countries. There are more than 700 rivers in the country including tributaries that flow through the country, the capital city of Bangladesh is one of the megacities in the world and it was established 400 years ago. This city was started in the northern part of the Buriganga River which was called at that time (the Ganges River) <sup>[1]</sup>. The capital city of Bangladesh is spread over an area of 1.5 to 1.7 kilometers square close to the connection of the Postogola and Buriganga Rivers <sup>[2]</sup>. The capital of Bangladesh, Dhaka city has the Buriganga (Old Ganga) river beside it which is one of the main rivers flows <sup>[3]</sup> in the area. Buriganga is mainly a part of the greater Ganges which is a transboundary river it flows through the country of India and Bangladesh. Buriganga is only 18 km long whereas the greater Ganges is 2525 km long <sup>[4]</sup>. In Dhaka city, river water pollution is an extreme problem right now. All the rivers around Dhaka city are getting polluted day by day including the Buriganga river <sup>[5]</sup>. Bangladesh is still a third world and one of the most densely populated countries. Almost 97% of its total population has access to water but the quality of water is still questionable <sup>[6]</sup>. Water pollution is the contaminated state of water and it could be groundwater or river water <sup>[7]</sup>. Water pollution is one of the biggest problems in Dhaka city as well as in Bangladesh and there are many rivers, man-made wells, lakes, and streams polluted by human activities, especially rivers surrounding Dhaka cities like Buriganga, Turag, Balu, Shitalakkhya, Daleshwari, and Bangshi River are being polluted due to high population living sides of that rivers and also because of the number of industries are growing very fast <sup>[8]</sup>. So this study will focus on the Buriganga River which is one of the most polluted rivers in Bangladesh and flows past the southwest outskirts of Dhaka city, this river has an average depth of 7.6 metres (25 ft) and its maximum depth reaches 18 metres (58 ft) <sup>[9]</sup>. This river is one of the most polluted rivers in the country and struggling for its existence, the Buriganga River is afflicted by the noisome problems of pollution as

the source of chemical wastes from industrial, medical wastes, household waste, sewage, plastics, dead animals and sometimes oils spilled by the boats and other river transportation system, furthermore, Dhaka city discharges into the Buriganga river more than 4,500 tons of solid wastes per day <sup>[10]</sup>. Different factors are affecting the quality of water in the Buriganga River and are also affecting its aquatic life forms. But the more concerning side is all the water parameters like pH, Biological Oxygen Demand (BOD), Dissolve Oxygen (DO), and chlorides hardly can satisfy the standard which is made by the Department of Environment, Bangladesh <sup>[11,3]</sup>. In the last years, the Buriganga River was going a very dangerous situation which led to being the most polluted river in Bangladesh, the main factors of this pollution are anthropogenic <sup>[12]</sup> and some other natural factors, many types of research said that main problem of the river is the rapid growth of Dhaka city, the industrial revolution, population density, and climate change, the combination of these factors caused Buriganga river to be more polluted than other rivers <sup>[4]</sup>. Many researchers proposed different sources but still, there is a variation in their findings, like the number of waste spilled into the river every day <sup>[13]</sup>, percentages of each waste, the role of society in keeping the safety of the river, legislation of the river safety, management of the river, So, these different results caused frustrate to understand specific factors causing the adverse situation of the Buriganga River, also it's tough to present the health status of the people living surrounding area of the river, the water quality of the river may change from months to months, year to year due to amount of waste entering the river <sup>[1]</sup> so it is needed to be tested every time to assess the current status of the river, Like Bangladesh Water pollution also become a severe problem in Malaysia and Philippine. Specially Kualalampur and Manila, the capital city of Malaysia and Philippine respectively. In Malaysia, the Department of Environment (DOE) monitored 473 rivers in 2014. On the basis of water quality parameters (e.g. dissolved oxygen (DO), biochemical oxygen demand (BOD), chemical oxygen demand (COD), ammoniacal nitrogen

(NH<sub>3</sub>-N), suspended solids (SS) and pH) DOE found that 244 (52%) were clean, 186 (39%) were slightly contaminated, and 43 (9%) were infected<sup>[14]</sup>. In Philippine also 50 out of 421 rivers are considered biologically dead, meaning that the rivers do not contain any oxygen and are unable to support most species of life<sup>[15]</sup>. According to the Environmental Management Bureau (EMB) out of 127 freshwater bodies of the Philippines, only 47% retain good water quality<sup>[15]</sup>. The Marilao River, which runs through the capital city, Manila, is included in the list of the Top 19 Most Polluted Rivers in the World. On the other hand, Kumar et al.<sup>[16]</sup> analyzed the water quality of the Pasig-Marikina River, Philippines, based on three indicators for aquatic ecosystem health viz. Biochemical Oxygen Demand (BOD), Chemical Oxygen Demand (COD), and Nitrate (NO<sub>3</sub>) stated that the water quality of the respected river will rapidly deteriorate and will be not suitable for any aquatic life in terms of major water quality parameters. Due to its enormous economic and material advancement since the 1950s, Taiwan has made notable social and political gains. The nation has undergone extensive industrial development and is presently regarded as having a top-tier semiconductor industry. However, the risks associated with such rapid growth have led to a serious deterioration of the environment, especially its scarce water resources. As rivers from all Asian countries are facing the impact of rapid urban and economic growth, the study intended to show the overall scenario of these rivers.

## 2. Objectives

The study will discuss what were the findings during the research work elaborately by focusing on the objectives of **a.** Identification of major causes of Asian River pollution including the Buriganga river from Bangladesh and **b.** Assessment of health status of community living beside the Buriganga river.

## 3. Materials and methods

### 3.1 Study area

The research study has been completed in a specific area of Dhaka city (**Figure 1**) which is one of the most populated cities in the world, specifically the target area of the study was the Buriganga river at the point of Showari ghat area which is very close to two police stations of Chakbazar Ward-66 (part) and Kotwali Word-68 (part), The geographical position of Showari ghat is 23.7113° N, 90.3944° E<sup>[8]</sup>. For the Initial Survey, the study considered the whole Showari ghat area. The study area is under the jurisdiction of Dhaka north city Corporation (DSCC) (**Figure 1**). There is an embankment that was constructed in 1980 which is now known as the Shadarghat-Gabtoli road<sup>[17]</sup>. There is a significant amount of change that can be noticed in the sociocultural characteristics of the area, because of the unplanned population growth, new settlements are being constructed without following any proper planning and rules<sup>[18]</sup>.

### 3.2 Data collection procedure

By asking the locals questions, this study utilised an indirect survey design and used qualitative research as part of the surveying process<sup>[19]</sup>. A questionnaire survey form was first developed to gather information, and then other researchers visited the study area with some locals to gather data by questioning them. It served as a translator because that is the simplest kind of communication<sup>[20]</sup>. Most of the questions were quantitative and were designed as optional questions<sup>[21]</sup>. It was very easy and possible for everyone to answer that's why the field study was successful and all the data have been collected previously.

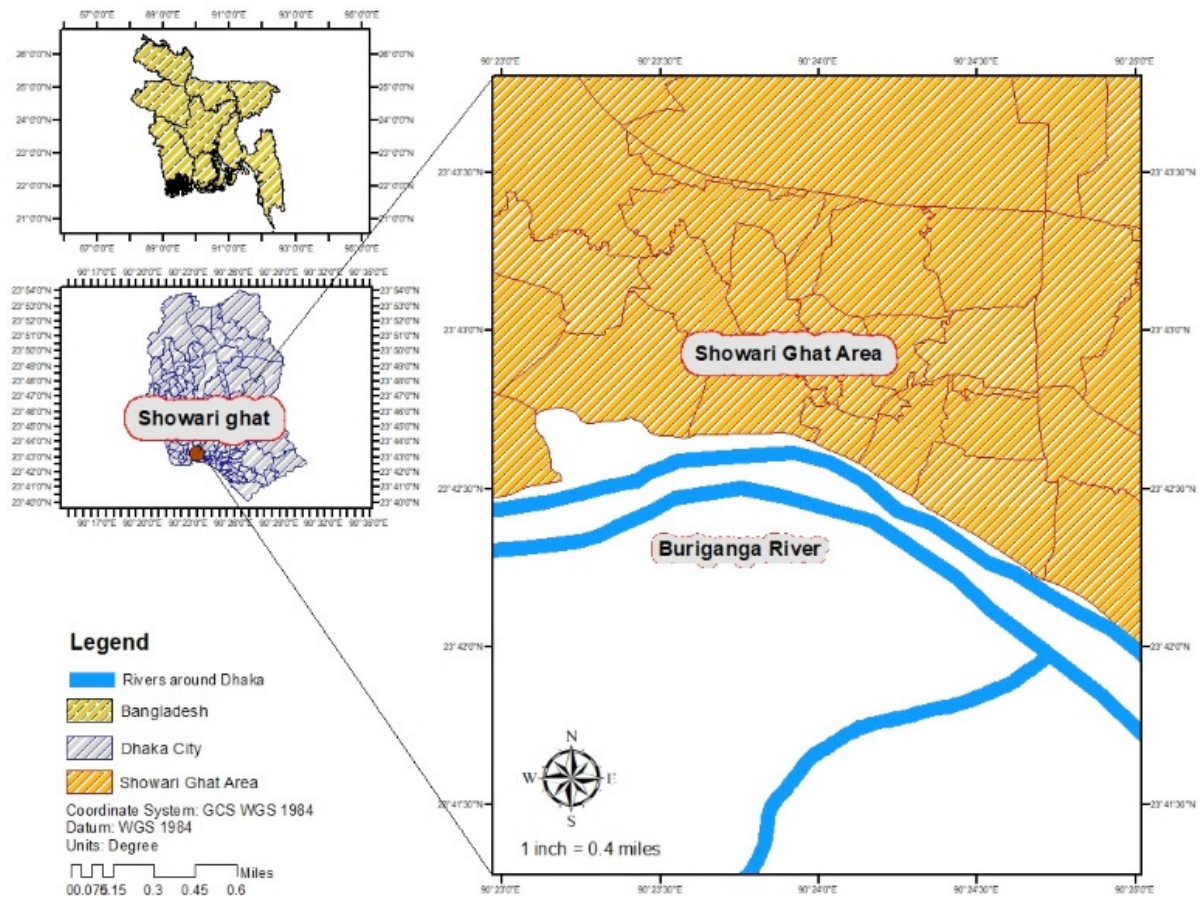


Figure 1. Study area.

### 3.3 Research population

The study of this research was conducted by the community living in the Buriganga river area. Both male and female, old and young people were a part of the study. The response was collected through random selection, so the study was successfully communicated to most of the community living in that area and they became a part of the study. 45 among society living there provided different responses. To determine the sample size of the study, the Slovine formula has been used.

$$n = N / (1 + N(e^2)) \quad n = ?$$

$$n = \text{sample size} \quad N = 51$$

$$N = \text{population size} \quad e = 5\% = 0.05$$

$$E = \text{margin of errors,} \quad \text{Therefore;}$$

$$n = 51 / (1 + 51 * 0.0025)$$

$$n = 45.2 = 45 \text{ respondent}$$

$$\text{Sample size} = 45 \text{ respondent}$$

### 3.4 Sampling technique

In this study, simple random sampling was applied<sup>[19]</sup>. The study has considered different selection criteria. Inclusion criteria were used to determine the accurate information from the targeted respondents (Figure 2). It prevents unwanted information to include in the survey<sup>[22]</sup>. Under this criterion, the study has also included the local community people for investigation so that the study can achieve a high level of accuracy during the survey (Figure 2). Exclusion criteria were also followed to prevent the unfavorable outcome. Under these criteria, the study carefully differentiates those who came for temporary visits<sup>[23]</sup>.

### 3.5 Data analysis plan

Data were analyzed by using SPSS, version 20.0, the data was cleaned and checked any possible missed data before it was processed<sup>[24]</sup>, the results

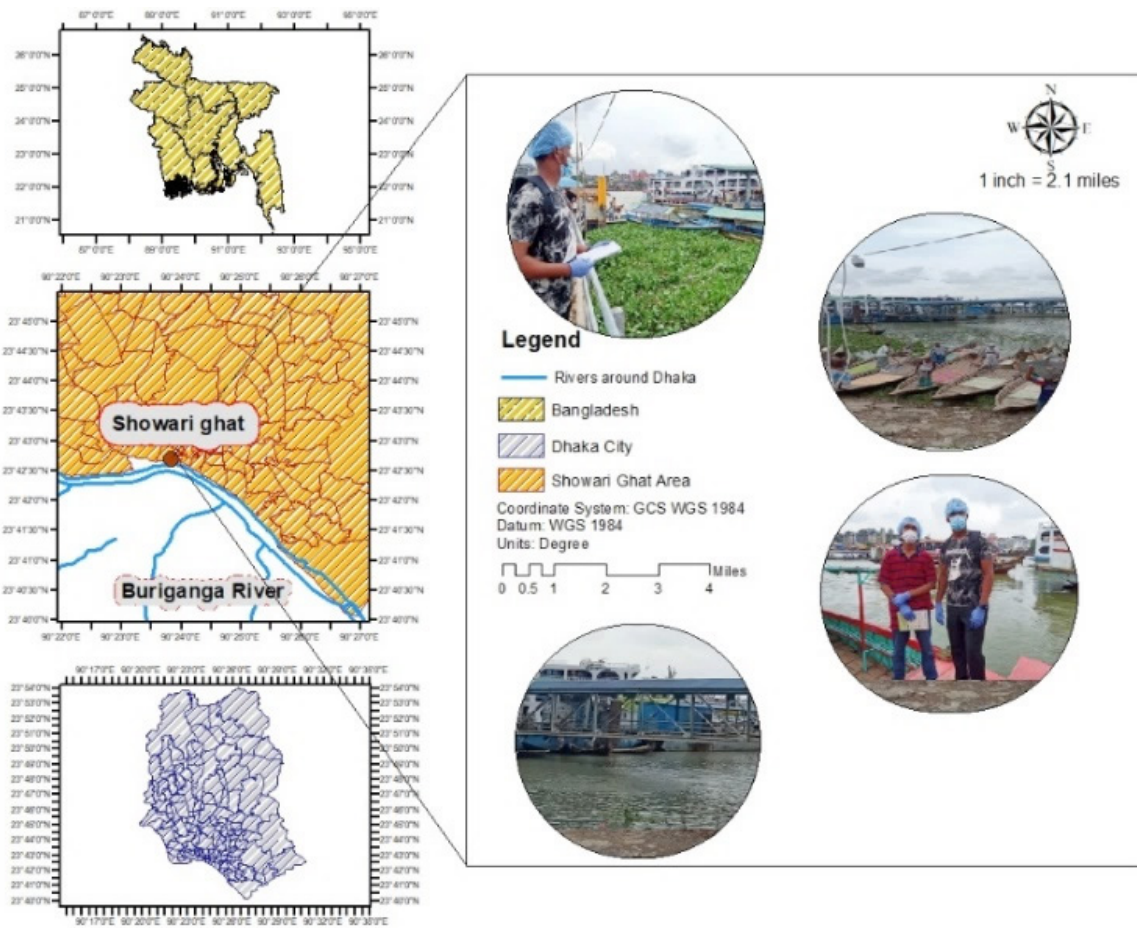


Figure 2. Sampling technique.

were entered in an open office spreadsheet (Excel) to obtain good and quality tables, bars, and pie charts, for a bivariate description of the statistics [25], and were transformed into Microsoft word. This chapter will present detailed information from the work and will decide the outcome of the research study. The study was analyzed through SPSS software and then interpreted understandably. Tables and all the charts of the research work will appear in this study. As the study is interpreted in this chapter that 45 persons participated in the research work, and all their responses are kept in this chapter elaborately.

#### 4. Results and discussion

The study was conducted under the supervision of experts in this field. So, the study showed some spectacular results. In total 45 respondents participated in this study (Table 1). The study result showed diversity between participants. Different age

groups and different professions of people have participated in the survey that's why the survey showed a diversified result on every question. The study also considered respondents' gender distribution and the occupation they are relying on (Table 1). Not only the basic category but also the study focused on the participants' family members and the amount of time they are related to the study area. During the survey, the study had more than 13 questions and asked every one of these 45 respondents to complete the survey, and the study found enough responses for the query. In Table 1 the general information of the respondent of the survey has been shown where it can be observed that almost 40% of the respondent has completed the higher secondary education level and 22% has completed their primary and undergraduate education level (Table 1), which indicated that the survey respondents are capable enough to understand the objectives of the survey. It was also observed

that most of the respondent was male and only about 31% of the respondent were female. The survey also indicated that most of the participants are living in the river area for at least 5 years (Table 1).

#### 4.1 Observation of people about Buriganga river and its environment

Table 2 is describing how people are concerned about environmental pollution or water pollution, and the study is showing 64.4% (29 people) of respondents are moderately concerned, 15.6% (7 people) are extremely concerned and 20% (9 people) are slightly concerned, which present those slightly concerned are more than for those extremely concerned and this is one of the factors causing water pollution in Buriganga river although those moderately concerned are higher than both others. Table 2 is showing the current status of the Buriganga river 64.4% (29 people) of the respondent responded Buriganga river is very polluted, while 31.1% (14 people) responded Buriganga river is polluted and

4.4% (2 people) responded Buriganga river is clean and save, this study is making thing clear that Buriganga river is very polluted, which is difficult to be used for drinking, cooking, and washing. Table 2 is stating the what are the major causes of Buriganga River pollution, after surveying we found 31.1% (14 people) are waste canals from industrial, 24.4% (11 people) are wasted, 17.8% (8 people) are household wastes, 11.1% (3 people) are rapid urbanization, 6.7% (5 people) are lack of awareness, 8.7% (4 people) are poor management, this study showed that human being is the major causes of Buriganga river pollution if we accumulate only the wastes will be around 73.3%. Table 2 is presenting here the most common diseases in the Buriganga river area, 56.6% (25 people) of the respondents said Diarrhea, 31.1% (14 people) said skin diseases, 11.1% (5 people) said Cholera, and 2.2% (1 person) malaria, so this study will let us know the most common diseases in Buriganga river area are Diarrhea and Skin Diseases. Table 2 is clarifying the existence of a water quali-

Table 1. Pilot survey information of primary respondents.

1. <b>Education Level:</b>	This study was participated by 45 respondents who were living in the Buriganga river area, the education level of respondents varied from person to person, 22.2% (10 people) among them were graduated from primary school, 40% (18 people) graduated from Higher Secondary School, 22.2% (10 people) graduated undergraduate, and 15.6% (7 people) were none educated people. This study showed that higher secondary school level participants were among the most.
2. <b>Age Distribution:</b>	In total 45 persons contributed to this research work, 21 among them (46.7%) were range between 15- 30 years old, while 24 among them (53.3%) were more than 30 years old, this will present us that most of the respondents were old or more than 30 years old.
3. <b>Gender Distribution:</b>	Among 45 respondents, 68.9% (31 people) of the respondent are male while 31.1% (14 people) are female which will declare that most people living/working Buriganga river area are male.
4. <b>Respondent's family members:</b>	Of the 45 respondents, 66.7% (30 people) of the respondents consist 0-5 family members, 31.1% (14 people) of the respondents consist of 5-10 members and 2.2% (1 person) consist of more than 10 members.
5. <b>Respondent's occupation level:</b>	Among 45 people, 48.9% (22 people) of the respondents are employees, 44.4% (20 people) are a businessman and 6.7% (3 people) are students, so we can understand the higher number of respondents are employees, those are not more concern for the Environment and water pollution.
6. <b>Respondent's living years in the Buriganga river area:</b>	This study will show us that 46.7% (21 people) of respondents were living in the Buriganga area for 1-5years, and 42.2% (19 people) of respondents were living for more than five years. 11.1% (5 people) of the respondent were living for less than 5 years.

Source: Survey Sept. 2020, Mustafe Said Nur.

**Table 2.** People’s concerns about the environment.

Q1.	How concerned are you about water pollution?	Frequency	Percentage
	Slightly concerned	9	20%
	Moderately concerned	29	64.4%
	Extremely concerned	7	15.6%
	Total	45	100%
Q2.	What do you think current Status of the Buriganga river	Frequency	Percentage
	Safe And Clean	2	4.4%
	Polluted	14	31.1%
	Very polluted	29	64.4%
	Total:	45	100%
Q3.	What do you think are the major causes of Buriganga river pollution?	Frequency	Percentage
	Wastes	11	24.4%
	Rapid urbanization	3	11.1%
	Lack of social awareness	5	6.7%
	Poor management	4	8.7%
	Waste canals from industries	14	31.1 %
	Household waste	8	17.8%
	Total:	45	100%
Q4.	What are the most common diseases in the Buriganga river area?	Frequency	Percentage
	Diarrhea	25	56.6%
	Skin diseases	14	31.1%
	Cholera	5	11.1%
	Malaria	1	2.2%
	Total	45	100%
Q5.	Is there regular examining /testing water quality of the Buriganga river?	Frequency	Percentage
	Yes	10	22.2%
	No	35	77.8%
	Total:	45	100%
Q6.	Are there well-equipped centers for disease control and prevention to prevent newly out-breaking diseases?	Frequency	Percentage
	Yes	1	2.2%
	No	44	97.8%
	Total:	45	100%

Source: Survey Sept. 2020, Mustafe Said Nur.

ty testing center in the Buriganga river area, 77.8% (35 people) of the respondents told us that there is no water quality testing center in the Buriganga river area, while 22.8% (10 people) told us there is a center, according to major of respondent’s this study will clear that there is no water quality testing center in Buriganga river area. **Table 2** is showing the availability of health centers in the Buriganga river area, 97.8% (44 people) of the respondent responded

NO, there is no health centers in the Buriganga river area while only 2.2% (1 person) responded there is a center, according to this study it’s tough to control and identify new diseases since there is lack of health center.

#### 4.2 Administration of Buriganga river protection

**Table 3** is stating the existence of strong admin-

istration in the Buriganga River area. According to the responses of interviewers 40% (18 people) of the respondents said disagree with the existence of strong administration in the Buriganga river area as well as that 40% (18 people) said strongly disagree, while only 11.1% (5 people) and 8.9% (4 people) agree, so this study declared that it is not a strong administration are Buriganga river area and this is one of the factors why Buriganga river is very polluted. **Table 3** is focusing on the government plan or how the government set plans for river protection according to respondent's responses there is a weakness in government preparation for river protection 46.7% (21 people) strongly agree that weakness and 28.9% (13 people) agreed but 11.1% (5 people) disagree also while only 13.3% (6 people) and strongly disagree that statements. **Table 3** is demonstrating the

level of rule and regulation in the river protection 44.4% (22 people) of the respondents said there is no rule and regulation in Buriganga river protection and they chose strongly disagree furthermore 20% (9 people) chose to disagree while only 17.8% (8 people) selected strongly agree and 17.8% (8 people) disagree so this table will clear us weaknesses of river protection. **Table 3** is focusing on the role of the community in Buriganga river protection and declared us there is a lack of community role and their missing are part of river pollution 57.8% (26 people) of the respondents selected strongly agree with the lack of community role and 20% (9 people) agreed that but 11.1% (5 people) disagreed also, while only 11.1% (5 people) strongly disagrees, so this will tell us community is missing in the river protection and they are part of the problem.

**Table 3.** Administration of Buriganga river protection.

Q1.	There is strong administration for Buriganga river protection?	Frequency	Percentage
	Agree	4	8.9%
	Disagree	18	40%
	Strongly agree	5	11.1%
	Strongly disagree	18	40%
	Total	45	100%
Q2.	Lack/weak of government plan are the part Buriganga river pollution	Frequency	Percentage
	Agree	13	28.9%
	Disagree	5	11.1%
	Strongly agree	21	46.7%
	Strongly disagree	6	13.3%
	Total	45	100%
Q3.	There is rule and regulation in the Buriganga river conservation	Frequency	Percentage
	Agree	8	17.8%
	Disagree	9	20 %
	Strongly agree	8	17.8%
	Strongly disagree	22	44.4%
	Total	45	100%
Q4.	The role of the community is missing in the Buriganga river protection	Frequency	Percentage
	Agree	9	20%
	Disagree	5	11.1 %
	Strongly agree	26	57.8%
	Strongly disagree	5	11.1%
	Total	45	100%

Source: Survey Sept. 2020, Mustafe Said Nur

### 4.3 Pearson correlation

To correlate with my question, the study was designed in four groups. Group 1 = Personal information of the respondents (Personal). Group 2: Measuring the level of the river (Measuring). Group 3: Rule and regulation of river protection (Regulations). Group 4: How are respondents aware of / concerned about river status (Aware)? After grouping and cor-

relating I found these results (Table 4).

To determine the linkage between the research constructs, a bivariate analysis of correlation has been used to pre-evaluate [26]. To be specific, the Pearson correlation analysis has been used to calculate the strength of the linear relationship between the variables and a strong correlation coefficient has been reported by bivariate analysis (significant at the level of 0.01) (Table 5).

Table 4. Pearson correlation.

Correlations					
		personal	measuring	regulation	aware
personal	Pearson Correlation	1	0.057	-0.086	-0.207
	Sig. (2-tailed)		0.712	0.575	0.172
	N	45	45	45	45
measuring	Pearson Correlation	0.057	1	0.570**	-0.126
	Sig. (2-tailed)	0.712		0.000	0.410
	N	45	45	45	45
regulation	Pearson Correlation	-0.086	0.570**	1	-0.021
	Sig. (2-tailed)	0.575	0.000		0.889
	N	45	45	45	45
aware	Pearson Correlation	-0.207	-0.126	-0.021	1
	Sig. (2-tailed)	0.172	0.410	0.889	
	N	45	45	45	45

\*\* . Correlation is significant at the 0.01 level (2-tailed).

Table 5. Cross-tabulation correlation.

Case Processing Summary						
	Cases					
	Valid		Missing		Total	
	N	Percent	N	Percent	N	Percent
What is your education level? * How concerned are you about -polluted water?	45	100.0%	0	0.0%	45	100.0%

What is your education level? * How concerned are you about -polluted water? Cross tabulation					
Count					
		How concerned are you about the pollution of water?			Total
		Slightly concerned	moderately concerned	extremely concerned	
What is your education level?	primary school	2	7	1	10
	higher secondary school	3	12	3	18
	undergraduate	0	7	3	10
	non-educated	4	3	0	7
Total		9	29	7	45

Table 5 continued

Case Processing Summary						
	Cases					
	Valid		Missing		Total	
	N	Percent	N	Percent	N	Percent
How long have you been living in the Buriganga river area? * What do you think current status of the Buriganga river?	45	100.0%	0	0.0%	45	100.0%

How long have you been living in the Buriganga river area? * What do you think current status of the Buriganga river? Cross tabulation						
Count						
		What do you think current status of the Buriganga river?				Total
		clean and safe	polluted	very polluted		
How long have you been living in the Buriganga river area?	less than one year	0	2	3	5	
	1-5 years	0	10	11	21	
	more than 5 years	2	2	15	19	
Total		2	14	29	45	

Case Processing Summary						
	Cases					
	Valid		Missing		Total	
	N	Percent	N	Percent	N	Percent
What do you think are the major causes of Buriganga river pollution? * Lack/weak government plan for river protection is part of the river pollution?	45	100.0%	0	0.0%	45	100.0%

What do you think are the major causes of Buriganga river pollution? * Lack/weak government plan for river protection is part of the river pollution? Cross tabulation						
Count						
		Lack/weak of government plans for river protection are part of the river pollution?				Total
		agree	disagree	strongly agree	strongly disagree	
What do you think are the major causes of Buriganga river pollution?	Wastes	1	2	6	2	11
	rapid urbanization	1	0	2	0	3
	lack of social awareness	0	1	3	1	5
	poor management	2	0	1	1	4
	waste canals from industries	5	1	6	2	14
	Household wastes	4	1	3	0	8
Total		13	5	21	6	45

#### 4.4 The main causes of Buriganga river pollution

Following the completion of the survey, the study discovered sufficient responses to the inquiry. During the survey, the study had more than 13 questions asked to each of these 45 respondents. One of the principal reasons for pollution is a lack of under-

standing and knowledge of the society that lives next to the river<sup>[3,27]</sup>. The respondent is informed that there is no ongoing or one-time awareness campaign for that society and that 20% of people are just mildly concerned about water contamination and the environment, compared to 60% who are not

particularly concerned. There aren't many educated people in that region; 40% of respondents only have a high school diploma, 22.2% have a primary school diploma, and 15.6% are uneducated. Only 22.2 respondents have completed an undergraduate degree program, and those who have aren't in the environmental sciences. Another significant source of pollution in this area is a lack of or inadequate government river protection plans <sup>[28]</sup>. 46.7% of the respondents responded strongly agree while 28.9% also responded agree this shows that weak government plans for river protection are part of Buriganga river pollution <sup>[3,27]</sup>, these weak plans will lead to a lack of rules and regulations for river protection and this will enhance pollution possibility since there are no rules which can punish those did anti-environmental activities. Waste canals from industries and household waste also make river pollution. In this study, it was quite understandable that industrial waste is the major cause of Buriganga pollution <sup>[29,28]</sup> and there are some canals from industrial that directly involve the river and impact its quality <sup>[3,27]</sup>, some other factors are also part of the Buriganga river pollution like after surveying we found 31.1% are waste canals from industrial, 24.4% are other wastes, 17.8% are household wastes, 11.1% are rapid urbanization, 6.7% are lack of awareness, 8.7% are poor management, this study has shown that human being is the major causes of Buriganga river pollution, if the study accumulates only the wastes it will be around 73.3%. The absence of a water quality testing center is also responsible for this condition water quality testing center contributes maintenance of water quality, if there is regular testing the possibility of pollution will be very rare <sup>[3]</sup> but unfortunately, the Buriganga river has no water quality center as 77.8% of the respondents said, and this is one of the factors causing Buriganga river pollution. Lack of community participation in river protection can play a key role in pollution <sup>[27]</sup>. The role of civil society is missing, no one is taking care of the river, no groups are protecting the river by their own decision, mostly they seem irresponsible in the case of river protection.

#### **4.5 Health status community living beside the river**

Buriganga River is very polluted, according to 64.4% of respondents, while 31.1% of respondents said the same. This study will make it clear that the river is very polluted, making it difficult to use it for drinking, cooking, or washing. As a result, the polluted water impacted the community living next to the river, and the researchers noted that the current situation is not good <sup>[30]</sup>, furthermore, there is no health center in that area, where the community can control or identify newly out broke diseases, it's very difficult to identify breaking diseases within a short time, due to a lack of health centers.

#### **4.6 Most common diseases in the Buriganga river area**

Finally, during the research work, the study identified the most common diseases in the Buriganga river area <sup>[30]</sup>. And they become like the following,

- 56.6% of the respondents said diarrhea,
- 31.1% said skin diseases,
- 11.1% said cholera,
- 2.2% malaria.

So, this study indicated that the most common diseases in the Buriganga river area are Diarrhea and Skin Diseases.

#### **4.7 River water pollution impacts health in Asian countries**

In Asia, resources like clean water, clean air, and a fresh environment are becoming increasingly scarce. Growing human populations, increased industrialisation, and agricultural expansion have had a major impact on natural ecosystems and water quality during the past 50 years. These issues could be made worse by climate change in the area <sup>[31]</sup>. Asia's fast industrializing and the urbanizing economy will have an impact on local, regional, and global surroundings as a result of the trajectory of social and technological change <sup>[32]</sup>. Because of industrialization and overpopulation the water quality of Asian

rivers is degrading. For example, in a study based on the Buriganga river of Bangladesh, it was shown that the river water quality is degrading. The degradation of the water quality has several health impacts [33]. In **Table 6** the major rivers from different countries

were considered to show how river pollution is impacting the health of the population where it can be observed that several countries from Asia have river pollution which is directly impacting the health of their population (**Table 6**).

**Table 6.** List of some major rivers, their sources of pollution, and their health impact on South-East Asian countries Malaysia and the Philippines.

Country	River Name	Source of Water pollution	Health Impact	References
Malaysia	Kuantan, Pahang	Manufacturing industries, chemical industry Agro-based Industries, Rubber Mills, Palm Oil Mill, Animal Pig, Sewage Treatment Plant, Food Services Establishment	The concentration of heavy metals in fish was found at a carcinogenic level which causes adverse effects on human life. Poor blood circulation, skin lesions, vomiting, and damage to the nervous system.	[34]
Malaysia, Kuala Lumpur	Jinjang River	Agricultural and development activities,	Extremely contaminated with fecal coliform bacteria (E. coli) create a health hazard.	[35]
Malaysia, Kuala Lumpur	Jinjang River	Leachate Treatment Plant	Leachate may affect human health as leachate contains heavy metals such as lead, cadmium, aluminum, copper sulfate, nickel, and zinc	[36]
Philippine, Manila	Pasig-Marikina River,	Industrial and household contamination	Water quality is not suitable for any aquatic life.	[16]
Philippines, Manila, Bulacan	Marilao River	Organic pollution and heavy metal pollution. Heavy metal pollution mainly comes from jewelry smelting, tanneries, used lead-acid battery recycling, and other industries dealing with heavy metals	Health risk to close communities that surround the stream water for fish ponds, bathing, and swimming that causes some health issues	[37]
Jakarta, Indonesia	Ciliwung River	Human waste, industries such as metal plating, and textile. food-processing, pharmaceutical, electronics, paint, and paper. fertilizer. chemicals	A high level of BOD can affect the underwater organism, contaminated with Faecal coli.	[38]
Eastern Jakarta, Indonesia	Sunter River	Industrial waste and Human waste	A low amount of DO can affect water quality, High BOD and Faecal coli make water unsuitable for aquatic organisms	[39]
North Jakarta, Indonesia	Jakarta Bay	Land drainage, urban stormwater runoff, atmospheric deposition, and industrial waste from r the metal, battery, leather, and textile industries.	effects of the volatile components of oil on corals, oil residues, heavy metals, and organic micro-pollutants have potential human health impacts.	[40]
Thailand	ThaChin river	Aquaculture plays the most important role in nutrient pollution, contributing 62% and 54% of the total NET N and P load to the river system also RICE farming is also a very significant pollution source, PIG farming, households, and industries.	Critical Dissolve Oxygen (DO) level resulting in fish death. low oxygen and elevated ammonia and phosphorus levels. The high nutrient concentrations lead to eutrophication.	[41]
India	Sutlej river	Industrial waste, sewage, and agricultural runoff are contaminating the Sutlej river in the Indian Punjab.	Cd > Ni > Cr > As was the metal with the highest potential of causing cancer, and regions along transboundary lines had the highest risk.	[42]
India	Ganga river	Fe, Mn, Zn, Cr and Pb are the main pollutant. The river water has been found to be severely contaminated due to heavy metals	Target cancer risk assessment showed high carcinogenic risk from As, Cr, Ni and Pb as well as residues of DDT and HCHs.	[43] [44]

Table 6 continued

India	Ajay River basin	The degree of contamination in the sediments of the Dikrong river, for the metals Al, Fe, Ti, Mn, Zn, Cu, Cr, Ni and Pb, has been evaluated. the water is highly contaminated through numerous geogenic and anthropogenic sources.	High load of Cd, Pb and Fe in water body could harm the population.	[45]
Pakistan	Siran river	Due to agricultural activities, the direct dumping of solid waste into rivers, and the discharge of domestic waste water effluent, the pollution level in the Siran River is rising.	High value of TSS, COD and E. coli can create major health impact.	[46]
Pakistan	Kabul River	One of the main sources of pollution in the Kabul River is textile effluent.	The substantial decrease in fish and crop which ultimately harm human health.	[47]
China	Wei River	Heavy metals (Hg, Cd, Cr(VI), Pb, and As)	With the exception of As, the five heavy metals in the area posed tolerable health risks. But Arsenic (As) in food and drinking water can cause cancer and skin sores when consumed over an extended period of time.	[48]
China	Huaihe River	Various organic pollutants, including Polycyclic Aromatic Hydrocarbons (PAHs), Organochlorine Pesticides (OCPs) and some other Semi-Volatile Organic Compounds (SVOCs)	high level of health risk in the study area mainly cancer.	[49]
Sri Lanka	River Mahaweli	Cadmium (Cd), Cadmium, derived from contaminated phosphate fertilizer, in irrigation water finds its way into reservoirs	Chronic renal failure (CRF)	[50]

## 5. Conclusions

One of the most crucial water sources for Bangladesh’s capital city of Dhaka is the Buriganga River. The Buriganga River serves as a key source of water for the city of Dhaka, however due to several shortcomings in the correct management system, it is unfortunately becoming increasingly polluted over time. Although the issue of water pollution is widely acknowledged and discussed, no appropriate steps have been made to address it. The study survey revealed how participants relate to the issue and how they accept accountability. Numerous issues have been found in the study as a result of the Buriganga river’s water pollution, and those issues directly affect the general public’s health in the area. So, the pollution rate of Buriganga reaches an alarming state where it can be a threat to the survival of Dhaka city. A proper step is mandatory to take immediately so that the pollution problem of the Buriganga river can be resolved.

## Conflict of Interest

There is no conflict of interest.

## Acknowledgment

The authors are highly obliged and thankful to all the co-authors and also those who have helped to complete the field survey successfully.

## References

- [1] Baki, M.A., Islam, M.R., Hossain, M.M., et al., 2015. Livelihood status and assessment of fishing community in adjacent area of Turag-Buriganga River, Dhaka, Bangladesh. *International Journal of Pure and Applied Zoology*. 3, 347-353.
- [2] Salman, M.A., Ahmed, S., Peas, M.H., et al., 2018. Water quality assessment of the Buriganga river, Dhaka, Bangladesh. *Journal of Environment and Earth Science*. 4(1), 47.

- [3] Bhowmik, A.K., 2007. Buriganga pollution: Reasons & prospects. Environment & urban development: Share your ideas and experiences, 1st edition. Urban and Rural Planning Discipline, Science, Engineering and Technology School, Khulna University: Bangladesh. pp. 87-97.
- [4] Ahammed, S.S., Tasfina, S., Rabbani, K.A., et al., 2016. An investigation into the water quality of Buriganga-A river running through Dhaka. International Journal of Scientific & Technology Research. 5, 36-41.
- [5] Halder, J.N., Islam, M.N., 2015. Water pollution and its impact on the human health. Journal of Environment & Human. 2, 36-46.
- [6] Hasan, M.K., Shahriar, A., Jim, K.U., 2019. Water pollution in Bangladesh and its impact on public health. Heliyon. 5, e02145.
- [7] Zaman, F.I., 2020. Determination of minimum inhibitory concentration of Chromium Salts on the microbial strains isolated from Buriganga River-bed soil [Bachelor's thesis]. Bangladesh: Brac University.
- [8] Ahmad, M.K., Islam, S., Rahman, S., et al., 2010. Heavy metals in water, sediment and some fishes of Buriganga River, Bangladesh. International Journal of Environmental Research. 4(2), 321-332.
- [9] Islam, M.S., Afroz, R., Mia, M.B., 2019. Investigation of surface water quality of the Buriganga river in Bangladesh: Laboratory and spatial analysis approaches. Dhaka University Journal of Biological Sciences. 28, 147-158.
- [10] Ahmed, M.K., Baki, M.A., Kundu, G.K., et al., 2016. Human health risks from heavy metals in fish of Buriganga river, Bangladesh. Springerplus. 5, 1-12.
- [11] Ali, M.Y., Amin, M.N., Alam, K., 2008. Ecological health risk of Buriganga river, Dhaka, Bangladesh. Hydro Nepal Journal of Water Energy & Environment. 3, 25-28.
- [12] Rahman, M.A., Bakri, D.A., 2010. A study on selected water quality parameters along the River Buriganga, Bangladesh. Iranica Journal of Energy & Environment. 1, 81-92.
- [13] Kamal, M.M., Malmgren-Hansen, A., Badruz-zaman, A.B.M., 1999. Assessment of pollution of the River Buriganga, Bangladesh, using a water quality model. Water Science & Technology. 40, 129-136.
- [14] Afroz, R., Rahman, A., 2017. Health impact of river water pollution in Malaysia. International Journal of Advanced & Applied Sciences. 4, 78-85.
- [15] Andrews, G., 2018. Resolving the water pollution crisis in the Philippines: The implications of water pollution on public health and the economy. Pepperdine Policy Review. 10, 2.
- [16] Kumar, P., Masago, Y., Mishra, B.K., et al., 2018. Evaluating future stress due to combined effect of climate change and rapid urbanization for Pasig-Marikina River, Manila. Groundwater for Sustainable Development. 6, 227-234.
- [17] Huq, R.N., 2016. Assessing architect's role in seismic evaluation and risk mitigation [Master's thesis]. Dhaka: BRAC University.
- [18] Islam, K.A., Hossain, M.R., Chowdhury, T.J., et al., 2017. Accessibility of emergency rescue vehicle in the road network of Old Dhaka, Bangladesh. International Interdisciplinary Journal of Scientific Research. 3, 91-107.
- [19] Mahmood, S., Nourin, F.T.J., Siddika, A., et al., 2017. Encroachment of the Buriganga river in Bangladesh. Journal of Minerals and Materials Characterization and Engineering. 5, 266-273.
- [20] Alam, K., 2008. Cost-benefit analysis of restoring Buriganga river, Bangladesh. International Journal of Water Resources Development. 24, 593-607.
- [21] Hossain, M., Baki, M., 2015. Present status of preliminary survey on avifauna diversity and distribution in the most polluted river Buriganga, Dhaka, Bangladesh. International Journal of Pure and Applied Zoology. 3, 59-69.
- [22] Stern, C., Jordan, Z., McArthur, A., 2014. Developing the review question and inclusion criteria. American Journal of Nursing Official Magazine of the American Nurses Association. 114, 53-56.

- [23] Patino, C.M., Ferreira, J.C., 2018. Inclusion and exclusion criteria in research studies: Definitions and why they matter. *Jornal Brasileiro De Pneumologia*. 44, 84.  
DOI: <https://doi.org/10.1590/s1806-3756201800000088>
- [24] Terera, S.R., Ngirande, H., 2014. The impact of rewards on job satisfaction and employee retention. *Mediterranean Journal of Social Sciences*. 5, 481.
- [25] Carlberg, C., 2014. *Statistical analysis: Microsoft excel 2013*. Que Publishing: Seattle, USA.
- [26] Reitsma, J.B., Glas, A.S., Rutjes, A.W.S., et al., 2005. Bivariate analysis of sensitivity and specificity produces informative summary measures in diagnostic reviews. *Journal of Clinical Epidemiology*. 58, 982-990.
- [27] Alam, M.K., Marinova, D., 2003. Ecological health of rivers: A case for integrating government, community and private sector. *Proceedings of the International Sustainability Conference: Regional Governance for Sustainability*. 48(7), 149-156.
- [28] Sarkar, M., Rahman, A.K.M.L., Islam, J.B., et al., 2015. Study of hydrochemistry and pollution status of the Buriganga river, Bangladesh. *Bangladesh Journal of Scientific & Industrial Research*. 50, 123-134.
- [29] Moniruzzaman, M., Alam, A.B.M.S., Rahman, M.S., et al., 2018. Contiguous reaction of manufacturing effluent on Buriganga river of Bangladesh. *Sciences (New York)*. 5, 102-109.
- [30] Reza, A., Bin Yousuf, T., 2016. Impacts of waste dumping on water quality in the Buriganga River, Bangladesh and possible mitigation measures. *Journal of the Environment*. 11, 35-40.
- [31] Khan, S., Hanjra, M.A., 2009. Footprints of water and energy inputs in food production—Global perspectives. *Food Policy*. 34, 130-140.
- [32] Angel, D., Rock, M.T., 2009. Environmental rationalities and the development state in East Asia: Prospects for a sustainability transition. *Technological Forecasting & Social Change*. 76, 229-240.
- [33] Pasha, A.B.M.K., Abdillahi, M.M., Rahman, S.M.M., et al., 2022. Studies on physicochemical properties of buriganga river water and the vegetation coverage of surrounding area, Dhaka, Bangladesh. *Sci. Int. (Lahore)*. 34(2),73-78.
- [34] Amirah, M.N., Afiza, A.S., Faizal, W.I.W., et al., 2013. Human health risk assessment of metal contamination through consumption of fish. *Journal of Environment Pollution & Human Health*. 1, 1-5.
- [35] Rashid, S.A.A., Gasim, M.B., Toriman, M.E., et al., 2013. Water quality deterioration of Jinjang River, Kuala Lumpur: Urban risk case water pollution. *Arab World Geographer*. 16, 349-362.
- [36] Chin, P.M., Naim, A.N., Suja, F., et al., 2020. Impact of effluent from the leachate treatment plant of Taman Beringin solid waste transfer station on the quality of Jinjang River. *Processes*. 8, 1553.
- [37] Victoriano, J.M., Santos, M.L.C., Vinluan, A.A., et al., 2022. Predicting pollution level using random forest: A case study of Marilao River in Bulacan Province, Philippines. *International Journal of Computing Sciences Research*. 3(1), 151-162.
- [38] Palupi, K., Sumengen, S., Inswiasri, S., et al., 1995. River water quality study in the vicinity of Jakarta. *Water Science & Technology*. 31, 17-25.
- [39] Martinus, Y., Astono, W., Hendrawan, D. (editors), 2018. *Water quality study of Sunter River in Jakarta, Indonesia*. IOP Conference Series Earth and Environmental Science; 2017 Aug 9-10; Jakarta, Indonesia. IOP Publishing: UK. p. 12022.
- [40] Gilbert, A., James, D., 1994. *Water pollution in Jakarta Bay. The Application of Economic Techniques in Environmental Impact Assessment*. Springer: Germany. pp. 111-142.
- [41] Schaffner, M., Bader, H.P., Scheidegger, R., 2009. Modeling the contribution of point sources and non-point sources to Thachin River water pollution. *Science of the Total Environment*. 407, 4902-4915.

- [42] Setia, R., Dhaliwal, S.S., Kumar, V., et al., 2020. Impact assessment of metal contamination in surface water of Sutlej River (India) on human health risks. *Environmental Pollution*. 265, 114907.
- [43] Chaudhary, M., Mishra, S., Kumar, A., 2017. Estimation of water pollution and probability of health risk due to imbalanced nutrients in River Ganga, India. *International Journal of River Basin Management*. 15, 53-60.
- [44] Prasad, S., Saluja, R., Joshi, V., et al., 2020. Heavy metal pollution in surface water of the Upper Ganga River, India human health risk assessment. *Environmental Monitoring & Assessment*. 192, 1-15.
- [45] Singh, U.K., Kumar, B., 2017. Pathways of heavy metals contamination and associated human health risk in Ajay River basin, India. *Chemosphere*. 174, 183-199.
- [46] Bibi, S.Z., Amir, H.M., Amir, W., et al., 2011. Water quality assessment of Siran river, Pakistan. *International Journal of Physical Sciences*. 6, 7789-7798.
- [47] Abrar, M., Hussain, Z., Akif, M., et al., 2011. Textile effluents and their contribution towards aquatic pollution in the Kabul River (Pakistan). *Journal—Chemical Society of Pakistan*. 24, 106.
- [48] Yang, X., Duan, J., Wang, L., et al., 2015. Heavy metal pollution and health risk assessment in the Wei River in China. *Environmental Monitoring and Assessment*. 187, 1-11.
- [49] Wang, B., Yu, G., Yu, Y.J., et al., 2009. Health risk assessment of organic pollutants in Jiangsu Reach of the Huaihe River, China. *Water Science & Technology*. 59, 907-916.
- [50] Bandara, J., Wijewardena, H.V.P., Bandara, Y., et al., 2011. Pollution of River Mahaweli and farmlands under irrigation by cadmium from agricultural inputs leading to a chronic renal failure epidemic among farmers in NCP, Sri Lanka. *Environmental Geochemistry and Health*. 33, 439-453.

ARTICLE

## Quantum Atmospheric Biophysics: A Comparison of Four Weather Stations in India on Average Monthly Temperatures Since 1892 and Forecasts to 2150

Mazurkin Peter Matveevich<sup>ORCID</sup>

Volga State University of Technology, Yoshkar-Ola, the Republic of Mari El, 424000, Russia

### ABSTRACT

The identification method revealed asymmetric wavelets of dynamics, as fractal quanta of the behavior of the surface air layer at a height of 2 m, according to the average monthly temperature at four weather stations in India (Srinagar, Jolhpur, New Delhi and Guvahati). For Srinagar station, the maximum for all years is observed in July, for Jolhpur and New Delhi stations it shifts to June, and for Guvahati it shifts to August. With a high correlation coefficient of 0.9659, 0.8640 and 0.8687, a three-factor model of the form was obtained. The altitude, longitude and latitude of the station are given sequentially. The hottest month for Srinagar over a period of 130 years is in July. At the same time, the temperature increased from 23.4 °C to 24.2 °C (by 3.31%). A noticeable decrease in the intensity of heat flows in June occurred at Jolhpur (over 125 years, a decrease from 36.2 °C to 33.3 °C, or by 8.71%) and New Delhi (over 90 years, a decrease from 35.1 °C to 32.4 °C, or by 7.69%). For almost 120 years, Guvahati has experienced complex climate changes: In 1902, the hottest month was July, but in 2021 it has shifted to August. The increase in temperature at various stations is considered. At Srinagar station in 2021, compared to 1892, temperatures increased in June, September and October. Guvahati has a 120-year increase in December, January, March and April. Temperatures have risen in February, March and April at Jolhpur in 125 years, but have risen in February and March at New Delhi Station in 90 years. Despite the presence of tropical evergreen forests, the area around Guvahati Station is expected to experience strong warming.

**Keywords:** India; 4 weather stations; Average monthly temperature; Waves of behavior; Sum of wavelets; Verification; Forecasts

#### \*CORRESPONDING AUTHOR:

Peter Matveevich Mazurkin, Volga State University of Technology, Yoshkar-Ola, the Republic of Mari El, 424000, Russia; Email: [kaf\\_po@mail.ru](mailto:kaf_po@mail.ru)

#### ARTICLE INFO

Received: 5 August 2022 | Revised: 5 March 2023 | Accepted: 14 March 2023 | Published Online: 24 March 2023

DOI: <https://doi.org/10.30564/jees.v5i1.4942>

#### CITATION

Mazurkin, M.P., 2023. Quantum Atmospheric Biophysics: A Comparison of Four Weather Stations in India on Average Monthly Temperatures Since 1892 and Forecasts to 2150. *Journal of Environmental & Earth Sciences*. 5(1): 17-32. DOI: <https://doi.org/10.30564/jees.v5i1.4942>

#### COPYRIGHT

Copyright © 2023 by the author(s). Published by Bilingual Publishing Group. This is an open access article under the Creative Commons Attribution-NonCommercial 4.0 International (CC BY-NC 4.0) License. (<https://creativecommons.org/licenses/by-nc/4.0/>).

## 1. Introduction

The farmers of India since ancient times waged a real war with the forests. They had to win back plots for crops <sup>[1]</sup>. Based on descriptive statistics from a large number of statistical samples, Kumar et al. <sup>[2]</sup> concluded that deforestation is the main cause of global warming and climate change.

Ullah et al. note that mountain ecosystems are considered sensitive indicators of global warming; even small variations in temperature can lead to significant shifts in the local climate <sup>[3]</sup>.

The main causes are greenhouse gases and deforestation. Appropriate policies are needed to conserve forests, wildlife, prevent hunting, control pollution, increase plantations, awareness, of climate change control, etc.

The climate of India is very diverse. Four types can be distinguished: Dry tropical, humid tropical, subequatorial monsoon and high mountain. In the north, the country is fenced off from the cold Asian winds by the Himalayas, and in the northwest, a large territory is occupied by the Thar Desert, which attracts warm, humid monsoons. They determine the peculiarities of the Indian climate <sup>[4]</sup>.

The results indicate that significant concentrations of areas with maximum dryness are located in the west-central part of India. In general, there is a gradual increase in the extent of the arid zone over a 60-year period, and spatially there is a maximum degree of percentage change in the area of aridity <sup>[5]</sup>.

Many countries have made ambitious commitments to increase forest area to mitigate climate change. However, the availability of land to achieve these goals is not yet well understood <sup>[6]</sup>.

The purpose of the article is to identify asymmetric wavelets of dynamics, as fractal quanta of the behavior of the surface air layer at a height of 2 m, by the method of identification <sup>[7-11]</sup>, based on the average monthly temperature on the territory of four weather stations in India (Srinagar, Jolhpur, New Delhi, Guvahati) from 1892 to 2021, i.e. over a period of 130 years, analyze the wave patterns of the regional climate, compare critical heat waves with forest types, and calculate monthly average tempera-

ture forecasts up to 2150.

## 2. The concept of quantum biophysics of the atmosphere in India

With the bifurcations of the atmosphere and climate, many natural landscapes do not change for thousands of years, for example, the grass cover of the steppes <sup>[10,11]</sup>. The grass appeared on the land about 100 million years ago. Maybe grass, as the strongest type of vegetation among the first three classes of soil cover according to the UN classification (grass, shrubs and trees—appeared about 400 million years ago), has such values of oscillatory adaptation parameters that it will survive any climate changes in the future. What are these limits of grass cover life?

For example, the Eurasian steppe is 8000 km long from Hungary to Inner Mongolia China? We believe that in India, the Thar desert should first be turned into steppes with grass cover. The succession processes of the vegetation cover are such that at first grass appears on human-modified land plots after a few years. After 7-10 years, bushes appear among the grass. And only after a few decades, the first deciduous forests appear on the grass cover and shrubs, which are replaced by conifers after 60-100 years.

Why such a natural order of change of types of vegetation cover?

The answer lies in the latest fundamental research on mushrooms.

Trees do not live without symbiosis with fungi. Only grass and shrubs begin to form mycelium. Therefore, even modern technologies for planting large-sized seedlings will lead to the almost complete death of trees, especially in strong heat waves and lack of precipitation for the months of the year.

To answer the questions of the symbiosis of plants and fungi, it is necessary not only to study the interactions between woody plants and fungi, but also to develop forecasts of meteorological climate parameters for specific land plots. In many ways, critical temperature waves on the ground appear due to the gradual reduction of forests, as higher plants live only in symbiosis with fungi. Harvesting timber

not only reduces forests, but also eliminates the symbiotic interaction between trees and mushrooms.

Then it is necessary to identify not only the behavioral quanta of the surface air layer at different points and regions of the Earth according to weather stations in the form of long time series, but also at least approximately determine the moments of a succession of the vegetation cover.

The role and mechanisms of climatic impact on plant productivity are multifaceted. Among the meteorological variables, the humidity index was found to have the greatest effect on plants. Climates, such as air temperature and rainfall, varies greatly between urban core and periphery areas, resulting in different growing conditions for trees<sup>[12]</sup>.

Roya et al. characterized and mapped the distribution of vegetation types in India by area, percentage of protected area covered by each vegetation type, altitude range, mean annual temperature and precipitation over the past 100 years. The natural vegetation was subdivided into forests, bushes and pastures, and these three types together make up the vegetation cover. This vegetation-type map is the most complete for India<sup>[13]</sup>.

However, over 100 years, the vegetation cover in this area has changed dramatically. First, forests die out, then the productivity of bushes and grass decreases. Desertification is taking place. At the same time, the temperature of the surface layer of the atmosphere at a height of 2 m rises sharply. But much more increases the temperature on the surface of the soil and especially roads. As a rule, this is the anthropogenic impact on the climate. Without man, all natural objects are in ecological balance. They have oscillatory adaptation to changes in each other's parameters and maintain climate stability for millennia. Under trees, bushes and grass, the temperature is lower compared to open ground, and even less so compared to roads.

The materials of the article<sup>[13]</sup> state well the state of the vegetation cover in India. However, a detailed classification of vegetation cannot be linked to the temperature dynamics over 100 years, since the average annual temperature and precipitation are

taken only as averages over 100 years. In further studies, two points should be taken into account: First, instead of the average annual values of temperature and precipitation, we should switch to average monthly values for 100 years; secondly, to adopt a system of vegetation quality parameters according to their typology, which will make it possible to identify at least rough trends in future changes in vegetation cover.

### 3. Materials and methods

We will not rush to identify cause-and-effect relationships in sharp warming in India according to four weather stations (Srinagar, Jolhpur, New Delhi, Guwahati), but we will compare these weather stations by the average monthly temperature for all years of measurements and show stable patterns of the dynamics of the average monthly temperature for 1892-2021. The series of mean monthly surface temperatures at a height of 2 m were taken from the site <http://www.pogodaiklimat.ru/history/42182.htm> (Accessed 06/23/2022).

**Table 1** gives fragments of initial data arrays for identifying asymmetric wavelets of the average monthly temperature dynamics.

The year 1892 ( $\tau = 0$  January 1) was adopted as the beginning of the time reference  $\tau$  (years) according to the dynamic temperature series of three meteorological stations (Srinagar, Jolhpur, Guwahati). For each month, its specific time is taken according to the expression  $(\text{Year} - 1892) + \text{month} / 12$ . Here the month is taken as follows: January = 1; February = 2, etc. Then 130 years have passed from January 1892 to December 2021, so the indicative forecast can be made for the forecast horizon equal to the forecast base, that is, until  $2021 + 130 = 2151$  years. Our calculations were performed until 2150. However, due to the sharp increase in temperature at Guwahati station, the forecast was only valid until 2080. At the same time, the temperature in New Delhi starts only from 1931, so a separate time scale was adopted for this time series.

**Table 1** gives a fragment of the data array of the average monthly temperature of the surface air layer

**Table 1.** Average monthly air temperatures (°C) at four weather stations in India.

Year	January			...	July			...	December	
	Time $\tau$	Temperat. $t$			Time $\tau$	Temperat. $t$			Time $\tau$	Temperat. $t$
Weather station Srinagar, Montane Forests <sup>[5]</sup> , 0.092-0.226 MgC/ha										
1892	0.083	4.7	...	0.583	23.4	...	1	3.2		
1893	1.083	0.6	...	1.583	23.4	...	2	3.9		
...	...	...	...	...	...	...	...	...		
2020	128.083	1.9	...	128.583	24.5	...	129	3.9		
2021	129.083	-0.1	...	129.583	24.2	...	130	3.0		
Weather station Jolhpur, Tropical Thorn Forests, 0.000-0.092 MgC/ha										
1897	5.083	17.1	...	5.583	32.6	...	6	18.6		
1898	6.083	19	...	6.583	32.1	...	7	18.4		
...	...	...	...	...	...	...	...	...		
2020	128.083	15.6	...	128.583	32.6	...	129	19.1		
2021	129.083	16.4	...	129.583	32.3	...	130	17.7		
Weather station New Delhi, Tropical Thorn Forests, 0.000-0.092 MgC/ha										
1931	0.083	15.4	...	0.583	31.7	...	1	15.5		
1932	1.083	15.6	...	1.583	31.7	...	2	14.7		
...	...	...	...	...	...	...	...	...		
2020	89.083	13.7	...	89.583	31.5	...	90	15.2		
2021	90.083	12.9	...	90.583	31.5	...	91	14.5		
Weather station Guwahati, Tropical Evergreen Forests, 0.226-0.524 MgC/ha										
1903	11.083	15.6	...	11.583	29.4	...	12	17.4		
1904	12.083	16.8	...	12.583	28.8	...	13	16.9		
...	...	...	...	...	...	...	...	...		
2020	128.083	17.6	...	128.583	29.1	...	129	19.5		
2021	129.083	17.9	...	129.583	29.0	...	130	19.1		

at a height of 2 m according to measurements at meteorological stations. In it, in the largest first array, there are  $130 \times 12 = 1560$  values of average monthly temperature in total. The representativeness of the time series is 100%.

Oscillations (asymmetric wavelet signals), as quanta of the behavior of a prism layer of air at a height of 2 m in New Delhi, in the general case, are written by the wave formula<sup>[7-10]</sup> of the general form:

$$y = \sum_{i=1}^m y_i, y_i = A_i \cos(\pi x / p_i - a_{8i}),$$

$$A_i = a_{1i} x^{a_{2i}} \exp(-a_{3i} x^{a_{4i}}), p_i = a_{5i} + a_{6i} x^{a_{7i}} \tag{1}$$

where  $y$  is the indicator (dependent factor),  $i$  is the number of the component of the model (1),  $m$  is the number of members in the model (1),  $x$  is the explanatory variable (influencing factor),  $a_1...a_8$  are the parameters of the model (1) that take numerical

values during structural and parametric identification program environment CurveExpert-1.40 (URL: <http://www.curveexpert.net/>) according to statistical data,  $A_i$  is the amplitude (half) of the wavelet (axis  $y$ ),  $p_i$  is the half-period of oscillation (axis  $x$ ).

## 4. Results and discussion

### 4.1. Comparison of monthly average temperature at weather stations

#### *Average temperature for all years of measurements*

**Table 2** compares four meteorological stations according to the total average monthly temperature for all years (**Figure 1**).

The maximum temperature for each weather station is different. For example, for Srinagar station,

the maximum for all years is observed in July, for Jolhpur and New Delhi stations, the maximum shifts to June, and for Guwahati station, it shifts to August.

**Table 2.** Average temperature of four weather stations in India for all years.

Month	Srinagar	Jolhpur	New Delhi	Guwahati
Jan	1.57	17.23	14.04	15.77
Feb	3.69	19.84	17.17	17.67
Mar	8.77	25.36	22.66	21.16
Apr	13.59	30.66	28.81	23.38
May	17.73	34.24	32.82	24.61
Jun	21.69	34.34	33.66	25.99
Jul	24.20	31.71	31.17	26.52
Aug	23.68	29.89	30.02	26.60
Sep	20.02	29.94	29.38	25.95
Oct	13.86	28.2	26.07	24.04
Nov	7.89	23.16	20.37	20.34
Dec	3.41	18.8	15.49	16.78

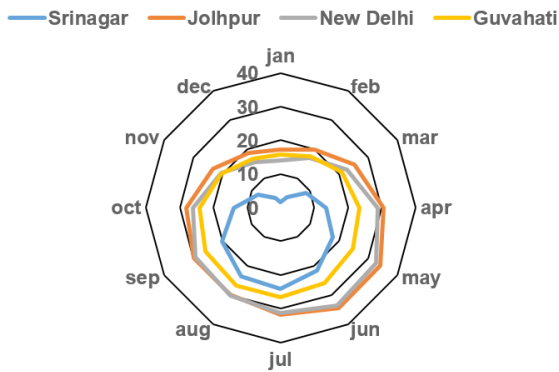


**Figure 1.** Monthly average temperature charts for all years.

**Figure 1** shows that Srinagar has the lowest temperatures as it lies within the other charts. Then the Guwahati chart is visible, after New Delhi. The hottest weather is observed for Jolhpur station in India.

**Influence of geographic coordinates on average temperature**

**Table 3** shows the geographical coordinates of

**Table 3.** Geographical coordinates of weather stations and average temperature.

Weather station	The months n, pcs.	Latitude $\alpha$ , °	Longitude $\beta$ , °	Height h, m	Temperature $\bar{t}$ , °C	Error $\Delta$ , %
Srinagar	1560	34.08	74.83	1587	13.34	0.43
Jolhpur	1500	26.30	73.02	224	26.95	<b>1.99</b>
New Delhi	1092	28.58	77.20	216	25.14	-0.91
Guwahati	1428	26.10	91.58	54	24.47	-1.50

four weather stations compared with the average monthly temperature for all years.

With a high correlation coefficient of 0.9659, 0.8640 and 0.8687, a three-factor model was obtained (**Figure 2**), which is valid only in the intervals of change of each influencing variable, of the form:

$$\bar{t} = 45.16459 - 0.0083426h - 0.16343\beta - 0.18818\alpha \quad (2)$$

The maximum relative error of 1.99% was obtained for the Jolhpur weather station. As a result, the three-factor model (2) receives a relative error of less than 5%, that is, the geographical location of weather stations greatly affects the overall average monthly temperature. Then a new direction opens in the geographical modeling of the parameters of global and regional climatic and meteorological processes.

**Figure 2** shows the graphs of the linear pattern for each of the influencing variables, and also shows the graph of the residuals after formula (2).

The linear model is the simplest in design. To identify an asymmetric wavelet (1), it is necessary to accept a data table for at least 15 stations.

**The range of average monthly temperature at weather stations**

It is important to know the intervals of change of the average monthly temperature for all the years of measurements.

**Table 4** shows such data for four weather stations.

The hottest month for Srinagar station over a period of 130 years at an altitude of 2 m is in July. At the same time, the temperature increased from 23.4 °C to 24.2 °C (an increase of 3.31%). A noticeable decrease in the intensity of heat flows in June occurred at Jolhpur stations (over 125 years, a decrease from 36.2 °C to 33.3 °C, or by 8.71%) and New Delhi (over 90 years, a decrease from 35.1 °C to 32.4 °C,

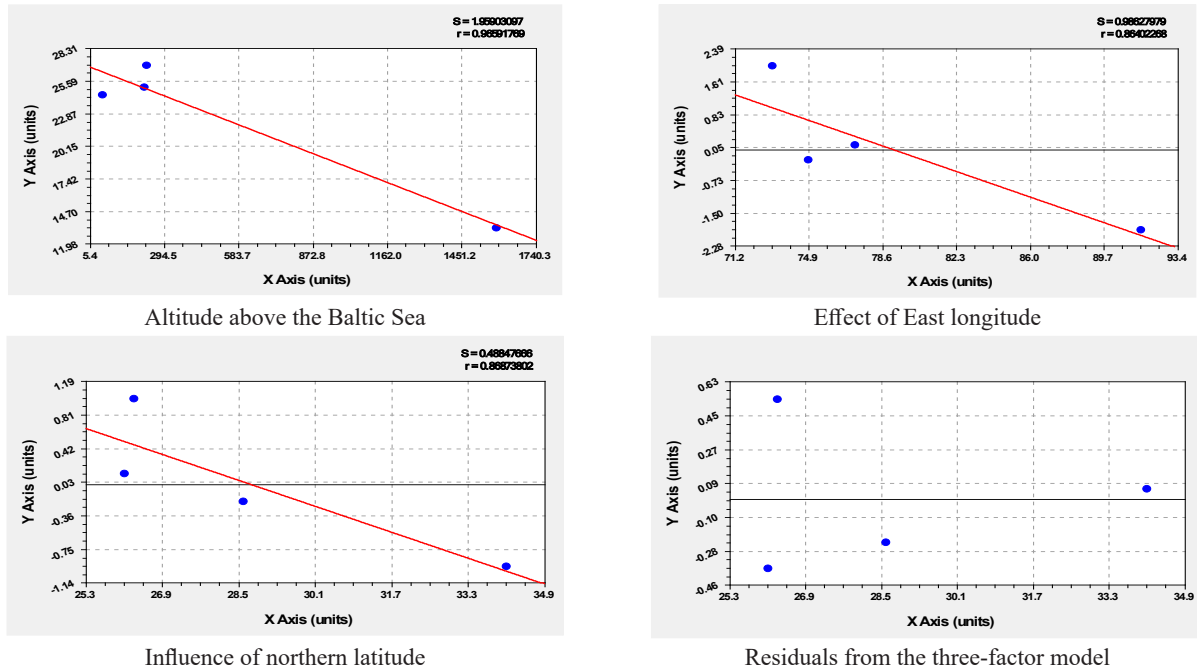


**Figure 2.** Graphs of the influence of the geographical coordinates of four weather stations in India on the average monthly temperature for all years from 1892 to 2021. (In the upper right corner: *S* standard deviation; *r* correlation coefficient.)

or by 7.69%). For almost 120 years, the Guwahati weather station has experienced complex climate changes: In 1902, the hottest month was July, but in 2021 it has shifted to August. However, at the same time, the maximum average monthly temperature decreased from 29.4 °C to 29.3 °C, or by 0.34%.

**Table 4.** Range of average monthly temperature at weather stations in India.

Month	Srinagar		Jolhpur		New Delhi		Guwahati	
	1892	2021	1897	2021	1931	2021	1902	2021
Jan	4.7	-0.1	17.1	16.4	15.4	12.9	15.6	17.9
Feb	5.6	5.8	18.9	21.3	15.2	18.6	18.3	20.3
Mar	10.8	10.1	24.3	27.8	21.2	25.0	22.1	24.1
Apr	16.3	12.8	30.2	31.6	29.7	28.6	25.7	26.4
May	18.2	17.5	35.7	32.8	33.1	30.4	26.8	26.9
Jun	19.5	22.1	36.2	33.3	35.1	32.4	27.6	28.7
Jul	23.4	24.2	32.6	32.3	31.7	31.5	29.4	29.0
Aug	23.1	23.3	30.7	31.5	30.3	30.9	28.5	29.3
Sep	18.9	21.9	30.5	29.7	28.6	29.0	28.4	29.0
Oct	12.3	14.0	26.9	28.2	25.3	26.0	27.1	27.8
Nov	6.9	6.0	22.8	22.1	19.1	18.8	22.1	22.2
Dec	3.2	3.0	18.6	17.7	15.5	14.5	17.4	19.1

**Figure 3** shows charts of the average monthly temperature.

Consider the rise in temperature at various sta-

tions. At Srinagar station in 2021, compared to 1892, there was an increase in the average monthly temperature in June, September and October. At Guwahati Station, the 120-year increase occurred in December, January, March, and April. In the remaining months, there was a slight increase in temperature. At Jolhpur weather station, temperatures have risen in February, March and April for over 125 years, but at New Delhi, for over 90 years, temperatures have risen in February and March.

Temperature is a physical quantity that is a measure of the average kinetic energy of the translational motion of molecules, in our case, air molecules in the surface layer at a height of 2 m above the land surface near weather stations. Therefore, the average monthly temperature is a continuous physical quantity, a number of values of which should not be subjected to transformations. Grouping by time intervals for subsuming under linear models is not allowed.

## 4.2 Wavelets of dynamics of mean monthly temperature

For calculations in the Excel software environment, we used all 11 significant figures in the models

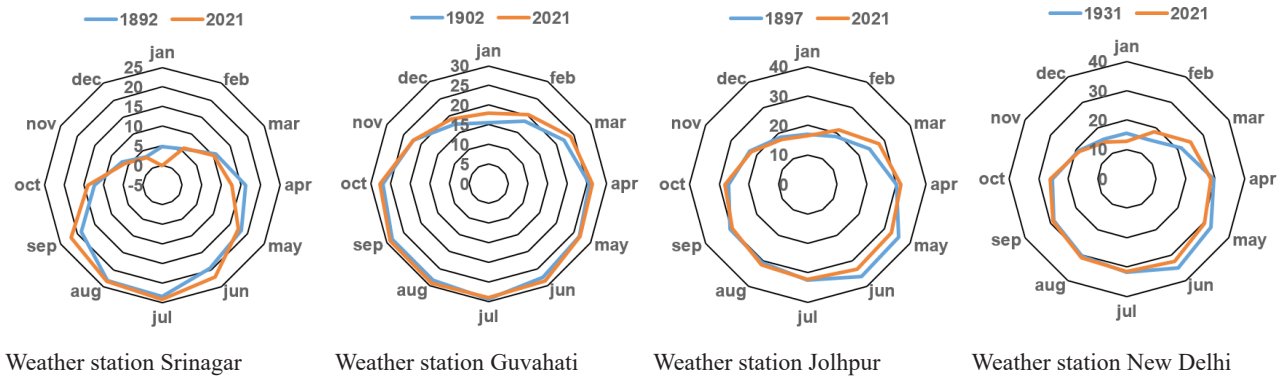


Figure 3. Diagrams of ranges of average monthly temperature.

obtained after identification (1).

**Model of monthly average temperature dynamics at Srinagar station**

The model with four components is written by the expression (Figure 4):

$$y = a * \exp(-b * x^{1.36897}) + c * x^d * \exp(e * x^{0.86543}) - f * \exp(-g * x^h) * \cos(\pi * x / 0.5 - i) - j * \exp(k * x^l) * \cos(\pi * x / 0.25 + m) \tag{3}$$

Coefficient Data:

a = 1.24394048550E + 001 b = 7.45229338864E - 004  
 c = 1.16911968898E - 001 d = 7.21207009207E - 001  
 e = 9.20205784898E - 003 f = 1.14194992983E + 001  
 g = 1.73618132791E - 006 h = 2.26550391088E + 000  
 i = 5.58834408527E - 001 j = 5.76818844755E - 001  
 k = 1.88218346333E - 002 l = 7.55117790741E - 001  
 m = 3.32301367687E - 002.

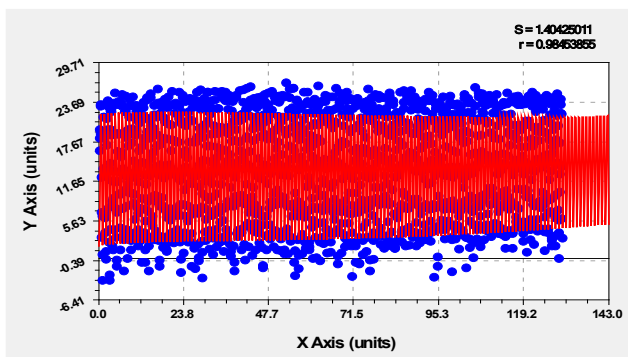


Figure 4. Plot of the four-term model for Srinagar station.

The method of identifying asymmetric wavelets (1) was performed with up to four components in series, while revealing the previous pattern. The arithmetic means a value of the mean monthly temperature was taken at the beginning of the simulation.

In formula (3), a two-term trend was then revealed,

containing two regularities. The first component is the Mandelbrot law (in physics)  $y = a \exp(-bx)$  after modification by us with the intensity parameter 1.36897 of the exponential decrease in the mean monthly temperature. This exponential formula shows the natural trend from 1892 to 2021 of a slow decrease in the average monthly temperature. Such a natural cause of the decline is the cosmic cold that endlessly surrounds the planet Earth. Therefore, with any oscillatory perturbations of the global or local climate in the Earth’s atmosphere, the planet will eventually cool down in billions of years.

The second component of the trend for Srinagar over 130 years increases with a mathematical power function  $y = ax^b$ . But it turned out that the influence of the Himalayas gives an increase in the average monthly temperature even according to the law of “double” growth according to the formula of the anomalous biotechnical [9-13] law of prof. P.M. Mazurkin  $y = ax^b \exp(cx^d)$ . Here, the sign of the process inhibition activity parameter in the model got a positive value, therefore, a product of two growth laws was formed - a power law and a modified Mandelbrot law of exponential growth under the condition  $d \neq 1$ .

A trend is always a special case of an asymmetric wavelet (1), provided that the half-period  $a_5$  of the oscillation is many times greater than the measurement time interval, in our case, several times more than 130 years.

The first oscillation in formula (3) is an infinite-dimensional wavelet, that is, it starts much earlier than 1892 and will continue much further

than 2021. This infinity is provided by the amplitude, which decreases with time according to the Mandelbrot law modified by us. Therefore, a distinctive feature of the annual cyclicality is the continuous decrease in the amplitude of the fluctuation, which will favorably affect the regional climate of India. In addition, the negative sign in front of the third component shows that the annual fluctuation is directed against the growth of the average monthly temperature.

The second fluctuation in formula (3) with a semi-annual cyclicality is typical not only for air temperature, but also for the concentrations of various greenhouse gases, especially for CO<sub>2</sub>. For carbon dioxide, it was assumed that the cycles of half a year are influenced by the vegetation cover of both hemispheres of the Earth.

However, the second wavelet, due to the negative sign, is also directed against the temperature increase, has an increasing amplitude according to the Mandelbrot law modified by us in the form of an exponential growth. Then it turns out that the mountain forests around the Srinagar weather station in the oscillatory adaptation of the local climate allow to reduce the monthly temperature.

All these four components were identified together in the CurveExpert-1.40 software environment. The standard deviation of model (3) in **Figure 4** is 1.4043 °C. At the same time, the correlation coefficient as a measure of adequacy is 0.9845, that is, the level of adequacy is much higher than 0.95 (super strong connection).

**Model of monthly mean temperature dynamics at Jolhpur station**

Similarly, a regularity was obtained (**Figure 5**):

User-Defined Model:  $y = a * \exp(b * x) - c * x^d * \exp(-e * x^f) - g * \exp(-h * x^i) * \cos(\pi * x / 0.5 - j) + k * \exp(l * x^m) * \cos(\pi * x / 0.25 - n)$  (4)

Coefficient Data:

- a = 2.70877885923E + 001    b = 5.92285934347E - 005
- c = 8.65551142868E - 025    d = 1.40728547169E + 001
- e = 3.08093570746E - 004    f = 2.26785746713E + 000
- g = 2.25700322305E + 001    h = 9.83571749288E - 001
- i = 2.44372396061E - 002    j = 2.85014519160E - 001

$k = 2.47130290654E + 000$      $l = 6.08247660824E - 004$   
 $m = 1.05183293355E + 000$      $n = 4.49918652932E + 000$ .

In formula (4), the first component is the Mandelbrot law (in physics) of exponential growth. The same law is known in mathematics as the Laplace law, in biology—Zipf-Pearl, in econometrics—Pareto. It shows the natural trend from 1897 to 2021 of an increase in the average monthly temperature. Moreover, desertification, of course, began much earlier. Apparently, the vegetation cover (grass + shrubs + trees) of India for 4000 years was severely depleted by people for the needs of agriculture. And now it is even proposed to relocate people and animals.

As a result, for the future, due to the first component around the Jolhpur weather station, local climate change coincides with the rate of global warming predicted in the IPCC CMIP5 report.

The second component of the trend for Jolhpur for 125 years is subtracted (negative sign) according to the biotechnical law of prof. P.M. Mazurkin. It may turn out that this dynamic is the result of environmental measures to combat desertification. The subsequent component with an annual cycle also has a negative sign, however, the Thar desert still wins due to the growth of the first component according to the Mandelbrot law.

In addition, people’s will and strength are weakening in the fight against the Thar Desert, as the amplitude of the annual fluctuation decreases.

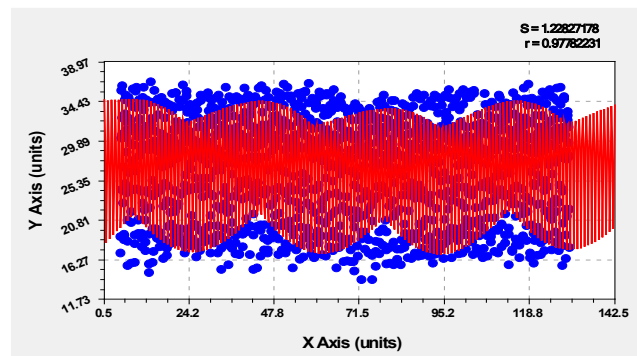


**Figure 5.** Plot of the model with four components for the Jolhpur station.

The second fluctuation (fourth component) in formula (4) with a semi-annual cyclicality has a positive sign and therefore acts in the direction of temperature increase. In this case, the oscillation amplitude

increases according to the modified Mandelbrot law. Apparently, the quality of vegetation around Jolhpur station is deteriorating further. This sad conclusion comes from the fact that semi-annual cycles characterize the influence of vegetation cover.

The standard deviation of the model (4) in **Figure 5** is 1.2283 °C, which is less in comparison with the previous weather station 1.4043 °C. At the same time, the correlation coefficient of 0.9778 is slightly less than 0.9845 for the previous weather station. But, the adequacy level is also much higher than 0.95 (super strong connection).

**Model of monthly average temperature dynamics at New Delhi station**

For a time interval of 90 years from 1931 to 2021, a model was obtained (**Figure 6**):

User-Defined Model:  $y = a \cdot \exp(-b \cdot x) + c \cdot x^d \cdot \exp(e \cdot x^f) - g \cdot \exp(-h \cdot x) \cdot \cos(\pi \cdot x / 0.5 - i) + j \cdot \exp(k \cdot x^l) \cdot \cos(\pi \cdot x / 0.25 - m)$  (5)

Coefficient Data:

a = 2.39931742757E + 001    b = 3.19834420708E – 003  
 c = 7.01935956544E – 001    d = 3.80930974140E – 001  
 e = 1.45040504760E – 002    f = 8.45501296252E – 001  
 g = 9.20090113775E + 000    h = 2.52299200889E – 004  
 i = 3.32186333451E – 001    j = 1.18493842254E + 000  
 k = 6.52201603490E – 001    l = 2.17933213594E – 002  
 m = 4.37689258906E + 000.

In formula (5), the first component is the Mandelbrot law (in physics)  $y = a \exp(-bx)$  of exponential decay. It shows a natural trend from 1931 to 2021 of a decrease in the average monthly temperature. Moreover, the New Delhi weather station is located on the northern border of the Thar Desert, so desertification, apparently, began much later than at the Jolhpur station. So far, the cosmic cold still showers on the natural first component.

The second component of the trend for New Delhi for 90 years is aimed at an increase in heat flux (positive sign) according to the anomalous biotechnical law of prof. P.M. Mazurkin. It may turn out that these dynamics are the result of the influence of two main reasons: firstly, desertification due to the excessive intensity of the reduction of vegetation and its

replacement with agricultural plants; secondly, the blockade of the Himalayan mountains to the penetration of northern winds from the Takla-Makan desert.

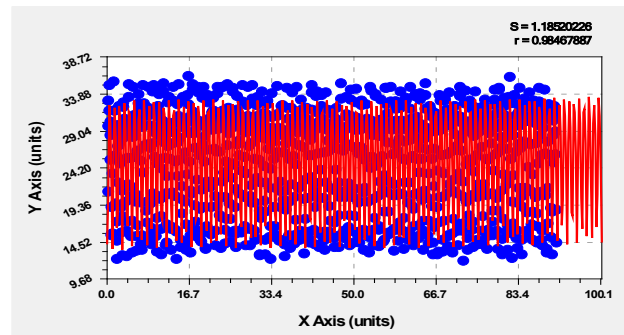


**Figure 6.** Plot of the model with four components for the New Delhi station.

The third component in the form of an asymmetric wavelet of a constant annual cycle reduces the temperature (negative sign). But this decrease in amplitude is due to the influence of the heat of the Thar desert.

The second fluctuation (fourth component) in formula (5) with a semi-annual cyclicality is similar in dynamics to the Jolhpur weather station. This fluctuation has a positive sign and therefore also acts in the direction of temperature increase. In this case, the oscillation amplitude increases according to the modified Mandelbrot law. It appears that the quality of vegetation around Jolhpur and New Delhi stations will deteriorate further. This conclusion comes from the fact that semi-annual cycles characterize the influence of vegetation cover.

The standard deviation of the model (5) in **Figure 6** is 1.1852 °C, which is less compared to the previous weather stations Srinagar (1.4043 °C) and Jolhpur (1.2283 °C). At the same time, the correlation coefficient of 0.9847 is higher than in the previous meteorological stations (respectively 0.9778 and 0.9845). The adequacy level is also much higher than 0.95 (super-strong relationship).

**Model of monthly mean temperature dynamics at Guwahati station**

A model was identified for this weather station (**Figure 7**):

User-Defined Model:  $y = a \cdot \exp(b \cdot x^c) + d \cdot x^e \cdot \exp(f \cdot x^g) - h \cdot \exp(-i \cdot x) \cdot \cos(\pi \cdot x / 0.5 - j) - k \cdot \exp(-l \cdot x) \cdot \cos(\pi \cdot x / 0.25 - m)$  (6)

Coefficient Data:

$a = 2.09342600977E + 001$   $b = 1.27606820953E - 001$   
 $c = 4.10051447152E - 002$   $d = 1.71595614539E - 014$   
 $e = 5.53047984248E + 000$   $f = 3.88234968065E - 001$   
 $g = 5.15888320178E - 001$   $h = 5.82759794304E + 000$   
 $i = 4.57908193581E - 004$   $j = 5.54099068359E - 001$   
 $k = 1.52263826552E + 000$   $l = 1.59877864528E - 004$   
 $m = 6.54574758515E - 001$ .

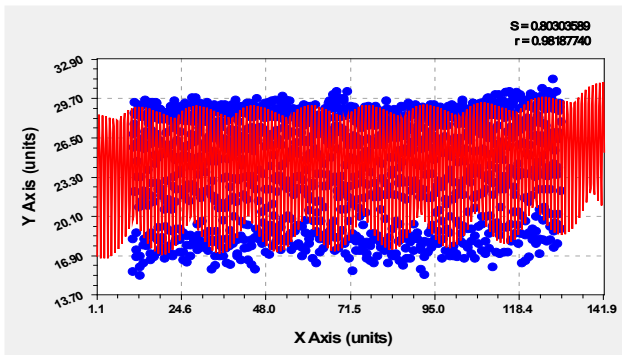


Figure 7. Plot of the model with four components for the station Guwahati.

The first component is the Mandelbrot law (in physics)  $y = a \exp(-bx)$  of the exponential decrease in the mean monthly temperature. This formula shows a natural trend from 1902 to 2021 of a slow decrease in temperature. The reason for this decrease is cosmic cold.

But it turned out that the influence of the Himalayas gives an increase in the average monthly temperature according to the second component for 120 years according to the law of “double” growth according to the formula of the anomalous biotechnical law  $y = ax^b \exp(cx^d)$ . It is this formula that has sharply raised the temperature according to the graph in Figure 7 in recent decades.

The first fluctuation in the formula (6) of the annual constant cycle also continuously decreases in amplitude. But, because of the negative sign before the third component, its influence will favorably affect the climate around the Guwahati station.

The second fluctuation in formula (6) with a

semi-annual cyclicality is typical not only for air temperature, but also for the concentrations of various greenhouse gases, especially for CO<sub>2</sub>. The negative sign before the fourth component is affected by tropical evergreen forests around Guwahati station. However, according to Mandelbrot’s law, the amplitude decreases over the years. That is, forests have an increasingly less favorable effect (this only means that people simply destroy their vegetation cover).

The standard deviation of the model (6) in Figure 7 is 0.8030 °C and it is significantly less in comparison with other weather stations Srinagar (1.4043 °C), Jolhpur (1.2283 °C) and New Delhi (1.1852 °C). At the same time, the correlation coefficient of 0.9819, as well as at other stations (Srinagar 0.9778, Jolhpur 0.9845, New Delhi 0.9847), is above the adequacy level of 0.95 (super strong connection).

### Relative errors of dynamics models

Table 5 shows the values of the relative modeling error for models containing four components each.

Table 5. Relative error (%) of the dynamics of the average monthly temperature.

Month	Srinagar	Jolhpur	New Delhi	Guvahati
Jan	167.17	5.38	5.26	3.48
Feb	146.88	5.69	5.92	3.33
Mar	15.84	4.43	4.83	3.33
Apr	8.19	3.63	3.80	3.32
May	7.19	2.60	3.18	2.32
Jun	4.96	2.79	3.57	1.66
Jul	3.72	2.59	3.10	1.47
Aug	2.72	3.36	2.51	1.30
Sep	4.54	3.29	2.81	1.52
Oct	7.09	3.40	2.71	1.93
Nov	9.58	4.13	3.30	2.67
Dec	44.18	4.49	4.82	2.85

It can be seen from the data in Table 5 (Figure 8) that the model for the Guwahati station has the smallest error of 1.30%. At the same time, August is the most accurate for the models of three weather stations. Only Jolhpur station receives the most accurate model in July.

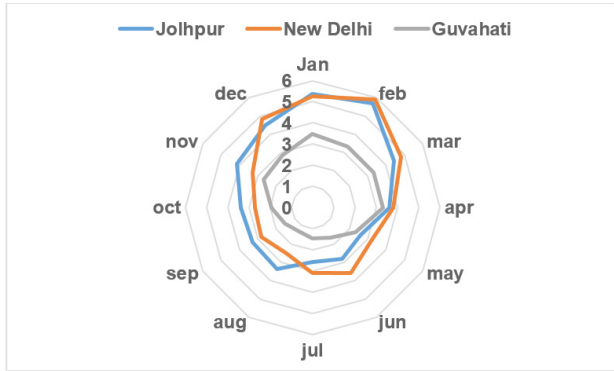


Figure 8. Diagrams of the relative error of three weather stations.

The Guwahati meteorological station has the lowest values of relative error.

### 5. Temperature forecast by months

Forecasting capabilities decrease with an increase in the number of wavelets in the general model (1) due to the fact that new micro-oscillations appear in the near future, which can dramatically change forecasting trends for the distant future. To verify the forecasts, it is enough to wait only one year (12 months) to obtain the actual average monthly temperature. Then, a predictive model is re-identified, which contains wavelets that affect the future. From the predictive model, those components are excluded, after identifying the wavelets according to formula (1), which are inside the basis of the forecast. This is how the forecasts are refined in the iterative forecasting mode every year.

#### 5.1 Monthly average temperature forecast at Srinagar station

After calculations in the Excel software environment using formula (3), graphs (Figure 9) of the average monthly temperature for each month from 1892 to 2150 were obtained.

The charts for all 12 months narrow over time. Due to this behavior of the local climate, the temperature, for example, in January, the monthly temperature rises more rapidly than in August. For 260 years, the surface layer of air at a height of 2 m at Srinagar station receives more warming in winter and autumn.

For forecasts in the month of August from Table

5 with a minimum relative error (Figure 10).

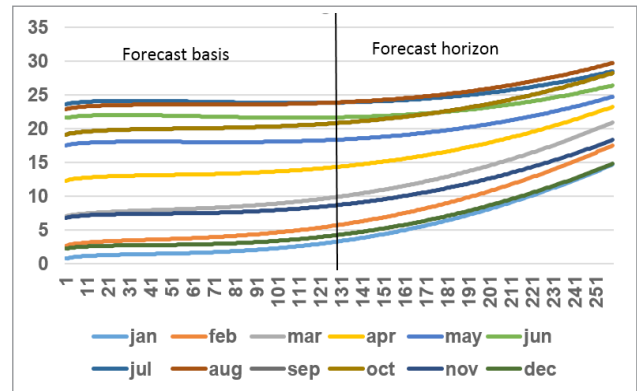


Figure 9. Srinagar monthly average temperature forecasts to 2150.

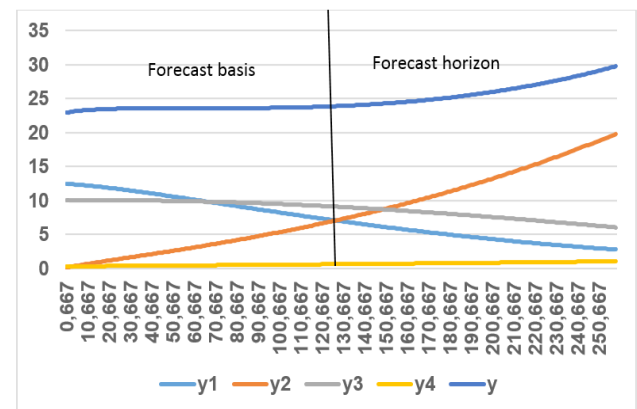


Figure 10. Temperature forecasts for Srinagar in August until 2150.

The first component of the influence of cosmic cold from 1892 to 2150 decreases. That is, the decline in the natural tendency will occur by  $12.43 - 2.78 = 9.65 \text{ }^\circ\text{C}$ . But, for the same period of time in 260 years. According to the second component in the form of an anomalous biotechnical law, the average August temperature will increase from  $0.09 \text{ }^\circ\text{C}$  to  $19.83 \text{ }^\circ\text{C}$ . That is, the increase in heat will be  $19.74 \text{ }^\circ\text{C}$ . This growth was influenced by two major reasons: Firstly, the anthropogenic reduction of the vegetation cover of India in favor of agricultural plants; secondly, the increasing geophysical influence of the Himalayas on plugging and isolating India's climate.

The annual cycles had a significant decrease in the dynamics of the August temperature from  $10.07 \text{ }^\circ\text{C}$  to  $6.06 \text{ }^\circ\text{C}$ , or the decrease occurred by  $4.01 \text{ }^\circ\text{C}$ . This decrease, of course, was influenced by the breath of the local mountain forests. However, their productivity and quality are declining due to anthropogenic

influence.

For the fourth component of the semi-annual cycle, there will be a slight increase in the August temperature from 0.31 °C to 1.07 °C, that is, an increase of 0.76 °C.

The critical thermal wave is created by the second component (3).

The total temperature at Srinagar station will increase from 22.91 to 29.75 over 260 years, or the increase in heat flow will be 6.84 °C. In 2021, the temperature was actually 23.3, theoretically 23.91, so the growth over the next 130 years will be 5.84 °C.

### 5.2 Average monthly temperature forecast at Jolhpur station

The graphs in **Figure 11** show that the Thar Desert ecosystem has become stable and therefore the monthly heat fluxes remain roughly the same for 250 years.

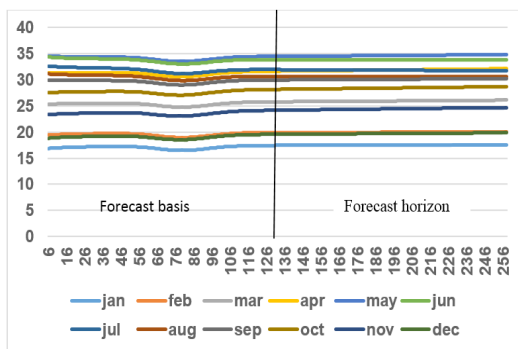


**Figure 11.** Jolhpur monthly average temperature forecasts up to 2145.

According to **Table 5**, July has the minimum relative error (**Figure 12**).

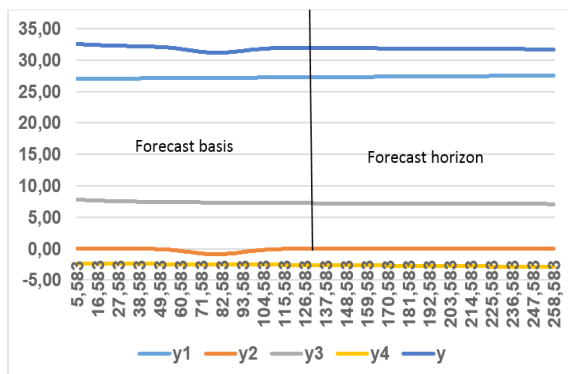


**Figure 12.** Temperature forecasts for Jolhpur in July until 2145.

The first component according to the law of exponential growth (Mandelbrot’s law) from 1897 to 2145 in July increases from a temperature of 27.10 °C to 27.50 °C, that is, according to the global warming scenario predicted in the IPCC report CMIP5 for the entire land of the Earth, there will be an increase of 0.40 °C. But, for the same period of time in 250 years. According to the second component in the form of a negative biotechnical law, there will be a change in the July temperature along a concave curve from 0.00 to 0.00 with a minimum of -0.89 °C in 1963-1967.

The annual cycles affected the July temperature dynamics by a slight decrease from 5.60 to 5.06, or the decrease occurred by 0.54 °C.

For the fourth component of the semi-annual cycle, there will be a slight increase in the July temperature from 1.83 to 2.25, that is, an increase of 0.42 °C.

The critical thermal wave is created by the first component (4).

The total temperature at Jolhpur station will increase from 34.53 to 34.82 over 250 years, or the increase in heat flow will be 0.29 °C. In 2021, the temperature was actually 32.3, theoretically 31.94, so the growth over the next 125 years will be 2.88 °C.

### 5.3 Monthly average temperature forecast at New Delhi station

As can be seen from **Figure 13**, all 12 graphs continue smoothly, but at the same time there will be an increase in the average monthly temperature.

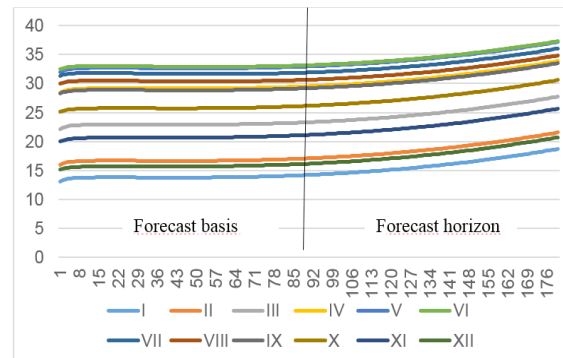


**Figure 13.** New Delhi monthly average temperature forecasts to 2110.

Further, for August, we consider separately the changes in the average monthly temperature for four components over the time interval from 1931 to 2110.

Figure 14 shows graphs for August, built according to formula (5).

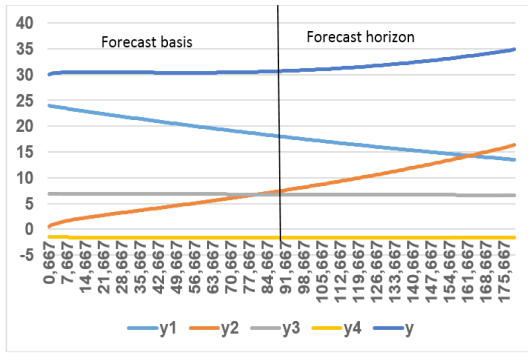


Figure 14. Temperature forecasts for New Delhi in August until 2110.

The first component of the effect of cosmic cold from 1931 to 2110 decreases from a temperature of 23.94 °C to 13.51 °C, that is, the decline in the natural tendency will occur by 23.94 – 13.51 = 10.43 °C. But, over the same period of 180 years, according to the second component in the form of an anomalous biotechnical law, the average August temperature will increase from 0.61 °C to 16.31 °C. That is, the increase in heat will be 15.70 °C. This growth was influenced by two major reasons: firstly, the anthropogenic reduction of the vegetation cover of India in favor of agricultural plants and the formation of the Thar Desert; secondly, the strengthening of the geophysical influence of the Himalayas on the blockage and isolation of the climate of the foothill regions of India.

The annual cycles affected the August temperature dynamics by a slight decrease from 6.93 to 6.63 or a decrease of 0.30 °C.

For the fourth component of the semi-annual cycle, there will be a slight decrease in August’s temperature from –1.47 °C to –1.60 °C, that is, a decrease of 0.13 °C.

The critical thermal wave is created by the second component (5).

The total temperature at the New Delhi station

will increase from 30.01 to 34.85 over 180 years, or the increase in heat flow will be 4.84 °C. In 2021, the temperature was actually 30.9, theoretically 30.68, so the growth over the next 90 years will be 4.17 °C.

### 5.4 Average monthly temperature forecast at Guwahati station

Despite the presence of tropical evergreen forests, the area around Guwahati station is expected to experience strong warming in the future. The article [14] shows a map of the types of vegetation in India, which clearly shows a strong mosaic of the vegetation cover. The fragmentation of forest land plots indicates a strong anthropogenic influence by the transformation of forests into agricultural land.

Figure 15 shows graphs of strong warming. At the same time, the rate of warming is much higher compared to the rate of the global warming scenario predicted in the IPCC report CMIP5 for the entire land mass of the Earth.

The graphs show an even change within the months of the year, but at the same time, all months begin to rise steeply in the direction of increasing temperature.

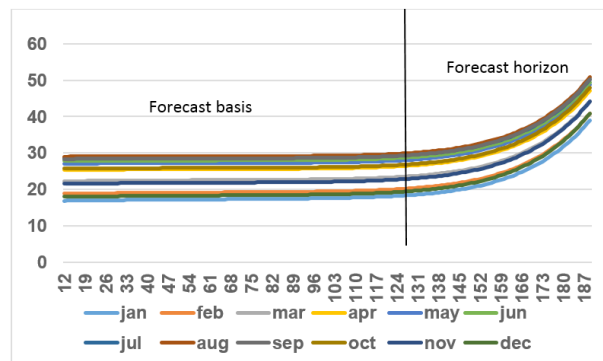


Figure 15. Guwahati monthly temperature predictions until 2080.

Due to a sharp increase in temperature, the forecast was stopped until 2080. Indian specialists will find ways to radically stop the sharp warming in the area around the Guwahati station.

According to Table 5, August has the minimum relative error (Figure 16).

The first component according to the law of exponential growth (the Mandelbrot law modified by

us) from 1902 to 2080 in August at the Guvahati station increases from a temperature of 24.10 °C to 24.50 °C, that is, according to the global warming scenario predicted in the IPCC CMIP5 report for the entire land mass of the Earth, growth by 0.40 °C.

However, over the same time period of 180 years, according to the second component in the form of a positively directed anomalous biotechnical law, there will be a sharp increase in the August temperature from 0.00 to 21.70. At the same time, the zero value continued until 1956, that is, for 55 years. Therefore, climatologists in India can compare these years with the events that were taken during this period. The average rate of warming will be equal to  $21.70 / 125 = 0.174$  °C.

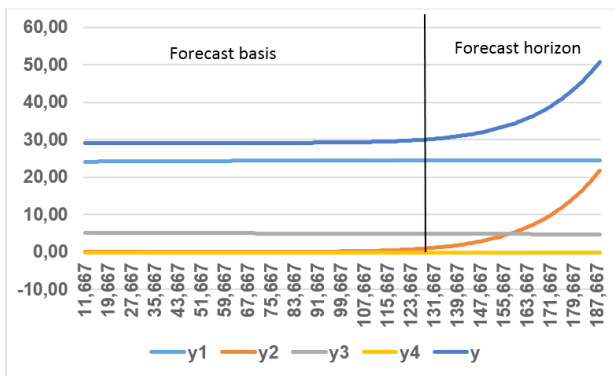


Figure 16. Temperature forecasts for Guvahati in August until 2080.

The annual cycles had a slight decrease from 5.10 to 4.70 on the dynamics of the August temperature, or a decrease of 0.40 °C. For the fourth component of the semi-annual cycle, there will be a constant value of the August temperature  $-0.19$  °C.

The critical thermal wave is created by the second component (6).

The total temperature at the Guvahati station will increase from 29.02 to 50.78 over 180 years, or the increase in heat flow will be 21.80 °C. In 2021, the temperature was actually 29.3, theoretically 30.69, so the growth over the next 60 years will be 20.09 °C.

### 5.5 Comparison of monthly average temperature forecasts

For 2080, a comparison was made (Table 6, Figure 17) of weather stations.

Table 6. Predicted temperature values for 2080.

Month	Srinagar	Jolhpur	New Delhi	Guvahati
Jan	7.09	17.49	16.6	38.98
Feb	9.69	19.95	19.44	40.88
Mar	13.56	25.92	25.63	44.21
Apr	17.15	31.85	31.80	47.13
May	20.14	34.62	35.14	48.74
Jun	22.78	33.87	35.30	49.47
Jul	24.94	31.83	34.03	49.47
Aug	25.45	30.60	32.82	50.15
Sep	23.04	30.08	31.44	50.78
Oct	17.85	28.40	28.49	50.33
Nov	11.77	24.41	23.53	47.96
Dec	7.70	19.70	18.58	40.87

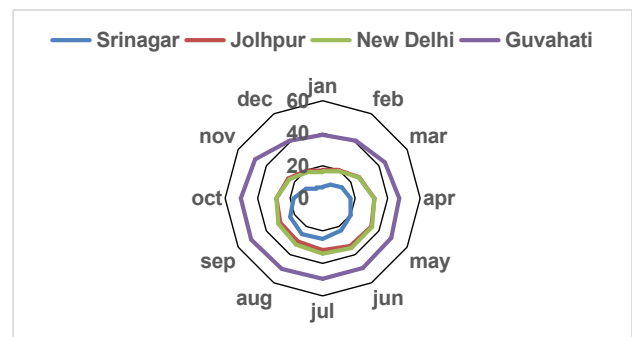


Figure 17. Diagrams of temperature forecasts up to 2080.

From a climatic point of view, the Guvahati station becomes the most dangerous.

## 6. Conclusions

Using the identification method [7-11], according to the actual data of the average monthly temperature, asymmetric wavelets of dynamics were identified as fractal quanta of the behavior of the surface air layer at a height of 2 m, on the territory of four weather stations in India (Srinagar, Jolhpur, New Delhi and Guvahati), an analysis of wave patterns was carried out.

The maximum temperature for each weather station is different. For example, for Srinagar station, the maximum for all years is observed in July, for Jolhpur and New Delhi stations, the maximum shifts to June, and for Guvahati station, it shifts to August.

With a high correlation coefficient of 0.9659, 0.8640 and 0.8687, a three-factor model of the form

was obtained  $\bar{t} = 45.16459 - 0.0083426h - 0.16343\beta - 0.18818\alpha$ . For this formula, the maximum relative error of 1.99% was obtained for the Jolhpur weather station. As a result, the three-factor model receives a relative error of less than 5%. That is, the geographical location of weather stations greatly affects the overall average monthly temperature. Then a new direction opens in the geographic modelling of the parameters of global and regional climatic and meteorological processes.

The hottest month for Srinagar station over a period of 130 years at an altitude of 2 m is in July. At the same time, the temperature increased from 23.4 °C to 24.2 °C (an increase of 3.31%). A noticeable decrease in the intensity of heat flows in June occurred at Jolhpur stations (over 125 years, a decrease from 36.2 °C to 33.3 °C, or by 8.71%) and New Delhi (over 90 years, a decrease from 35.1 °C to 32.4 °C, or by 7.69%). For almost 120 years, the Guwahati weather station has experienced complex climate changes: In 1902, the hottest month was July, but in 2021 it has shifted to August. However, at the same time, the maximum average monthly temperature decreased from 29.4 °C to 29.3 °C, or by 0.34%.

The increase in temperature at various stations is considered. At Srinagar station in 2021, compared to 1892, there was an increase in the average monthly temperature in June, September and October. At Guwahati Station, the 120-year increase occurred in December, January, March, and April. In the remaining months, there was a slight increase in temperature. At Jolhpur weather station, temperatures have risen in February, March and April for over 125 years, but at New Delhi, for over 90 years, temperatures have risen in February and March.

Despite the presence of tropical evergreen forests, the area around Guwahati station is expected to experience strong warming in the future. At the same time, the rate of warming is much higher compared to the rate of the global warming scenario predicted in the IPCC report CMIP5 for the entire land area of the Earth.

The first component of the model of four components according to the law of exponential growth (the

Mandelbrot law modified by us) from 1902 to 2080 in August at Guwahati station increases from a temperature of 24.10 °C to 24.50 °C, that is, according to the global warming scenario predicted in the IPCC report CMIP5 for the entire land of the Earth, there will be an increase of 0.40 °C.

However, over the same period of 180 years until 2080, according to the second component in the form of a positively directed anomalous biotechnical law, there will be a sharp increase in the August temperature from 0.00 to 21.70. At the same time, the zero temperature value lasted from 1902 to 1956, that is, for 55 years. Climatologists in India can compare these years with the events that took place during this period. The average rate of warming until 2080 will be equal to  $21.70 / 125 = 0.174$  °C.

The annual cycles had a slight decrease from 5.10 to 4.70 on the dynamics of the August temperature at Guwahati station, or a decrease occurred by 0.40 °C. For the fourth component of the semi-annual cycle, there will be a constant value of the August temperature  $-0.19$  °C. The critical heat wave is created by the second component. The total temperature at the Guwahati station will increase from 29.02 to 50.78 over 180 years, or the increase in heat flow will be 21.80 °C. In 2021, the temperature was actually 29.3, theoretically 30.69, so the growth over the next 60 years will be 20.09 °C.

## Conflict of Interest

There is no conflict of interest.

## Funding

This research received no external funding.

## References

- [1] Ancient India [Internet] [cited 2022 Apr 22]. Available from: <https://history.wikireading.ru/314323>
- [2] Kumar, B., Asad, A.I., Chandraaroy, B., et al., 2019. Perception and knowledge on climate change: A case study of university students in

- Bangladesh. *Journal of Atmospheric Science Research*. 2(3), 17-22.  
DOI: <https://doi.org/10.30564/jasr.v2i3.1542>
- [3] India Getting Warmer, Hotter: 2021 Fifth Warmest Year Since 1901, Says IMD [Internet] [cited 2022 Apr 22]. Available from: [https://www.business-standard.com/article/current-affairs/india-getting-warmer-hotter-2021-fifth-warmest-year-since-1901-says-imd-122011401133\\_1.html](https://www.business-standard.com/article/current-affairs/india-getting-warmer-hotter-2021-fifth-warmest-year-since-1901-says-imd-122011401133_1.html)
- [4] Climate of India [Internet] [cited 2022 Apr 22]. Available from: <https://fb.ru/article/146454/klimat-indii-osobennosti-klimata-indii>
- [5] Kumar, P., Pinjarla, B., Joshi, P.K., et al., 2021. Long term spatio-temporal variations of seasonal and decadal aridity in India. *Journal of Atmospheric Science Research*. 4(3), 29-45.  
DOI: <https://doi.org/10.30564/jasr.v4i3.3475>
- [6] Gopalakrishna, T., Lomax, G., Aguirre-Gutiérrez, J., et al., 2022. Existing land uses constrain climate change mitigation potential of forest restoration in India. *Conservation Letters*. e12867.  
DOI: <https://doi.org/10.1111/conl.12867>
- [7] Mazurkin, P.M., 2022. Asymmetric mean annual temperature wavelets surface air layer of Berlin for 1701-2021. *Journal of Atmospheric Science Research*. 5(3), 1-9.  
DOI: <https://doi.org/10.30564/jasr.v5i3.4674>
- [8] Mazurkin, P.M., 2022. Quantum Biophysics of the atmosphere: Asymmetric wavelets of the average annual air temperature of Irkutsk for 1820-2019. *Journal of Environmental & Earth Sciences*. 4(2), 1-16.  
DOI: <https://doi.org/10.30564/jees.v4i2.4586>
- [9] Mazurkin, P.M., 2022. Wave dynamics of the average annual temperature surface air layer New Delhi for 1931-2021. *Journal of Atmospheric Science Research*. 5(2), 52-66.  
DOI: <https://doi.org/10.30564/jasr.v5i2.4639>
- [10] Mazurkin, P.M., 2021. Bioclimatic regularities of change in the density of organic carbon of the steppe soil in different regions of the World. *Journal of Atmospheric Science Research*. 4(1), 16-25.  
DOI: <https://doi.org/10.30564/jasr.v4i1.2521>
- [11] Mazurkin, P.M., 2021. Factor analysis of the parameters of samples of the steppe soil and grass of Mongolia and Inland Mongolia of China on the eastern transect of the Eurasian steppe. *Journal of Geological Research*. 3(1), 1-10.  
DOI: <https://doi.org/10.30564/jgr.v3i1.2520>
- [12] Dahlhausen, J., Rötzer, T., Biber, P., et al., 2018. Urban climate modifies tree growth in Berlin. *International Journal of Biometeorology*. 62, 795-808.  
DOI: <https://doi.org/10.1007/s00484-017-1481-3>
- [13] Roy, P.S., Behera, M.D., Murthy, M.S.R., et al., 2015. New vegetation type map of India prepared using satellite remote sensing: Comparison with global vegetation maps and utilities. *International Journal of Applied Earth Observation and Geoinformation*. 39, 142-159.  
DOI: <http://dx.doi.org/10.1016/j.jag.2015.03.003>

REVIEW

## Deep Learning Methods Used in Remote Sensing Images: A Review

Ekram M. Rewhel<sup>1</sup> , Jianqiang Li<sup>1</sup>, Amal A. Hamed<sup>2</sup>, Hatem M. Keshk<sup>2\*</sup>, Amira S. Mahmoud<sup>2</sup>, Sayed A. Sayed<sup>2</sup>, Ehab Samir<sup>2</sup>, Hind H. Zeyada<sup>2</sup>, Sayed A. Mohamed<sup>2</sup>, Marwa S. Moustafa<sup>2</sup>, Ayman H. Nasr<sup>2</sup>, Ashraf K. Helmy<sup>2</sup>

<sup>1</sup> School of Software Engineering, Beijing University of Science and Technology, Beijing, 100083, China

<sup>2</sup> Data Reception, Analysis and Receiving Station Division, National Authority for Remote Sensing and Space Science, Cairo, 1564, Egypt

### ABSTRACT

Undeniably, Deep Learning (DL) has rapidly eroded traditional machine learning in Remote Sensing (RS) and geoscience domains with applications such as scene understanding, material identification, extreme weather detection, oil spill identification, among many others. Traditional machine learning algorithms are given less and less attention in the era of big data. Recently, a substantial amount of work aimed at developing image classification approaches based on the DL model's success in computer vision. The number of relevant articles has nearly doubled every year since 2015. Advances in remote sensing technology, as well as the rapidly expanding volume of publicly available satellite imagery on a worldwide scale, have opened up the possibilities for a wide range of modern applications. However, there are some challenges related to the availability of annotated data, the complex nature of data, and model parameterization, which strongly impact performance. In this article, a comprehensive review of the literature encompassing a broad spectrum of pioneer work in remote sensing image classification is presented including network architectures (vintage Convolutional Neural Network, CNN; Fully Convolutional Networks, FCN; encoder-decoder, recurrent networks; attention models, and generative adversarial models). The characteristics, capabilities, and limitations of current DL models were examined, and potential research directions were discussed.

**Keywords:** Deep Learning (DL); Satellite imaging; Image classification; Segmentation and object detection

#### \*CORRESPONDING AUTHOR:

Hatem M. Keshk, Data Reception, Analysis and Receiving Station Division, National Authority for Remote Sensing and Space Science, Cairo, 1564, Egypt; Email: [hatem.magdy@narss.sci.eg](mailto:hatem.magdy@narss.sci.eg)

#### ARTICLE INFO

Received: 3 November 2022 | Revised: 9 February 2023 | Accepted: 20 February 2023 | Published Online: 4 April 2023

DOI: <https://doi.org/10.30564/jees.v5i1.5232>

#### CITATION

Rewhel, E.M., Li, J.Q., Hamed, A.A., et al., 2023. Deep Learning Methods Used in Remote Sensing Images: A Review. *Journal of Environmental & Earth Sciences*. 5(1): 33-64. DOI: <https://doi.org/10.30564/jees.v5i1.5232>

#### COPYRIGHT

Copyright © 2023 by the author(s). Published by Bilingual Publishing Group. This is an open access article under the Creative Commons Attribution-NonCommercial 4.0 International (CC BY-NC 4.0) License. (<https://creativecommons.org/licenses/by-nc/4.0/>).

# 1. Introduction

The swift development in remote sensing (RS) platforms and instruments have increased the accessibility of earth observation to help Earth's surface measuring feature. Satellite platforms accumulate images at frequent intervals which results in a growing exponential volume of data. In the digital era, data become not only valuable but also intelligent. Big Data (BD) term has been introduced in mid-2011 to describe a broad set of heterogeneous large volumes of data that can hardly be managed and processed using conventional approaches. Technically, the five main dimensions that characterize BD <sup>[1]</sup> are: A massive amount of data, speed of data generation and delivery, structured and unstructured data sources, veracity, and value <sup>[2]</sup>. BD and open-source RS data open the door to improving DL approaches by extracting insights from the collected RS data to help establish more robust and effective models for RS applications.

Meanwhile, several attempts to use DL in RS have been made <sup>[3]</sup>. Scientists use contemporary technologies and different RS data sources to improve context-based feature learning and exploit the potential classification for massive volumes of remote sensing imageries.

Modern RS applications <sup>[4]</sup> rely basically on image classification techniques. Typically, image classification in the remote sensing domain is grouped into supervised, non-supervised, and object-based approaches. Other criteria to group image classification are by a number of labels per image: Single and multi-label classification. RS classification pipeline <sup>[5]</sup> is composed of four main steps namely: Pre-processing, feature engineering, classification, and post-processing (see **Figure 1a**) whereas each step may include sub-tasks. A solid breakdown of the process into sub-tasks with specific assumptions helps develop standalone sub-problems with solutions or models that can be integrated into the classification pipeline task. The preparation process includes correcting, de-noising, and synchronizing data to increase the process performance. The feature engineering process involves removing noisy data from the input image, lowering dimensionality, and establishing a collection of suitable

representations (features) for the input from which the Machine Learning (ML) model may utilize to predict the target classes. The adopted model is built based on the training samples in order to recognize the association between the training data features/representation. After training, testing, and validation, the adopted model predicts fresh data. Finally, in pixel-level classification, post-processing is a collection of procedures used to improve the final classified image <sup>[6]</sup>.

Recently, the increased capability of DL has led to its use in a wide spectrum of applications in the RS domain. End-to-end architecture generalizes (**Figure 1b**) hierarchical rich feature learning. The current focus of the DL model was improved due to computing capability in new processor generations. In this context, object detection, image segmentation and scene understanding were considered typical tasks where classification approaches were empowered.

The main contributions can be summarized as follows:

- This survey analyzes the most recent publications with respect to image classification, object detection, and image segmentation problems in the remote sensing domain.
- Different DL aspects were reviewed including network architectures, loss functions, training strategies, and key contributions.
- Drawing from the latest progress by the computer vision community, several promising future directions for future research were described and how they can be integrated to value-add existing and inspire RS applications.

The rest of this article is organized as: Section 3 provides histories of remote sensing imageries. The history of deep learning architectures is summarized in Section 4. Section 5 discusses the recent efforts of deep learning in remote sensing classification, segmentation, and object detection tasks. In Section 6, the main challenges were discussed. Section 7 illustrates future directions for DL-based classification methods for Earth Observation (EO) imageries. DL-based image classification applications were highlighted in Section 8. Finally, conclusions were presented in Section 9.

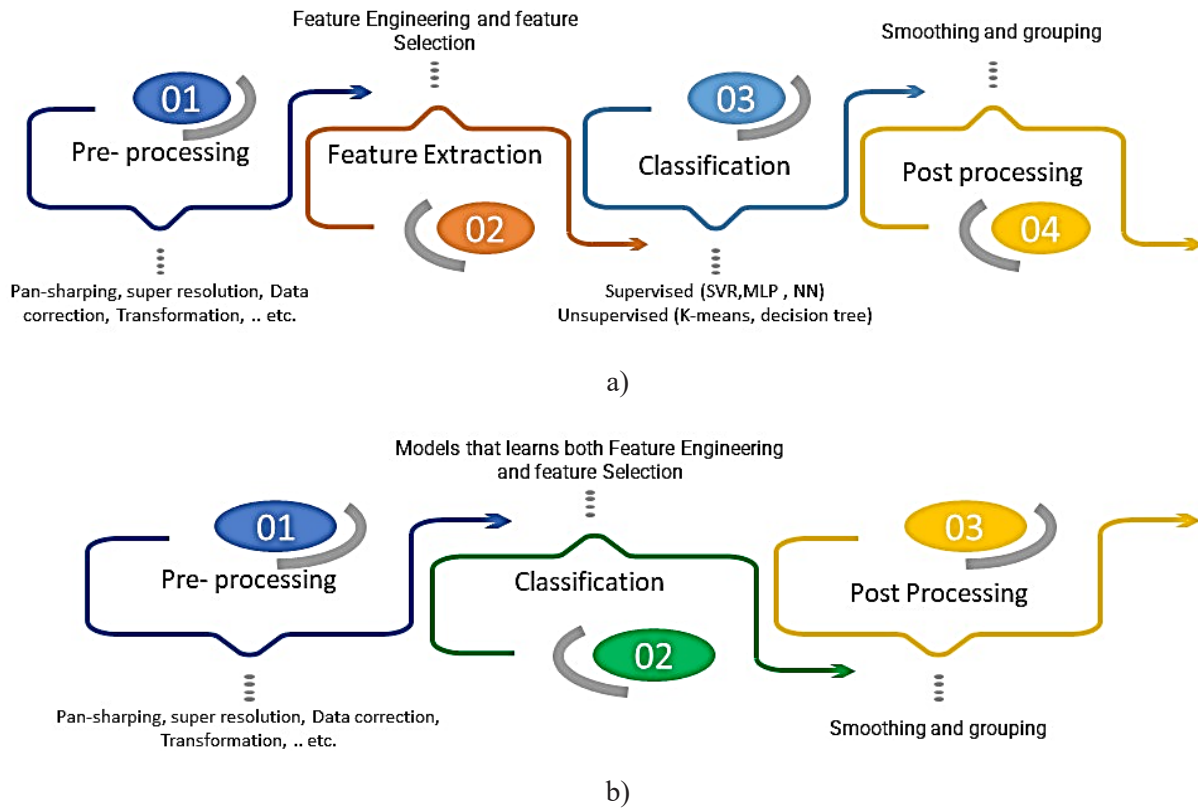


**Figure 1.** Comparison between the common steps of a) the typical machine learning approaches, and b) the modern end-to-end DL structure.

## 2. Overview of remote sensing imageries

Remote sensing accumulates information about an object, area, or phenomenon with no contact with it [7]. Data collection and data analysis are considered two key processes in **Figure 2**, which displays the generalized processes and elements involved in remote sensing. The data collection process includes a) energy sources, b) energy propagation through the atmosphere, c) energy interactions with earth surface features, d) energy retransmission through the atmosphere, (e) and (f) airborne and/or spaceborne sensors monitor changes in the way earth surface features reflect and emit electromagnetic energy. g) To analyze the collected data, various viewing and interpretation equipment is used. When available, the reference data (such as soil maps, crop statistics, or field-check data) are used to aid in data analysis and help in determining the extent, location, and condition acquired by the sensors. Finally, (h) and (i) the data are compiled, usually as maps, tables, or digital

spatial data. Finally, the obtained information is delivered to users who utilize it to make decisions.

The latest generation of sensors produces explosion volumes of different resolution images for Earth, which created a new processing challenge. The development of an efficient image classification method for massive remote sensing imagery is critical for modern applications.

Earth observation technology is not limited to traditional platforms but extended to Light Detection and Ranging (LiDAR), and Unmanned Aerial Vehicle (UAV). As shown in **Figure 3**, the sensors are categorized as active and passive. The sun provides a convenient source of energy for remote sensing. The sun's energy is reflected, as it is for visible wavelengths, or absorbed and then re-emitted. Remote sensing instruments measure the energy that is naturally available and is called passive sensors. Some examples of passive sensors include panchromatic, multi-spectral, hyperspectral imagery. Alternatively, active sensors provide their own energy source for

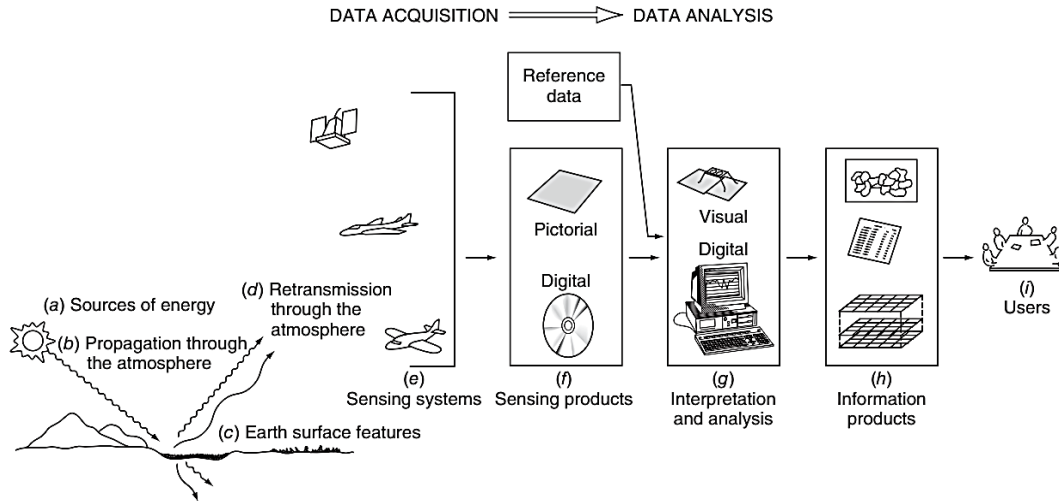


Figure 2. Remote Sensing (RS) processes and elements.

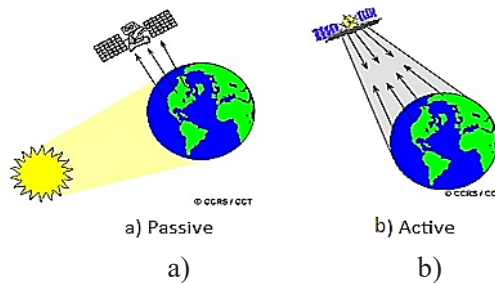


Figure 3. A graphical representation of a) passive versus b) active sensing.

illumination. The sensor emits radiation which is directed toward the target to be investigated.

The radiation reflected from that target is detected and measured by the sensor. Some examples of active sensors are LiDAR and Synthetic Aperture Radar (SAR).

**Table 1** demonstrates the spatial, spectral, and temporal resolution of several common RS satellites. The spectral capabilities of the Landsat (7,8) and Sentinel (1,2) satellite missions complement each other, and with their open and cost-free access ar-

chives. The spatial resolution of images can be classified into three categories in this review: 1) High Resolution (HR) sensors (5-30 m), 2) Very High Resolution (VHR) sensors (4-m multispectral pixel size), and 3) medium to coarse resolution sensors (> 60 m multispectral pixel size). Spatial resolution is important for various applications. Coarse-resolution sensors are suitable for large-scale observation, but not for characterizing urban in compact zones. Very high- and high-resolution sensors help obtain more details.

Table 1. Specification of the common remote satellites/sensors' specifications [8].

Mission Properties	Sentinel-2	Landsat 7	Landsat 8	MODIS
Spatial resolution (m)	10, 20, 60	(15), 30, 60	(15), 30, 100	250, 500, 1000
Temporal resolution (days)	2-3	16	16	1-2
Spectral resolution	13 bands	8 bands	11 bands	25 bands
Radiometric resolution	12-bit	8-bit	16-bit	12-bit
Swath width (km)	290	185	185	2330
Wavelength range (nm)	442-2186	450-12,500	433-12,500	459-2155
Supported study area scale	local, national	national, regional	national, regional	national, regional

### 3. History of deep learning

This section discusses the most frequently DL architectures, including Convolutional Neural Networks (CNNs) [9], Recurrent Neural Networks (RNNs), Long Short-Term Memory (LSTM) [10], Encoder-Decoders (EDs) [11], and Generative Adversarial Networks (GANs) [12]. Numerous upgrades have been proposed in response to the sudden popularity growth of DL, including capsule networks, attentions, and deep belief networks. It is worth noting that in some instances, DL models are trained from scratch on new datasets (given the appropriate quality and amount of labelled data). However, transfer learning [13,14] is frequently employed to deal with incompletely labelled datasets. As illustrated in Figure 4, DL-based architectures were classified into eight groups based on their primary technical contributions.

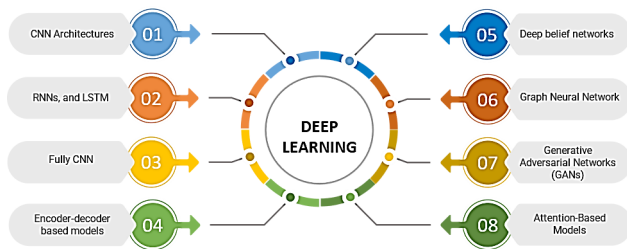


Figure 4. Deep learning architecture taxonomy.

#### 3.1 CNN architectures

CNN family has grown since 2012, AlexNet [15] was presented at the ImageNet Large Scale Visual Recognition Challenge (ILSVRC). A standard CNN composes of three types of layers: i) convolutional layer, where filter (kernel) of weights is convolved to extract feature maps; ii) nonlinear layers, which apply an activation function on feature maps (usually elementwise) to enable the modeling of non-linear functions by the network; and iii) pooling layers, to reduce feature map spatially based on statistical information (mean, max, etc.) of a neighborhood.

Convolutional layer [16]: The input (image) is convolved then the result is passed to the next layer. Convolutional layers require four main pieces of information (filter size, number of filters, stride, and

padding). The obtained result is a number of abstract feature maps equal to the number of used filters.

Pooling layer: A spatial reduction to the feature maps to minimize CNN parameters. The pooling layer has no impact on volume depth [9]. The most frequent approaches are max and average pooling [10].

Fully Connected Layer: A typical Multilayer perceptron (MLP) that transfers 2-D feature maps to 1-D vectors [11]. Figure 5 shows that adding more parameters does not always improve precision [12]. The following sections investigate CNNs from a broader perspective.

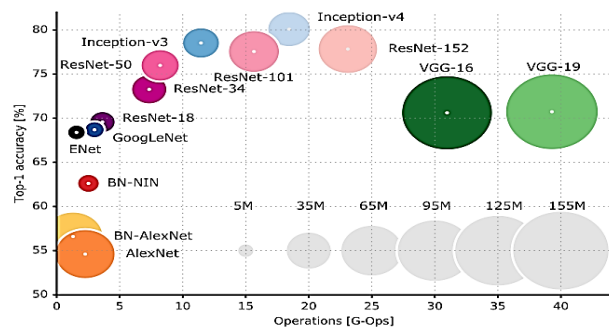


Figure 5. Summary of deep learning in terms of architecture, parameters, top-1 accuracy [12].

#### Vintage CNN architectures

Vintage CNN architectures include: AlexNet [15], ZFNet [17] and VGGNet [18] named after Alex Krizhevsky, Zeiler and Fergus, Visual Geometry Group [13], as shown in Figure 6. AlexNet is regarded as the root of CNN architectures family. The three vintage networks share a similar architecture called “template”: Stacking convolution with non-linear activation followed by pooling layers to extract hierarchical features from an input image and ending with a fully connected classifier head [14]. The model provides and predicts the probability for each possible class based on the extracted features. To sum up, the main contribution of vintage architectures can be summarized as follows:

- Consisting of multiple convolutions to boost feature depth and scaling methods such as pooling with stride 2 to reduce the resolution.
- Activating the ReLU after convolutional layers speeds up backpropagation using stochas-

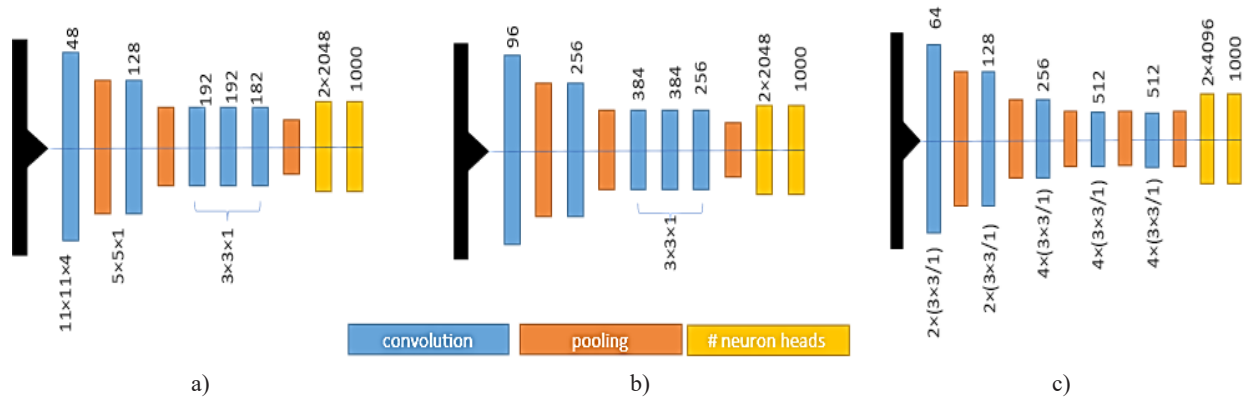


Figure 6. Conceptual overview of the three Vintage Architectures: a) AlexNet<sup>[15]</sup>, b) ZFNet<sup>[17]</sup>, c) VGG-16<sup>[18]</sup>.

tic gradient descent.

- A wide range of deep networks were created by repeated building blocks such as VGG-19.

### Inception family

In 2015, Google introduced a novel architecture called GoogLeNet which considered a starting point of the Inception Family and sometimes called Inception-V1. The network was built on VGG architecture in which, the Inception modules (see Figure 7a) with occasional max pooling to reduce the dimension (see Figure 7b) are stacked after the stem of the first convolutions. A typical Inception module is composed of parallel convolutions of various kernel sizes and max pooling which results in a variety of different feature maps (see Figure 7b). Various updated Inception versions were proposed<sup>[19-21]</sup> to boost performance using the revised sparsely connected topologies. To sum up, the Inception Family proposed a significant update to classical CNN as follows:

- Bottleneck designs and complex building block structures.

- Batch normalization to enable faster training via stochastic gradient descent.
- Factorization of convolutions in space and depth.

### ResNet family

Despite their better representational ability, deeper neural networks are hard to train due to the vanishing gradient problem. As a result, the network’s performance degrades dramatically as it becomes deeper. ResNet<sup>[22]</sup> was designed to facilitate training deeper neural networks and overcome the vanishing gradient problem. As shown in Figure 8, the primary idea of ResNet is to introduce an “identity shortcut link” that bypasses one or more layers (see Figure 8a). ResNet adheres to the VGG design principles while adding an identity shortcut in the residual module. Tuning a hyper-parameter is pointless because there isn’t one. The pros of ResNet<sup>[23]</sup> include a) Training speed up, b) Improving the performance of classification. c) Release the power of a deeper neural network.

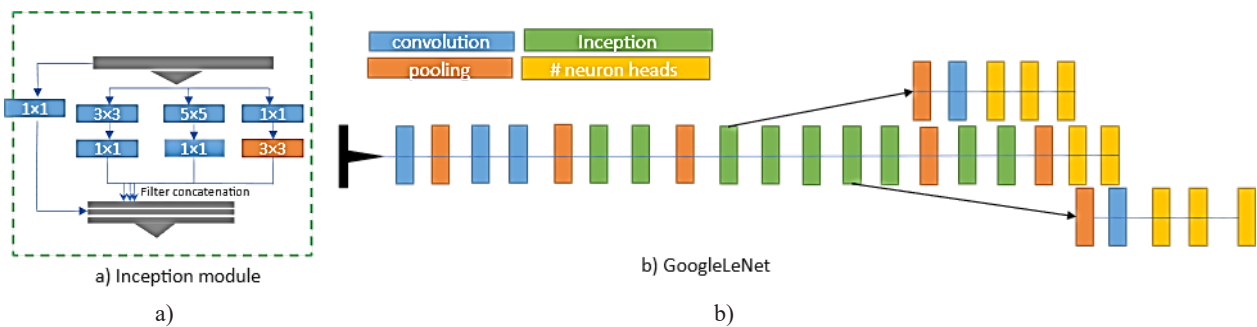


Figure 7. Conceptual overview of a) Inception module and b) Inception V-1 architecture.

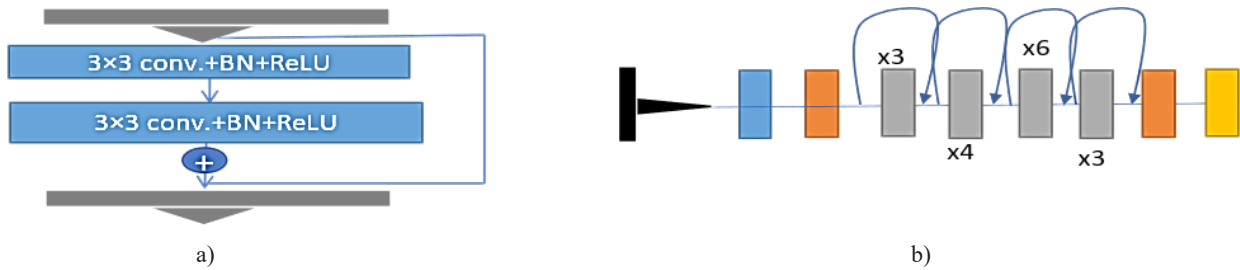


Figure 8. Conceptual overview of a) residual module and b) ResNet-50 architecture.

The architecture of ResNet has been widely investigated due to its popularity among researchers. A slew of innovative ResNet-based architectures has been revealed such as ResNeXt<sup>[23]</sup>, SENet<sup>[24]</sup>, SKNet<sup>[25]</sup> and ResNeSt<sup>[26]</sup>.

**Recent convolutions architecture**

Despite their computational overhead, Vintage CNNs have shown exceptional performance in RS applications<sup>[19]</sup>. CSPNet was developed by Wang et al.<sup>[27]</sup> to reduce duplicate gradient information in the network and hence reduce inference costs. The CSPNet design reduces parameter count, increases CPU use, and reduces memory footprint<sup>[20]</sup>. CSPNet was adopted in many generic architectures such as ResNet<sup>[21]</sup>, ResNeXt<sup>[24]</sup>, DenseNet<sup>[23]</sup>, and Scaled-YOLOv4<sup>[26]</sup>. The CSPNet network reduces computations by 10%-20% while preserving or boosting accuracy in various recent detector types, mobile and edge devices.

Typically, the modification of the network in any of the three dimensions (depth, width, and resolution) impacted its performance. For example, increasing model depth helps capture more complex characteristics, but the model tends to become harder to train. Similarly, increasing network width captures fine-grained data but

not high-level information. EfficientNet<sup>[28]</sup> is a simple architecture that uses a compound coefficient to uniformly scale all three dimensions. **Table 2** compares different deep learning models in terms of a number of parameters, accuracy.

**3.2 Recurrent Neural Networks (RNNs) and Long Short-Term Memory (LSTM)**

Recurrent Neural Networks (RNNs)<sup>[29]</sup> are extensively employed to process temporal data (speech, text, and videos) where data at each time is dependent on prior data. While CNNs were a natural fit for 2D images, RNNs are very effective for modeling short/long-term pixel dependencies to enhance feature map estimation. Using RNNs, pixels may be linked together and processed sequentially to model global contexts and improve classification and segmentation. RNNs are unable to connect the relevant information. To handle the “long-term dependencies, Long Short-Term Memory (LSTM)<sup>[30,31]</sup> was proposed, an end-to-end Attention Recurrent Convolutional Network (ARCNet) was introduced to help focus on important high-level features in order to improve classification results.

A cascaded RNN<sup>[32]</sup> model was proposed using

Table 2. A comparison of CNN architectures.

Year	Model	Layers	Top-1 acc%	Parameters (Millions)
2012	AlexNet	7	63.3	62.4
2014	VGG-16	16	73	138.4
2014	GoogLeNet	22	-	6.7
2015	ResNet-50	50	76	25.6
2016	ResNeXt-50	50	77.8	25
2019	CSPResNeXt-50 <sup>[27]</sup>	59	78.2	20.5
2019	EfficientNet-B4	160	83	19

gated recurrent units to explore discriminative features from Hyperspectral Images (HSIs). The RNN layers help in eliminating redundant information between adjacent spectral bands and learning complementary information from nonadjacent spectral bands. An end-to-end trainable Recurrent Convolutional Neural Network (ReCNN) <sup>[33]</sup>, architecture was introduced for change detection in multispectral images. The proposed architecture combined convolutional and recurrent neural networks to extract rich spectral-spatial feature representations and evaluate temporal dependency. A Siamese network based on a multi-layer Recurrent Neural Network (RNN) (SiamCRNN) <sup>[34]</sup>, was designed to handle multisource multitemporal images to detect changes. SiamCRNN is an integration of three subnetworks: Deep Siamese Convolutional Neural Network (DSCNN), multiple-layers RNN (MRNN), and Fully Connected (FC) layers.

A Gated Recurrent Multi-Attention Neural Network (GRMA-Net) <sup>[35]</sup>, was proposed to collect spatial informative features sequences from multi-spectral images afterward fed to a Deep-Gated Recurrent Unit (GRU) to capture long-range dependency and contextual relationship.

### 3.3 Fully convolutional neural network

To achieve a pixel-based classification, segmentation approaches based on a Fully Convolutional Network (FCN) were proposed <sup>[36]</sup>. FCN, inspired by VGG architecture (see **Figure 9a**), contains three fundamental layers: Multi-layer convolution, deconvolution, and fusion. The fully connected layer in VGG was replaced by Convolutional layers. To compute a score for each class, a  $1 \times 1$  convolution is adopted. The output is smaller than the input image due to pooling procedures after the convolutional layers. Deconvolution is used to bilinearly upsample these coarse outputs to regain the original image size. It works similarly to convolution but “enlarges” the input by padding the matrix and combining parts within a deconvolution filter. The deconvolution stride is inversely proportional to the upsampling factor. Deconvolution produces a scaled label seg-

mented image. Although deconvolution recovers the original image’s size, the class scores are diluted, and features are lost. To create the final segmentation, a skip architecture combines semantic information collected from a deep layer with location details from its preceding levels. The upsampled deep layer is added element-by-element to the shallow layer output.

### 3.4 Encoder-decoder and auto-encoder models

U-Net <sup>[37]</sup> (see **Figure 9b**) was originally designed to segment biological images. It consists of two symmetric blocks namely: the encoder and decoder. The encoder network is constructed on the basis of the FCN architecture to capture image features map. The decoder network, on the other hand, upsampled the derived feature map while lowering the number of filters. The encoder block of the original U-Net design comprises two  $3 \times 3$  convolutions and a  $2 \times 2$  max pooling operation with stride 2 in the encoder block. As a result, the feature map is gradually downsampled while the number of feature channels is increased. Correspondingly, the decoder block gradually raises the spatial resolution by up-sampling the feature map at each step, and then applies  $2 \times 2$  convolution (“up-convolution”) to lower the number of feature channels. To further reduce information loss, at each step of the decoder, the up-sampled feature map is concatenated with high-resolution features from the corresponding step of the encoder to avoid information loss. This is followed by two consecutive  $3 \times 3$  convolutions that halve the feature map channel dimension. Finally, a  $1 \times 1$  convolution is employed in the decoder’s output to map the feature vector of each pixel to the appropriate number of classes, producing a pixel-wise mask.

SegNet <sup>[38]</sup> (see **Figure 9c**) incorporates two sub-networks: encoder and decoder. The encoder network uses convolution and max pooling to extract features, similar to FCNs. This network’s deeper layer extracts semantic meanings. SegNet maintains the element index (i.e., the location of an element within the filter window) and uses it in the decoder network’s upsampling process. Like the encoder net-

work, the decoder network is symmetric. It translates low-resolution features to higher-resolution ones using convolutions and guided upsampling with the encoder network’s pooling index. For example, a  $2 \times 2$  low-resolution feature map becomes a  $4 \times 4$  zero-filled matrix. This reuse of the pooling index improves boundary precision and recovers spatial information. Unlike U-Net, SegNet does not feed extracted features to decoders, which are then concatenated into upsampled feature maps.

DeepLab<sup>[39]</sup> (see **Figure 9d**) applies “Atrous convolution” with upsampled filters for dense feature extraction. Furthermore, Atrous spatial pyramid pooling encodes objects and visual context at many scales. The authors used deep convolutional neural networks and fully connected conditional random fields to yield semantically correct predictions and comprehensive object segmentation maps.

### 3.5 Deep belief network

The Deep Belief Network (DBN)<sup>[40]</sup>, shown in **Figure 10**, is a subtype of Deep Neural Network made up of stacked layers of Restricted Boltzmann Machines (RBMs). It is a generative model that Geoffrey Hinton introduced in 2006<sup>[41]</sup>. DBN may be used to solve unsupervised learning problems in order to reduce the dimension of features, as well as supervised learning tasks in order to construct classification or regression models. Two phases are required to train a DBN: Layer-by-layer training and fine-tuning. The terms “layer-by-layer training” relate to the unsupervised training of each RBM, while “fine-tuning” refers to the employment of error back-propagation techniques to fine-tune the parameters of the DBN following the unsupervised training.

Hinton suggested stacking RBMs on top of each other to train DBN quickly. During training, the lowest level RBM learns the data distribution. By sampling the previous hidden layer’s hidden units, the following RBM block learns high-order correlation between them. This is done for each concealed layer up to the top.

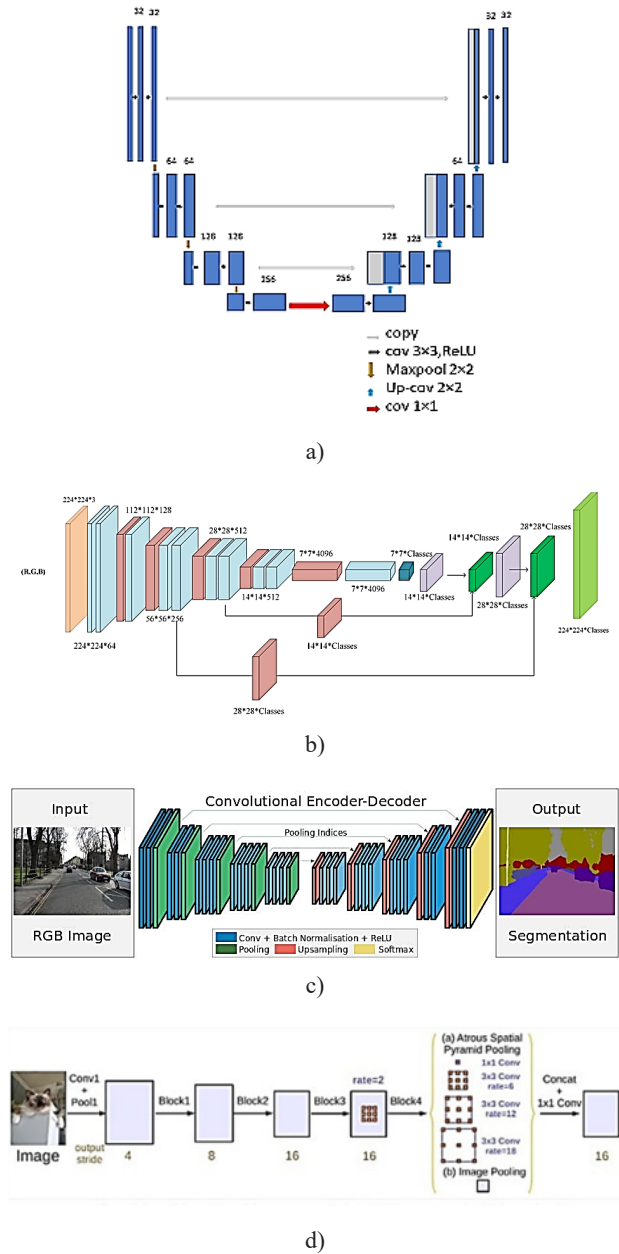


**Figure 9.** Fully CNN architecture a) FCN-8, b) UNet, c) SgNet, and d) DeepLab.

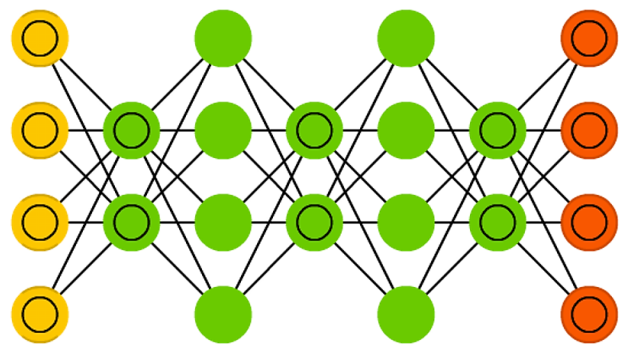


**Figure 10.** Graphical abstract of deep belief neural network.

### 3.6 Graph Neural Network (GNNs)

Graph, a data structure, represents a set of objects (nodes) and their connections (edges). Recent studies on graphs with machine learning have gained popularity due to their ability to represent a wide range of systems in different fields such as social science, natural science (physical systems) and protein-protein interaction networks [42]. Graph analysis is adopted for non-Euclidean data format in machine learning. Typical CNNs operate only with standard Euclidean data like images (2-D grids) and text (1-D sequences). Therefore, Geometric DL is the extension of deep neural models to the non-Euclidean setting. Recently, Graph Neural Network (GNNs) has recently gained popularity due to their superior performance.

Conventional CNNs are inefficient at handling spatial vectors. However, it can only be modeled as graph structures. First graph Fourier transform and convolution theorem [43], were adopted to convert vector data from the vertex domain into a point-wise product in the Fourier domain. Then, a Graph Convolutional Neural Network (GCNN) model was introduced for building pattern classification. The obtained results confirmed a satisfactory result in identifying regular and irregular building patterns. A further improvement could be considered in the potential analysis of graph-structured spatial vector data. In their pioneer work [44], a novel two-stream architecture combining global visual and object-based location features is established to enhance feature representation capabilities. First, CNN was used to extract visual features from a scene image. To learn spatial position attributes of ground objects based on GCN. The proposed architecture examines object dependencies in remote sensing scene classification for hyperspectral data.

An attempt to tackle multi-label RS image classification. This research provides a revolutionary DL-based framework called MLRSSC-CNN-GNN [45]. Basically, CNN is used to learn visual perception and create high-level appearance attributes. Each scene graph is built using the trained CNN, with nodes representing super-pixel portions of the scene. The multi-layer-integration Graph Attention Network (GAT) model is proposed to handle Multi-Label Remote Sensing Image Scene Classification (MLRSSC), where the GAT is one of the latest advancements in GNN. Extensive trials on two public MLRSSC datasets show that the proposed approach outperforms other approaches.

Several Graph Convolutional Networks (GCNs) [46], were investigated to analyze RS images to better understand their semantics which could be effective in land cover mapping. The simplification of the complexity, and the optimal control of the number of influential neighbors of the nodes were serious challenges.

High-order graph convolutional network was adopted for remote sensing scene categorization (H-GCN) [47]. During CNN feature learning, the proposed method incorporates an attention mechanism to focus on critical image components. An advanced graph convolutional network is used to analyze class dependencies (see **Figure 11**). An attentive CNN feature from each semantic class describes each node in the graph. It is possible to obtain a more informative representation of nodes by blending neighbour information of nodes in different orders. The discriminative feature representation for scene classification eventually combines H-GCN and attention CNN node representations. A summary of the current application of GNN in the RS domain is illustrated in **Table 3**.

**Table 3.** A summary of GNN for image analysis applications.

Summary	Architecture	Application
In object detection, and region classification. GNNs are used to calculate interested features, and region classification respectively.	Graph Attention Network	Object detection
	Graph Neural Network	Object detection
	Graph CNN	Classification
In Semantic segmentation, GNN is utilized to handle regions in images which are often not grid-like and need non-local information	Graph LSTM/Gated Graph Neural Network / Graph CNN/Graph Neural Network	Semantic Segmentation

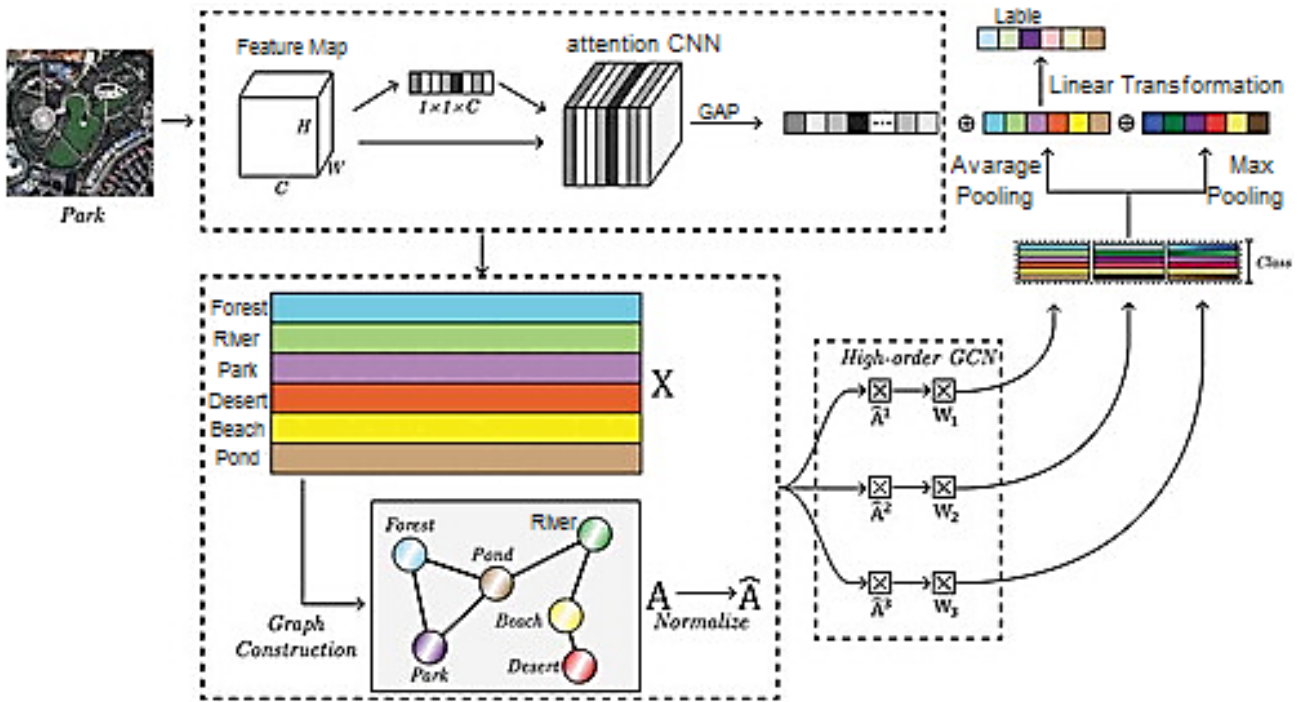


Figure 11. Scene classification framework of [47] method.

### 3.7 Generative Adversarial Networks (GANs)

Generative adversarial networks (GANs) [48], were presented as a novel technique for general data samples that simulate the original data distribution. Typically, GAN network is comprised of two sub-networks: Generative (G) and Discriminative (D). The Generative Network (G) maps a nonlinear function between random vectors and the desired image space. Under other conditions, the Discriminative Network (D) differentiates whether the produced data belong to the probability distribution of real data. Theoretically, GANs are built upon a game theoretical scenario whereas the generator had to compete against a discriminator [40].

Figure 12 depicts a GAN general structure. The generator network (G) directly generates samples shares training data distribution using random noise (v). The discriminator network (D) seeks to distinguish between samples from the training data and those from the generator. While the discriminator D is taught to maximize  $\log(D(G(x))) \log(D(G(x)))$ . The generator block G is trained to minimize  $\log(1 - D(G(z))) \log(1 - D(G(z)))$  [42]. D and G thus play a

two-player minimax game as:

$$GAN = \arg \min_D \max_G L_{GAN}(G, D)$$

where  $L_{GAN}(G, D) = E_{x \sim p(x)}[\log D(x)] + E_{z \sim p(z)}[\log(1 - D(G(z)))]$

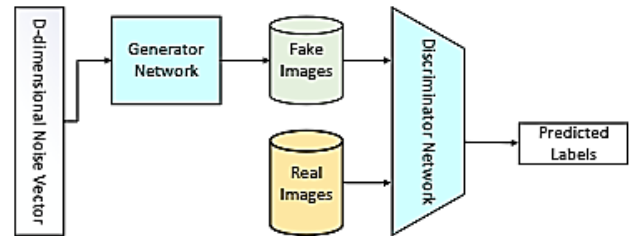


Figure 12. A typical GAN architecture in classification context.

To tackle hyperspectral challenges, the authors presented the Caps-TripleGAN framework [49], that integrated generative adversarial and CapsNet. The proposed end-to-end framework utilized a 1-D structure for sample generation. Another work introduced adversarial learning and the Variational Autoencoder (VAE) [50] was integrated to effectively classify hyperspectral imagery. The proposed method employed a conditional variational autoencoder with an adversarial training process to produce a spectral sample.

Since the introduction of GANs different types had been proposed such as conditional GAN. The

authors offer new sample weighting and class adversarial training algorithms that combine SAR complementary characteristics <sup>[51]</sup>. A distribution and structure match auxiliary classifier generative adversarial network (DSM-ACGAN) was built. In DSM-ACGAN class adversarial training, statistical distribution and spatial structure are concurrently explored. DSM-ACGAN, on the other hand, uses real SAR image features to train generative models for each category. However, it also instructs the discriminator to capture both statistical and structural aspects. Class adversarial processing increases discriminative feature learning and adds to classification. It is also possible to generate class-balanced samples.

An improved GAN framework incorporated with Autoencoder (AE) to extract features advances semi-supervised and unsupervised learning <sup>[52]</sup>. The extracted features are combined with Multi-Classifer (MC) for better context classification. SAR multi frequency bands (L, C and X-bands) were effectively classified demonstrating the superiority of the proposed framework in terms of training stability and mode preservation. The authors presented GAN for land cover classification for different sources. The proposed GAN utilized FCN network for pixel classification of land covers <sup>[53]</sup>. A sea fog detection approach using Super-Pixel-Based Fully Convolutional Network (SFCNet) <sup>[54]</sup>, named SFCNet was introduced. A fully connected Conditional Random Field (CRF) model was integrated to map the pixels' dependencies.

### 3.8 Attention-based models

Recently, attention has become a key term in DL

architectures thanks to its ability to simulate human biological systems by focusing on distinct sections when processing enormous volumes of data. This section provides an overview of recent attention models. So far, DL has been difficult to interpret due to the lack of interpretability in practical and ethical concerns. The attention mechanism <sup>[55,56]</sup> helps to give distinct information with varying weights. Giving larger weights to important data draws the DL model's attention to it. Typically, existing attention models can be categorized based on four criteria: Softness of attention, input feature types, input representation, and output representation (see **Figure 13**).

Accordingly, attentions are grouped in the RS domain <sup>[57]</sup> into two main types namely: Channel and spatial, as shown in **Figure 14**. A new deep learning framework, named attentive weakly Supervised Satellite image time series classifier (TASSEL) <sup>[58]</sup>, was introduced to tackle time series land cover mapping. The proposed framework utilizes multifarious information instead of aggregating item statistics via the integration of graph attention mechanism and self-attention mechanism. A Spectral-Spatial Self-Attention Network (SSAN) for HSI classification was proposed <sup>[59]</sup>. The proposed architecture is composed of two subnetworks namely spatial and spectral. The spatial self-attention module is integrated into the spatial subnetwork to enrich patch-based contextual information about the center pixel. On the other hand, a spectral self-attention module was integrated into the spectral subnetwork to take use of long-range spectral correlation over local spectral features.

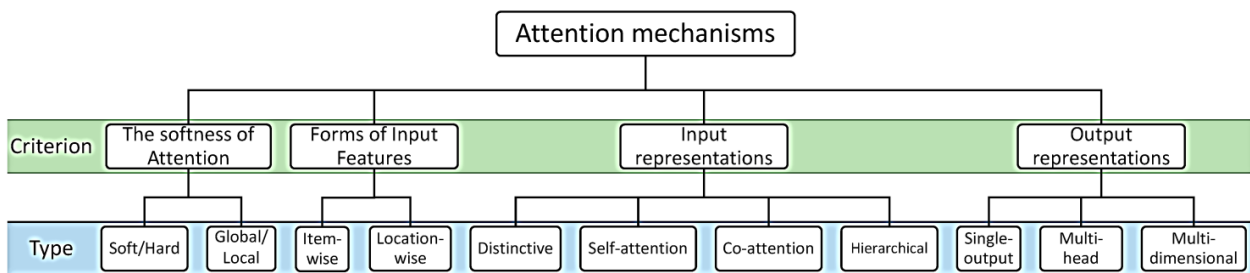
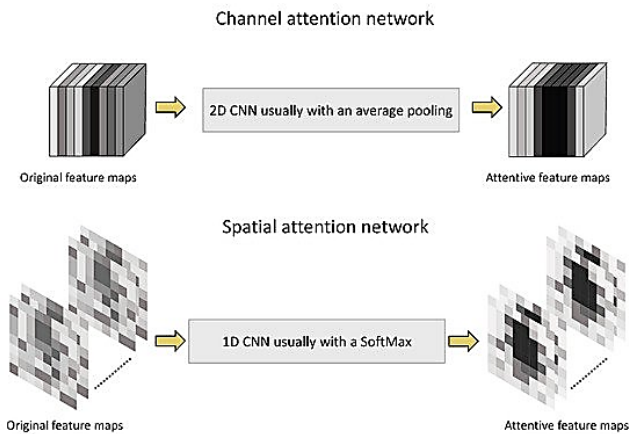


Figure 13. Several typical approaches of attention mechanisms <sup>[56]</sup>.



**Figure 14.** A simple illustration of the channel and spatial attention types/networks, and their effects on the feature maps <sup>[57]</sup>.

### 3.9 Deep learning optimization techniques

Traditional machine learning has traditionally avoided the general optimization complexity by carefully crafting the objective function and constraints to ensure the convexity of the problem of optimization. In training neural networks, the general non-convex situation had to be addressed. This section outlines the most influential challenges involved in optimizing deep model learning such as:

**Local Minima:** The grandfather of all optimization problems. The local minima is a permanent challenge in the optimization of any deep learning algorithm. The local minima problem arises when the gradient encounters many local minimums that are different and not correlated to a global minimum for the cost function.

**Inexact Gradients:** Many deep learning models in which the cost function is intractable force an inexact estimation of the gradient. In these cases, the inexact gradients introduce a second layer of uncertainty in the model.

**Flat Regions:** In deep learning optimization models, flat regions are common areas that represent both a local minimum for a sub-region and a local maximum for another. That duality often causes the gradient to get stuck.

**Local vs. Global Structures:** Another very common challenge in the optimization of deep learning

models is that local regions of the cost function don't correspond with its global structure producing a misleading gradient.

The most popular optimization method for deep learning is Stochastic Gradient Descent (SGD) <sup>[60]</sup>. The gradient estimates downwards. The learning rate is an important element in SGD. The learning rate must be decreased gradually in practice. The learning rate is one of the most difficult hyperparameters to establish in neural networks since it affects model performance. It uses a heuristic method to modify individual model parameter learning rates during training <sup>[61]</sup>. The concept is simple: If the partial derivative of the loss is positive, the learning rate should be positive. This should slow learning if the partial derivative changes sign. Examples include Adaptive Gradient Algorithm (AdaGrad), Root Mean Square Propagation (RMSProp), and Adaptive Moment Estimation (Adam).

The AdaGrad algorithm individually adapts all model parameters to their learning rates by inversely proportionally scaling them to the square root of the sum of all the squared historical gradient values <sup>[62]</sup>. The parameters with the largest partial derivatives of the loss decreased their learning rate rapidly while the parameters with small partial derivatives decreased their learning rate slowly. The RMSProp algorithm <sup>[63]</sup> modifies AdaGrad to improve non-convex performance by changing the accumulation of gradients to an exponentially weighted moving average. In a convex function, AdaGrad is designed to converge rapidly. Empirically, RMSProp has been shown to be an efficient and practical optimization algorithm for deep neural networks. Another adaptive algorithm for optimizing the learning rate is Adam <sup>[64]</sup>.

## 4. Deep learning in remote sensing

As mentioned before, RS image classification is not limited to classification approaches, but extended to image segmentation, and object detection. This section discusses the recent efforts introduced by RS scientists.

## 4.1 Image classification

Recent efforts had successfully generalized to boost the performance of vintage CNNs in remote sensing classification problems. However, the insufficient number of labelled remote sensing and the complex nature of remote sensing imageries are still considered a limitation to supers the CNN performance in the remote sensing domain. Transfer learning, fine-tuning and ensemble learning were popular strategies to alleviate this limitation.

Xie et al. presented a scale-free CNN (SF-CNN) model for remote sensing scene classification <sup>[65]</sup>. The proposed architecture effectively overcomes the problem of fixed-size input images for pre-trained CNN architecture. The proposed model contains two main components: Fully Convolution Layers (FCLs) and an extra Global Average Pooling (GAP) layer. Experiments conducted on real data sets showed the superior performance of the proposed model compared with other classification methods.

In an end-to-end Feature Aggregation CNN (FACNN) was presented that utilized the intermediate features. The pre-trained VGG-16 model was adopted as a backbone to extract the intermediate features and then fed to the feature encoding module. To obtain discriminative scene representation, the classic SoftMax classifier is employed to obtain the semantic labels from the scene representations. An end-to-end learning model called Skip-Connected Covariance (SCCov) network was introduced for scene classification <sup>[66]</sup>. Skip connections and covariance pooling are embedded into the traditional CNN model. To achieve a more representative feature, skip connections architecture allows multi-resolution feature maps to combine together, and the covariance pooling to fully exploit the second-order information contained in such multi-resolution feature maps. The proposed architecture has only 10% of the parameters used by its counterparts. Experimental results demonstrate the effectiveness of the proposed model compared with the state-of-the-art techniques.

Fang et al. <sup>[67]</sup> introduced a feature representation method that incorporates frequency domain with traditional space domain. A weight spatial pyramid

matching scheme was investigated to improve the performance of classification <sup>[68]</sup>. Several experiments on benchmark datasets demonstrate the superior performance of the proposed algorithm. Liu et al. introduced Siamese CNN, which combined the identification and verification models of CNNs. In addition to a metric learning regularization term imposed through CNNs to enforce more robust with the Siamese networks <sup>[69]</sup>.

A bidirectional adaptive feature fusion strategy was investigated <sup>[70]</sup>. Deep features and the SIFT features were extracted using CNN and SIFT filters respectively, then fused both features to obtain a more discriminative representation and overcome the scale and rotation variability with the usage of the SIFT feature. Zhang et al. <sup>[71]</sup> proposed a new architecture named CNN-Caps Net. The proposed architecture has two parts. The first part is a pre-trained VGG-16 whose intermediate convolutional layer is utilized as a primary feature extractor. In the second part, the extracted features are fed into CapsNet. To overcome the scarcity of labelled samples, unsupervised learning-based generative adversarial networks <sup>[72]</sup> were introduced to generate training samples instead of augmentation techniques.

## 4.2 Image segmentation

Various efforts had been conducted to integrate the recent DL semantic segmentation techniques in the RS domain. DL image segmentation models in computer vision have been on the rise since 2014, as seen in **Figure 15**. An adaptive mask Region-based Convolutional Network (Mask-RCNN) <sup>[73]</sup> is developed for multi-class object detection in remote sensing images. Data augmentation, and transfer learning were used to address a variety of scales, sizes, and densities of remote-sensing objects. Another effort was developed <sup>[74]</sup>, to extract crops from satellite imageries based on Mask RCNN. A road segmentation approach based on DeepLab v3 <sup>[75]</sup> was proposed by incorporating Squeeze-and-Excitation (SE) module in order to apply weights to different feature channels and performs multi-scale upsampling to preserve and fuse shallow and deep information. Unbal-

anced road samples problem in RS images, different loss functions and backbone network modules were evaluated during training.

A cone karst landscape identification based on DeepLab V3+ network [76] was proposed for multi-source data. Optical images and DEM data were used to generate the training samples. The input module of DeepLab V3+ network was altered in order to handle a four-channel image.

### 4.3 Object detection

Extensive studies have been devoted to studying object detection in optical and SAR images [79]. Figure 16 illustrated the history of DL image object detection models in computer vision since 2014. Many researchers in the RS domain are using the R-CNN pipeline to recognize various geographical items in remote sensing imageries due to its superior performance in detecting natural scene image objects [77-79].

The authors [66,80] integrated a rotation-invariant CNN within the R-CNN framework for effective multi-class geospatial object detection. To further boost state-of-the-art of object detection. A novel strategy to train the CNN model called (RIFD-CNN) [81], was proposed by applying a rotation-invariant regularizer and a fisher discrimination regularizer. To accom-

plish precise localization of geospatial objects in HR images. Long et al. proposed an RCNN-based Unsupervised Score-Based Bounding Box Regression (USB-BBR) technique [78]. Despite the fact that the aforementioned strategies have shown to be effective in the RS community, they are nonetheless time-consuming since these methods rely on human-designed object proposal-generating methods, which consume the majority of running time. Furthermore, the quality of region suggestions developed based on hand-engineered low-level characteristics is poor, resulting in poor object identification performance.

Several studies extended the architecture of Faster R-CNN to the earth observation community [82-88]. For instance, Li et al. [84] developed a rotation-insensitive Region Proposal Network (RPN) by inserting multi-angle anchors into the existing RPN based on the Faster RCNN pipeline.

A double-channel feature combination network is also meant to learn local and contextual properties to address appearance uncertainty. Zhong et al. [85] used PSB to improve the quality of generated region proposals. For object detection, the suggested PSB framework featured FCN [36] based on the residual network [22]. The authors proposed a deformable CNN to model object changes in which non-maximum suppression [88,89] bound was established by as-

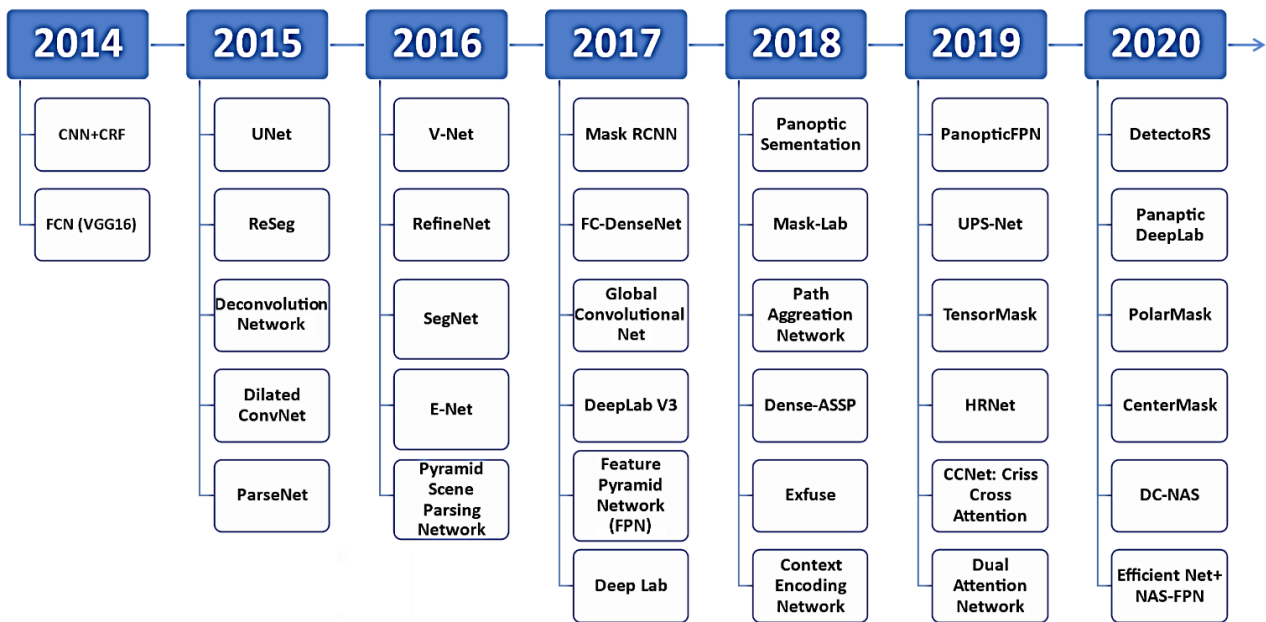


Figure 15. Timeline of representative DL-based image segmentation algorithms.

pect ratio to eliminate misleading region proposals.

To increase vehicle detection accuracy, the authors presented a Hyper Region Proposal Network (HRPN) to locate vehicle-like regions [90]. Although applying region proposal-based methods such as R-CNN, Faster R-CNN, and its variations to recognize geographical objects in Earth observation photos shows tremendous promise, amazing efforts have been made to explore other deep learning-based methods [91-95]. To determine object centroids, a rotation-invariant method [95] was employed based on super-pixel segmentation to build local patches, deep Boltzmann machines to construct high-level feature representations of local patches, and finally a series of multi-scale Hough forests to cast rotation-invariant votes. To detect ships, Zou and Shi [96] employed a singular value decomposition network to create ship-like regions, followed by feature pooling and a linear support vector machine classifier. While this detection approach is intriguing, the training method is cumbersome and slow.

Recently, some studies have attempted to translate regression-based object detection approaches developed for natural scene images to remote sensing images. Tang et al. [94] used a regression-based object detector to detect vehicle targets. Specifically, the detection bounding boxes are generated by adopting a set of default boxes with different scales per feature map location. Moreover, for each default box the offsets are predicted to better fit the object shape. Liu et al. [92] adopted a single-shot multi-box detector

(SSD) framework but replaced the traditional bounding box with a rotatable bounding box from [97], in order to help to estimate objects despite their orientation angles. Liu et al. [93] developed an effective approach to detect arbitrary-oriented ships based on YOLOv2 architecture.

In addition, hard example mining [90,94], transfer learning [83], multi-feature fusion [98], and non-maximum suppression [89] are widely designed for geospatial object detection and enhance the performance of computer vision deep learning-based approaches [82]. The current stream of deep learning-based methods (e.g., R-CNN, Faster R-CNN, SSD, etc.) has proven substantial achievement in detecting geospatial objects. Earth observation photographs vary considerably from natural scene images, particularly in terms of rotation, scale variation, and complex and cluttered backgrounds [87].

#### 4.4 Training strategies

A deep Convolutional Neural Network (CNN) can be challenging to train from scratch since it requires a significant quantity of labelled training data and much skill to guarantee that the network converges properly. Typically, feature extraction and fine-tuning of an already pre-trained network are potential options to be considered in RS (Figure 17).

Feature Extraction: The pre-trained CNN is employed as a feature generator. Specifically, an input image is fed to the pre-trained CNN, which then ex-

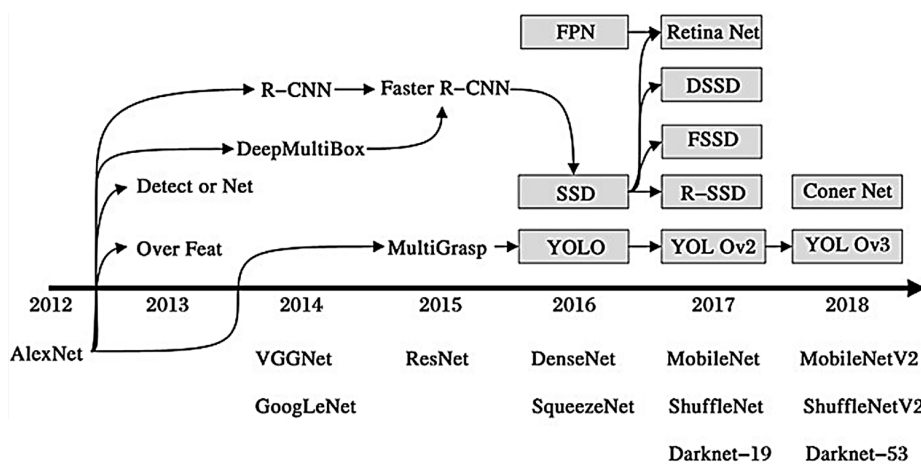
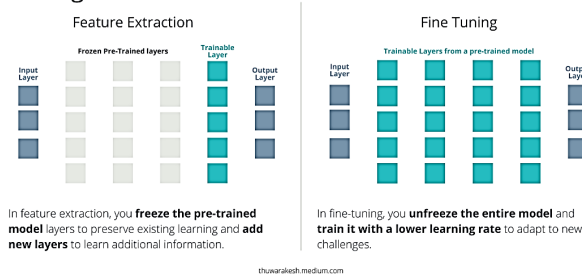


Figure 16. Timeline of progress of deep learning object detection methods.

tracts features from a specific layer of the network. The features are utilized to train a new pattern classifier. In another word, to transfer knowledge from one model to another with no training involved, the feature extraction technique is considered the key to learning features from a pre-trained model and training another (much smaller model) in order to achieve an outstanding result in a short amount of time.

**Fine-Tuning:** The weights of the early convolution layers are freezing while fully connected layers may be replaced with a new logistic layer relative to the application in hand. A labeled dataset is adopted to train the model while lowering the learning rate.

**Transfer Learning:** How Feature Extraction & Fine-Tuning work?



**Figure 17.** A comparison between feature extraction and fine-tuning training strategies.

**4.5 Loss functions**

Typically, the loss functions applied in image classification problems are categorized into distribution-based losses (minimize dissimilarity between two distributions), and region-based losses (minimize the mismatch or maximize the overlap regions between the two images) [99,100]. A common practice is to evaluate a small subset of the available loss function to avoid the impracticability of experimenting with all available loss functions.

Several studies compared the performance of different loss functions namely: Cross-entropy loss, focal loss, Tversky loss, dice loss, and contrastive loss to evaluate their performance in RS datasets. One can conclude that contrastive loss and weighted combined loss are widely used in RS applications due to the complex distribution of objects and their imbalance nature. **Figure 18** depicted the famous

distribution-based, region-based, and compound loss functions adopted in DL for the RS domain.

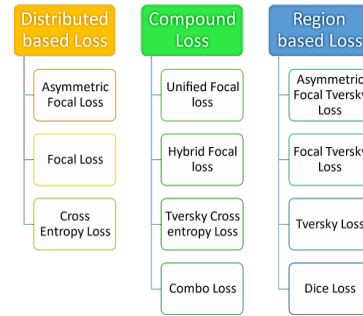


**Figure 18.** The famous distribution-based, region based, and compound loss functions.

**4.6 Performance evaluation**

Typically, the preparation of training examples is generally challenging as it requires significant labor and time to evaluate the DL performance model. Various evaluation metrics were employed that are commonly used in classification problems as described in **Table 4**. Typically, True positive (TP), False Negative (FN), False Positive (FP) and True Negative (TN).

**Table 4.** Classification evaluation metrics.

Evaluation metric	Value
True Positive Rate (TPR)	$\frac{TP}{TP+FN}$
False Positive Rate (FPR)	$\frac{FP}{TP+FN}$
False Negative Rate (FNR)	$\frac{FN}{TP+FN}$
Precision	$\frac{TP}{TP+FP}$
F-Measure	$\frac{2 \times TP}{2 \times TP + FP + FN}$
Accuracy	$100 \times \frac{TP + TN}{TP + FN + TN + FP}$
Matthews Correlation Coefficient (MCC)	$\frac{TP \times TN - FP \times FN}{\sqrt{(TP+FP)(TP+FN)(TN+FP)(TN+FN)}}$

**5. Deep learning challenges in remote sensing domain**

Undoubtedly, RS image classification has benefited tremendously from DL models. DL approaches have suppressed human-level accuracy. This section discusses the exciting challenges to tackle.

### 5.1 Uncertainty and balance between accuracy and efficiency

Models should establish their trustworthiness. The proposed models in the RS domain should utilize Bayesian/probabilistic inference to explicitly describe and propagate uncertainty. Identifying and treating extrapolation is also important. The contradiction between the accuracy and efficiency obtained from the models is considered a major challenge. The models with good efficiency (e.g., SegNet and ENet) fail to provide sufficiently accurate results in the RS domain.

### 5.2 Dependency on high-quality training data

To achieve acceptable accuracy, high-quality training datasets are required. However, collecting high-quality training data (sufficiently labeled on pixel-level annotation) is considered a hard and time-consuming task that depends on human labor.

### 5.3 Domain gap across different datasets

A domain gap is derived from the fact that typical deep learning models were introduced for vision tasks. The complexity of RS data impacts model performance in almost all RS applications. Since different datasets are created for different RS applications, they may differ in class number, scene look, dataset size, object size, etc. In this case, the discrepancies widen the distance between heterogeneous areas. Therefore, RS are encouraged to consider different techniques (transfer learning, data augmentation, etc.) to overcome the domain gap issue when applying DL models in their applications.

## 6. Recent deep learning advances in remote sensing domain

This section introduces several promising research directions to advance RS image classification algorithms.

### 6.1 Reinforcement learning

Reinforcement learning (RL), is an area of Ma-

chine Learning, which involves taking suitable action to maximize reward in a given scenario. It is employed by various software and machines to find the best possible behavior or path it should take in a specific situation. Reinforcement learning differs from supervised learning in a way that in supervised learning the training data has the answer key with it, so the model is trained with the correct answer itself whereas in reinforcement learning, there is no answer but the reinforcement agent decides what to do to perform the given task. In the absence of a training dataset, it is bound to learn from its experience. Combining HR images with machine learning<sup>[101]</sup>, enables the scientist to address the poverty mapping problem. However, HR images come with costs and limits of scalability. RL may be utilized in combination with free low-resolution photography to dynamically identify where to gather expensive HR imagery, before doing deep learning on the HR images. Another work was introduced to utilize reinforcement learning in searching optimized parameters of deep learning model<sup>[102]</sup>.

### 6.2 Knowledge distillation

Deep neural network shows a staining performance at the research level. However, its deployment is troublesome to utilize in limited hardware or in real-world environments due to the high computational cost and the required massive volumes of labeled data in training. To address the above problems, several model compression methods were studied to transfer the knowledge from complex architecture neural networks to compact lightweight models while sustaining performance<sup>[103]</sup>.

Neural network compression is categorized into four main groups: Pruning and quantization<sup>[104]</sup>, low-rank factorization<sup>[105]</sup>, compact convolution filters<sup>[106]</sup>, and Knowledge Distillation (KD) (Hinton et al., 2015). Pruning demands a massive number of iterations to converge to eliminate the nonessential parameters of the performance. Low-rank factorization utilized the matrix decomposition to estimate relevant parameters and remove the rest using tensor decomposition. Compact convolution filters sub-

stitute extensive parameter convolution filters with lightweight blocks. Finally, KD <sup>[103]</sup> is a simple yet effective approach to transfer or distill the representative knowledge from the large neural network (teacher) into the thin compressed network (student). The main objective of the KD is minimizing the divergence of the probabilistic outputs of teacher and student networks. The student network is trained to capture the teacher network's significant representation. Knowledge distillation <sup>[107]</sup> has been widely adopted by different architectures <sup>[108]</sup> and learning tasks <sup>[109]</sup>. Adversarial methods also have been utilized for modeling knowledge transfer between teacher and student <sup>[108]</sup>.

### 6.3 More challenging datasets

Several large-scale RS image datasets have been created for object-based and pixel-based classification. However, more challenging datasets for different types of RS images are still required. Datasets containing a large number of overlapping objects of varying spatial resolutions would be very valuable. This can improve training models that are better at handling common scenarios in the real-world. Large-scale 3D RS image collections are in high demand because of the increasing popularity of 3D RS image datasets. These datasets are more difficult to create and effectively annotated compared with their lower-dimensional counterparts. Most 3D datasets are typically too small, and some are synthetic, therefore larger, and more challenging 3D image datasets can be extremely valuable.

### 6.4 Interpretable deep models

Despite the encouraging performance of DL modes, several concerns remain. For example, how and what do deep models learn? What is a minimal neural architecture that can accurately classify datasets? While methods exist to visualize the learned convolutional kernels, a detailed analysis of their behavior/dynamics is missing. A better understanding of the conceptual and theoretical aspects of the models may lead to improved models tailored to specific

classification scenarios.

### 6.5 Weakly-supervised and unsupervised learning

Unsupervised learning and weakly supervised (few-shots) are currently hot research topics. Collecting labelled samples for RS pixel-based classification is difficult in many application areas. Transfer learning, which adopted a trained model on a large number of labelled examples (from a public benchmark), then fine-tuned on a few samples from a target application. Self-supervised learning is gaining popularity in several areas. Self-supervised learning can collect features to train efficient classification models with significantly fewer training data. Reinforcement learning models may potentially be a future approach for RS image classification.

### 6.6 Real-time models

Accuracy is considered a significant factor in model performance, however many applications (autonomous driving, disaster management, and land cover mapping) require running in real or near real-time. Also, some applications may be installed in limited memory and processing setting (mobile applications), but to fit them into specific devices, such as mobile phones, the networks must be simplified. Dilated convolution models, simpler models, and knowledge distillation approaches help speed up segmentation models, but there is always room for improvement.

### 6.7 Zero-shot learning

Zero-Shot Learning (ZSL) <sup>[110]</sup> uses the derived intermediate semantic knowledge to detect objects that have not been observed during training, which potentially extends the ability of machine learning algorithms in problem-solving skills. ZSL transmits semantic knowledge, making it an excellent complement to supervised learning. Thus, ZSL may learn to detect novel unseen classes that have no training examples by connecting them to see classes that were previously learnt. A Generalized Zero-Shot Learning

(GZSL)-based PolSAR land cover classification system is proposed<sup>[111]</sup>. Initially, basic semantic features were gathered to define typical land cover categories in PolSAR images. In the training stage, latent embedding may be used to get the projection between mid-level polarimetric information and semantic characteristics. Semantic relevance and mid-level polarimetric characteristics form the GZSL model for PolSAR data. Finally, the test instances' labels may be anticipated for some unknown classes.

## 6.8 UAVS, drones, and LiDAR

UAVs, as well as drones, deliver images and videos with very high-resolution amenable to be utilized in various applications<sup>[112]</sup> such as live-stock monitoring, crop production, yield prediction, and soil mapping<sup>[113]</sup>. Many sensors can be embedded in a UAV or drone, such as weather sensors, cameras, and LiDAR sensors. The obtained sensor data can be integrated into real-time decision-making in many fields<sup>[114]</sup>. LiDAR technology can create detailed topography maps and Digital Elevation Models (DEMs) necessary for land segmentation, and crop analysis field management. LiDAR technology is highly valuable in the geospatial community, with the massive data amounts amenable to utilization in a diversity of applications. Point clouds are 3D unstructured data that present many challenges for classic CNN settings. Few studies have focused on 3D point clouds. However, the 3D point cloud is gaining popularity in many applications in 3D modelling (self-driving and building modelling). Graph-based deep models may be considered as a potential area for point-clouds classification.

## 7. Recent deep learning in remote sensing application

This article briefly compares different deep-learning methods in the field of RS. Typically, one can observe that CNN is the most popular DL model to study and spectral-spatial features of earth observation images in classification, and object detection. The following sections review the most frequent RS

applications.

### 7.1 Agriculture applications

Agriculture researchers have introduced some approaches, such as Transformation Learning (TL)<sup>[26]</sup> and Low Batch Learning (FSL)<sup>[27]</sup>, so that deep learning models are not dependent on datasets<sup>[115]</sup>. The TL has been successfully used to identify herbs and diseases<sup>[30]</sup>. Also, FSL was found to be useful in identifying plant diseases<sup>[31-33]</sup>. The research estimates the growth stage of wheat and barley by classifying nearby images using Convolutional Neural Networks (ConvNets), and the classification was done using three different machine learning methodologies: A 5-layer ConvNet model, a transfer learning based on a VGG19 pre-trained network, and a support vector machine with conventional feature extraction<sup>[116]</sup>. Regarding the growth classification, the ConvNet learning transfer network has a much smaller training time than the built-in ConvNet model from scratch. The objectives of the research are to develop raw image-based deep learning methods for predicting the outcome in the field, and to study the sharing of multi-time images for grain quantities produced using handcrafted features and WorldView-3 and PlanetScope images, respectively<sup>[117]</sup>.

### 7.2 Oceanography and sea ice mapping

Ocean remote sensing has reached the five-V (volume, variety, value, velocity, and veracity) age with the continual advancement of space and sensor technology over the previous 40 years. Globally, ocean remote sensing data archives top tens of petabytes, and satellite data is gathered regularly. It's difficult to harvest meaningful information from ocean remote sensing data sets. Its advantage over traditional physical or statistical-based methods for image extraction in several industrial fields has sparked interest in ocean remote-sensing applications. Two deep-learning frameworks were examined for the classification of ocean internal-wave/eddy/oil-spill/coastal-inundation/sea-ice/green-algae, and ship/coral-reef mapping<sup>[118]</sup>. SAR images were analyzed,

ice charts as labelled data, and neural networks could efficiently classify ice kinds <sup>[119]</sup>. The SAR pictures were cropped into sub-regions based on the Canadian Ice Service (CIS) image analysis ice chart's latitude and longitude coordinates, and each sub-region was handled as an independent sample. Two neural networks namely: A modified U-Net and a DenseNet were adopted on the three-class dataset with dual-pol HH and HV setup, DenseNet obtained the greatest overall accuracy of 94.02 percent and ice accuracy of 91.75 percent.

For sea-ice image classification, the architecture of the SAR & optical images deep learning network was designed by extracting features and merging heterogeneous data at the feature level <sup>[120]</sup>. For the SAR images, the enhanced Spatial Pyramid Pooling (SPP) network was used and texture information about sea ice was extracted at different scales depending on the depth. As for the optical data, multilevel feature information about sea ice such as spatial and spectral information of different types of sea ice was extracted using Path Aggregation Network (PANet), which allowed the use of low-level features due to the feature of incremental extraction by the convolutional neural network. An advanced deep learning (DL) model was introduced to classify sea ice and open water from synthetic aperture radar (SAR) images <sup>[121]</sup>. U-Net was used as a backbone model for pixel-level segmentation. A DL-based feature extraction model, ResNet-34, was used as an U-Net encoder. To increase the accuracy of classifications, the original U-Net is combined with the dual attention mechanism, so as to obtain a better representation of the features, and also to form a dual attention U-Net (DAU-Net) model. The MobileNetV3 deep learning model is used as the backbone network <sup>[122]</sup>, and the input samples are multi-scales, and merge the backbone network with multiscale feature fusion methods to develop a deep learning model named Multiscale MobileNet (MSMN). The MSMN accuracy was about 95% classification using SAR sea ice images and results show that dual-polarization data achieve better classification accuracy. For comparison, other classification models were trained using

the training data of this paper, and the average accuracy of MSMN was found to be higher than that obtained from the model made using Convolutional Neural Networks (CNNs) and ResNet18 models. To improve classification performance, a framework for raindrop removal was introduced <sup>[123]</sup>. Images of sea ice are categorized into ice, water, ship and sky <sup>[86]</sup>, by training three deep learning semantic segmentation networks, they are VGG-16, FCN, and pyramid scene parsing network. To make the training process better, transfer learning is done in addition to data augmentation. The results showed that data augmentation operations improved the performance of the three models. Also, the raindrop removal framework improves performance, the average intersection is higher than that of the VGG-16 Union.

### **7.3 Disaster and environmental monitoring**

There is no doubt that the era of big data and deep learning has opened new options for disaster management, thanks to the diverse capabilities it provides in visualizing, analyzing, and predicting disasters. The integration of big data and DL has completely altered the strategies followed by human societies and disaster management agencies to reduce human suffering and economic losses resulting from disasters. In our world which is now mainly dependent on information technology, the main goal of computer experts and decision-makers is to make the best of model by gathering information from different sources and formats and storing it in effective ways to be used effectively in different stages of disaster management. The availability of various big data sources such as satellite imageries, Global Positioning System (GPS) traces, mobile Call Detail Records (CDRs), social media posts, etc., in conjunction with the enhancements in data analytic techniques (e.g., data mining, machine learning, and deep learning) can facilitate geospatial information extraction, that is crucial for immediate and effective disaster response. The research <sup>[124]</sup> introduced a deep neural network approach for detecting submerged stop signs in images of flooded roads and intersections, as well as detecting Canny and probabilistic

Hough transform for estimating pole length and floodwater depth. They developed a classification model using deep neural networks that successfully identified affected areas using grounded images<sup>[125]</sup>. These areas were removed from social media platforms that were downloaded immediately after the disaster. Thus, this can facilitate the acceleration of the recovery process, by marking the areas where the disaster has a greater impact than other areas.

#### 7.4 Archaeology applications

Geospatial data and imageries are the most active field for archaeologists utilizing deep learning. Rarely can archaeology create the vast volumes of systematically coded data required for ML<sup>[126]</sup>. As a result, the increased availability of large-scale lidar, satellite, and aerial photography is changing archaeology globally, notably the finding and mapping of ancient sites. DL algorithms can analyze geographical data to find locations in various contexts. This method can determine the contribution of different variables that predict where sites are found across landscapes. Its many sizes enable archaeologists to better manage and investigate heritage at a global level. These historic landscape ML methods can help mitigate some of the challenges of predictive modeling for cultural resource management. This covers ways to assess the ML predictions' internal coherence and to investigate the factors that influence the presence or absence of archaeological sites in a landscape. This is essential in places where archaeological sites are difficult to access<sup>[127]</sup>. Two artificial intelligence approaches are introduced<sup>[128]</sup> over two areas of interest in the image processing field. They implemented a random forest classifier in their paper using the cloud platform of the Google Earth Engine data and a Single Shot Detector neural network is developed too. The final results show that this approach can be used in the future to detect scattered pottery pieces during the pedestrian archaeological survey, even if there is a great spectral similarity between the pottery and the surface of the earth. The U-Net neural network has been made to perform semantic segmentation of the data derived from airborne laser

scanning cameras for the extraction of archaeological features in the Białowieża Forest in Poland<sup>[129]</sup>. The evaluation of the U-Net segmentation model is done using a pixel-level similarity measure between the ground truth and the predicted segmentation masks. The results indicated that the U-Net deep learning model is very good at a semantic segmentation of images.

#### 7.5 Interferometry applications

While CNNs have shown high object identification accuracy in aerial pictures, few researchers have used deep-learning techniques and CNNs to identify landslides. Yu et al.<sup>[130]</sup> utilized a CNN and an enhanced region growth algorithm (RSG-R) to detect landslides. They used the RSG-R algorithm to extract discriminant information such as the area and border of landslides and determined that their CNN approach had excellent detection accuracy for detecting landslide features. Landslide identification using GF-1 images with four spectral bands and 8 m spatial resolution for Shenzhen was assessed<sup>[131]</sup>. Their automated landslide detection technique has a 72.5% detection rate, a 10.2% false positive rate, and a 67% overall accuracy. This review indicates the potential of employing CNNs for landslide detection has not yet been completely explored. CNN was adopted to identify landslides using optical satellite images from the Rapid Eye sensor (see **Figure 19**) then the obtained results were compared to state-of-the-art ML techniques, ANN, and SVM<sup>[132]</sup>.

In Wenchuan Baoxing in Sichuan Province, China, images of areas where the landslide disaster occurred are captured using low-altitude unmanned aerial vehicles (UAV) for research<sup>[133]</sup>. A landslide extraction approach based on Transfer Learning (TL) model and object-oriented image analysis (TLOEL) was introduced; the TLOEL results were compared with those of the object-oriented nearest neighbor classification (NNC). It is approved that the accuracy of the TLOEL method is better than the NNC method, which helps to detect and extract finely distributed medium and small landslides, not just large landslides.

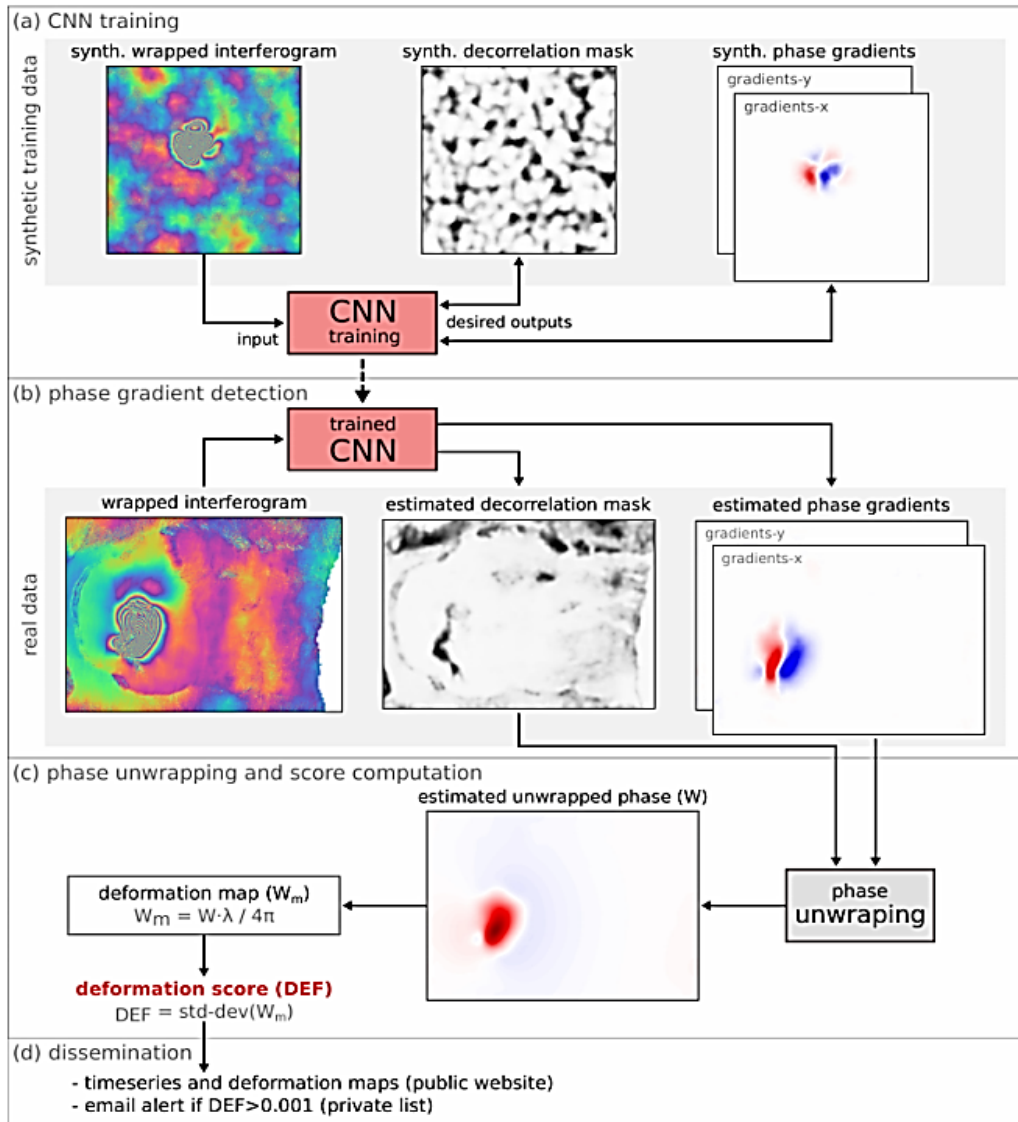


Figure 19. Landslides identification using deep learning framework <sup>[132]</sup>.

Another work introduced <sup>[134]</sup> for volcano deformation detection. The CNN is trained on simulated data and is later used to detect phase gradients and a decorrelation mask from input-wrapped interferograms to locate ground deformation caused by volcanoes. The paper <sup>[135]</sup> proposes the use of self-supervised contrastive learning to learn high-quality visual representations within interferometric synthetic aperture radar (InSAR) data. A SimCLR framework is achieved to find a solution based on a specialized architecture or a large classified or synthetic dataset. The self-supervised pipeline has been shown to give higher accuracy compared to the state-of-the-

art methods and shows good generalization for the out-of-distribution test data also. The approach is approved for its high potential for detecting unrest episodes prior to the recent Icelandic volcanic eruption.

## 7.6 Climate and environmental applications

The remarkable flexibility and adaptability of deep learning models enable scientists to identify, classify and localize extreme weather events under various climate change scenarios. Several attempts had been conducted to adopt DL models to study climate and environment. ClimateNet <sup>[136]</sup> is pioneer re-

search introduced to analyze a pixel-based detection for tropical cyclones (TCs) and atmospheric rivers (AC). Another study was conducted to develop the Optimized Ensemble Deep Learning (OEDL) framework<sup>[137]</sup> to forecast waves.

Reiersen et al. have developed a database named ReforesTree that includes data on carbon stocks in some forests in Ecuador<sup>[138]</sup>. The project aims to overcome the carbon deficiency in some interested forests. A comprehensive deep learning-based model that detects trees individually in RGB drone images has demonstrated that the forest carbon stocks can be professionally calculated according to the official standards of carbon offset certification.

Researchers<sup>[139]</sup> proposed a deep learning-based approach (i.e., U-Net) using the landscape pattern using Sentinel-1 data to produce forest harvesting maps per month within three years. The variable harvest pattern was obtained from Sentinel-1 data using the U-Net bottleneck block as the integrated entities. This modern approach is an important step in the mapping of forest harvesting at monthly intervals of forest harvesting as well as in the development of a sustainable forest management strategy to assist the beneficiaries.

The collection of remote sensing and social sensing data was studied<sup>[140]</sup> to make informational maps showing the extent of the flood. That is why deep learning methods are used to deal with heterogeneous data. Regarding remote sensing data, it turns out that the given deep learning models predict flood water much better. In the case of social sensing, two layers of data were used as related tweet text and images for the case study areas, thus heterogeneous data sources could be combined to complement each other. After analyzing the results of this study, three types of signals are defined: (1) definite signals from the two sources, which confirm that water has flooded a specific area, (2) complementary signals that give multiple information in a context such as requirements and needs, disaster outcomes or reports, and (3) New signals in the event that the two sources do not overlap and their information is not repeat-

ed. (4) Novel signals when both data sources do not overlap and provide unique information.

## 8. Conclusions

This article conducted a comparative review to inspect the recent cutting-edge research of DL in the remote sensing field. DL can help remote sensing scientists overcome several challenges in real-world applications, such as urban planning, natural hazards detection, environment monitoring, vegetation mapping, and geospatial object identification. However, it required a hefty investment to be integrated. This context introduced reviews in DL in RS classification, indicating DL's prominent role in tackling the RS challenges. Therefore, ample conclusions were drawn:

- The up-raising trend in adopting DL architectures in different applications, the availability of free satellite imagery, and the massive computational capabilities and efficient learning algorithms help researchers gain insights and recommend solutions to several modern challenges.
- Freely available satellite imageries were employed effectively in agriculture applications and change maps, especially Landsat and Sentinel-2 imagery.
- Extensive studies adopted different machine learning methods for RS data processing. In the last five years, DL had been adopted in several studies, especially in crop mapping and Interferometry applications.
- The use of the recent CNN advances (attention, GNN, uncertainty) for various applications has significantly increased since 2018. This increased rate in modern architectures in RS image classification highlights its effectiveness and popularity.

## Conflict of Interest

The authors declare no conflict of interest.

## Acknowledgment

This study was partially supported by National Authority for Remote Sensing and Space Science.

## References

- [1] Emani, C.K., Cullot, N., Nicolle, C., 2015. Understandable big data: A survey. *Computer Science Review*. 17, 70-81.
- [2] Kamilaris, A., Kartakoullis, A., Prenafeta-Boldú, F.X., 2017. A review on the practice of big data analysis in agriculture. *Computers and Electronics in Agriculture*. 143, 23-37.
- [3] Fernandez, A., Insfran, E., Abrahão, S., 2011. Usability evaluation methods for the web: A systematic mapping study. *Information and Software Technology*. 53(8), 789-817.
- [4] Li, Y., Ma, L., Zhong, Z., et al., 2020. Deep learning for LiDAR point clouds in autonomous driving: A review. *IEEE Transactions on Neural Networks and Learning Systems*. 32(8), 3412-3432.  
DOI: <https://doi.org/10.1109/TNNLS.2020.3015992>
- [5] Fayyad, J., Jaradat, M.A., Gruyer, D., et al., 2020. Deep learning sensor fusion for autonomous vehicle perception and localization: A review. *Sensors*. 20(15), 4220.
- [6] Zhang, P., Du, P., Lin, C., et al., 2020. A hybrid attention-aware fusion network (HAFNet) for building extraction from high-resolution imagery and LiDAR Data. *Remote Sensing*. 12(22), 3764.
- [7] Lillesand, T., Kiefer, R.W., Chipman, J., 2015. *Remote sensing and image interpretation*. John Wiley & Sons: New York.
- [8] Radočaj, D., Obhodaš, J., Jurišić, M., et al., 2020. Global open data remote sensing satellite missions for land monitoring and conservation: A review. *Land*. 9(11), 402.
- [9] Voulodimos, A., Doulamis, N., Doulamis, A., et al., 2018. Deep learning for computer vision: A brief review. *Computational Intelligence and Neuroscience*. 2018(Pt.I).  
DOI: <https://doi.org/10.1155/2018/7068349>
- [10] Bulo, S.R., Neuhold, G., Kotschieder, P. (editors), 2017. Loss max-pooling for semantic image segmentation. 2017 IEEE Conference on Computer Vision and Pattern Recognition (CVPR); 2017 Jul 21-26; Honolulu, HI, USA. USA: IEEE. p. 7082-7091.
- [11] Asokan, A., Anitha, J., Patrut, B., et al., 2021. Deep feature extraction and feature fusion for bi-temporal satellite image classification. *CMC-Computers Materials & Continua*. 66(1), 373-388.
- [12] Bianco, S., Cadene, R., Celona, L., et al., 2018. Benchmark analysis of representative deep neural network architectures. *IEEE Access*. 6, 64270-64277.
- [13] Mahmoud, A., Mohamed, S., El-Khoribi, R., et al., 2020. Object detection using adaptive mask RCNN in optical remote sensing images. *International Journal of Intelligent Systems*. 13, 65-76.
- [14] Chen, L.C., Papandreou, G., Kokkinos, I., et al., 2017. DeepLab: Semantic image segmentation with deep convolutional Nets, Atrous convolution, and fully connected CRFs. *IEEE Transactions on Pattern Analysis and Machine Intelligence*. 40(4), 834-848.
- [15] Krizhevsky, A., Sutskever, I., Hinton, G.E., 2012. ImageNet classification with deep convolutional neural networks. *Advances in Neural Information Processing Systems*. 25, 1097-1105.
- [16] Yamashita, R., Nishio, M., Do, R.K.G., et al., 2018. Convolutional neural networks: An overview and application in radiology. *Insights into Imaging*. 9(4), 611-629.
- [17] Zeiler, M.D., Fergus, R., 2014. Visualizing and understanding convolutional networks. *European Conference on Computer Vision*. 8689, 818-833.
- [18] Simonyan, K., Zisserman, A., 2014. Very deep convolutional networks for large-scale image recognition. *arXiv:1409.1556*.  
DOI: <https://doi.org/10.48550/arXiv.1409.1556>
- [19] Ioffe, S., Szegedy, C., 2015. Batch normalization: Accelerating deep network training by reducing

- internal covariate shift. arXiv:1502.03167.  
DOI: <https://doi.org/10.48550/arXiv.1502.03167>
- [20] Szegedy, C., Vanhoucke, V., Ioffe, S., et al. (editors), 2016. Rethinking the inception architecture for computer vision. Proceedings of the IEEE Conference on Computer Vision and Pattern Recognition; 2016 Jun 27-30; Las Vegas, NV, USA. USA: IEEE. p. 2818-2826.
- [21] Szegedy, C., Ioffe, S., Vanhoucke, V. (editors), et al., 2017. Inception-v4, inception-Resnet and the impact of residual connections on learning. Thirty-first AAAI Conference on Artificial Intelligence. 31(1).  
DOI: <https://doi.org/10.1609/aaai.v31i1.11231>
- [22] He, K., Zhang, X., Ren, S., et al. (editors), 2016. Deep residual learning for image recognition. Proceedings of the IEEE Conference on Computer Vision and Pattern Recognition; 2016 Jun 27-30; Las Vegas, NV, USA. USA: IEEE. p. 770-778.
- [23] Xie, S., Girshick, R., Dollár, P., et al. (editors), 2017. Aggregated residual transformations for deep neural networks. Proceedings of the IEEE Conference on Computer Vision and Pattern Recognition; 2017 Jul 21-26; Honolulu, HI, USA. USA: IEEE. p. 1492-1500.
- [24] Cheng, D., Meng, G., Cheng, G., et al., 2016. SeNet: Structured edge network for sea-land segmentation. *IEEE Geoscience and Remote Sensing Letters*. 14(2), 247-251.
- [25] Wu, W., Zhang, Y., Wang, D., et al., 2020. SK-Net: Deep learning on point cloud via end-to-end discovery of spatial keypoints. Proceedings of the AAAI Conference on Artificial Intelligence. 34(4), 6422-6429.
- [26] Zhang, H., Wu, Ch.R., Zhang, Zh.Y., et al., 2020. ResNeSt: Split-attention networks. arXiv:2004.08955.  
DOI: <https://doi.org/10.48550/arXiv.2004.08955>
- [27] Wang, C.Y., Liao, H.Y.M., Wu, Y.H., et al., 2020. CSPNet: A new backbone that can enhance learning capability of CNN. arXiv:1911.11929.  
DOI: <https://doi.org/10.48550/arXiv.1911.11929>
- [28] Tan, M., Le, Q. (editors), 2019. EfficientNet: Rethinking model scaling for convolutional neural networks. Proceedings of the 36th International Conference on Machine Learning, PMLR. 97, 6105-6114.
- [29] Yu, Y., Si, X., Hu, C., et al., 2019. A review of recurrent neural networks: LSTM cells and network architectures. *Neural Computation*. 31(7), 1235-1270.
- [30] Hochreiter, S., Schmidhuber, J., 1997. Long short-term memory. *Neural Computation*. 9(8), 1735-1780.
- [31] Wang, Q., Liu, S., Chanussot, J., et al., 2019. Scene classification with recurrent attention of VHR remote sensing images. *IEEE Transactions on Geoscience and Remote Sensing*. 57(2), 1155-1167.
- [32] Hang, R., Liu, Q., Hong, D., et al., 2019. Cascaded recurrent neural networks for hyperspectral image classification. *IEEE Transactions on Geoscience and Remote Sensing*. 57(8), 5384-5394.
- [33] Mou, L., Bruzzone, L., Zhu, X.X., 2019. Learning spectral-spatial-temporal features via a recurrent convolutional neural network for change detection in multispectral imagery. *IEEE Transactions on Geoscience and Remote Sensing*. 57(2), 924-935.
- [34] Chen, H., Wu, C., Du, B., et al., 2020. Change detection in multisource VHR images via deep siamese convolutional multiple-layers recurrent neural network. *IEEE Transactions on Geoscience and Remote Sensing*. 58(4), 2848-2864.
- [35] Li, B., Guo, Y., Yang, J., et al., 2021. Gated recurrent multiattention network for VHR remote sensing image classification. *IEEE Transactions on Geoscience and Remote Sensing*. 60, 1-13.
- [36] Long, J., Shelhamer, E., Darrell, T. (editors), 2015. Fully convolutional networks for semantic segmentation. Proceedings of the IEEE Conference on Computer Vision and Pattern Recognition; 2015 Jun 7-12; Boston, MA, USA. USA: IEEE. p. 3431-3440.
- [37] Ronneberger, O., Fischer, P., Brox, T., 2015.

- U-net: Convolutional networks for biomedical image segmentation. *International Conference on Medical Image Computing and Computer-assisted Intervention*. 9351, 234-241.
- [38] Badrinarayanan, V., Kendall, A., Cipolla, R., 2017. SegNet: A deep convolutional encoder-decoder architecture for image segmentation. *IEEE Transactions on Pattern Analysis and Machine Intelligence*. 39(12), 2481-2495.
- [39] Chen, X., Girshick, R., He, K. (editors), et al., 2019. TensorMask: A Foundation for Dense Object Segmentation [Internet]. *Proceedings of the IEEE/CVF International Conference on Computer Vision*. Available from: [https://open-access.thecvf.com/content\\_ICCV\\_2019/papers/Chen\\_TensorMask\\_A\\_Foundation\\_for\\_Dense\\_Object\\_Segmentation\\_ICCV\\_2019\\_paper.pdf](https://open-access.thecvf.com/content_ICCV_2019/papers/Chen_TensorMask_A_Foundation_for_Dense_Object_Segmentation_ICCV_2019_paper.pdf)
- [40] Goodfellow, I., Bengio, Y., Courville, A., 2016. *Deep learning*. MIT Press: Cambridge.
- [41] Hinton, G.E., Salakhutdinov, R.R., 2006. Reducing the dimensionality of data with neural networks. *Science*. 313(5786), 504-507.
- [42] Fout, A.M. (editor), 2017. Protein interface prediction using graph convolutional networks. *Proceedings of the 31st International Conference on Neural Information Processing Systems; 2017 Dec.* p. 6533-6542.
- [43] Yan, X., Ai, T., Yang, M., et al., 2019. A graph convolutional neural network for classification of building patterns using spatial vector data. *ISPRS Journal of Photogrammetry and Remote Sensing*. 150, 259-273.
- [44] Liang, J., Deng, Y., Zeng, D., 2020. A deep neural network combined CNN and GCN for remote sensing scene classification. *IEEE Journal of Selected Topics in Applied Earth Observations and Remote Sensing*. 13, 4325-4338.
- [45] Li, Y., Chen, R., Zhang, Y., et al., 2020. Multi-label remote sensing image scene classification by combining a convolutional neural network and a graph neural network. *Remote Sensing*. 12(23), 4003.
- [46] Baroud, S., Chokri, S., Belhaous, S., et al., 2021. A brief review of graph convolutional neural network based learning for classifying remote sensing images. *Procedia Computer Science*. 191, 349-354.
- [47] Gao, Y., Shi, J., Li, J., et al., 2021. Remote sensing scene classification based on high-order graph convolutional network. *European Journal of Remote Sensing*. 54(sup1), 141-155.
- [48] Goodfellow, I., Pouget-Abadie, J., Mirza, M., et al., 2020. Generative adversarial networks. *Communications of the ACM*. 63(11), 139-144.
- [49] Wang, X., Tan, K., Du, Q., et al., 2019. Caps-TripleGAN: GAN-Assisted CapsNet for Hyperspectral Image Classification. *IEEE Transactions on Geoscience and Remote Sensing*. 57(9), 7232-7245.
- [50] Wang, X., Tan, K., Du, Q., et al., 2020. CVA-E: A conditional variational autoencoder with an adversarial training process for hyperspectral imagery classification. *IEEE Transactions on Geoscience and Remote Sensing*. 58(8), 5676-5692.
- [51] Ren, Z., Hou, B., Wu, Q., et al., 2020. A distribution and structure match generative adversarial network for SAR image classification. *IEEE Transactions on Geoscience and Remote Sensing*. 58(6), 3864-3880.
- [52] Zhang, Z., Yang, J., Du, Y., 2020. Deep convolutional generative adversarial network with autoencoder for semi supervised SAR image classification. *IEEE Geoscience and Remote Sensing Letters*. 19, 1-5.
- [53] Ji, S., Wang, D., Luo, M., 2021. Generative adversarial network-based full-space domain adaptation for land cover classification from multiple-source remote sensing images. *IEEE Transactions on Geoscience and Remote Sensing*. 59(5), 3816-3828.
- [54] Huang, Y., Wu, M., Guo, J., et al., 2021. A correlation context-driven method for sea fog detection in meteorological satellite imagery. *IEEE Geoscience and Remote Sensing Letters*. 19, 1-5.
- [55] Guidotti, R., Monreale, A., Ruggieri, S., et al., 2018. A survey of methods for explaining black

- box models. *ACM Computing Surveys (CSUR)*. 51(5), 1-42.
- [56] Niu, Z., Zhong, G., Yu, H., 2021. A review on the attention mechanism of deep learning. *Neurocomputing*. 452, 48-62.
- [57] Ghaffarian, S., Valente, J., van der Voort, M., et al., 2021. Effect of attention mechanism in deep learning-based remote sensing image processing: A systematic literature review. *Remote Sensing*. 13(15).
- [58] Ienco, D., Gbodjo, Y.J.E., Gaetano, R., et al., 2020. Weakly supervised learning for land cover mapping of satellite image time series via attention-based CNN. *IEEE Access*. 8, 179547-179560.
- [59] Zhang, X., Sun, G.Y., Jia, X.P., et al., 2021. Spectral-spatial self-attention networks for hyperspectral image classification. *IEEE Transactions on Geoscience and Remote Sensing*. 60, 1-15.
- [60] Robbins, H., Monro, S., 1951. A stochastic approximation method. *The Annals of Mathematical Statistics*. 22(3), 400-407.
- [61] Jacobs, R.A., 1988. Increased rates of convergence through learning rate adaptation. *Neural Networks*. 1(4), 295-307.
- [62] Duchi, J., Hazan, E., Singer, Y., 2011. Adaptive subgradient methods for online learning and stochastic optimization. *Journal of Machine Learning Research*. 12(7), 257-269.
- [63] Tieleman, T., Hinton, G., 2012. Lecture 6.5-rmsprop: Divide the gradient by a running average of its recent magnitude. *COURSERA: Neural Networks for Machine Learning*. 4(2), 26-31.
- [64] Kingma, D.P., Ba, J., 2014. Adam: A method for stochastic optimization. *arXiv:1412.6980*. DOI: <https://doi.org/10.48550/arXiv.1412.6980>
- [65] Xie, J., He, N., Fang, L., et al., 2019. Scale-free convolutional neural network for remote sensing scene classification. *IEEE Transactions on Geoscience and Remote Sensing*. 57(9), 6916-6928.
- [66] He, N., Fang, L., Li, S., et al., 2019. Skip-connected covariance network for remote sensing scene classification. *IEEE Transactions on Neural Networks and Learning Systems*. 31(5), 1461-1474.
- [67] Fang, J., Yuan, Y., Lu, X., et al., 2019. Robust space-frequency joint representation for remote sensing image scene classification. *IEEE Transactions on Geoscience and Remote Sensing*. 57(10), 7492-7502.
- [68] Liu, B.D., Meng, J., Xie, W.Y., et al., 2019. Weighted spatial pyramid matching collaborative representation for remote-sensing-image scene classification. *Remote Sensing*. 11(5), 518.
- [69] Liu, X., Zhou, Y., Zhao, J., et al., 2019. Siamese convolutional neural networks for remote sensing scene classification. *IEEE Geoscience and Remote Sensing Letters*. 16(8), 1200-1204.
- [70] Lu, X., Ji, W., Li, X., et al., 2019. Bidirectional adaptive feature fusion for remote sensing scene classification. *Neurocomputing*. 328, 135-146.
- [71] Zhang, W., Tang, P., Zhao, L., 2019. Remote sensing image scene classification using CNN-CapsNet. *Remote Sensing*. 11(5), 494.
- [72] Ma, D., Tang, P., Zhao, L., 2019. SiftingGAN: Generating and sifting labeled samples to improve the remote sensing image scene classification baseline in vitro. *IEEE Geoscience and Remote Sensing Letters*. 16(7), 1046-1050.
- [73] Keshk, H.M., Yin, X.C., 2020. Change detection in SAR images based on deep learning. *International Journal of Aeronautical and Space Sciences*. 21, 549-559. DOI: <https://doi.org/10.1007/s42405-019-00222-0>
- [74] Wang, S., Sun, G., Zheng, B., et al., 2021. A crop image segmentation and extraction algorithm based on mask RCNN. *Entropy*. 23(9), 1160.
- [75] Lin, Y., Xu, D., Wang, N., et al., 2020. Road extraction from very-high-resolution remote sensing images via a nested SE-DeepLab model. *Remote Sensing*. 12(18), 2985.
- [76] Fu, H., Fu, B., Shi, P., 2021. An improved segmentation method for automatic mapping of cone karst from remote sensing data based on DeepLab V3+ Model. *Remote Sensing*. 13(3), 441.

- [77] Cheng, G., Zhou, P., Han, J., 2016. Learning rotation-invariant convolutional neural networks for object detection in VHR optical remote sensing images. *IEEE Transactions on Geoscience and Remote Sensing*. 54(12), 7405-7415.
- [78] Long, Y., Gong, Y., Xiao, Z., et al., 2017. Accurate object localization in remote sensing images based on convolutional neural networks. *IEEE Transactions on Geoscience and Remote Sensing*. 55(5), 2486-2498.
- [79] Ševo, I., Avramović, A., 2016. Convolutional neural network based automatic object detection on aerial images. *IEEE Geoscience and Remote Sensing Letters*. 13(5), 740-744.
- [80] Deng, Z., Sun, H., Zhou, S., et al., 2017. Toward fast and accurate vehicle detection in aerial images using coupled region-based convolutional neural networks. *IEEE Journal of Selected Topics in Applied Earth Observations and Remote Sensing*. 10(8), 3652-3664.
- [81] Cheng, G., Han, J., Zhou, P., et al., 2018. Learning rotation-invariant and fisher discriminative convolutional neural networks for object detection. *IEEE Transactions on Image Processing*. 28(1), 265-278.
- [82] Guo, W., Yang, W., Zhang, H., et al., 2018. Geospatial object detection in high resolution satellite images based on multi-scale convolutional neural network. *Remote Sensing*. 10(1), 131.
- [83] Han, X., Zhong, Y., Zhang, L., 2017. An efficient and robust integrated geospatial object detection framework for high spatial resolution remote sensing imagery. *Remote Sensing*. 9(7), 666.
- [84] Li, K., Cheng, G., Bu, S., et al., 2017. Rotation-insensitive and context-augmented object detection in remote sensing images. *IEEE Transactions on Geoscience and Remote Sensing*. 56(4), 2337-2348.
- [85] Zhong, Y., Han, X., Zhang, L., 2018. Multi-class geospatial object detection based on a position-sensitive balancing framework for high spatial resolution remote sensing imagery. *ISPRS Journal of Photogrammetry and Remote Sensing*. 138, 281-294.
- [86] Yao, Y., Jiang, Z., Zhang, H., et al., 2017. Ship detection in optical remote sensing images based on deep convolutional neural networks. *Journal of Applied Remote Sensing*. 11(4), 042611.
- [87] Yang, Y., Zhuang, Y., Bi, F., et al., 2017. M-FCN: Effective fully convolutional network-based airplane detection framework. *IEEE Geoscience and Remote Sensing Letters*. 14(8), 1293-1297.
- [88] Yang, J., Zhu, Y., Jiang, B., et al., 2018. Aircraft detection in remote sensing images based on a deep residual network and super-vector coding. *Remote Sensing Letters*. 9(3), 228-236.
- [89] Xu, Z., Xu, X., Wang, L., et al., 2017. Deformable convnet with aspect ratio constrained NMS for object detection in remote sensing imagery. *Remote Sensing*. 9(12), 1312.
- [90] Tang, T., Zhou, S., Deng, Z., et al., 2017. Vehicle detection in aerial images based on region convolutional neural networks and hard negative example mining. *Sensors*. 17(2), 336.
- [91] Lin, H., Shi, Z., Zou, Z., 2017. Fully convolutional network with task partitioning for inshore ship detection in optical remote sensing images. *IEEE Geoscience and Remote Sensing Letters*. 14(10), 1665-1669.
- [92] Liu, L., Pan, Z., Lei, B., 2017. Learning a rotation invariant detector with rotatable bounding box. *arXiv:1711.09405*. DOI: <https://doi.org/10.48550/arXiv.1711.09405>
- [93] Liu, W., Ma, L., Chen, H., 2018. Arbitrary-oriented ship detection framework in optical remote-sensing images. *IEEE Geoscience and Remote Sensing Letters*. 15(6), 937-941.
- [94] Tang, T., Zhou, S., Deng, Z., et al., 2017. Arbitrary-oriented vehicle detection in aerial imagery with single convolutional neural networks. *Remote Sensing*. 9(11), 1170.
- [95] Yu, Y., Guan, H., Ji, Z., 2015. Rotation-invariant object detection in high-resolution satellite imagery using superpixel-based deep Hough forests. *IEEE Geoscience and Remote Sensing Letters*. 12(11), 2183-2187.
- [96] Zou, Z., Shi, Z., 2016. Ship detection in space-

- borne optical image with SVD networks. *IEEE Transactions on Geoscience and Remote Sensing*. 54(10), 5832-5845.
- [97] Liu, W., Anguelov, D., Erhan, D., et al., 2016. SSD: Single shot multibox detector. arXiv:1512.02325. DOI: <https://doi.org/10.48550/arXiv.1512.02325>
- [98] Zhong, J., Lei, T., Yao, G., 2017. Robust vehicle detection in aerial images based on cascaded convolutional neural networks. *Sensors*. 17(12), 2720.
- [99] Ma, J., Chen, J., Ng, M., et al., 2021. Loss odyssey in medical image segmentation. *Medical Image Analysis*. 71, 102035.
- [100] Yeung, M., Sala, E., Schönlieb, C.B., et al., 2021. A mixed focal loss function for handling class imbalanced medical image segmentation. arXiv:2102.04525. DOI: <https://doi.org/10.48550/arXiv.2102.04525>
- [101] Ayush, K., Uzcent, B., Tanmay, K., et al., 2020. Efficient poverty mapping using deep reinforcement learning. arXiv:2006.04224. DOI: <https://doi.org/10.48550/arXiv.2006.04224>
- [102] Zoph, B., Le, Q.V., 2016. Neural architecture search with reinforcement learning. arXiv:1611.01578. DOI: <https://doi.org/10.48550/arXiv.1611.01578>
- [103] Tian, Y., Krishnan, D., Isola, P., 2019. Contrastive representation distillation. arXiv:1910.10699. DOI: <https://doi.org/10.48550/arXiv.1910.10699>
- [104] Guerra, L., Zhuang, B., Reid, I., et al. (editors), 2020. Automatic pruning for quantized neural networks. 2021 *Digital Image Computing: Techniques and Applications (DICTA)*; 2021 Nov 29-Dec 1; Gold Coast, Australia; USA: IEEE. p. 1-8.
- [105] Yaguchi, A., Suzuki, T., Nitta, S., et al., 2019. Decomposable-Net: Scalable low-rank compression for neural networks. arXiv:1910.13141. DOI: <https://doi.org/10.48550/arXiv.1910.13141>
- [106] Zhou, D., Jin, X., Hou, Q., et al., 2019. Neural epitome search for architecture-agnostic network compression. arXiv:1907.05642. DOI: <https://doi.org/10.48550/arXiv.1907.05642>
- [107] Heo, B., Lee, M., Yun, S., et al., 2019. Knowledge distillation with adversarial samples supporting decision boundary. *Proceedings of the AAAI Conference on Artificial Intelligence*. 33(1), 3771-3778.
- [108] Xu, Z., Hsu, Y.C., Huang, J., 2017. Training shallow and thin networks for acceleration via knowledge distillation with conditional adversarial networks. arXiv:1709.00513. DOI: <https://doi.org/10.48550/arXiv.1709.00513>
- [109] Heo, B., Lee, M., Yun, S., et al., 2018. Knowledge Distillation with Adversarial Samples Supporting Decision Boundary [Internet]. Available from: <https://arxiv.org/pdf/1805.05532.pdf>
- [110] Xian, Y., Schiele, B., Akata, Z., 2017. Zero-shot learning-the good, the bad and the ugly. arXiv:1703.04394. DOI: <https://doi.org/10.48550/arXiv.1703.04394>
- [111] Gui, R., Xu, X., Wang, L., et al., 2018. A generalized zero-shot learning framework for PolSAR land cover classification. *Remote Sensing*. 10(8), 1307.
- [112] Haddeler, G., Aybakan, A., Akay, M.C., et al., 2020. Evaluation of 3D LiDAR sensor setup for heterogeneous robot team. *Journal of Intelligent & Robotic Systems*. 100(2), 689-709.
- [113] Zhou, L., Gu, X., Cheng, S., et al., 2020. Analysis of plant height changes of lodged maize using UAV-LiDAR data. *Agriculture*. 10(5), 146.
- [114] Raj, R., Kar, S., Nandan, R., et al., 2020. Precision agriculture and unmanned aerial vehicles (UAVs). *Unmanned aerial vehicle: Applications in agriculture and environment*. Springer: Berlin. pp. 7-23.
- [115] Wang, D., Cao, W., Zhang, F., et al., 2022. A review of deep learning in multiscale agricultural sensing. *Remote Sensing*. 14(3), 559.
- [116] Rasti, S., Bleakley, C.J., Silvestre, G., et al., 2021. Crop growth stage estimation prior to canopy closure using deep learning algorithms.

- Neural Computing and Applications. 33(5), 1733-1743.
- [117] Sagan, V., Maimaitijiang, M., Bhadra, S., et al., 2021. Field-scale crop yield prediction using multi-temporal WorldView-3 and PlanetScope satellite data and deep learning. *ISPRS Journal of Photogrammetry and Remote Sensing*. 174, 265-285.
- [118] Li, X.F., Liu, B., Zheng, G., et al., 2020. Deep-learning-based information mining from ocean remote-sensing imagery. *National Science Review*. 7(10), 1584-1605.
- [119] Kruk, R., Fuller, M.C., Komarov, A.S., et al., 2020. Proof of concept for sea ice stage of development classification using deep learning. *Remote Sensing*. 12(15), 2486.
- [120] Han, Y., Liu, Y., Hong, Z., et al., 2021. Sea ice image classification based on heterogeneous data fusion and deep learning. *Remote Sensing*. 13(4), 592.
- [121] Ren, Y., Li, X., Yang, X., et al., 2021. Development of a dual-attention U-Net model for sea ice and open water classification on SAR images. *IEEE Geoscience and Remote Sensing Letters*. 19, 1-5.
- [122] Zhang, J., Zhang, W., Hu, Y., et al., 2022. An improved sea ice classification algorithm with Gaofen-3 dual-polarization SAR data based on deep convolutional neural networks. *Remote Sensing*. 14(4), 906.
- [123] Alsharay, N.M., Chen, Y., Dobre, O.A., et al., 2022. Improved sea-ice identification using semantic segmentation with raindrop removal. *IEEE Access*. 10, 21599-21607.
- [124] Kharazi, B.A., Behzadan, A.H., 2021. Flood depth mapping in street photos with image processing and deep neural networks. *Computers, Environment and Urban Systems*. 88, 101628.
- [125] Singh, S., Ghosh, S., Maity, A., et al., 2022. DisasterNet: A multi-label disaster aftermath image classification model. *ICT systems and sustainability*. Springer: Singapore. pp. 481-490.
- [126] Bickler, S.H., 2021. Machine learning arrives in archaeology. *Advances in Archaeological Practice*. 9(2), 186-191.
- [127] Chatterjee, R., Chatterjee, A., Halder, R. (editors), 2021. Impact of deep learning on arts and archaeology: An image classification point of view. *Proceedings of International Conference on Machine Intelligence and Data Science Applications*; 2021 Aug; India. p. 801-810.
- [128] Agapiou, A., Vionis, A., Papantoniou, G., 2021. Detection of archaeological surface ceramics using deep learning image-based methods and very high-resolution UAV imageries. *Land*. 10(12), 1365.
- [129] Banasiak, P.Z., Berezowski, P.L., Zapłata, R., et al., 2022. Semantic segmentation (U-Net) of archaeological features in airborne laser scanning—Example of the Białowieża Forest. *Remote Sensing*. 14(4), 995.
- [130] Yu, H., Ma, Y., Wang, L., et al. (editors), 2017. A landslide intelligent detection method based on CNN and RSG\_R. *2017 IEEE International Conference on Mechatronics and Automation (ICMA)*; 2017 Aug 6-9; Takamatsu, Japan. USA: IEEE. p. 40-44.
- [131] Ding, A., Zhang, Q., Zhou, X., et al. (editors), 2016. Automatic recognition of landslide based on CNN and texture change detection. *2016 31st Youth Academic Annual Conference of Chinese Association of Automation (YAC)*; 2016 Nov 11-13; Wuhan, China. USA: IEEE. p. 444-448.
- [132] Ghorbanzadeh, O., Blaschke, T., Gholamnia, K., et al., 2019. Evaluation of different machine learning methods and deep-learning convolutional neural networks for landslide detection. *Remote Sensing*. 11(2), 196.
- [133] Lu, H., Ma, L., Fu, X., et al., 2020. Landslides information extraction using object-oriented image analysis paradigm based on deep learning and transfer learning. *Remote Sensing*. 12(5), 752.
- [134] Valade, S., Ley, A., Massimetti, F., et al., 2019. Towards global volcano monitoring using multisensor sentinel missions and artificial in-

- telligence: The MOUNTS monitoring system. *Remote Sensing*. 11(13), 1528.
- [135] Bountos, N.I., Papoutsis, I., Michail, D., et al., 2021. Self-supervised contrastive learning for volcanic unrest detection. *IEEE Geoscience and Remote Sensing Letters*. 19, 1-5.
- [136] Kashinath, K., Mudigonda, M., Kim, S., et al., 2020. ClimateNet: An expert-labeled open dataset and deep learning architecture for enabling high-precision analyses of extreme weather. *Geoscientific Model Development*. 14(1), 107-124.
- [137] Ray, A., Chakraborty, T., Ghosh, D., 2021. Optimized ensemble deep learning framework for scalable forecasting of dynamics containing extreme events. arXiv:2106.08968.
- [138] Reiersen, G., Dao, D., Lütjens, B., et al., 2022. ReforesTree: A dataset for estimating tropical forest carbon stock with deep learning and aerial imagery. arXiv:2201.11192. DOI: <https://doi.org/10.1063/5.0074213>
- [139] Zhao, F., Sun, R., Zhong, L., et al., 2022. Monthly mapping of forest harvesting using dense time series Sentinel-1 SAR imagery and deep learning. *Remote Sensing of Environment*. 269, 112822.
- [140] Sadiq, R., Akhtar, Z., Imran, M., et al., 2022. Integrating remote sensing and social sensing for flood mapping. *Remote Sensing Applications: Society and Environment*. 25, 100697.

ARTICLE

## Source, Contamination Assessment and Risk Evaluation of Heavy Metals in the Stream Sediments of Rivers around Olode Area SW, Nigeria

*Stellamaris Isioma Okonkwo<sup>1</sup>, Sunday Ojochogwu Idakwo<sup>2\*</sup>, Mofolorunsho Samuel Kolawole<sup>3</sup>, Olufemi Faloye<sup>4</sup>, Anthony Azubuikie Elueze<sup>4</sup>*

<sup>1</sup>Department of Geology, Federal University of Technology, Owerri, Owerri, Imo State, 460114, Nigeria

<sup>2</sup>Department of Geology and Mining, Ibrahim Badamasi Babangida University, Lapai, Niger State, 740005, Nigeria

<sup>3</sup>Department of Geology, Federal University, Oye-Ekiti, Ekiti State, 360001, Nigeria

<sup>4</sup>Department of Geology, University of Ibadan, Ibadan, 200005, Nigeria

### ABSTRACT

In order to investigate the source, contamination, and risk of heavy metals such as Pb, Zn, Cu, Ni, Co, Fe, Mn, and Cr, twelve (12) stream sediments and ten (10) rock samples were collected from pegmatite mining sites at Olode and its environs inside Ibadan, Southwestern Nigeria. The average values and order of abundance obtained followed the pattern: Mn (595.09) > Ba (80) > Cr (50.82) > V (45.09) > Zn (29.73) > Cu (13.82) > Co (13.82) > Sr (10.46) > Ni (9.73) > Pb (9.09) > Fe (1.59). These were greater than the background values, indicating that mining has a negative impact on the study area, as indicated by the high coefficient of variation and correlation values (> 0.6) for Copper-Lead (0.929), Copper-Vanadium (0.970), Copper-Chromium (0.815), Lead-Vanadium (0.884), and others. On the basis of the enrichment factor (EF), the Olode sediments show extremely high enrichment for Mn and Ba in the research region. Cu and Ni are most likely to blame for the elevated contamination levels, according to CF values. The degree of contamination (CD), pollution load index (PLI), pollution index (PI), and modified pollution index (MPI) all revealed high levels of contamination in all stream sediment samples, whereas Igeo shows that the Olode stream sediments are “practically uncontaminated to extremely contaminated by Ni, Co, and Mn”. Ni and Cu are the major regulating factors that are most likely causing the possible Er<sup>i</sup>. As a result, these findings give important information for conducting appropriate ecological management research.

**Keywords:** Olode; Heavy metals; Stream sediments; Risk assessment; Contamination indices

#### \*CORRESPONDING AUTHOR:

Sunday Ojochogwu Idakwo, Department of Geology and Mining, Ibrahim Badamasi Babangida University, Lapai, Niger State, 740005, Nigeria; Email: idakwo@ibbu.edu.ng

#### ARTICLE INFO

Received: 12 September 2022 | Revised: 18 March 2023 | Accepted: 21 March 2023 | Published Online: 13 April 2023

DOI: <https://doi.org/10.30564/jees.v5i1.5060>

#### CITATION

Okonkwo, S.I., Idakwo, S.O., Kolawole, M.S., et al., 2023. Source, Contamination Assessment and Risk Evaluation of Heavy Metals in the Stream Sediments of Rivers around Olode Area SW, Nigeria. *Journal of Environmental & Earth Sciences*. 5(1): 65-84. DOI: <https://doi.org/10.30564/jees.v5i1.5060>

#### COPYRIGHT

Copyright © 2023 by the author(s). Published by Bilingual Publishing Group. This is an open access article under the Creative Commons Attribution-NonCommercial 4.0 International (CC BY-NC 4.0) License. (<https://creativecommons.org/licenses/by-nc/4.0/>).

## 1. Introduction

River sediments are a primary transporter of heavy metals in the aquatic environment all over the world. Sediments are the mixture of mineral and organic debris that act as a final sink for heavy metals released into the environment. Due to their consistency, non-degradability, and toxic nature, the presence of these heavy metals in stream sediments has been shown to be a significant environmental problem<sup>[1,2]</sup>. According to Lei<sup>[3]</sup>, the most harmful toxic metals in the environment are Cr, Cu, Cd, Pb, and As. These metals enter the environment through anthropogenic processes (e.g. mining and indiscriminate dumping of mine wastes) or geogenic processes (e.g. weathering of parent rocks)<sup>[4-7]</sup>. While some of these metals are necessary for individual survival, only minute amounts are required, according to international organizations such as the World Health Organization (WHO) and the Environmental Protection Agency (EPA)<sup>[8,9]</sup>. Sediment quality has recently been regarded as a key indicator of pollution because it is a major sink for a variety of pollutants<sup>[8]</sup>. Heavy metals are carried by contaminated sediments into the water body, resulting in a reduction in water quality<sup>[10-13]</sup>.

Several researchers, including but not limited to: Atgin<sup>[14]</sup>; Salah et al.<sup>[12]</sup>; Adamu, et al.<sup>[15]</sup>; Oyebami-ji, et al.<sup>[16]</sup>; Kolawole, et al.<sup>[17]</sup>; Boroumandi, et al.<sup>[18]</sup>; Madukwe, et al.<sup>[19]</sup>; Adewumi and Laniyan<sup>[13]</sup> have carried out extensive research into heavy metal contamination in sediments. The findings revealed the accumulation of heavy metals in sediments from various environments and places around the globe. Despite this, there is a paucity of published studies on the distribution and sources of heavy metals in stream sediments near the Olode mining area, and Nigeria has yet to adopt a strategic policy aimed at coordinating and monitoring environmental management and long-term development<sup>[20,21]</sup>. The study is aimed at assessing the degree of heavy metal concentrations in stream sediments of the study area in order to identify the level of metal pollution, source of heavy metal contamination and appraise the risks associated with heavy metals.

## 2. Materials and methods

### 2.1 Study area

Within the Ibadan sheet 261 S.E., the research area is located in the south-western section of Nigeria, between latitudes 7° 08'N and 7° 13.30'N and longitudes 3° 55'E and 3° 59'E. In the area, there are two significant mining operations<sup>[22]</sup>. They are in the Oluyole Local Government Area of Oyo State, in the Gbayo and Falansa localities (**Figures 1A and 1B**). The terrain is undulating, with elevations varying from 300 to 500 feet above sea level. Pegmatites and associated rocks are usually found as flat tabular masses and are found in low-lying areas. The majority of the streams flow south, but tributaries flow southeast and southwest, draining into the Omi and Opedi rivers, respectively. The majority of streams and their tributaries dry up during the dry season, with the exception of a few perennial streams. The climate of the research region is tropical rainforest, with a wet season that lasts from March to October and a dry season that lasts from November to March. Annual rainfall varies from 788 mm to 1844 mm<sup>[23]</sup>. Temperatures range from 23 to 32 degrees Celsius, indicating a high-temperate climate<sup>[22]</sup>.

### 2.2 Sample collection and geochemical analysis

In total, 12 stream sediment samples were collected, with a geochemical sampling of active stream sediments using the natural drainage system in the study area at an interval of about 1 km (**Figure 1A and 1B; Table 1**), with samples taken at meanders and from the center of stream courses to obtain more recent and active sediments. A Global Positioning System (GPS) Margillean 315, 2000 model was used to appropriately locate the sample sites on the topographical map. To avoid particle loss when the flow velocity was high, sediment samples were collected in a plastic cup.

Hand trowels were utilized to collect at each spot where the flow velocity was low. Organic materials and bank sediments were strictly avoided. The bedrock and its surroundings were also recorded. The

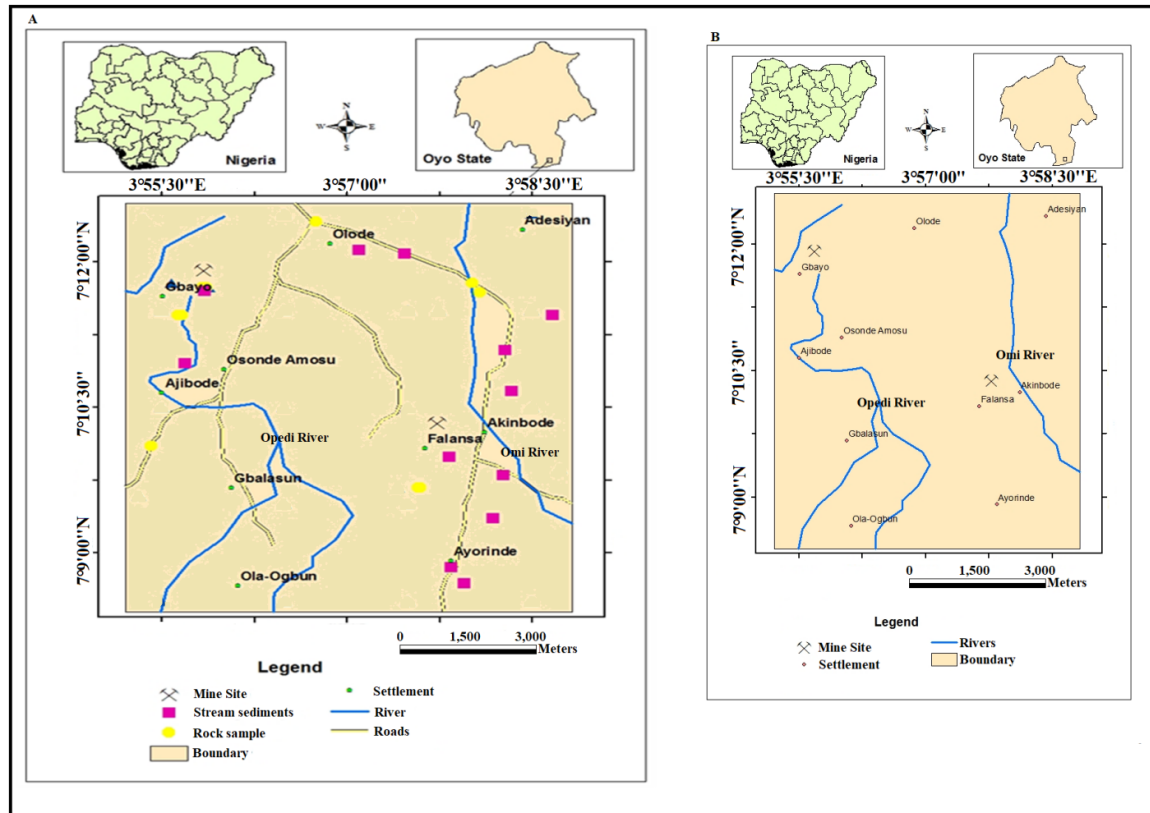


Figure 1. Map of the study area showing: A) Different sampling (media) points and B) Drainage patterns (Adapted from Okonkwo et al. [22]).

Table 1. Stream sediments description (hand specimen) and sample locations.

Sample Numbers ↓	Co-ordinates		Sample Description		pH	Bedrock
	Latitude	Longitude	Grain Size	Colour		
SS01	7°12'07"N	3°57'06"E	gritty	Dark-brown	7	Pegmatite
SS02	7°12'05"N	3°57'28"E	Smooth to fine	Dark brown	8	Pegmatite
SS03	7°11'51"N	3°58'10"E	Smooth to fine	Greyish-white	8	Pegmatite
SS04	7°11'27"N	3°58'40"E	Smooth to fine	Brown	7	Pegmatite
SS05	7°10'40"N	3°58'20"E	Smooth to fine	Brownish-white	7	Pegmatite
SS06	7°11'05"N	3°56'15"E	gummy to sticky	Dark –grey	8	Pegmatite
SS07	7°09'59"N	3°57'50"E	Smooth to fine	Brown	8	Pegmatite
SS08	7°09'48"N	3°58'15"E	Smooth to fine	Brown	7	Pegmatite
SS09	7°09'21"N	3°58'11"E	Smooth to fine	Greyish white	7	Pegmatite
SS10	7°08'50"N	3°57'50"E	Smooth to fine	Grey	8	Pegmatite
SS11	7°08'41"N	3°57'43"E	gritty	Brown	7	Pegmatite
SS12	7°11'42"N	3°55'51"E	gummy to sticky	Greyish-white	8	Pegmatite

texture of the samples was characterized in hand specimens, with the majority of the samples being fine and medium-grained (Table 1). The pH of the streams where the sediment samples were taken was measured in situ using a pH indicator paper with a

pH range of 1 to 11 (Table 1). The samples were collected in thick polythene bags and labelled.

Air-dried stream sediment samples were desegregated, sieved, and divided into size fractions with sieve size fractions of 1180 m, 1000 m, 850 m, 600 m,

425 m, 300 m, 212 m, 180 m, 150 m, 100 m, and 63 m. Aqua regia was used to digest 0.5 g of crushed stream sediment samples (100 m) (3 part HCl and 1 part HNO<sub>3</sub>) and the trace elements (Pb, Ba, V, Sr, Zn, Cu, Ni, Co, Fe, Mn, and Cr) were determined using the Inductively Coupled Plasma- Atomic Emission Spectrometry (ICP AES) in the ACME Laboratory (Bureau Veritas Mineral Laboratories) in Canada, following a near-total inclusion by hydrofluoric-perchloric acid. The analytical methods were performed with precision in accordance with Dulski's recommendations [24]. These data produced acceptable results, with precision values for various elements ranging from 1% to 10%.

In eight sample locations (Olode, Gbayo, Osonde,

Onipede, Sanku, Falansa, Moleke, and Olojuoro), ten rock samples were obtained (**Figures 1A, 2** and **Table 2**). The major research area, pegmatites mining regions, are Falansa and part of Gbayo, whereas non-mining areas are Olode, part of Gbayo, Olojuoro, Onipede, Osonde, and Moleke, despite the fact that these areas were blasted for gemstone (Beryl) but were later abandoned because nothing was discovered [22]. The rock samples were pulverized and placed in cellophane paper, which was then carefully sealed, tagged, and packaged for trace elemental (Pb, Ba, V, Sr, Zn, Cu, Ni, Co, Fe, Mn, and Cr) analysis in ACME Laboratory (Bureau Veritas Mineral Laboratories) utilizing Inductively Coupled Plasma-Atomic Emission Spectrometry (ICP AES).

**Table 2.** Rock descriptions (hand specimen) and sample locations.

Serial Numbers	Co-ordinates	Texture	Mineralogy	Rock type	Location
LO 1= (RR01)	Lat. 7°12'25"N Long. 3°56'46"E Elevation 541 ft	Medium coarse grained	Quartz, feldspar, muscovite, and biotite	Pegmatite	Olode
LO 2= (RR02)	Lat. 7°11'47"N Long. 3°58'01"E Elevation 451 ft	Medium grained	Quartz, biotite, and feldspar	Granite gneiss	Ori-Oke Olojuoro
LO 3= (RR03)	Lat. 7°11'40"N Long. 3°58'04"E Elevation 461 ft	Medium grained	Quartz, biotite, and feldspar	Granite granite	Ori-Oke Olojuoro
LO 4= (RR04) & (RR05)	Lat. 7°9'40"N Long. 3°57'25"E Elevation 365 ft	Course grained	Quartz, muscovite, biotite, beryl, feldspar(mica) dark-brown, specks of garnet	Pegmatite and mica schist	Falansa Mine
LO 5= (RR06) & (RR07)	Lat. 7°11'27"N Long. 3°55'36"E Elevation 443 ft	Course grained	Quartz, muscovite, feldspar(mica), brown pitches of garnet with very limited amount of biotite	Pegmatite and mica schist	Gbayo (Active and abandoned mine)
LO6= (RR08) & (RR09)	Lat. 7°11'44"N Long. 3°55'50"E Elevation 448 ft	Medium to course grained	Quartz, feldspar, biotite, and medium grained size muscovite	Pegmatite and mica schist	Gbayo ( an abandoned mine)
LO 7	Lat. 7°10'30"N Long. 3°55'59"E Elevation 459 ft	Medium grained	Quartz, biotite and feldspar	Granite gneiss	Sanku
LO 8= (RR10)	Lat. 7°10'06"N Long. 3°55'25"E Elevation 437 ft	Medium grained	Quartz, biotite, and feldspar	Granite gneiss	Onipede

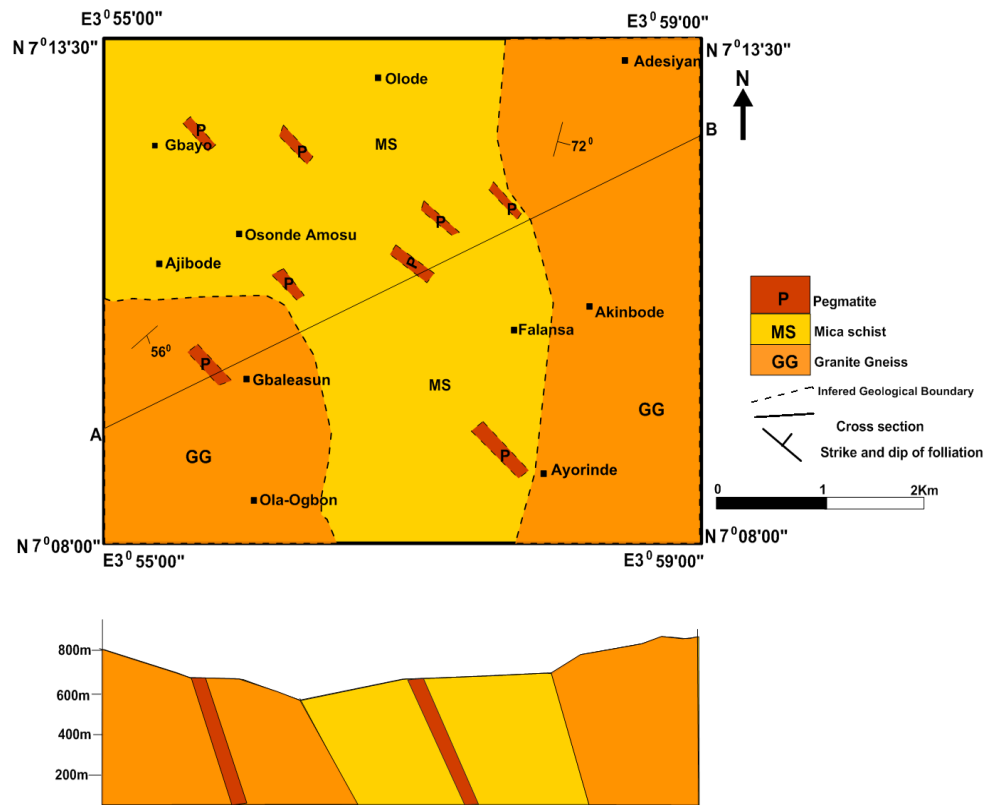


Figure 2. Geological map of the study area (Adapted from Okonkwo et al. [22]).

### 2.3 Assessment of metal contamination

#### Single-element pollution indices

Single pollution indices are employed in the assessment of metal contamination because they show how concentrated an element is in a certain location in comparison to a background. As an example:

**Contamination factor (Cf)** is a quantitative evaluation of the contaminant’s level and sources. The following is how CF is assessed:

$$Cf = C_m\text{Sample} / C_m\text{Background}$$

where  $C_m\text{Sample}$  = concentration of a given metal in the sediment,  $C_m\text{Background}$  = Background value of the metal of interest at a site [25,26]. The following four classes were established (Table 3).

Table 3. Contamination factor (CF) and level of contamination [27].

Contamination Factor (CF)	Contamination Level
$CF < 1$	Low contamination
$1 \leq CF < 3$	Moderate contamination
$3 \leq CF < 6$	Considerable contamination
$CF > 6$	Very high contamination

**Enrichment factors (Ef)** are a useful indicator of

contamination status and level in the research environment [28]. As seen below, the EF computation compares each value to a certain (control sample) background level in order to identify possible sources:

$$EF = (Me/Fe)_{\text{Sample}} / (Me/Fe)_{\text{background}}$$

where  $(Me/Fe)_{\text{sample}}$  = the metal to Fe ratio in the sample under study;  $(Me/Fe)_{\text{background}}$  is the natural background value of metal to Fe ratio. We used metal background values from roughly 4.5 kilometers away for this study. Iron was chosen as a normalization factor since its natural sources (1.5 percent) have a significant influence on its input [29]. Table 4 shows the many types of enrichment factors.

Table 4. Enrichment factor (EF) categories [30].

Enrichment factor (EF)	Enrichment factor (EF) Categories
$EF < 2$	Deficiency to minimal enrichment
$2 \leq EF < 5$	Moderate enrichment
$5 \leq EF < 20$	Significant enrichment
$20 \leq EF < 40$	Very high enrichment
$EF \geq 40$	Extremely high enrichment

**The Igeo index** is used to classify and identify environmental control exerted by anthropogenic

activities. Igeo was determined using the following formula:

$$I_{geo} = \text{Log}_2 [C_m \text{Sample} / (1.5 \times C_m \text{Background})]^{[26]}$$

where  $C_m \text{Sample}$  = measured concentration of an element in the sediment sample and  $C_m \text{Background}$  = geochemical background value. To account for possible fluctuations in baseline values for a specific metal in the environment as well as very modest anthropogenic influences, a factor of 1.5 was utilized. Muller<sup>[31]</sup> recognized seven levels of qualification (Table 5).

**Table 5.** Muller’s classification for geo-accumulation index (Igeo).

Igeo Values	Class	Sediment Quality
≤ 0	0	Unpolluted
0-1	1	From unpolluted to moderately polluted
1-2	2	Moderately polluted
2-3	3	From moderately to strongly polluted
3-4	4	Strongly polluted
4-5	5	From strongly to extremely polluted
> 6	6	Extremely polluted

**Multi-element pollution indices**

Due to some inherent limitations that single-element pollution indices have, multi-element pollution indices were also used<sup>[32]</sup>. The followings are the most common and regularly used:

**The contamination degree (Cd)** is calculated as the sum of contamination factors (CF of the study region) for all elements examined, as shown below<sup>[27]</sup>.

$$C_d = \sum_{i=1}^n C_f^i \Sigma$$

This is intended to establish a standard of overall effluence intensity in surface layers in a specific area.

**Pollution Index (PI)** equation derived by Hakanson<sup>[27]</sup> and Nemerow<sup>[33]</sup> is as follow:

$$PI = \sqrt{\frac{(C_{f_{average}})^2 + (C_{f_{max}})^2}{2}}$$

where  $C_{f_{average}}$  = average of contamination factor and  $C_{f_{max}}$  = maximum contamination factors. Categories for PI are:  $PI < 0.7$ —Unpolluted,  $0.7 < PI < 1$ —

Slightly polluted,  $1 < PI < 2$ —Moderately polluted,  $2 < PI < 3$ —Severely polluted,  $PI > 3$ —Heavily polluted.

**Modified Pollution Index (MPI):** In their calculation, Brady et al.<sup>[25]</sup> used enrichment factors instead of contamination factors.

$$MPI = \sqrt{\frac{(E_{f_{average}})^2 + (E_{f_{max}})^2}{2}}$$

where  $E_{f_{average}}$  = average of enrichment factors and  $E_{f_{max}}$  = maximum enrichment factor.

Categories for MPI are:  $MPI < 1$ —Unpolluted,  $1 < MPI < 2$ —Slightly polluted,  $2 < MPI < 5$ —Moderately polluted,  $3 < MPI < 5$ —Moderately-heavily polluted,  $5 < MPI < 10$ —Severely polluted and  $MPI > 10$ —Heavily polluted.

PI and MPI are both used in the same way. This takes into account background concentrations as well as the sediments’ complex, non-conservative behaviour<sup>[27,33,25]</sup>.

**The pollution load index (PLI)** provides a simple but relative method of evaluating an area’s suitability for human well-being. Tomlinson et al.<sup>[34]</sup> devised this method, and the degree of metal pollution in the research area was determined using the formula below:

$$PLI = (CF_1 \times CF_2 \times CF_3 \times \dots \times CF_n)^{1/n}$$

where  $C_{f1} = CF$ ,  $n$  = number of metals. According to Brady et al. (2015), the degree of heavy metal risk assessed by PLI is mainly divided into  $PLI < 0.7$ —Unpolluted;  $0.7 < PLI < 1$ —Slightly polluted;  $1 < PLI < 2$ —Moderately polluted;  $2 < PLI < 3$ —Severely polluted;  $PLI > 3$ —Heavily polluted.

**The ecological risk index (ERI)** is a useful technique for determining heavy metal pollution in soil and its ecological and environmental consequences. The ecological risk factor ( $Er^i$ ) can be stated mathematically using the following equation:

$$Er = Tr^i * C^i F$$

where  $Tr^i$  = toxic-response factor for a given element; Hakanson<sup>[27]</sup> defined a “toxic-response factor” ( $Tr$ ) for a specific substance and found values of 30, 5, 5, 5, 2, 1, 1 for Cd, Cu, Pb, Ni, Cr, Zn, and Mn, respectively;  $C^i f$  = contamination factor.

The potential ecological risk index (PERI) is expressed after Wang et al. [35] as:

$$R.I = \sum_{i=1}^6 Er^i$$

where R.I = requested potential ecological risk index for the environment and  $Er^i$  is the ecological risk factor for a given element  $i$  to semi-quantitatively determine the pollution level in an area.

### 3. Results and discussion

#### 3.1 Heavy metals concentration in the stream sediments

Table 6 shows the results of the geochemical analysis of stream sediment. Copper (Cu), lead (Pb), zinc (Zn), nickel (Ni), cobalt (Co), manganese (Mn), strontium (Sr), vanadium (V), cadmium (Cd), chromium (Cr), barium (Ba), and iron (Fe) were among the heavy metals evaluated in this work (Fe). For the most part, the concentrations of heavy metals were found to have a relatively wide range of values.

Table 7 shows the descriptive statistics for the obtained data set relating to the stream sediments under research in Olode and its environs, as well as background geochemical data. Cu, Pb, Zn, Ni, Co, Mn, Sr, V, Cr, and Ba have mean concentrations of 16.25,

10.60, 27.83, 9.00, 13.90, 553, 9.83, 42.08, 47.42, 74.5, respectively. Heavy metal mean values were higher than background values (samples collected 4 km away from the mining site at Ayorinde), indicating that mining activities had an impact on the study area. Although the abundance of these heavy metals analysed in stream sediments was  $Mn > Ba > Cr > V > Zn > Cu > Co > Pb > Sr > Ni > Fe$ , the highest metal concentrations were found in rock and stream sediment samples from the mine area, particularly from abandoned mines in Gbayo. The coefficient of variation (CV), a powerful tool for measuring relative variability, was used in this work to compare the degree of variation from one data sequence to the next [12-14,18,19,22]. Sr had the lowest CV of 6.12, followed by V and Cr with 85.08 and 92.13 percent, respectively. Pb, Ni, Cu, and Ba had CVs of 110.30, 111.1, 114.58, and 119.79 percent, respectively, while Zn Mn and Co had CVs of 124.69, 148.00, and 171.22 percent. Cr, Pb, Ni, Cu, Ba, Zn, Mn, and Co exhibited a CV of over 90%. Although sampling methods and preparations with analytical techniques may be responsible for the large coefficient variation across the area under investigation, the obtained CV (CV < 90%) values of heavy metals dominated by anthropogenic sources are generally greater than (CV > 90%) dominated by geogenic sources [19,13,22] (Table 7).

Table 6. Concentration (ppm) of heavy elements in the stream sediment samples around Olode Pegmatite Mine.

Locations	Gbayo	Gbayo	Olojuoro	Olojuoro	Akinbode	Olojuoro	Falansa	Adeoro	Agbeja	Elerin	Gbayo
Sample Numbers	SS01	SS02	SS03	SS04	SS05	SS06	SS07	SS08	SS10	SS11	SS12
Cu	12	33	7	6	8	17	14	8	14	59	15
Pb	7	13	5	3	8	5	12	5	3	40	8
Zn	19	36	16	13	13	18	88	16	16	55	37
Ni	11	48	3	3	2	4	11	3	7	9	6
Co	6	85	1	4	3	3	13	4	8	22	3
Mn	121	4330	36	188	148	76	690	157	193	447	160
Sr	17	31	6	4	4	12	10	5	8	13	5
Cd	0.5	0.5	0.5	0.5	0.5	0.5	0.5	0.5	0.5	0.5	0.5
V	28	90	21	13	27	65	43	15	24	135	35
Cr	46	161	18	12	29	36	54	14	34	113	42
Ba	91	354	21	25	23	53	75	24	71	107	36
Fe	0.97	4.29	0.42	0.52	0.89	1.32	1.51	0.57	0.91	4.98	1.08

All values are in part per milliomm (mg/kg) except Fe in %.

**Table 7.** The summary of chemical parameters of the stream sediment samples of Olode area.

Elements	Min.	Max.	Mean	STD	Coefficient of variation (%)	Background value	WHO
Cu	2	59	16.25	18.62	114.58	2	25
Pb	3	40	10.6	9.61	110.30	3	---
Zn	7	88	27.83	22.32	124.69	7	123
Ni	1	48	9	8.10	111.1	1	20
Co	2	85	13.90	23.80	171.22	2	---
Mn	36	4330	553	33.82	148	90	---
Sr	3	31	9.83	7.57	6.12	3	---
V	9	135	42.08	35.80	85.08	9	---
Cr	10	161	47.42	43.69	92.13	10	25
Ba	14	354	74.5	89.24	119.79	14	---
Fe	0.42	4.98	1.59			0.33	

### 3.2 Spatial distribution/variation of heavy metals

In order to evaluate the likely sources of enrichment and identify possible hotspot sections of the study area with high metal concentrations, the spatial distribution/variation of heavy metals was investigated for both stream sediment and rock samples <sup>[36,22]</sup> (**Figure 3**).

Copper concentrations in rock and stream sediment samples are 30 and 16.25 ppm on average, respectively (**Figure 3A**). Falansa (122,1 ppm) and Gbayo (122,1 ppm) have high copper values in their rocks (95.6 ppm). All of these were collected in the research region near the operating and abandoned mines of Falansa and Gbayo.

Lead concentrations in rock samples average 2.81 ppm, whereas stream sediment samples average 10.60 ppm (**Table 7** and **Figure 3B**). The highest Lead concentration in rock samples (10.7 ppm) was found in the Onipede area, implying that the concentration of Lead in the research area is due to anthropogenic sources such as waste dumps, incineration point leaching, atmospheric deposition, and the use of agrochemicals <sup>[13,22]</sup>.

Zinc concentrations of 72 ppm were found in rocks at Gbayo and 88 ppm in sediments near Falansa (**Table 7** and **Figure 3C**). Many of the high zinc concentrations were found in rock and stream sediment samples taken near abandoned mines. The existence of high zinc values in the studied area

could possibly be due to an anthropogenic source <sup>[22]</sup>.

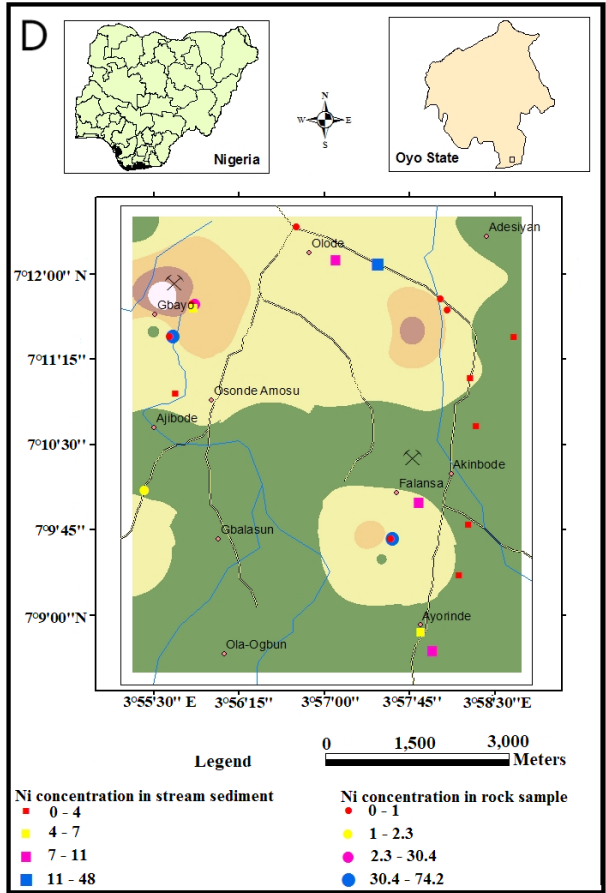
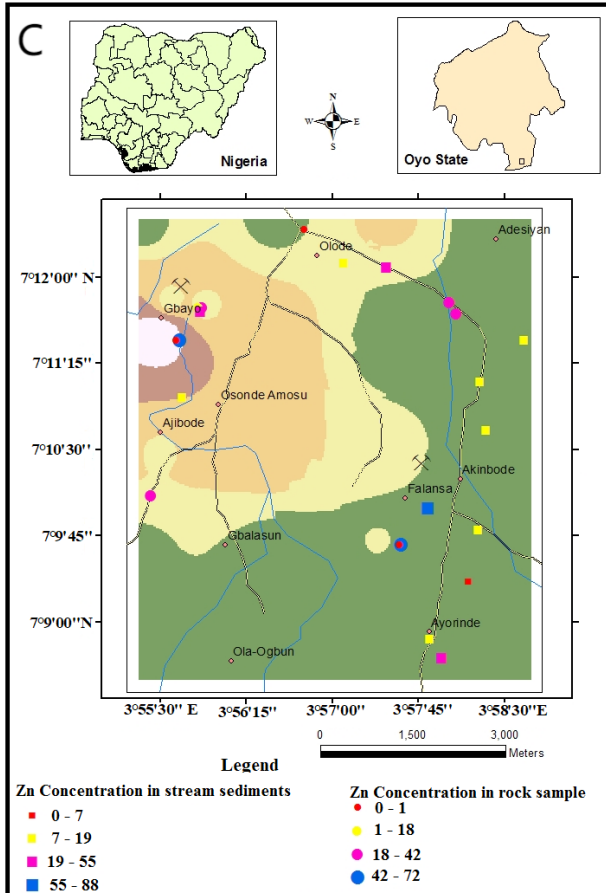
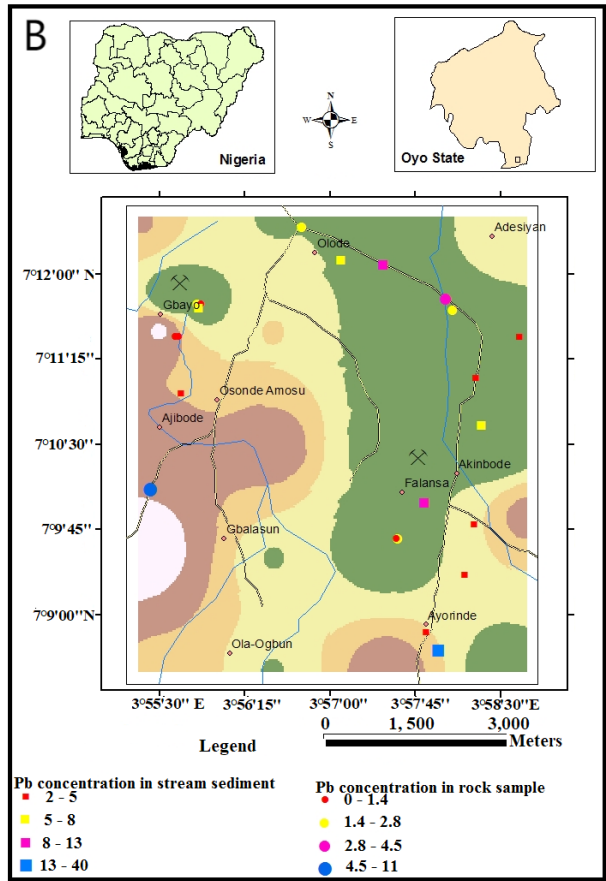
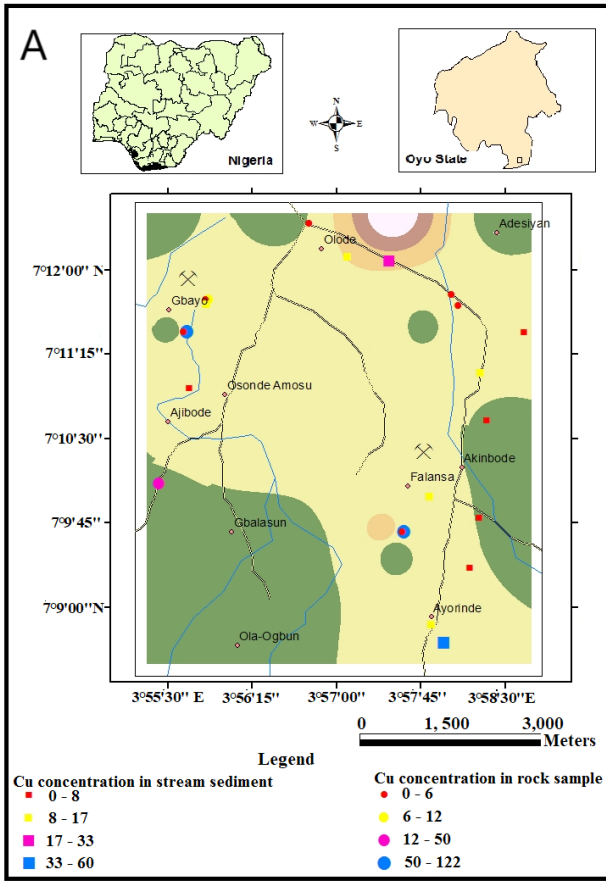
Nickel concentrations were moderately high in the area of the mine and the abandoned Falansa mines (**Table 3** and **Figure 3D**). Nickel concentrations in rock samples average 58.67 ppm, while stream sediment samples average 9.00 ppm (**Table 7**).

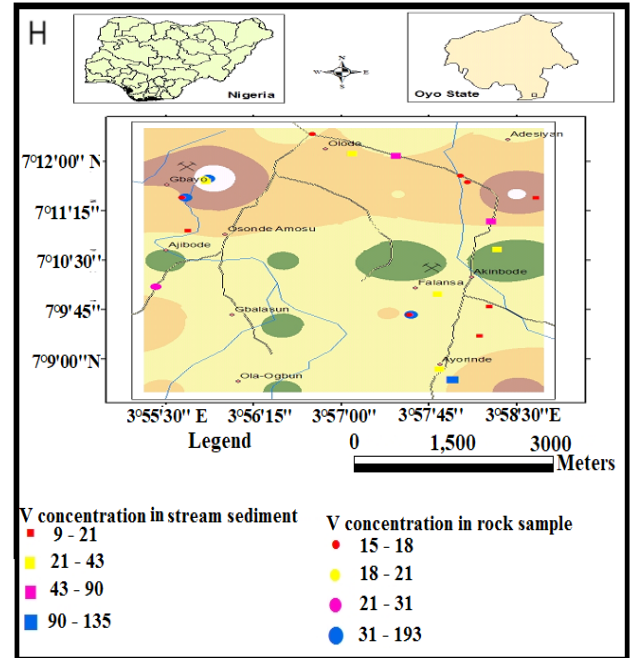
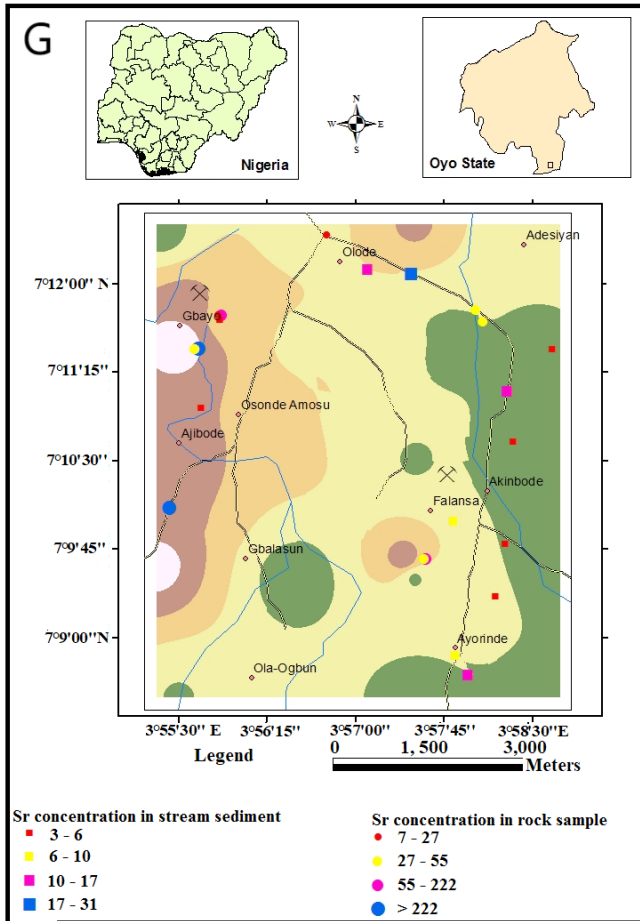
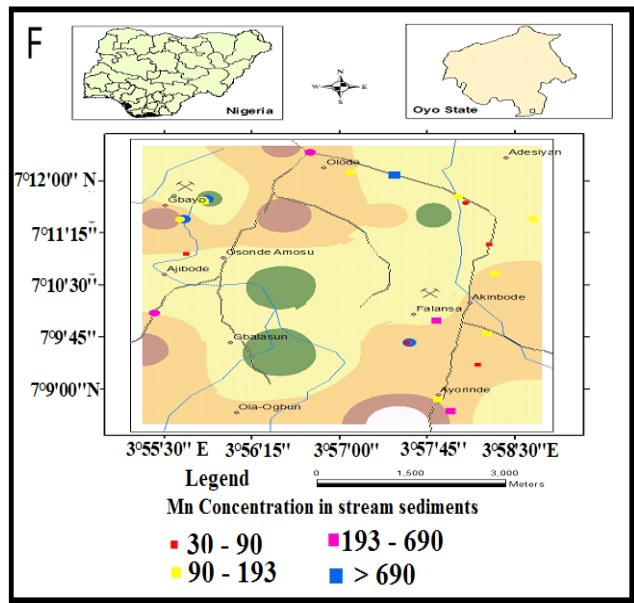
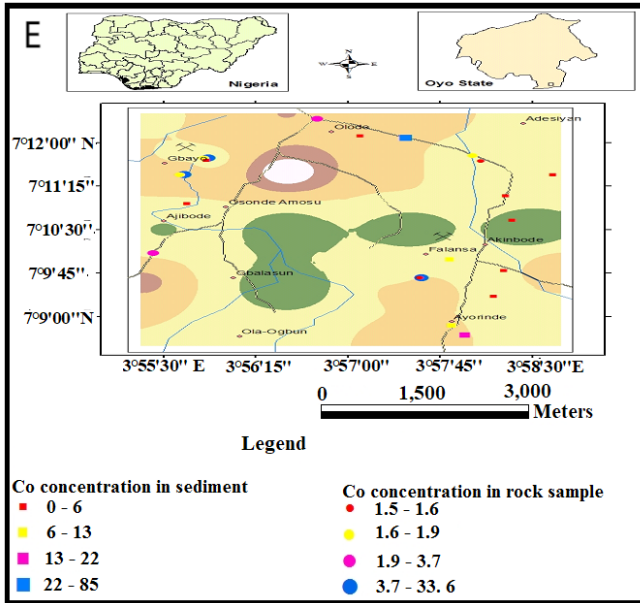
Cobalt concentrations in rocks and stream sediment samples average 9.67 and 13.91 ppm, respectively (**Table 7** and **Figure 3E**). The locations with high Cobalt concentration values in the sediment in Gbayo have the highest with 85 ppm, which could be caused by anthropogenic sources such as waste dump sites, leaching from incineration points, discharge from domestic waste, agro-chemicals, and others, but these are evidently very low in the rock samples of the areas, limiting the sources to lithogenic sources (**Figure 3E**).

Extraordinarily high manganese concentration values were found in stream sediments from Gbayo, with the highest concentration of (4330 ppm). The occurrence of extremely high manganese concentrations in the area is likely due to run-off from the habitats (**Table 3** and **Figure 3F**).

In rock and stream sediment samples, the average levels of strontium were found to be 221.12 ppm and 9.83 ppm, respectively (**Table 7**). The amount of strontium in the rocks in the research area is higher than in stream sediment samples, indicating that the metal derives from a natural (geogenic) source in the rock types studied <sup>[18]</sup>.

Furthermore, substantial strontium concentrations





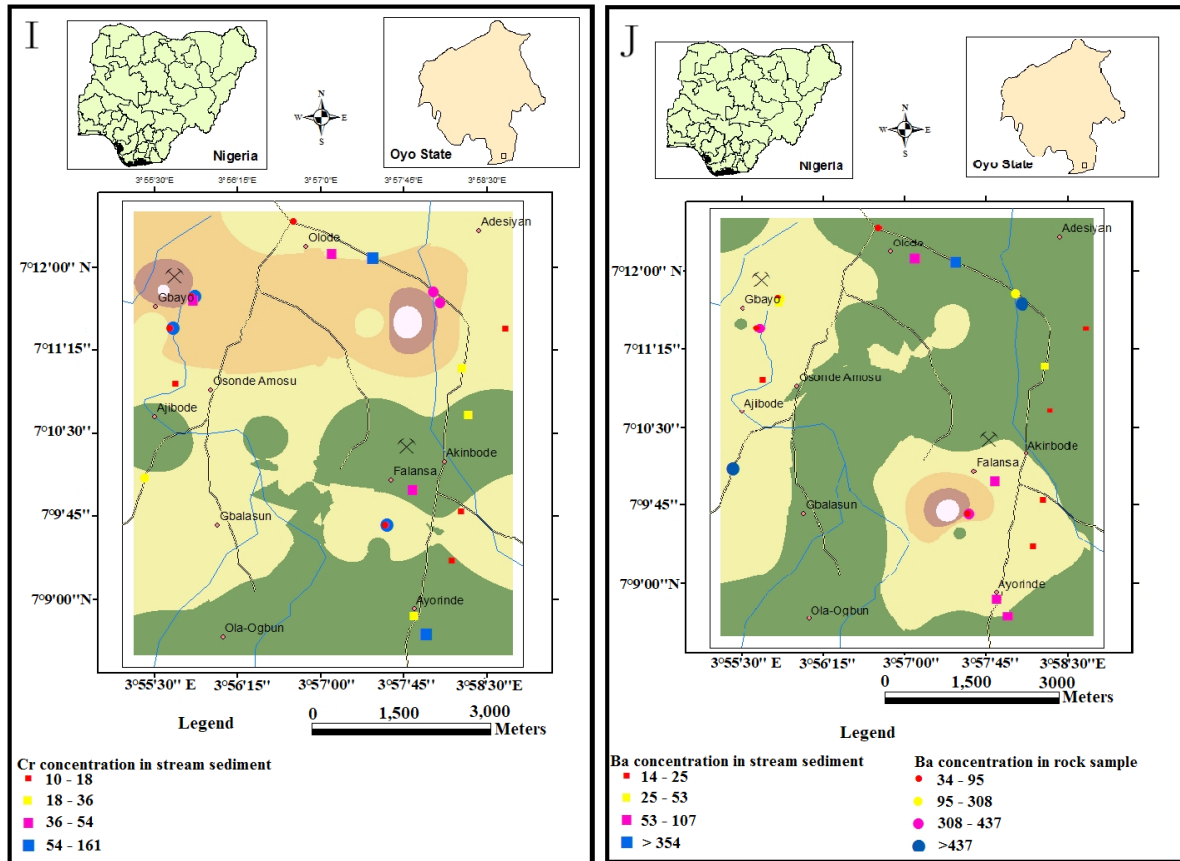


**Figure 3.** Map of the study area showing distribution of : (A) Copper, (B) Lead, (C) Zinc, (D) Nickel, (E) Cobalt, (F) Manganese, (G) Strontium, (H) Vanadium, (I) Chromium and (J) Barium in the stream sediment and rock samples within the study area (Modified after Okonwo et al. [22]).

were found in rock samples collected in Onipede (864.7 ppm), Gbayo (685.8 ppm, 213.5 ppm), and Falansa (222.3 ppm). It's worth noting that the levels of strontium in all of the stream sediment samples are modest (**Figure 3G**).

Vanadium concentrations of 193 ppm, 173 ppm, and 170 ppm were found in rock samples, while 135 ppm, 90 ppm, and 65 ppm were found in stream sediment samples from the research area, indicating a natural (geogenic) contribution of this metal from the rock types to the environment (**Figure 3H**).

High chromium concentration levels were found to be centered around the stream sediment samples, with high concentration values in Gbayo (161 ppm) and Elerin (113 ppm) (**Table 7** and **Figure 3I**). Chromium compounds attach to soil and are unlikely to travel to groundwater, but they persist in water sediments.

Barium levels were found to be high in rock and

stream sediment samples collected in the Falansa, Gbayo, Ayominde, Olojuoro, Onipede, and Ajibode locations. The rock samples had high concentration levels of 737 ppm, 594 ppm, 437 ppm, 412 ppm, 308 ppm, and 209 ppm, whereas the stream sediment samples had 107 ppm and 354 ppm (**Table 7** and **Figure 3J**). Vomiting, abdominal cramps, diarrhea, difficulty breathing, elevated or lowered blood pressure, numbness around the face, and muscle weakness can all be symptoms of exposure to this metal. High blood pressure, heart rhythm abnormalities, paralysis, and death are all possible side effects of consuming large doses of barium [13].

The stream sediments showed a low concentration of Fe (**Table 6**).

### 3.3 Heavy metal sourcing

To determine the contribution of various factors

to the concentrations of metals in the samples and so infer the sources of metal pollution, the data were subjected to Pearson’s correlation statistical analysis [13,22] (Table 8). High positive and significant correlation values (> 0.65) were discovered in the acquired data for stream sediment samples from Olode and its vicinity; Copper-Lead (0.929), Copper-Vanadium (0.970), Copper-Chromium (0.815), Lead-Vanadium (0.884), Lead-Chromium (0.660), Nickel-Cobalt (0.978), Nickel-Manganese (0.979), Nickel-Strontium (0.925), Nickel-Chromium (0.875), Nickel-Barium (0.989), Cobalt-Manganese (0.986), Cobalt-Strontium (0.884), Cobalt-Chromium (0.905), Cobalt-Barium (0.982), Manganese-Chromium (0.838), Manganese-Barium (0.961), Strontium-Chromium (0.878), Strontium-Barium (0.950), Vanadium-Chromium (0.840), and Chromium-Barium (0.917) (Table 8). These significant correlation values indicate that the origin of metals in the studied area is strongly linked to abandoned mine water, mining activities, and emissions from fossil fuel combustion, among other things [22].

Nickel, Manganese, Copper, Lead, Chromium, Vanadium, Barium, and Cobalt have high correlation values, indicating that these metals were anthropogenically added to stream sediment samples. However, the strong correlations between Nickel-Cobalt (0.978), Nickel-Manganese (0.979), Nickel-Strontium (0.925), Nickel-Barium (0.989), Manganese-Barium (0.961), Strontium-Barium (0.950), Chromium-Barium (0.917) imply a natural (geogenic) contribution of metals from the rock types ob-

served in the research area [36,13].

Zinc, Copper, Cadmium, and Lead are frequently found together in geochemical research [37,38]. Lead had weak positive correlation values with Zinc, Cobalt, and Manganese, indicating that these metals may have contributed to the stream sediment samples from various undefined sources, both naturally and anthropogenically, whereas Lead had high correlation values with Copper, Vanadium, and Chromium, indicating that these metals may have come from a natural source.

### 3.4 Single-element indices

To determine the environmental effects, a quantitative analysis of heavy metal pollution estimation surrounding the pegmatite mining site in Olode and its vicinity was conducted using single-element indices [13]. These indices used include:

#### Contamination factor

The result for this index, as shown in Table 9, was calculated by comparing the measured heavy metal concentration with background values for stream sediments collected in an uninterrupted area inside the research area at Ayorinde, about 4 kilometers from the Falansa mine. On average, the CF values found were in the following order: Cu > Co > Mn > V > Ba > Cr > Zn > Pb. The results for these metals ranged from extremely low to very high contamination (CF = CF1; 1CF > 6) (Table 4), indicating that their prevalence was anthropogenic [18].

Table 8. Correlations matrix for heavy metals in stream sediment samples of Olode area.

	Cu	Pb	Zn	Ni	Co	Mn	Sr	V	Cr	Ba
Cu	1									
Pb	0.929	1								
Zn	0.497	0.575	1							
Ni	0.450	0.235	0.296	1						
Co	0.537	0.334	0.287	0.978	1					
Mn	0.402	0.200	0.250	0.979	0.986	1				
Sr	0.552	0.333	0.285	0.925	0.884	0.853	1			
V	0.970	0.884	0.515	0.499	0.580	0.463	0.619	1		
Cr	0.815	0.660	0.487	0.875	0.905	0.838	0.878	0.840	1	
Ba	0.548	0.323	0.290	0.989	0.982	0.961	0.950	0.593	0.917	1

**Table 9.** Contamination factor (CF) for the heavy metals of Olode stream sediments.

	<b>Cu</b>	<b>Pb</b>	<b>Zn</b>	<b>Ni</b>	<b>Co</b>	<b>Mn</b>	<b>Sr</b>	<b>Cd</b>	<b>V</b>	<b>Cr</b>	<b>Ba</b>
SS01	6	2.33	2.71	11	3	1.34	5.67	1	3.11	4.6	6.5
SS02	16.5	4.33	5.14	48	42.5	48.11	10.33	1	10	16.1	25.29
SS03	3.5	1.67	2.89	3	0.5	0.4	2	1	2.33	1.8	1.5
S004	3	1	1.86	3	2	2.09	1.33	1	1.44	1.2	1.79
SS05	4	2.67	1.86	2	1.5	1.64	1.33	1	3	2.9	1.64
SS06	8.5	1.67	2.57	4	1.5	0.84	4	1	21.67	3.6	3.79
SS07	7	3	12.57	11	6.5	7.67	3.33	1	4.78	5.4	5.36
SS08	4	1.67	2.28	3	2	1.74	1.67	1	1.67	1.4	1.71
SS10	7	1	2.29	7	4	2.14	2.67	1	2.67	3.4	5.07
SS11	39.5	13.33	7.86	9	11	4.97	4.33	1	15	11.3	7.64
SS12	7.5	12.33	5.29	6	1.5	1.78	1.67	1	3.89	4.2	2.57
Range	3-39.50	1-13.33	1.86-12.57	2-48	0.5-42.5	0.4-48.11	1.33-10.33	1	1.44-21.67	1.2-16.10	1.5-25.29
CD	106.5	45	47.32	107	76	72.72	38.33	11	69.56	55.9	62.86

\*CD = Degree of contamination.

**The enrichment factor (EF)**

Table 10 shows the heavy metal concentrations found in the Olode stream sediments.

EF is a tool that can be used to compare areas by providing a concise assessment of geochemical trends [39]. The computed enrichment factor for all heavy metals was  $EF < 2$ , showing a lack of minimal enrichment in diverse places.

**The geo-accumulation index (Igeo)**

The obtained calculated Igeo values, based on background values are listed in Table 11. The Igeo

values for each heavy metal are: Cu (-1 to 3), Pb (-1 to 3), Zn (-1 to 3), Ni (-1 to 5), Co (-1 to 5), Mn (-1 to 6), Sr (0-3), V (0-3), Cr (0-4) and Ba (-1 to 4) (Figures 4-8). The Igeo values for the Olode stream sediments were in the following sequence of abundance:  $Mn > Co > Ni > Cr > Ba > Sr > Ba > Pb > Zn$ . Obtained values for Cu, Pb, Zn, Sr, V, Cr and Ba revealed practically uncontaminated to “moderately to heavily” contaminated except values for Ni, Co and Mn that indicated practically uncontaminated to extremely contaminated [31,26] (Table 11).

**Table 10.** Calculated enrichment factors of heavy metals in Olode stream sediments.

<b>Sample Numbers</b>	<b>SS01</b>	<b>SS02</b>	<b>SS03</b>	<b>SS04</b>	<b>SS05</b>	<b>SS06</b>	<b>SS07</b>	<b>SS08</b>	<b>SS10</b>	<b>SS11</b>	<b>SS12</b>
Unit	(ppm)										
Cu	2.04	1.3	2.75	1.9	1.48	2.13	1.53	2.32	2.54	1.96	2.29
Pb	1.19	3.03	1.96	0.95	1.48	0.63	1.31	1.45	0.54	1.3	1.22
Zn	3.23	1.38	6.29	4.13	2.41	2.25	9.62	4.63	2.90	1.85	5.65
Ni	1.87	1.85	1.18	0.95	0.37	0.5	1.2	0.87	1.27	0.3	0.92
Co	1.01	3.27	0.39	1.27	0.57	0.38	1.42	1.16	1.45	4.42	0.46
Mn	20.58	166.56	14.14	59.66	27.44	9.5	75.4	45.45	35	14.81	24.45
Sr	2.89	1.19	2.36	1.27	0.74	1.5	1.09	1.45	1.45	0.43	0.76
Cd	0.09	0.02	0.02	0.2	0.09	0.06	0.05	0.14	0.09	0.02	0.08
V	4.76	3.46	8.25	4.12	5.01	8.13	4.67	4.34	4.35	4.47	5.35
Cr	7.83	6.20	7.07	3.80	5.38	4.5	5.9	4.05	6.17	3.74	6.42
Ba	15.48	13.62	8.25	7.93	4.26	6.63	8.20	6.94	12.87	3.55	5.5

Table 11. Geo-accumulation index of Olode sediments.

Metals	Igeo range in the Sediments	Interpretation
Cu	-1 to 3	Practically uncontaminated to “moderately to heavily” contaminated
Pb	-1 to 3	Practically uncontaminated to “moderately to heavily” contaminated
Zn	-1 to 3	Practically uncontaminated to “moderately to heavily” contaminated
Ni	-1 to 5	Practically uncontaminated to extremely contaminated
Co	-1 to 5	Practically uncontaminated to extremely contaminated
Mn	-1 to 6	Practically uncontaminated to extremely contaminated
Sr	0-3	Practically uncontaminated to “moderately to heavily” contaminated
V	0-3	Practically uncontaminated to “moderately to heavily” contaminated
Cr	0-4	Practically uncontaminated to “moderately to heavily” contaminated
Ba	-1 to 4	Practically uncontaminated to “moderately to heavily” contaminated

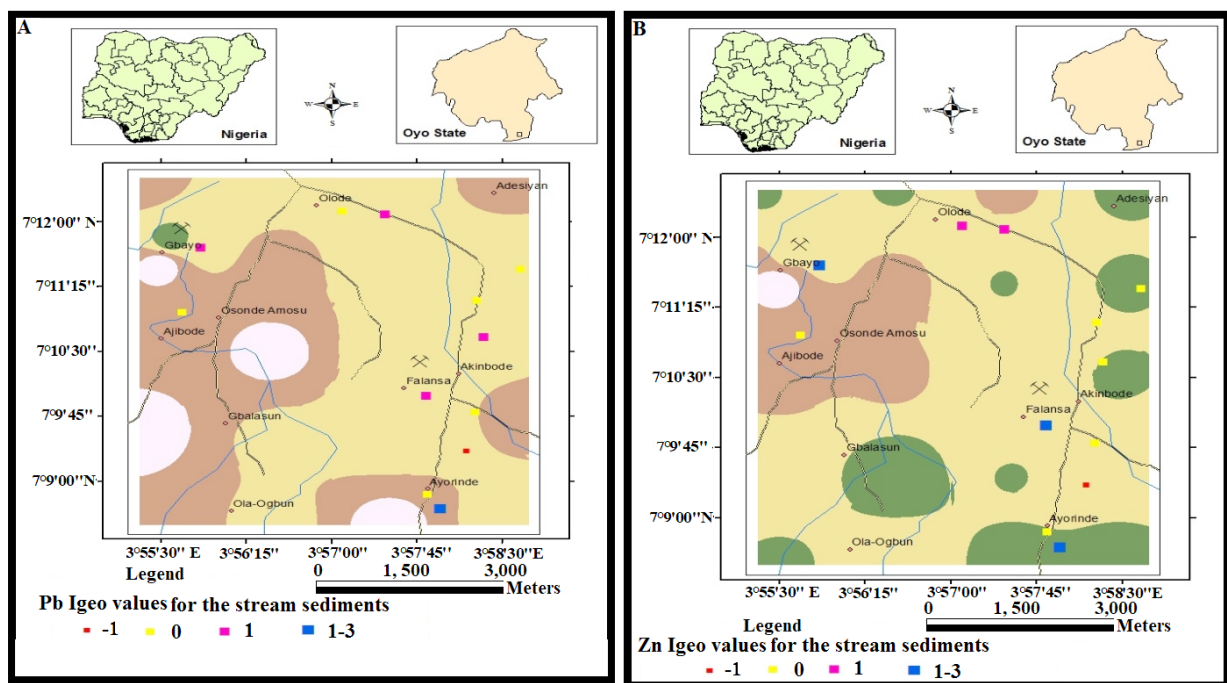


Figure 4. Igeo maps of : A) Lead and B) Zinc within the study area.

### 3.5 Multi-element pollution indices

The following indices were employed due to some inherent limitations that single-element pollution indices [32].

#### The degree of contamination (CD)

The degree of contamination (CD) is obtained by adding all of the computed CFs for each metal (Table 9), ranging from moderate to extremely high, signifying a significant human influence. With the exception of Cd, which is moderately contaminated, all of the heavy metals tested exhibited very high levels of

contamination, indicating a worrying anthropogenic input as a result of mining and probably increased agricultural activity in the studied area.

#### Pollution load index (PLI)

The pollutant load index (PLI) was used to properly assess the level of environmental contamination caused by mining activity [34,40,22]. All of the PLI values obtained for the Olode stream sediments were more than one (Table 12). This indicates that the sampling site is significantly polluted/degraded, implying anthropogenic contamination. This index (PLI), which gives a simple, comparative approach

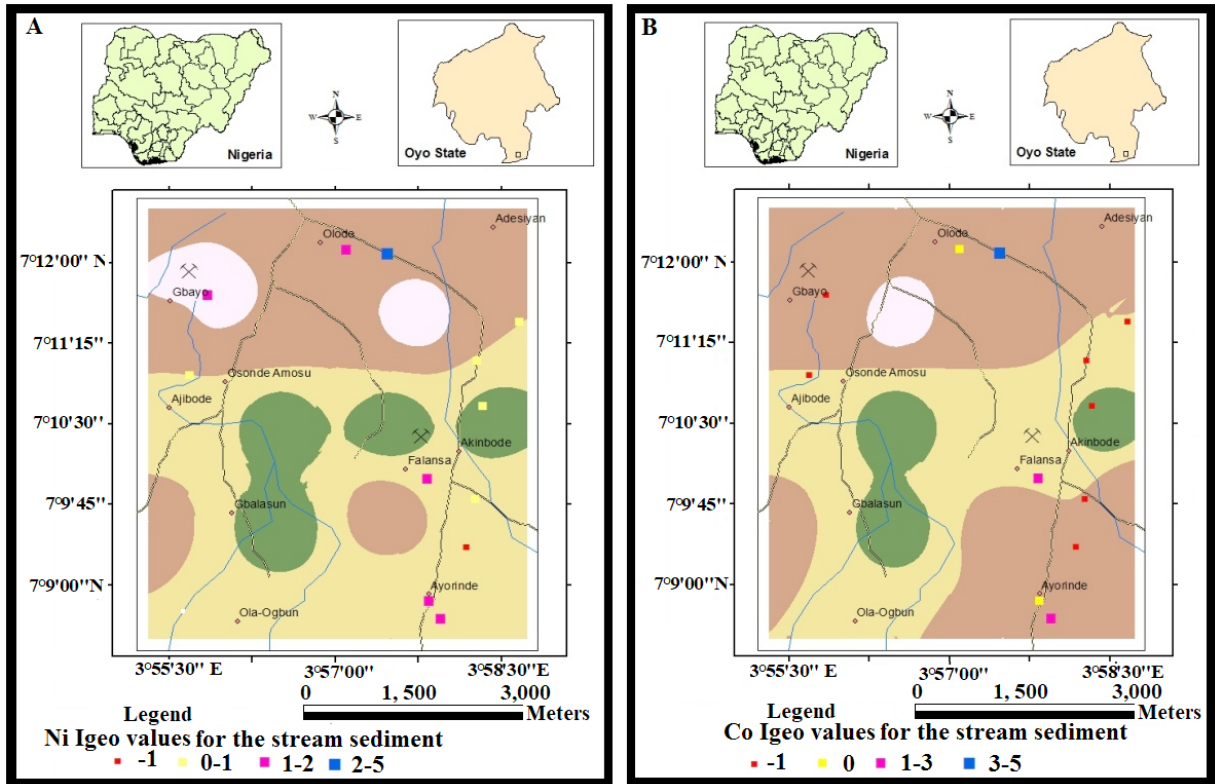


Figure 5. Igeo maps of A) Nickel and B) Cobalt within the study area.

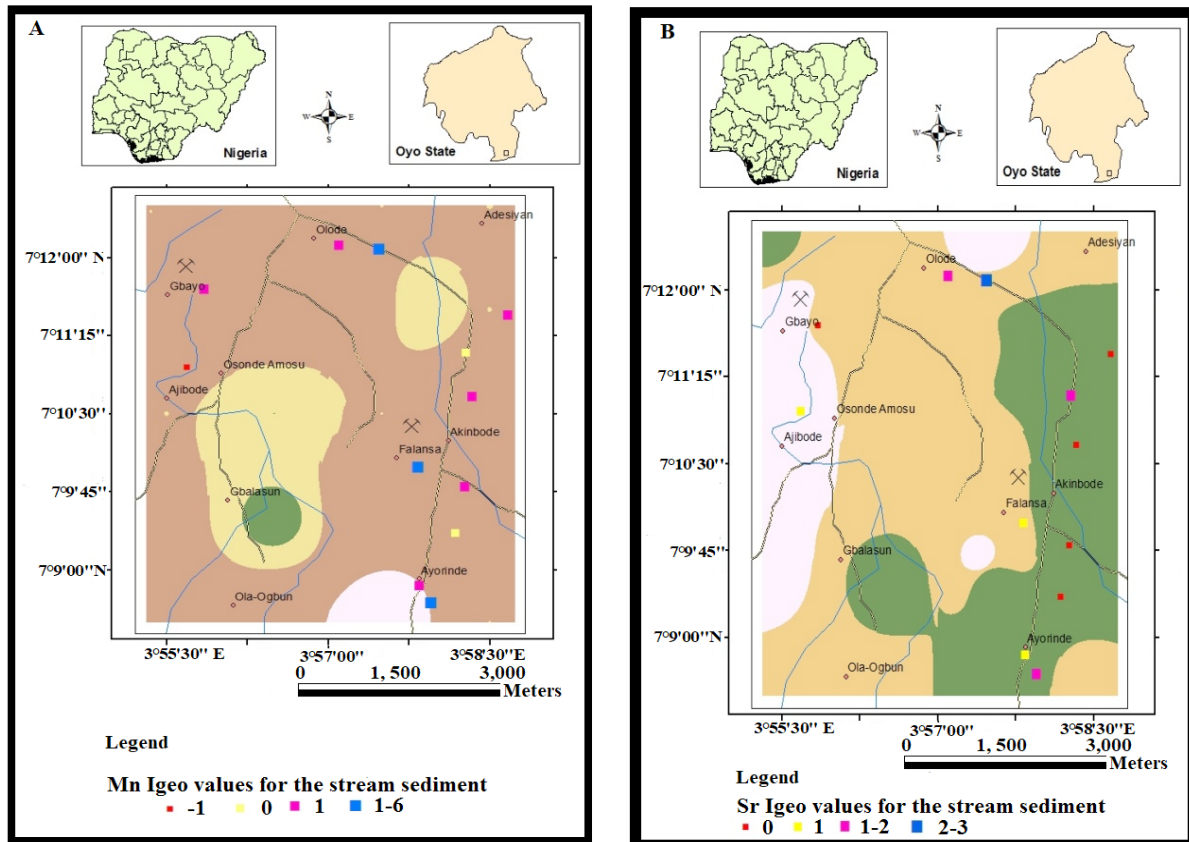


Figure 6. Igeo maps of A) Manganese and B) Strontium within the study area.

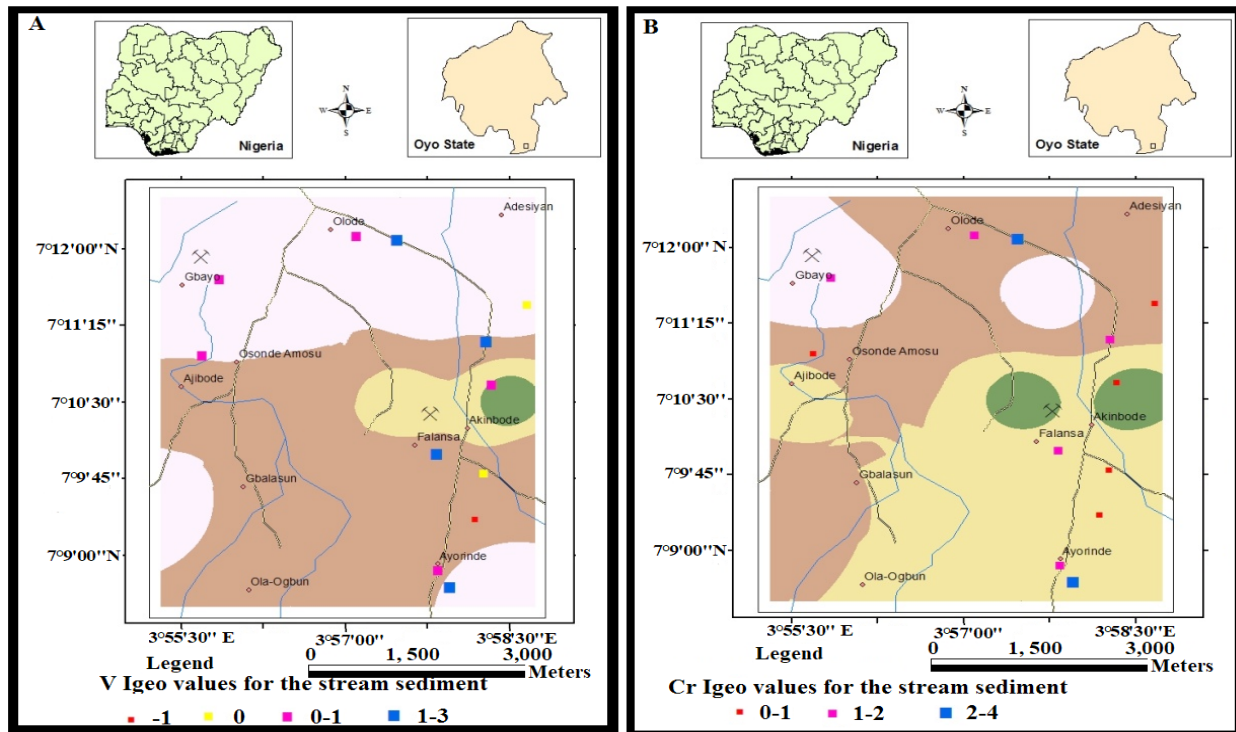


Figure 7. Igeo maps of A) Vanadium and B) Chromium within the study area.

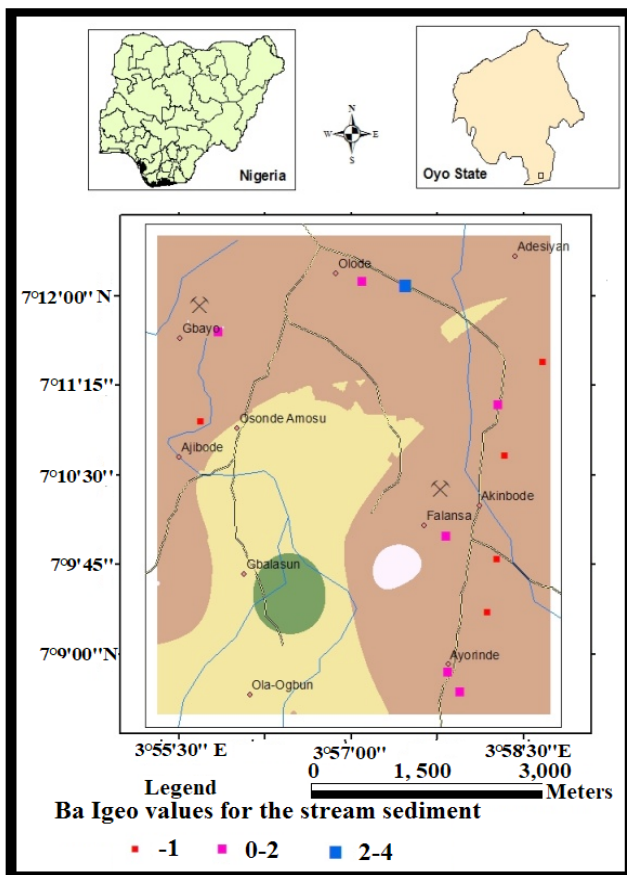


Figure 8. Igeo maps of Barium within the study area.

to measuring the degree of heavy metals contamination in a site, states that  $PLI = 0$  indicates perfection,  $PLI = 1$  indicates just baseline levels of pollutants, and  $PLI > 1$  indicates progressive site deterioration [34,40].

### Pollution Index (PI)

The Olode stream sediments can be classified according to the PI categories. SS03 and SS04 were moderately polluted (1PI2), SS05 and SS08 were severely polluted (2PI3), while the remaining eight samples (8) were significantly polluted ( $PI > 3$ ) (Table 12). Thus, PI appeared to have an advantage over other underestimating indices, as it easily classifies high-risk sediments within a specific area/site of habitation [26,13].

### Modified Pollution Index (MPI)

The MPI clearly distinguishes between three levels of pollution: moderately contaminated (2MPI5; SS 06), “moderately-heavily polluted” (Severely polluted; SS 03), and the other ten samples heavily polluted [27,33,25] ( $MPI > 10$ ; S7, S10, S13, and S19; Table 12). This shows that 83.33% of the area under investigation was heavily polluted implying great

anthropogenic contribution.

**Table 12.** Pollution Load Index (PLI), Pollution Index (PI) and Modified Pollution Index values for heavy metals in Olode stream sediments.

Sampling sites	PLI	PI	MPI
SS01	85.14	5.91	10.66
SS02	39.48	20.18	83.78
SS03	1.02	1.98	7.46
S004	3.25	1.75	30.09
SS05	6.13	2.27	13.89
SS06	40.34	52.33	2.01
SS07	30.96	7	38,02
SS08	2.93	2.24	22.96
SS10	30.96	3.91	17.78
SS11	29.66	20.55	7.57
SS12	2.46	6.53	12.46

**Pollution Load Index:**  $PLI < 0.7$ —Unpolluted;  $0.7 < PLI < 1$ —Slightly polluted;  $1 < PLI < 2$ —Moderately polluted;  $2 < PLI < 3$ —Severely polluted;  $PLI > 3$ —Heavily polluted.

**Pollution Index:**  $PI < 0.7$ —Unpolluted,  $0.7 < PI < 1$ —Slightly polluted,  $1 < PI < 2$ —Moderately polluted,  $2 < PI < 3$ —Severely polluted,  $PI > 3$ —Heavily polluted.

**Modified Pollution Index:**  $MPI < 1$ —Unpolluted,  $1 < MPI < 2$ —Slightly polluted,  $2 < MPI < 5$ —Moderately polluted,  $3 < MPI < 5$ —Moderately-heavily polluted,  $5 < MPI < 10$ —Severely polluted and  $MPI > 10$ —Heavily polluted.

### Ecological risk evaluation

**Table 13** displays the value of the ecological risk index. The results demonstrated that the potential  $Er^i$

for heavy metals in Olode stream sediments followed a pattern of heavy metal contamination:  $Cu > Ni > Cd > Pb > Mn > Zn$  (**Table 8**). For all of the heavy metals in the sediment, the obtained potential  $Er^i$  values indicated a low to moderate ecological danger.

## 4. Conclusions

In Olode and its environs, southwestern Nigeria, a combination of geochemical tests, statistical approaches, and eight indices were utilized to identify heavy metal sources and assess pollution in stream sediments inside an active and abandoned mining site. The goal of this study was to determine the distribution of heavy metals in stream sediments, as well as the level of pollution, ecological danger, and potential sources of heavy metals. In order to investigate the source, contamination, and risk of heavy metals such as Pb, Zn, Cu, Ni, Co, Fe, Mn, and Cr, twelve (12) stream sediments and ten (10) rock samples were collected from pegmatite mining sites at Olode and its environs inside Ibadan, Southwestern Nigeria. The average values and order of abundance obtained followed the following pattern: ppm Mn (595.09) > Ba (80) > Cr (50.82) > V (45.09) > Zn (29.73) > Cu (13.82) > Co (13.82) > Sr (10.46) > Ni (9.73) > Pb (9.09) and Fe (1.59). The mean values

**Table 13.** Ecological risk index of heavy metals in the Olode stream sediments.

Sample	Cu	Pb	Zn	Ni	Mn	Cd	Cr	RI
SS01	30	11.65	2.71	55	1.34	30	9.2	139.9
SS02	82.5	21.65	5.14	240	48.11	30	32.2	459.6
SS03	17.5	8.35	2.89	15	0.4	30	3.6	77.74
S004	15	5	1.86	15	2.09	30	2.4	71.35
SS05	20	13.35	1.86	10	1.64	30	5.8	82.65
SS06	42.5	8.35	2.57	20	0.84	30	7.2	111.46
SS07	7	3	12.57	11	7.67	1	5.4	47.64
SS08	20	8.35	2.28	15	1.74	30	2.8	80.17
SS10	35	5	2.29	35	2.14	30	6.8	116.23
SS11	197.5	66.65	7.86	45	4.97	30	22.6	374.58
SS12	37.5	61.65	5.29	30	1.78	30	8.4	174.62
Average	45.86	19.36	4.30	44.64	6.61	27.36	9.67	157.81

Category:  $Er^i < 40$ —Low potential ecological risk;  $40 \leq Er^i \leq 80$ —Moderate potential ecological risk;  $80 \leq Er^i \leq 160$ —Considerable potential ecological risk;  $160 \leq Er^i \leq 320$ —High potential ecological risk;  $Er^i > 320$ —Very high ecological risk at hand for the substance in question.

for the heavy metals were higher than the background values, indicating that mining activities have a negative impact on the study area, as evidenced by the high coefficient of variation and correlation values ( $> 0.6$ ). Copper-Lead (0.929), Copper-Vanadium (0.970), Copper-Chromium (0.815), Lead-Vanadium (0.884), Lead-Chromium, Nickel-Cobalt, Nickel-Manganese, Nickel-Strontium.

Based on the enrichment factor (EF), the Olode sediments show exceptionally significant enrichment for Mn and Ba when compared to other sediments in the research area. Cu and Ni are most likely responsible for the high contamination, according to contamination factor (CF) values. According to Igeo, the Olode stream sediments are practically uncontaminated to extremely contaminated by Ni, Co, and Mn, as measured by the degree of contamination (CD), pollution load index (PLI), pollution index (PI), and modified pollution index (MPI). Ni and Cu are the major regulating factors that are most likely causing the possible  $Er^i$ . Even though the results for the different indices varied, the combined eight (8) indices supplied us with an all-encompassing picture of heavy metal dangers in the Olode stream sediments. This aids in the development of an appropriate ecological management strategy for reducing the impact of heavy metal contamination from active and abandoned mining sites in Nigeria and other similar places.

## Author Contribution

Authors whose names appear on the submission have contributed sufficiently to the scientific work. It is the M.Sc research of the first author supervised by the fourth author, research article drafted by the second and third authors respectively.

## Conflict of Interests

The authors declare no conflict of interest.

## Funding

The authors did not receive support from any or-

ganization for the submitted work.

## References

- [1] Wuana, R.A., Okeimen, F.E., 2011. Heavy metals in contaminated soils: A review of sources, chemistry, risks and best available strategies for remediation. *International Scholarly Research Notices*. Article ID 402647. DOI: <https://doi.org/10.5402/2011/402647>
- [2] Islam, S., Ahmed, K., Al-Mamun, H., et al., 2019. Sources and ecological risk of heavy metals in soils of different land uses in Bangladesh. *Pedosphere*. 29(5), 665-675. DOI: [https://doi.org/10.1016/S1002-0160\(17\)60394-1](https://doi.org/10.1016/S1002-0160(17)60394-1)
- [3] Lei, M., Zhang, Y., Khan, S., et al., 2010. Pollution, fractionation, and mobility of Pb, Cd, Cu, and Zn in garden and paddy soils from a Pb/Zn Mining area. *Environmental Monitoring and Assessment*. 168(1-4), 215-222. DOI: <https://doi.org/10.1007/s10661-009-1105-4>
- [4] Lottermoser, B., 2007. *Mine wastes: Characterization, treatment and environmental impacts*. Springer: New York. pp. 1-290.
- [5] Fashola, M.O., Ngole-Jeme, V.M., Babalola, O.O., 2016. Heavy metal pollution from gold mines: environmental effects and bacterial strategies for resistance. *International Journal of Environmental Research and Public Health*. 13(11), 1047. DOI: <https://doi.org/10.3390/ijerph13111047>
- [6] Finkelman, R.B., Orem, W.H., Plumlee, G.S., et al., 2018. Applications of geochemistry to medical geology. *Environmental geochemistry: Site characterization, data analysis and case histories*. Elsevier: Amsterdam. pp. 435-465. DOI: <https://doi.org/10.1016/b978-0-444-63763-5.00018-5>
- [7] Ayuso, R.A., Foley, N.K., 2018. Lead and strontium isotopes as monitors of anthropogenic contaminants in the surficial environment. *Environmental geochemistry: Site characterization, data analysis and case histories*. Elsevier: Amsterdam. pp. 307-362. DOI: <https://doi.org/10.1016/b978-0-444->

- 63763-5.00013-6
- [8] Zarei, I., Pourkhabbaz, A., Khuzestani, R.B., 2014. An assessment of metal contamination risk in sediments of Hara Biosphere Reserve, southern Iran with a focus on application of pollution indicators. *Environmental Monitoring and Assessment*. 186, 6047-6060.
- [9] Kumar, S., Trivedi, P.K., 2016. Heavy metal stress signaling in plants. *Plant metal interaction*. Elsevier: Amsterdam. pp. 585-603.  
DOI: <https://doi.org/10.1016/b978-0-12-803158-2.00025-4>
- [10] Zhang, W., You, M., Hu, Y., 2016. The distribution and accumulation characteristics of heavy metals in soil and plant from Huainan coalfield, China. *Environmental Progress & Sustainable Energy*. 35(4), 1098-1104.  
DOI: <https://doi.org/10.1002/ep.12336>
- [11] Atkinson, C., Jolley, D., Simpson, S., 2007. Effect of over-lying water pH, dissolved oxygen, salinity and sediment disturbances on metal release and sequestration from metal contaminated marine sediments. *Chemosphere*. 69(9), 1428-1437.  
DOI: <https://doi.org/10.1016/j.chemosphere.2007.04.068>
- [12] Salah, E.A., Turki, A.M., Mahal, S.N., 2015. Chemometric evaluation of the heavy metals in urban soil of Fallujah City, Iraq. *Journal of Environmental Protection*. 6, 1279-1292.
- [13] Adewumi, A.J., Laniyan, T.A., 2020. Contamination, sources and risk assessments of metals in media from Anka artisanal gold mining area, Northwest Nigeria. *Science of the Total Environment*. 718(137235), 1-14.
- [14] Atgin, R.S., El-Agha, O., Zararsız, A., et al., 2000. Investigation of the sediment pollution in Izmir Bay: Trace elements. *Spectrochimica Acta Part B*. 55, 1151-1164.  
DOI: [https://doi.org/10.1016/S0584-8547\(00\)00231-7](https://doi.org/10.1016/S0584-8547(00)00231-7)
- [15] Adamu, C.I., Nganje, T.N., Edet, A., 2014. Heavy metal contamination and health risk assessment associated with abandoned barite mines in Cross River State, south-eastern Nigeria. *Environmental Nanotechnology, Monitoring & Management*. 3, 10-21.  
DOI: <http://dx.doi.org/10.1016/j.enmm.2014.11.001>
- [16] Oyebamiji, A., Odebunmi, A., Ruizhong, H., et al., 2018. Assessment of trace metals contamination in stream sediments and soils in Abuja leather mining, southwestern Nigeria. *Acta Geochimica*. 37(4), 592-613.  
DOI: <https://doi.org/10.1007/s11631-017-0256-1>
- [17] Kolawole, T.O., Olatunji, A.S., Jimoh, M.T., et al., 2018. Heavy metal contamination and ecological risk assessment in soils and sediments of an Industrial area in Southwestern Nigeria. *Journal of Health and Pollution*. 8(19), 1-16.
- [18] Boroumandi, M., Khamehchiyan, M., Nikoudel, M.R., et al., 2019. Evaluation of soil pollution sources using multivariate analysis combined with geostatistical methods in Zanjan Basin, Iran. *Geopersia*. 9(2), 293-304.  
DOI: <https://doi.org/10.22059/GEOPE.2019.263512.648406>
- [19] Madukwe, H.Y., Ibigbami, O.A., Obasi, R.A., 2020. Assessment of trace and rare earth element levels in stream sediments in Ijero-Ekiti Area, Southwest Nigeria. *Nature Environment and Pollution Technology*. 19(2), 421-439.
- [20] Aina, A.T., Salau, A.T. (editors), 1992. The challenge of sustainable development in Nigeria. An NGO Report Prepared for the United Nations Conference on Environment and Development; 1992 Jun 1-12; Rio de Janeiro, Brazil. NEST: Nigeria. pp. 16-44.
- [21] Bell, R.G., Rusell, C., 2002. Environmental policy for developing countries. *Issues in Science and Technology*. 18(3), 63-70.
- [22] Okonkwo, S.I., Idakwo, S.O., Ameh, E.G., 2021. Heavy metal contamination and ecological risk assessment of soils around the pegmatite mining sites at Olode area, Ibadan southwestern Nigeria. *Environmental Nanotechnology, Monitoring & Management*. 15, 100424.  
DOI: <https://doi.org/10.1016/j.enmm.2020.100424>
- [23] Egbinola, C.N., Amobichukwu, A.C., 2013. Climate variation assessment based on rainfall and

- temperature in Ibadan, South-Western, Nigeria. *Journal of Environment and Earth Science*. 3(11), 32-45.
- [24] Dulski, P., 2001. Reference materials for geochemical studies: new analytical data by ICP-MS and critical discussion of reference values. *Geostandards Newsletter*. 25(1), 87-125. DOI: <https://doi.org/10.1111/ggr.2001.25.issue-1>
- [25] Brady, J.P., Ayoko, G.A., Martens, W.N., et al., 2015. Development of a hybrid pollution index for heavy metals in marine and estuarine sediments. *Environmental Monitoring and Assessment*. 187(5), 306.
- [26] Qingjie, G., Jun, D., Yunchuan, X., et al., 2008. Calculating pollution indices by heavy metals in ecological geochemistry assessment and a case study in parks of Beijing. *Journal of China University of Geosciences*. 19(3), 230-241. DOI: [https://doi.org/10.1016/S1002-0705\(08\)60042-4](https://doi.org/10.1016/S1002-0705(08)60042-4)
- [27] Hakanson, L., 1980. An ecological risk index for aquatic pollution control a sedimentological approaches. *Water Research*. 14(8), 975-1001. DOI: [https://doi.org/10.1016/0043-1354\(80\)90143-8](https://doi.org/10.1016/0043-1354(80)90143-8)
- [28] Feng, H., Han, X., Zhang, W.G., et al., 2004. A preliminary study of heavy metal contamination in Yangtze River Intertidal Zone Due to urbanization. *Marine Pollution Bulletin*. 49(11-12), 910-915. DOI: <https://doi.org/10.1016/j.marpolbul.2004.06.014>
- [29] Tippie, V.K., 1984. An environmental characterization of Chesapeake Bay and a frame work for action. The estuary as a filter. Academic Press: New York.
- [30] Mmolawa, K., Likuku, A., Gaboutloeloe, G., 2011. Assessment of heavy metal pollution in soils along roadside areas in Botswana. *African Journal of Environmental Science and Technology*. 5(3), 186-196.
- [31] Muller, G., 1969. Index of geoaccumulation in sediments of the Rhine River. *GeoJournal*. 2(3), 108-118.
- [32] Duodu, G.O., Goonetilleke, A., Ayoko, G.A., 2016. Comparison of pollution indices for the assessment of heavy metal in Brisbane River sediment. *Environmental Pollution*. 219, 1077-1091. DOI: <https://doi.org/10.1016/j.envpol.2016.09.008>
- [33] Nemerow, N.L., 1991. Stream, lake, estuary, and ocean pollution. Van Nostrand Reinhold: New York. pp. 472.
- [34] Tomlinson, D., Wilson, J., Harris, C., et al., 1980. Problems in the assessment of heavy-metal levels in estuaries and the formation of a pollution index. *Helgolinder Meeresuntersuchungen*. 33, 566-575.
- [35] Wang, Z., Wang, Y., Chen, L., et al., 2015. Assessment of metal contamination in coastal sediments of the Maluan Bay (China) using geochemical indices and multivariate statistical approaches. *Marine Pollution Bulletin*. 99(1-2), 43-53. DOI: <https://doi.org/10.1016/j.marpolbul.2015.07.064>
- [36] Li, C., Lu, F.Y., Zhang, Y., et al., 2008. Spatial distribution characteristics of heavy metals in street dust in Shenyang city. *Ecology Environment*. 17(2), 560-564.
- [37] Buchauer, M.J., 1973. Contamination of soil and vegetation near a Zinc smelter by Zn, Cd, Cu and Pb. *Environmental Science and Technology*. 7, 131-135.
- [38] Ward, N.E., Brooks, R.R., Reeves, R.D., 1976. Cd, Cu, Pb and Zn in soils, stream sediments, waters around tin mine. *New Zealand Journal of Science*. 19, 81-99.
- [39] Sinex, S., Helz, G., 1981. Regional geochemistry of trace elements in Chesapeak Bay sediments. *Environmental Geology*. 3, 315-323. DOI: <https://doi.org/10.1007/BF02473521>
- [40] Chakravarty, M., Patgiri, A., 2009. Metal pollution assessment in sediments of the Dikrong River, N. E. India. *Journal of Human Ecology*. 27(1), 63-67.

ARTICLE

## Statistical Characteristics of the Temporal Spectrum of Scattered Radiation in the Equatorial Ionosphere

George Jandieri<sup>1</sup> , Nika Tugushi<sup>2\*</sup>

<sup>1</sup> IVSB—Technical University of Ostrava, Ostrava, 70800, Czech Republic

<sup>2</sup> Tbilisi State University, Tbilisi, 0128, Georgia

### ABSTRACT

On the basis of the solution of the space-time characteristic system by the method of geometric optics using symbolic calculations, analytical and numerical simulation of the propagation of the ordinary and extraordinary radio waves in the conducting equatorial ionospheric plasma was made considering the anisotropy of plasma irregularities and non-stationary nature of propagation medium. Broadening of the spectrum and the displacement of its maximum contain velocity of a turbulent plasma flow and parameters characterizing anisotropic plasmonic structures. Statistical moments of both radio waves do not depend on the absorption sign and are valid for both active and absorptive random media. Temporal pulsations and conductivity of a turbulent ionospheric plasma have an influence on the evaluation of the spectrum-varying propagation distances travelling by these waves. The new double-humped effect in the temporal spectrum has been revealed for the ordinary wave varying anisotropy coefficient and dip angle of stretched plasmonic structures. From a theoretical point of view, the algorithms developed in this work allow effective modelling of the propagation of both radio signals in the equatorial conductive ionospheric plasma, considering the external magnetic field, inhomogeneities of electron density in-homogeneities, as well as non-stationary.

**Keywords:** Electromagnetic waves; Turbulence; Statistical characteristics; Waves propagation; Atmosphere; Ionosphere; Conductivity

## 1. Introduction

This paper reports a study of the features of radio

wave propagation in the equatorial ionosphere of the Earth. The relevance of the work is determined by the wide use of decameter and decimeter radio

### \*CORRESPONDING AUTHOR:

Nika Tugushi, Tbilisi State University, Tbilisi, 0128, Georgia; Email: [tugushinika96@gmail.com](mailto:tugushinika96@gmail.com)

### ARTICLE INFO

Received: 2 February 2023 | Revised: 6 March 2023 | Accepted: 13 March 2023 | Published Online: 13 April 2023

DOI: <https://doi.org/10.30564/jees.v5i1.5442>

### CITATION

Jandieri, G., Tugushi, N., 2023. Statistical Characteristics of the Temporal Spectrum of Scattered Radiation in the Equatorial Ionosphere. *Journal of Environmental & Earth Sciences*. 5(1): 85-94. DOI: <https://doi.org/10.30564/jees.v5i1.5442>

### COPYRIGHT

Copyright © 2023 by the author(s). Published by Bilingual Publishing Group. This is an open access article under the Creative Commons Attribution-NonCommercial 4.0 International (CC BY-NC 4.0) License. (<https://creativecommons.org/licenses/by-nc/4.0/>).

waves to provide long-range radio communication, radio navigation, and radar, as well as to study the structure of the Earth's upper atmosphere. It should be noted that, despite numerous studies conducted by Ishimaru, Tatarskii, Gershman and Rytov<sup>[1-4]</sup>, second-order statistical moments of scattered electromagnetic waves in the equatorial anisotropic ionosphere have not yet been studied enough and need both the development of new methods for modeling the propagation of electromagnetic radiation.

The ray theory is the main theoretical tool for describing the propagation of short radio waves in the Earth's equatorial ionosphere. It is based on the integration of stochastic differential equations, which describe the trajectories of rays in an in-homogeneous magnetized plasma. In addition, the calculation of the ray trajectories allows you to calculate the phase and take into account the absorption along the trajectories.

In the study by Jandieri et al.<sup>[5-10]</sup>, peculiarities of the spatial power spectrum (SPS) of radio waves in the polar ionosphere were investigated by applying ray approximation. It has been established that randomly varying electron density and the ambient magnetic field and the anisotropy and dip angle of elongated inhomogeneities relative to the ambient magnetic field may increase the intensity of the frequency fluctuations of propagating radio waves in the terrestrial ionospheric plasma. Multiple scattered effects of waves are revealed more strongly at large scales with slowly varying time irregularities when secondary waves with close frequencies propagate in a narrow spatial angle near the direction of an initial wave.

The equatorial region of the terrestrial ionosphere is of great interest. Plasma bubbles, with a concentration greatly reduced relative to the background, are regularly observed in the equatorial region. These are relatively stable and rather large structures, the transverse size of which can reach hundreds of kilometers. When they rise, they stretch strongly along the magnetic force line, relying on their bases for the maximum of layer F2. The transverse dimension of the bubble measured along the parallel is about 450

km. The concentration inside the bud was reduced by about four times relative to the background. Statistical characteristics of propagating and scattered radio waves in the conductive equatorial ionosphere were not considered till now.

In reality, inhomogeneous media randomly vary both in space and in time. Harmonic waves scattered by the irregularities become nonharmonic. Spectral lines broaden. Generally, the propagation of a wave with a complex spectral structure continuously changes its spectrum. The features of the temporal spectrum in the polar ionosphere have been considered in the study by Jandieri et al.<sup>[11]</sup>.

Important aspects of scattered ordinary (O-wave) and extraordinary (E-wave) radio waves propagating in the equatorial ionosphere, which vary slowly with position and time, are considered using the ray approximation. We will investigate the influence of the absorption on the second-order statistical moments of scattered radio waves in the collision-conductive ionospheric turbulent plasma using the stochastic transfer equation for the complex frequency based on the WKB (Wentzel-Kramers-Brillouin) method. Evaluation of the temporal (broadening and displacement of maximum) contains: the homogeneous external magnetic field, velocity of plasma flow; Hall, Pedersen, and longitudinal conductivities, anisotropy factor of electron density irregularities and the dip angle of prolate plasmonic structures with respect to the geomagnetic lines of forces.

Section 2 considers the ray approximation, spatial-temporal geometric optics (STGO), and ST rays in the equatorial ionospheric plasma. Expression of the complex refractive index of equatorial conducting magnetized plasma is obtained. A stochastic differential transfer equation for complex frequency fluctuation is given, describing the propagation of radio waves in plasma; statistical moments of the temporal spectrum describing scattering features of both ordinary and extraordinary radio waves are investigated. Numerical calculations are presented in Section 3 using the anisotropic spatial-temporal spectrum of electron density inhomogeneities and the velocity of turbulent plasma movement, applying

the experimental data. Some conclusions and discussions are made in Section 4.

## 2. Materials and methods

Asymptotic and integrated methods are traditional instruments for studying radio waves' propagation in random media. Currently, the most developed and justified both theoretically and experimentally method of describing the mechanism of propagation of short (2-40 MHz) electromagnetic waves in the Earth's ionosphere is geometric optics—a method of approximate representation of wave fields in smoothly inhomogeneous media. The field of the monochromatic wave in a medium with a refractive index  $N(\mathbf{r})$  in a scalar approximation is described by the Helmholtz equation which is given by Ishimaru, Tatarskii, Kravtsov et al. <sup>[1,2,12]</sup>.

In the case of ionospheric propagation, the following inequality is usually satisfied:  $l \gg \lambda$  ( $\lambda$  is the wavelength of the wave). This inequality implies that only forward scattering is important in the random scattering process and the WKB solution is valid for the wave propagation. The phase satisfying the eikonal equation for each normal wave can be written as  $c^2 k^2 = \omega^2 N^2(\omega, \mathbf{k}, n)$ , where  $\mathbf{k}(\mathbf{r}, t) = -\nabla\varphi$ ,  $\omega(\mathbf{r}, t) = \partial\varphi / \partial t$  are the local wave vector and the frequency, respectively, are spatial-temporal slowly-varying functions;  $n(\mathbf{r}, t)$  is a fluctuating component of the electron density of a turbulent plasma at the point  $\mathbf{r}$ ;  $N^2(\omega, \mathbf{k})$  is the complex refractive index,  $c$  is the speed of light.

Statistical analysis of a phase and its derivatives applying the WKB method is generally difficult, especially in a non-stationary medium when  $\omega(\mathbf{r}, t)$  is one of an unknown quantity. In quasi-monochromatic small-angle approximation, at smoothness electron density fluctuations  $n(\mathbf{r}, t) = n_0 + n_1(\mathbf{r}, t)$ ,  $|n_1| \ll n_0$ , first term is a homogeneous component, the second one is spatial-temporal stochastic function describing electron density random variations. For complex refractive index  $N(\mathbf{r}, t) = N_0(\mathbf{r}, t) - iN_1(\mathbf{r}, t)$ , we investigate statistical characteristics of the frequency fluctuations of electromagnetic waves propagating and scattering in the equatorial ionosphere. The imaginary

component of the refraction index in inhomogeneous anisotropic conductive plasma within the framework of the ray approximation is connected with a complex wave vector. The real part of this vector is connected with both turbulent plasma inhomogeneity and refraction of waves, whereas the complex part of the inhomogeneous wave ( $\text{Im}\mathbf{k} \neq 0$ ) describes the evolution of inhomogeneous waves including diffraction.

Let the ambient magnetic field is directed along the Y-axis. Components of the complex permittivity tensor in this case are:  $\tilde{\epsilon}_{xx} = \tilde{\epsilon}_{zz} = \epsilon_{\perp} - i(\tilde{\sigma}_{\perp} + sg)$ ,  $\tilde{\epsilon}_{xz} = -s\mathbf{a}\delta + i(\tilde{\sigma}_H + \mathbf{a})$ ,  $\tilde{\epsilon}_{yy} = (\epsilon_{\perp} + p_0u) - i(\tilde{\sigma}_{\parallel} + sv)$ ,  $\tilde{\epsilon}_{xx} = \tilde{\epsilon}_{zz}$ ,  $\tilde{\epsilon}_{zx} = -\tilde{\epsilon}_{xz}$ ,  $\epsilon_{xy} = \epsilon_{yx} = \epsilon_{yz} = \epsilon_{zy} = 0$ ; here:  $p_0 = v / (1-u)$ ,  $g = p_0(1+u) / (1-u)$ ,  $\delta = 2 / (1-u)$ ,  $g_{\parallel} = (3-u) / (1-u)$ ,  $\mathbf{a} = p_0\sqrt{u}$ . Plasma parameters  $v(\mathbf{r}) = \omega_p^2(\mathbf{r}) / \omega^2$  and  $u = (eH_0 / m_e c \omega)^2$  contains the plasma frequency  $\omega_p(\mathbf{r}) = [4\pi N_e(\mathbf{r})e^2 / m_e]^{1/2}$  and the cyclotron frequency. Normalized conductivity tensor  $\tilde{\sigma} = 4\pi\hat{\sigma} / k_0 c$  of ionospheric turbulent plasma for equatorial latitude was given in the study by Aydogdu et al. <sup>[13]</sup> contains the Hall's  $\sigma_H$ , Pedersen  $\sigma_{\perp}$  and longitudinal  $\sigma_{\parallel}$  conductivities:

$$\begin{aligned} \sigma_H &= e^2 n_e \left( \frac{\omega_e}{m_e(v_e^2 + \omega_e^2)} - \frac{\omega_i}{m_i(v_i^2 + \omega_i^2)} \right), \\ \sigma_{\perp} &= e^2 n_e \left( \frac{v_e}{m_e(v_e^2 + \omega_e^2)} + \frac{v_i}{m_i(v_i^2 + \omega_i^2)} \right), \\ \sigma_{\parallel} &= e^2 n_e \left( \frac{1}{m_e v_e} + \frac{1}{m_m v_i} \right) \end{aligned}$$

Here,  $k_0 = \omega_0 / c$ ,  $e$  and  $m_e$  are the charge and mass of an electron,  $v_{e,i}$  is the electron or ion collisional frequency with neutral molecules;  $\omega_e$  and  $\omega_i$  are the angular gyrofrequency of an electron and ion, respectively,  $m_i$  is the mass of ion.

Complex refractive index  $N$  of the conductive collision equatorial ionospheric plasma at  $s \neq 0$ ,  $\tilde{\sigma}_{ij} \neq 0$  and  $s \ll \epsilon_{ij}$ ,  $\tilde{\sigma}_{ij}$  is as follows:

$$N^2(n, \omega) = \Gamma_0(n_0, \omega) + i\Gamma_1(n, \omega), \tag{1}$$

where:  $\Gamma_0 = 1 - 2(T_1 T_0 - T_2 \beta_2) / (T_1^2 + T_2^2)$ ,

$$\Gamma_1 = 2(T_2 T_0 + T_1 \beta_2) / (T_1^2 + T_2^2),$$

$$T_1 = A \pm D_1, T_2 = R_1 \pm D_2, D_1 = \sqrt{(r_1 + B) / 2}, r_1 = \sqrt{B^2 + C^2},$$

$$\begin{aligned}
 D_2 &= \sqrt{(r_1 - B)/2} \\
 T_0 &= p_0 v (1 - v) + \beta_1, \beta_1 = \Lambda_1 (\sin^2 \theta - \varepsilon_{\parallel}) + \tilde{\sigma}_{\parallel} \tilde{\sigma}_{\perp} (1 + \cos^2 \theta - 2\varepsilon_{\perp} \varepsilon_{\parallel}), \\
 C &= \beta_6 - \beta_8, \beta_2 = \tilde{\sigma}_{\perp} \sin^2 \theta + \tilde{\sigma}_{\parallel} \cos^2 \theta - \Lambda_2 + 2\varepsilon_{\parallel} \varepsilon_{\perp} \tilde{\sigma}_{\perp} + \tilde{\sigma}_{\parallel} \\
 &\quad (\varepsilon_{\perp}^2 - \varepsilon^2 - \Lambda_1), \\
 \Lambda_1 &= \tilde{\sigma}_{\perp}^2 + \tilde{\sigma}_H^2 + 2\varepsilon \tilde{\sigma}_H, \beta_3 = \Lambda_1 \sin^2 \theta + \tilde{\sigma}_{\parallel} \tilde{\sigma}_{\perp} (1 + \cos^2 \theta), \\
 a &= 1 - p_0 (1 - u \cos^2 \theta) \Lambda_2 = 2\varepsilon_{\perp} \tilde{\sigma}_{\perp} \sin^2 \theta + (\varepsilon_{\parallel} \tilde{\sigma}_{\perp} + \varepsilon_{\perp} \tilde{\sigma}_{\parallel}) \\
 &\quad (1 + \cos^2 \theta), \\
 c &= (1 - v) [(1 - v)^2 - u] / (1 - u), \\
 b &= [2(1 - v)^2 - 2u + v u (1 + \cos^2 \theta)] (1 - u)^{-1}, A = p_0 [2(1 - v) \\
 &\quad - u \sin^2 \theta], \\
 \beta_4 &= \Lambda_2 - 2(\tilde{\sigma}_{\perp} \sin^2 \theta + \tilde{\sigma}_{\parallel} \cos^2 \theta), \\
 \beta_6 &= 2\Lambda_2 [\Lambda_1 \sin^2 \theta + \tilde{\sigma}_{\parallel} \tilde{\sigma}_{\perp} (1 + \cos^2 \theta) - b], \\
 B &= (\beta_5 - \beta_7) + p_0^2 [u^2 \sin^4 \theta + 4u(1 - v)^2 \cos^2 \theta], \\
 \Lambda_3 &= (\tilde{\sigma}_{\perp} \sin^2 \theta + \tilde{\sigma}_{\parallel} \cos^2 \theta) [2\varepsilon_{\parallel} \varepsilon_{\perp} \tilde{\sigma}_{\perp} + \tilde{\sigma}_{\parallel} (\varepsilon_{\perp}^2 - \varepsilon^2 - \Lambda_1)], \\
 \beta_5 &= \Lambda_1^2 \sin^4 \theta + \tilde{\sigma}_{\parallel}^2 \tilde{\sigma}_{\perp}^2 (1 + \cos^2 \theta)^2 - \Lambda_2^2 - 2b [\Lambda_1 \sin^2 \theta + \tilde{\sigma}_{\parallel} \tilde{\sigma}_{\perp} \\
 &\quad (1 + \cos^2 \theta)] + 2\Lambda_1 \tilde{\sigma}_{\parallel} \tilde{\sigma}_{\perp} \sin^2 \theta \cdot (1 + \cos^2 \theta), \\
 \beta_7 &= 4 [\Lambda_3 + a \varepsilon_{\parallel} (\Lambda_1 + 2\varepsilon_{\perp} \tilde{\sigma}_{\parallel} \tilde{\sigma}_{\perp})], \\
 \beta_8 &= a [2\varepsilon_{\parallel} \varepsilon_{\perp} \tilde{\sigma}_{\perp} + \tilde{\sigma}_{\parallel} (\varepsilon_{\perp}^2 - \varepsilon^2 - \Lambda_1)] + (\tilde{\sigma}_{\perp} \sin^2 \theta + \tilde{\sigma}_{\parallel} \cos^2 \theta) \\
 &\quad [c - \varepsilon_{\parallel} (\Lambda_1 + 2\varepsilon_{\perp} \tilde{\sigma}_{\parallel} \tilde{\sigma}_{\perp})]
 \end{aligned}$$

The upper sign is devoted to the O-wave, lower sign to the E-wave;  $\theta$  is the angle between the wave vector  $\mathbf{k}_0$  and the applied magnetic field  $\mathbf{H}_0$ . The refracting index of the equatorial ionosphere is complex. The absorption is always dissipative and represents a conversion of the wave energy into heat through the collision process. The presence of the geomagnetic field leads to birefringence and anisotropy. For collisionless and nonconductive turbulent plasma we obtain the well-known formula given in the study by Ginzburg et al. <sup>[14]</sup>.

As is well known from the studies of Ishimaru, Tatarskii, Gershman, Rytov et al. <sup>[1-4]</sup>, radio signals propagate in a non-stationary, turbulent plasma, the Doppler shift is small compared with the transmitter frequency, and the spectrum broadens. Quantitative estimation of the frequency fluctuations is important, as the broadening of a spectrum limits the resolution of a Doppler method studying the structure of the receiving signal. On the other hand, by measuring the width of the Doppler spectrum, it is possible to solve

the reversal tasks by receiving information on statistical properties of turbulent plasma. The ratios connecting changes in frequency with the parameters of moving turbulent plasma irregularities make the application of statistical methods as a tool for solving direct and reverse problems of radio wave propagation in a non-stationary turbulent plasma necessary.

Neglecting polarization effects, in the geometrical optics approximation, the frequency of the radio wave satisfies the stochastic differential transport equation which is given in the study by Gavrilenko, Kravtsov et al. <sup>[15,16]</sup> for an arbitrary spatial-temporal dispersion:

$$\left( \frac{\partial}{\partial t} + (\mathbf{u}_{gr} \nabla) \right) \omega = -\frac{\omega u}{c} \sum \frac{\partial N}{\partial p_i} \frac{\partial p_i}{\partial t} \quad (2)$$

where:  $N(\omega, p_i) = ck/\omega$  is the complex refractive index,  $\mathbf{u} = (d\omega/d\mathbf{k})_{p_i}$  is the group velocity of the wave;  $p_i$  is an arbitrary parameter characterizing turbulent plasma. We assume that an incident plane wave propagates in the y direction. The eikonal equation describes virtual ray trajectories, which can be measured experimentally. Ray paths deviate toward an increase in the index of refraction. Radio waves propagating in the lower ionosphere, the ray path deviates towards the Earth; at the propagation of these waves through the upper ionosphere ray path deviates to the opposite direction.

Second-order statistical moment: the variance of the frequency fluctuations of radio signals is one of the important spectral characteristics that can be found by the measurement of random variations of a phase. It describes the broadening of the temporal spectrum in the ionospheric plasma. Applying equation (2) in a first approximation frequency fluctuation satisfies the stochastic transport differential equation:

$$\frac{\partial \omega_1}{\partial y} + \frac{q_0}{c} (1 + i\Lambda_0) \frac{\partial \omega_1}{\partial t} = -k_0 (\Lambda_1 + i\Lambda_2) \frac{\partial n_1}{\partial t}, \quad (3)$$

where:  $q_0 = N_0 + \omega_0 \partial N_0 / \partial \omega$ ,  $\Lambda_0 = \frac{1}{q_0} \left( N_1 + \omega_0 \frac{\partial N_1}{\partial \omega_0} \right)$ ,

$$\Lambda_1 = \frac{\partial N_0}{\partial n_0}, \quad \Lambda_2 = \frac{\partial N_1}{\partial n_0},$$

$$\Lambda_1 = \frac{1}{4N_0} \left[ \left( \frac{\Gamma_0}{r_1} + 1 \right) \frac{\partial \Gamma_0}{\partial n_0} + \frac{1}{r_1} \Gamma_1 \frac{\partial \Gamma_1}{\partial n_0} \right],$$

$$\Lambda_2 = \frac{1}{4N_1} \left[ \left( \frac{\Gamma_0}{r_1} - 1 \right) \frac{\partial \Gamma_0}{\partial n_0} + \frac{1}{r_1} \Gamma_1 \frac{\partial \Gamma_1}{\partial n_0} \right]$$

is the group velocity of an unperturbed wave propagating along the y-axis in a conductive absorptive turbulent ionospheric magnetoplasma. In the anisotropic absorbing turbulent plasma, the direction of group speed and a wave vector cannot coincide. The energy flux of a wave propagating along the ray path at each point coincides with the group velocity  $v_{gr}$ . In the absence of the spatial dispersion, it also coincides with the direction of an average Poynting vector. However, the conductivity of turbulent plasma can lead to the opposite directions of Poynting's vector and a wave vector, and, hence, the group velocity will become negative.

For the solution of equation (3) we will apply the Fourier transform:

$$\omega_1(\mathbf{r}, t) = \int_{-\infty}^{\infty} dv \Omega(\mathbf{r}, v) \exp(ivt) .$$

Let a plasma slab having thickness  $L$  ( $0 < y < L$ ) contains electron density inhomogeneities with the linear scale  $l$ ; a vacuum is at  $y < 0$  and the observation point is located out of a plasma slab  $y > 0$ . We obtain:

$$\Omega(\mathbf{p}_\perp, y, v) = k_0 v (\Lambda_2 - i \Lambda_1) \exp \left[ \frac{v}{c} q_0 (\Lambda_0 - i) y \right] \int_0^L d\zeta n_1(\mathbf{p}_\perp, \zeta, v) \exp \left[ \frac{v}{c} q_0 (-\Lambda_0 + i) \zeta \right], \quad (4)$$

here  $\mathbf{p}_\perp = \{x, z\}$ . Spatial-temporal fluctuations of an instantaneous local frequency are caused by multiple scattering of radio waves propagating in a turbulent ionospheric plasma with a group velocity  $V_{gr} = c(1 - i\Lambda_0)/q_0$ .

Non-stationarity is caused by moving turbulent plasma flow and spatial-temporal variations of electron density fluctuations. Monochromatic waves scattered on the electron density fluctuations become nonmonochromatic. Spectral lines broaden. Generally, waves with a complex spectral structure continuously change the spectrum. The spectrum of the receiving signal broadens and reaches its maximum

during the Doppler shift due to irregularities and temporal fluctuations in electron density.

Statistical characteristics of the frequency fluctuation of radio waves propagating and scattering in a weakly absorptive  $q_0 < 1$  equatorial ionosphere plasma at  $L \gg 1$  can be written as:

$$\Delta_1 = \pi (\Lambda_1^2 + \Lambda_2^2) \frac{c k_0^2}{q_0 \Lambda_0} \int_{-\infty}^{\infty} dv v \int_{-\infty}^{\infty} d\mathbf{k}_\perp W_n(\mathbf{k}_\perp, k_y, v) \left\{ \exp \left( 2 \frac{q_0 \Lambda_0}{c} y v \right) - \exp \left[ 2 \frac{q_0 \Lambda_0}{c} (y - L) v \right] \right\} \exp(i \mathbf{k}_\perp \mathbf{p}_\perp), \quad (5)$$

$$\Delta_2 = \pi k_0^2 L (\Lambda_1^2 - \Lambda_2^2) \int_{-\infty}^{\infty} dv v^2 \int_{-\infty}^{\infty} d\mathbf{k}_\perp W_n(\mathbf{k}_\perp, k_y, v) \exp(i \mathbf{k}_\perp \mathbf{p}_\perp), \quad (6)$$

where the asterisk means complex conjugation,  $\mathbf{k}_\perp = (k_x, k_z)$ .

$$W_n(\mathbf{k}_\perp, k_y, v) = \frac{1}{(2\pi)^4} \int_{-\infty}^{\infty} d\mathbf{p}_\perp \int_{-\infty}^{\infty} d\rho_y \int_{-\infty}^{\infty} d\tau V_n(\rho_\perp, \rho_y, \tau) \exp(i \mathbf{k}_\perp \mathbf{p}_\perp + i k_y \rho_y - i v \tau)$$

is an arbitrary spatial-temporal autocorrelation function of electron density fluctuations,  $k_y = v q_0 / c$ . Temporal spectrum is calculated by the formula:

$$\Delta = \Delta_1 + \Delta_2, \quad (7)$$

Broadening of the temporal power spectrum  $\Delta \equiv \langle \omega^2 \rangle / \omega_0^2$  is an experimentally measurable parameter;  $\Delta_1 \equiv \langle \omega_1 \omega_1^* \rangle / 2\omega_0^2$ ,  $\Delta_2 \equiv \text{Re} \langle \omega_1 \omega_1 \rangle / 2\omega_0^2$ ; the pointed brackets indicate the ensemble average. Coherency impairment of the field of the receiving signal caused by phase fluctuations in the ionospheric plasma with large-scale inhomogeneities allows us to suggest that variance of the frequency fluctuations  $\langle \omega_1^2 \rangle$  is also applicable at diffraction. At strong absorption the second term of equation (6) is much less than the first one.

Diffraction effects have a substantial influence on this second-order statistical moment only in Fraunhofer's zone  $(y / k_0 l^2) \gg 1$ .

This means that radio waves scattered under a big angle attenuate faster along the y axis.

### 3. Results

Experimental measurements of artificial large-scale electron density inhomogeneities generation in the ionospheric  $F_2$  region by ‘‘SURA’’ heating facility by powerful radio waves were given in the study by Frolov et al. [17]. Transverse scale of these irregularities  $l_{\perp}$  varies from a few meters up to tens of a hundred kilometers. Large-scale turbulent plasma irregularities along the sight beam on the satellite can have the sizes  $l_{\parallel} = 30$  km, the drift velocity  $30 \pm 35$  m/s.

Observations of drift small-scale field-aligned inhomogeneities in the F ionosphere have shown in the study by Kvavadze et al. [18] that they have elongated shape, anisotropy factor varies from 1 to 3 moving with the drift velocity 40-100 meter/sec S-W direction. Small-scale irregularities with Gaussian spectrum are responsible for polarization fluctuations at the frequency band of 20-50 MHz.

Experimental measurements at Kingston, Jamaica show that field-aligned electron density inhomogeneities in the F-ionosphere are existing between altitudes 153 km and 617 km. Defiant scintillations of signals from the moving earth satellites were given in the study by Chen et al. [19]. Dip angle of these inhomogeneities relative to the ambient magnetic field was about  $16^{\circ}$ . Electron density irregularities are described by anisotropic Gaussian and power-law spectral functions. For F region large-scale sizes irregularities ( $\sim 10$  km) become unstable, and dissipate their energy by generating small-sized irregularities, as is the case in turbulence. In the equatorial region the large-scale irregularities are most likely produced by a convective electric field.

Analytical calculations are carried out using a spatial-temporal spectral function of electron density irregularities given in the study by Jandieri et al. [20]:

$$V_n(\mathbf{k}, \nu) = \frac{\sigma_n^2}{16\pi^2} \frac{l_{\parallel}^3}{\chi^2 \left\{ 1 + l_{\perp}^2 \left[ k_x^2 + (\nu q_0 / c)^2 \right] + l_{\parallel}^2 k_z^2 \right\}^2} \cdot \exp \left( -\frac{k_x^2 l_{\perp}^2}{4} - m_0^2 \frac{k_y^2 l_{\parallel}^2}{4} - m_1 \frac{k_z l_{\parallel}}{4} \nu T - m_2 \frac{\nu^2 T^2}{4} \right), \quad (8)$$

where:  $m_0^2 = a_0 - 1 / (p_2 \chi^2)$ ,  $a_0 = (\Upsilon_1^2 / a_1) + p_2 (\Upsilon_2^2 / \Upsilon_0^2)$

$$\begin{aligned} a_0 &= (\Upsilon_1^2 / a_1) + p_2 (\Upsilon_2^2 / \Upsilon_0^2), \quad p_2 = (\sin^2 \gamma_0 + \chi^2 \cos^2 \gamma_0) / \chi^2, \\ a_1 &= 1 + \zeta^2 (l_* / l_{\perp})^2, \quad m_2 = c_0 + p_2 q_0^2 \zeta_0^2 / \Upsilon_0^2, \\ l_* &= l_{\perp} l_{\parallel} (l_{\perp}^2 \sin^2 \gamma_0 + l_{\parallel}^2 \cos^2 \gamma_0)^{-1/2}, \quad \zeta = V_0 T / l_{\parallel}, \\ \Upsilon_0 &= [1 - \zeta / (2a_1)]^{1/2}, \quad c_0 = (1 / a_1) + p_2 \Upsilon_3^2 / \Upsilon_0^2, \\ \Upsilon_1 &= (\chi^2 - 1) \zeta \sin \gamma_0 \cos \gamma_0 / \chi^2 p_2, \quad \Upsilon_3 = \zeta / (a_1 p_2), \\ m_1 &= b_0 + p_2 \Upsilon_2 \zeta_0 q_0 / \Upsilon_0^2, \quad b_0 = (\Upsilon_1 / a_1) - p_2 \Upsilon_2 \Upsilon_3 / \Upsilon_0^2, \\ \zeta_0 &= (l_{\parallel} / cT), \quad \Upsilon_2 = (\chi^2 - 1) \sin \gamma_0 \cos \gamma_0 / (\sin^2 \gamma_0 + \chi^2 \cos^2 \gamma_0) - (\zeta \Upsilon_1 / a_1 p_2). \end{aligned}$$

Diffusion processes in the ionosphere along and across directions relative to the external magnetic field lead to the anisotropy of elongated plasmonic structures. These inhomogeneities can be characterized by two anisotropy parameters: Anisotropy coefficient  $\chi = l_{\parallel} / l_{\perp}$ , which is the ratio of characteristic linear scales along and across the ambient magnetic field; and inclination angle  $\gamma_0$  of electron density irregularities relative to the lines of forces of geomagnetic field;  $T = l / V$  is the characteristic temporal scale of electron density fluctuations,  $\nu_0 = 1 / T$  is the frequency of the ionospheric irregularities. Drift velocity exceeds the velocity of the shape changes of the inhomogeneities themselves. If  $V_0 = 0$  we obtain studies given by Jandieri et al. [8-10,20].

Substituting (8) into equations (5) and (6) we obtain the broadening of the temporal spectrum of scattered ordinary and extraordinary waves in the equatorial ionosphere:

$$\Delta_1 \approx \frac{\xi^2}{\chi} \frac{L}{l_{\parallel}} \left( \frac{\nu_0}{\omega_0} \right)^2 \frac{\sqrt{p_2} (\Lambda_1^2 + \Lambda_2^2)}{a_1 \Upsilon_0 t_0 \delta_1^3} \left\{ \frac{y}{L} - \left( \frac{y}{L} - 1 \right) \cdot \exp \left[ -4 \frac{\Lambda_0^2 q_0^2}{\delta_1^2} \zeta^2 \left( \frac{L}{l_{\parallel}} \right)^2 \left( 2 \frac{y}{L} - 1 \right) \right] \right\} \quad (9)$$

$$\begin{aligned} & \cdot \left[ 1 + 4 m_2 \left( \frac{\delta_2}{\delta_1} \right)^2 \right]^{-2} \exp \left[ 4 \frac{\Lambda_0^2 q_0^2}{\delta_1^2} \zeta^2 \left( \frac{y}{L} \right)^2 \left( \frac{L}{l_{\parallel}} \right)^2 \right], \\ \Delta_2 & \approx \frac{\xi^2 \delta_2^2}{\chi} \frac{L}{l_{\parallel}} \left( \frac{\nu_0}{\omega_0} \right)^2 \frac{\sqrt{p_2} (\Lambda_1^2 - \Lambda_2^2)}{a_1 \Upsilon_0 t_0 \delta_1^5} \left[ 1 + 4 m_2 \left( \frac{\delta_2}{\delta_1} \right)^2 \right]^{-2} \exp \left( \frac{\delta_2^2}{\delta_1^2} \right), \quad (10) \end{aligned}$$

where:  $\delta_1 = [n_2 - (n_1^2 / n_0^2)]^{1/2}$ ,  $\delta_2 = 2 q_0 \zeta^2 \Lambda_0 (L / l_{||}) [1 - (y / L)]$ ,  $m_2 = (n_1^2 / n_0^4) + \zeta^2 (q_0^2 / \chi^2)$ ,  $L$  is slab thickness.

Analyses show that frequency fluctuations grow faster than in nonabsorbing medium given in the studies by Gavrilenko, Kravtsov et al. [15,16] if distance travelling by wave in the turbulent plasma exceeds the distance of weak attenuation even at  $y > L$ .

It is essential to emphasize that second-order statistical moment (9) does not depend on a sign of the parameter  $\psi_0$ . So, the obtained result is valid for both absorbing, and active media. The reason for this effect is that, frequency perturbations in a medium with complex refractive index not only are transferred along  $Y$  axes with a group velocity given in the study by Kravtsov et al. [16], but also amplify. A similar effect can take place for an incident frequency-modulated wave in a homogeneous medium with a complex refractive index. The modulator in our case is a turbulent plasma layer.

**Figures 1 and 2** illustrate ray trajectories of radio wave propagation in the turbulent anisotropic, inhomogeneous, non-stationary ionospheric plasma. Two groups of curves are highlighted. For higher frequencies propagating through the ionosphere, absorption is low. Lower frequencies are reflected from the layer. The characteristic maximum on curves is the reflection point. These rays spend a lot of time in the lower ionosphere and test active absorption. Absorption increases inversely in proportion to the frequency. Comparing the figures extraordinary wave is absorbed more than the ordinary one.

**Figure 3** illustrates the behavior of the spectrum for different anisotropy factor. Analyses show that varying anisotropic parameters in the interval  $3 \leq \chi \leq 18$  maximum, spectrum broadening increases and its maximum shifts to the left.

Curves describing the broadening of the temporal spectrum of O-wave scattered in the turbulent ionospheric plasma at an anisotropy factor  $\chi = 3$  varying distance  $0 \leq (y / L) \leq 10.5$  are plotted in **Figure 4**. Numerical calculations show that at  $\gamma_0 = 17^0$  two

humps arise; broadening of the first hump is very small. At  $\gamma_0 = 19^0$  these humps have the same widths. Increasing the inclination angle up to  $\gamma_0 = 21^0$  the second hump is disappeared. The same behavior of the curves is observed at  $\chi = 6$ , but the broadening of a second curve becomes substantially small at  $\gamma_0 = 9$ . Precursor in the temporal spectrum does not arise for E-wave.

Numerical calculations show that the broadening of the temporal spectrum of both O- and E-waves increases in proportion to the temporal parameter  $v_0 / \omega_0$  and the distance propagating by radio waves in the equatorial ionosphere.

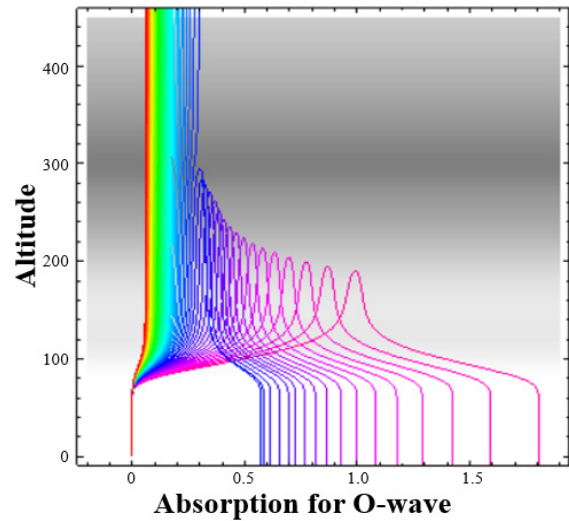


Figure 1. Altitude-absorption diagram for O-wave.

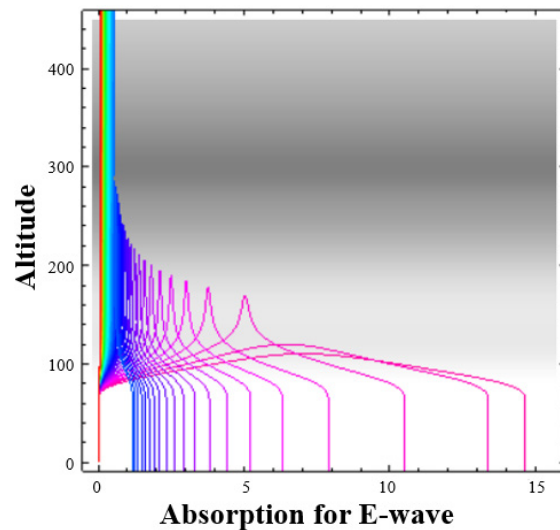
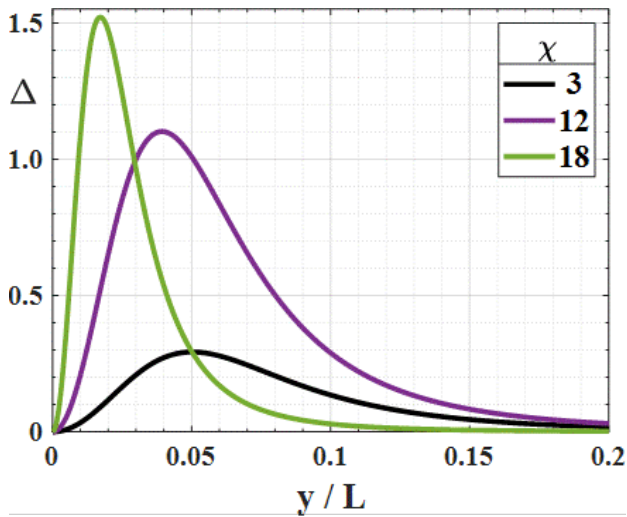
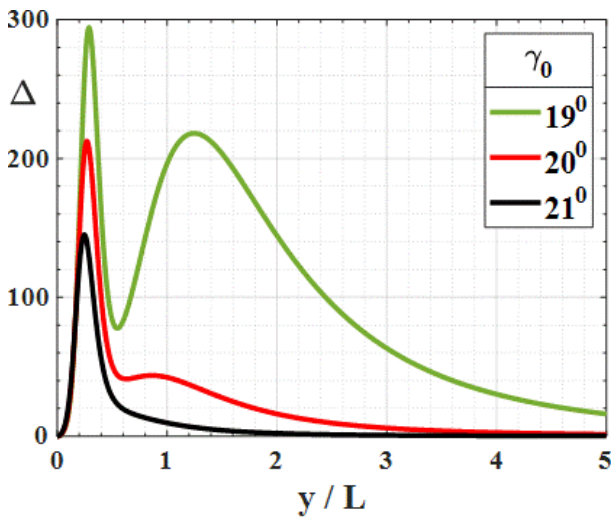


Figure 2. Altitude-absorption diagram for E-wave.



**Figure 3.**  $\Delta - y/L$  diagram showing spectrum broadening for different anisotropy factor.



**Figure 4.**  $\Delta - y/L$  diagram showing evaluation of the spectrum at different inclination angle of O-wave.

#### 4. Discussion

When constructing a uniform asymptotic theory describing the processes of propagation and diffraction of electromagnetic waves (for example, radio pulses) in inhomogeneous anisotropic media in a short-wave approximation, geometric optics is the traditional method. Mathematical modeling of the features of the propagation of radio waves in the ionospheric plasma in the decameter range was carried out, taking into account artificial and natural inhomogeneities.

The refractive index, one of the important parameters characterizing the equatorial ionosphere, has been derived for the first time. Second-order statistical moments of the temporal spectrum (broadening and displacement) of scattered ordinary and extraordinary radio waves propagating and scattering in the conductive turbulent plasma are investigated in the geometrical optics approximation.

Second-order statistical moments of the temporal spectrum: Correlation function and variance of the frequency fluctuations describing the broadening and shift of its maximum have been obtained for the arbitrary autocorrelation function of electron density fluctuations.

Numerical modeling was carried out for the spatial-temporal spectrum of electron density fluctuations containing anisotropic parameters characterizing turbulent ionospheric turbulent plasma: turbulent plasma velocity, anisotropy coefficient, and dip angle of stretched plasmonic structures relative to the lines of forces of the geomagnetic field. Investigations show that the anisotropy coefficient and dip angle of electron density inhomogeneities have a substantial influence on the broadening of the temporal power spectrum and the displacement of its maximum in scattered O- and E-waves in the equatorial ionosphere. A new double-humped effect has been revealed in the temporal spectrum of scattered O-waves in the equatorial ionosphere, contrary to the polar ionosphere. Diffraction effects have a substantial influence on the variance of the frequency fluctuations in the nonstationary turbulent plasma at longitudinal propagation, when the absorption is essential.

The relevance of the problem of studying the propagation of electromagnetic waves in the upper atmosphere is determined by the need to solve the problems of long-distance radio communication, radio navigation, radar location, as well as the problems of diagnosing the structure of the ionosphere propagation medium and also studying of the structure of an ionosphere—the upper atmosphere of Earth by methods of remote sensing and a radio tomography. Measurements of the statistical characteristics of scattered electromagnetic waves by satellite,

ground-based radar systems, or meteorological-ionospheric stations give information about ionospheric turbulent plasma irregularities. Relevance of research is defined by the active use of electromagnetic waves of a short-wave band in the antenna equipment, for providing long-distance radio communication, radio navigation, a radar location, and also studying of the structure of an ionosphere—the upper atmosphere of Earth by methods of remote sensing and a radio tomography.

## Conflict of Interest

There is no conflict of interest.

## Acknowledgment

This work was supported by Shota Rustaveli National Science Foundation of Georgia (SRNSFG), grant NFR-21-316 “Investigation of the statistical characteristics of scattered electromagnetic waves in the terrestrial atmosphere and application”.

## References

- [1] Ishimaru, A., 1997. Wave propagation and scattering in random media, Vol. 2. Academic Press: New York.
- [2] Tatarskii, V.I., 1967. Wave propagation in a turbulent medium. Dover: New York.
- [3] Гершман, Б.Н., Ерухимов, Л.М., Яшин, Ю.Я., 1984. Волновые процессы в ионосфере и космической плазме (Russian) [Wave phenomena in the Ionosphere and Space Plasma]. Nauka: Moscow.
- [4] Rytov, S.M., Kravtsov, Y.A., Tatarskii, V.I., 1989. Principles of statistical radiophysics: Wave propagation through random media, Vol. 4. Springer: Berlin.
- [5] Jandieri, G., Ishimaru, A., Rawat, B., et al., 2018. Statistical moments and scintillation level of scattered electromagnetic waves in the magnetized plasma. *Advanced Electromagnetics*. 7(3), 1-10.
- [6] Jandieri, G., Ishimaru, A., Rawat, B., 2015. Peculiarities of the spatial power spectrum of scattered electromagnetic waves in the turbulent collision magnetized plasma. *Progress in Electromagnetics Research*. 152, 137-149.
- [7] Jandieri, G., Zhukova, N., Jandieri, I., 2012. Statistical characteristics of scattered radiation in medium with spatial-temporal fluctuations of electron density and external magnetic field. *Journal of Electromagnetic Analysis and Application*. 4, 243-251.
- [8] Jandieri, G., Ishimaru, A., Jandieri, V., et al., 2007. Model computations of angular power spectra for anisotropic absorptive turbulent magnetized plasma. *Progress in Electromagnetics Research*. 70, 307-328.
- [9] Jandieri, G., 2016. Double-humped effect in the turbulent magnetized plasma. *Progress in Electromagnetics Research*. 48, 95-102.
- [10] Jandieri, G., Diasamidze, M., Takidze, I., et al. (editors), 2016. Second order statistical moments of the phase fluctuations of scattered radiation in the collision magnetized plasma. *The 2016 World Congress in Computer Science, Computer Engineering and Applied Computing*; 2016 Oct 19-21; San Francisco. p. 190-194.
- [11] Jandieri, G., Ishimaru, A., Rawat, B., et al., 2022. Temporal spectrum of scattered electromagnetic waves in the conductive collision turbulent magnetized plasma. *Advanced Electromagnetics*. 11(1), 1-8.
- [12] Кравцов, Ю.А., Орлов, Ю.И., 1980. Геометрическая оптика неоднородных сред (Russian) [Geometrical optics of Inhomogeneous Media]. Nauka: Moscow.
- [13] Aydogdu, M., Guzel, E., Yesil, A., et al., Comparison of the calculated absorption and the measured field strength of HF waves reflected from the ionosphere. *Nuovo Cimento*. 30(3), 243-253.
- [14] Ginzburg, V.L., Sadowski, W.L., Gallik, D.M., et al., 1961. Propagation of electromagnetic waves in plasma. Gordon and Beach: New York.
- [15] Gavrilenko, V.G., Stepanov, N.S., 1987. Statistical characteristics of waves in the chaotically

- media with spatial-temporal irregularities. *Radio-physics and Quantum Electronics*. 30(1), 1-29.
- [16] Kravtsov, Y.A., Ostrovsky, L.A., Stepanov, N.S., 1974. Geometrical optics of inhomogeneous and nonstationary dispersive media. *Proceedings of the IEEE*. 62(11), 1492-1510.
- [17] Frolov, V.L., Shorokhova, E.A., Kunitsyn, V.E., et al., 2015. Peculiarities of excitation of large-scale plasma density irregularities HF-induced by modification of the ionospheric region. *Izvestia VUZ-ov Radiophysics*. 58(10), 797-810.
- [18] Kvavadze, N.D., Liadze, Z.L., Mosashvili, N.V., et al., 1988. The phenomenon of F-scattering and drift of small-scale irregularities at night low latitudes F-region of an ionosphere. *Geomagnetism and Aeronomy*. 28(1), 139-141.
- [19] Chen, A.A., Kent, G.S., 1972. Determination of the orientation of ionospheric irregularities causing scintillation of signals from earth satellites. *Journal of Atmospheric and Terrestrial Physics*. 34(8), 1411-1414.
- [20] Jandieri, G.V., Ishimaru, A., Rawat. B., et al., 2017. Power spectra of ionospheric scintillations. *Advanced Electromagnetics*. 6(4), 42-51.

ARTICLE

## Landfill Site Suitability Assessment Using Geographic Information System (GIS) and Analytic Hierarchy Process (AHP) in Butuan City, Philippines

Francis Jhun T. Macalam<sup>1\*</sup>, Kaleb P. Arreza<sup>2</sup>, Angelica T. Magpantay<sup>3</sup>, Kristine Y. Rabaño<sup>4</sup>

<sup>1</sup> Department of Environmental Science and Technology, College of Science and Mathematics, University of Science and Technology of Southern Philippines, Cagayan de Oro Campus, 9000, Philippines

<sup>2</sup> Department of Environmental Science, College of Forestry and Environmental Studies, Mindanao State University, 9023, Philippines

<sup>3</sup> Interdisciplinary Studies Center for Integrated Natural Resources and Environment Management, College of Forestry and Natural Resources, University of the Philippines Los Baños, Laguna, 4031, Philippines

<sup>4</sup> School of Environmental Science and Management, University of the Philippines Los Baños, Laguna, 4031, Philippines

### ABSTRACT

Landfilling is one of the most effective and responsible ways to dispose of municipal solid waste (MSW). Identifying landfill sites, however, is a challenging and complex undertaking because it depends on social, environmental, technical, economic, and legal issues. This study aims to map the optimal sites that were environmentally suitable for locating a landfill site in Butuan City, Philippines. With reference to the policy requirements from DENR Section I, Landfill Site Identification Criteria and Screening Guidelines of National Solid Waste Management Commission, the integration of a Geographic Information System (GIS) model builder and Analytical Hierarchy Process (AHP) has been used in this study to address the aforementioned challenges related to the landfill site suitability analysis. Based on the generated sanitary landfill suitability map, results showed that Barangay Tungao (1131.42967 ha) and Florida (518.48 ha) were able to meet and consider the three (3) main components, namely economic, environmental, and physical criteria, and are highly suitable as landfill site locations in Butuan City. It is recommended that there will conduct a geotechnical evaluation, involving rigorous geological and hydrogeological assessment employing a combination of site investigation and laboratory techniques. In addition, additional specific social, ecological, climatic, and economic factors need to be considered (i.e. including impact on humans, flora, fauna, soil, water, air, climate, and landscape).

**Keywords:** Geographic information system; Sanitary landfill; Analytic hierarchy process; Butuan City; Site suitability

#### \*CORRESPONDING AUTHOR:

Francis Jhun T. Macalam, Department of Environmental Science and Technology, College of Science and Mathematics, University of Science and Technology of Southern Philippines, Cagayan de Oro Campus, 9000, Philippines; Email: francis061593@gmail.com

#### ARTICLE INFO

Received: 2 January 2023 | Revised: 16 April 2023 | Accepted: 18 April 2023 | Published Online: 23 April 2023

DOI: <https://doi.org/10.30564/jees.v5i1.5381>

#### CITATION

Macalam, F.J.T., Arreza, K.P., Magpantay, A.T., et al., 2023. Landfill Site Suitability Assessment Using Geographic Information System (GIS) and Analytic Hierarchy Process (AHP) in Butuan City, Philippines. *Journal of Environmental & Earth Sciences*. 5(1): 95-107. DOI: <https://doi.org/10.30564/jees.v5i1.5381>

#### COPYRIGHT

Copyright © 2023 by the author(s). Published by Bilingual Publishing Group. This is an open access article under the Creative Commons Attribution-NonCommercial 4.0 International (CC BY-NC 4.0) License. (<https://creativecommons.org/licenses/by-nc/4.0/>).

## 1. Introduction

Landfill site suitability assessment is a crucial task in solid waste management, as it involves identifying the most suitable location for a landfill site. The process involves considering various factors such as topography, geology, hydrology, and land use, among others. The use of Geographic Information Systems (GIS) and the Analytic Hierarchy Process (AHP) has gained significant popularity in recent years in the assessment of landfill site suitability. GIS is a powerful tool that allows for the visualization, analysis, and interpretation of spatial data, while AHP is a decision-making technique that facilitates the prioritization of different factors based on their relative importance.

Several studies have been conducted on landfill site suitability assessment using GIS and AHP. For instance, in a study by Li et al. <sup>[1]</sup>, the authors used GIS and AHP to assess landfill site suitability in a rural area of China. The study identified various factors that were crucial in the selection of a suitable landfill site, including topography, distance to settlements, and distance to water sources. The results of the study indicated that GIS and AHP are effective tools for landfill site suitability assessment. In another study by Mohammadi et al. <sup>[2]</sup>, the authors used GIS and AHP to assess landfill site suitability in Iran. The study identified various factors that were crucial in the selection of a suitable landfill site, including distance to transportation routes, distance to settlements, and soil type. The study concluded that the use of GIS and AHP is an effective approach to landfill site suitability assessment.

Numerous studies have demonstrated the efficacy of using GIS and AHP for landfill site suitability assessment. For example, Abbas and Ahamad <sup>[3]</sup> used GIS and AHP to assess landfill site suitability in India. The study identified several factors that played a significant role in the selection of a suitable landfill site, including land use, distance to settlements, and slope. The authors concluded that GIS and AHP are effective tools for landfill site suitability assessment.

In a study by Villanueva et al. <sup>[4]</sup>, they used multi-criteria decision-making (MCDM) approach to

evaluate and rank potential landfill sites in the municipality of San Nicolas, Pangasinan, Philippines. The study identified suitable landfill sites based on several criteria, including distance from residential areas, distance from water bodies, and accessibility to transportation routes. The results of the study can assist local decision-makers in identifying suitable landfill sites in accordance with the guidelines set forth by Republic Act 9003: Ecological Solid Waste Management Act of 2000 <sup>[5]</sup>. The study highlights the importance of proper waste management in ensuring environmental sustainability and public health.

As Butuan City in the Philippines has become one of the most heavily populated cities in the country, there is a need for the consequent wastes generated to be properly disposed of and catered to that will prevent its possible negative impacts on the people and the environment. This leads to an area meeting certain criteria for it to be the proposed area for building a sanitary landfill. Because of this, the city will benefit from this research by achieving sustainable landfill standards that are acceptable to the surrounding community and environmentally responsive.

Generally, the study aims to map the optimal sites that were environmentally suitable for locating a landfill site in Butuan City, Philippines. Specifically, it aims to identify a set of criteria for siting sanitary landfill and utilize the analytic hierarchy process (AHP) in providing weights for the identified criteria by generating a landfill suitability map based on the identified criteria and its corresponding weights using a Geographic Information System (GIS) in Butuan City, Philippines.

## 2. Methodology

### 2.1 Study area

Butuan City (8°57'N 125°32'E) is the 1st District of Agusan del Norte (**Figure 1**). Its total population according to the 2015 census is 337,063 with a density of 410/km<sup>2</sup>. It is considered to be a 1st city income class and was declared as a highly urbanized city on February 7, 1995. It has a land area of 816.62

km<sup>2</sup> (315.30 sq mi) approximately considered to be 4.1% of the total area of the Caraga region covering 86 barangays which are categorized into 27 Urban and 59 Rural. Its land use involves agriculture area (397.23 km<sup>2</sup>), forestland (268 km<sup>2</sup>), grass/shrub/pasture land (61.14 km<sup>2</sup>), and other uses (90.242 km<sup>2</sup>). Production forest and protection forest areas cover 105 km<sup>2</sup> and 167.5 km<sup>2</sup> of the total forestland. Butuan City has a tropical rainforest climate, which is characterized by high temperatures and abundant rainfall throughout the year. The city experiences two distinct seasons: The wet season, which usually lasts from May to November, and the dry season, which usually lasts from December to April. During the wet season, Butuan City receives an average of 300 to 400 millimeters of rainfall per month. The heaviest rainfall usually occurs in October and November. The high humidity and rainfall during this season can sometimes lead to flooding in low-lying areas. During the dry season, the city experiences warm and dry weather, with temperatures averaging around 28 to 32 degrees Celsius during the day and around 22 to 24 degrees Celsius at night. The dry season is also characterized by occasional thunder-

storms and occasional brief rainfall. Overall, Butuan City has a warm and humid climate throughout the year, with temperatures averaging around 26 to 28 degrees Celsius.

## 2.2 Data collection

A total of twelve (12) data sets were gathered and processed from various sources in the conduct of the study. **Table 1** lists the inventory of the data requirements with their corresponding sources. First, distance from urban areas was generated using the population per barangay data from Philippine Statistics Authority (PSA) census in 2010 [6] by identifying the urban areas following the condition set by the aforementioned agency. According to PSA, a barangay is considered urban if its population reaches 500 and above per square kilometer. Second, the slope was generated from a 30-meter resolution ASTER DEM data downloaded from the USGS Earth Explorer [7]. Third, road network distance from settlements data was generated from the OpenStreetMap [8] to identify the distance between the road and settlement areas. Fourth, the surface water or stream network data were digitized from the 1:250,000 topographic

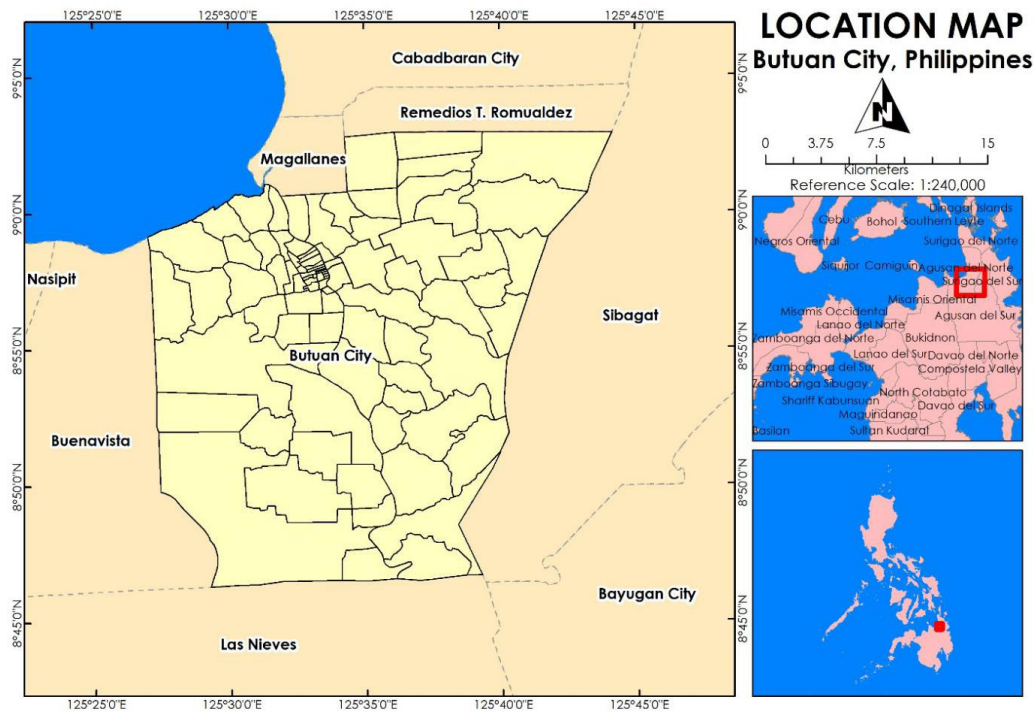


Figure 1. Location map of Butuan City, Philippines.

maps of NAMRIA <sup>[9]</sup> and land cover maps. Fifth, groundwater point source coordinates were gathered from the Philippine Groundwater Data Bank <sup>[10]</sup> and were then converted into shapefile. Identification of cultural sites using Google Earth <sup>[11]</sup> to locate sites in those areas with cultural importance. Other data were just downloaded, projected, and then clipped to the administrative boundary of Butuan City in the Geoportal PH <sup>[12]</sup>, LiPAD Portal <sup>[13]</sup>, DA-BSWM <sup>[14]</sup>, and DOST-PHIVOLCS <sup>[15]</sup>.

### 2.3 Landfill site selection criteria

After conducting a review of relevant literature, establishing a hierarchy of criteria and sub-criteria is a crucial step in any land suitability analysis. The selection of criteria and sub-criteria depends on the study’s objectives and scope based on the study by Ali et al. <sup>[15]</sup>. Moreover, **Table 2** shows the hierarchy of criteria and sub-criteria consisting of three primary criteria, namely economic, environmental, and physical, along with twelve sub-criteria described in a study by Kara and Doratli <sup>[16]</sup>.

This broad classification will each include various criteria that are necessary for the determination of

the optimal site for a landfill. A detailed list of factors with their scale classification is provided in **Table 2**. The classification was revised for it to be tailor-fitted to local conditions, especially with the policies. The policy guidelines were taken from Section I. Landfill Site Identification Criteria and Screening Guidelines of NSWMC Resolution No. 64, Series of 2013.

### 2.4 Analytic hierarchy process

The Analytical Hierarchy Process (AHP) is a powerful tool that helps decision-makers tackle complex decision-making challenges by assisting them in prioritizing options to arrive at the best decision. On the other hand, the Multi-Criteria Decision Analysis (MCDA) method supports the framework, design, evaluation, and prioritization of alternatives in decision problems. Among the different decision-making techniques used by both decision-makers and researchers, the Analytical Hierarchy Process is one of the most frequently utilized techniques by Sari et al. <sup>[18]</sup>

Moreover, it generates a weight for each criterion according to the decision maker’s pairwise comparison of the criteria. For a fixed criterion, the AHP as-

**Table 1.** List of all the data requirements and their sources for landfill suitability mapping.

Main Criteria	Criteria	Dataset Requirement	Data Source
Economic	Distance from urban areas	Population Density per barangay	PSA (Census 2010) <sup>[6]</sup>
	Slope	ASTER DEM (30 m resolution)	USGS Earth Explorer <sup>[7]</sup>
	Distance from roads	Road Network	OpenStreetMap (as of June 2020) <sup>[8]</sup>
Environmental	Distance from surface waters	Digitized stream network from NAMRIA topographic maps	NAMRIA <sup>[9]</sup>
	Distance from groundwaters	Groundwater point sources	Philippine Groundwater Data Bank <sup>[10]</sup>
	Distance from environmentally sensitive areas	Taguibo watershed (listed in critical watersheds in the Philippines)	Geoportal PH <sup>[12]</sup>
	Land Cover	Land cover map	NAMRIA (2010) <sup>[8]</sup>
	Flood Susceptibility	Flood Susceptibility map (25-year return period)	LiPAD Portal <sup>[13]</sup>
	Soil permeability	Soil types	DA-BSWM <sup>[14]</sup>
Physical	Distance from settlements	Building dataset	OpenStreetMap (as of June 2020) <sup>[8]</sup>
	Distance from cultural heritage	POIs of cultural sites	Google Earth <sup>[11]</sup>
	Distance to Faults (Seismic Conditions)	Active Faults	DOST PHIVOLCS <sup>[15]</sup>

Source: <sup>[16]</sup>.

**Table 2.** Identified landfill site selection criteria with policies/considerations, exclusionary zones and sub-criterion zones for Butuan City, Philippines.

Main Criteria	Criteria	Policies / Considerations	Exclusionary Zones	Sub-criterion zones	Suitability Classification
Economic	Distance from urban areas	Urban Areas are those areas with at least 500 persons per square kilometer (PSA)	-	0-10 km 10-25 km 25-50 km > 50 km	Low Moderate High Very High
	Distance from roads	The site shall be accessible from major roadways and thoroughfares provided that if it is not accessible the project design shall include means of access.	100 m from the main roads	100-250 m 250-500 m 500-750 m > 750 m	Low Moderate High Very High
	Slope	Ideally, the site has a gently sloped topography. Areas above 18% slope should be avoided. The slope is classified according to the DENR-LMB classification.	Areas with above 18%	0-8% 8-18% 18-30% 30-50%	Very High High Moderate Low
Environmental	Distance from surface waters	The site shall not be located within 300 meters of watershed areas or upgradient (point of intake) of any surface waters used for public or private drinking water supply irrigation or livestock.	300 m from surface waters	300-1000 m 1000-1500 m 1500-2000 m 2000-2500 m > 2500 m	Low Moderate High Very High Very High
	Distance from groundwaters	The site shall not be located on shallow unconfined aquifers. Areas in or within 500 meters up a gradient of groundwater reservoir or water supply intakes used for private or public drinking irrigation or livestock shall also be excluded.	500 m from aquifers	500-1000 m 1000-1500 m 1500-2000 m 2000-2500 m > 2500 m	Low Moderate High Very High Very High
	Distance from environmentally sensitive areas	The site shall not be located within 500 meters of the boundaries of ecologically sensitive areas proclaimed as protected areas under the National Integrated Protected Areas System (NIPAS) Act.	500 m from environmentally sensitive areas	500-1000 m 1000-1500 m 1500-2000 m > 2000 m	Low Moderate High Very High
	Land cover	Avoid areas with valuable mineral and energy resources, tourist destinations or across major transportation routes, water gas, electrical power or communication transmission infrastructures.	Inland Water, Fishponds, Open Forest, Broadleaf Mangrove Forest	Grassland Bare/pasture Bare/sand/ rock Forest scrub/	Low Moderate High Very High
	Flood Susceptibility	Avoid locating sites in areas that may be subject to washout or inundation during a major flood	Areas with moderate and high susceptibility	Not flood prone Low susceptibility	Very high
	Soil permeability	The site shall not be located in unstable, very soft, and settling soils (sand, coarse sand, or fine sand) with high potential for liquefaction, slumping or erosion.	-	Nearly impermeable Low impermeable Conditionally Permeable Permeable	Very high High Moderate Low
	Physical	Distance from settlements	The sites shall not be located in or within 250 meters of existing or proposed residential, commercial or urban development areas among other land use classes	250 m from settlements	250-1000 m 1000-1500 m 1500-2000 m 2000-2500 m > 2500 m

Table 2 continued

Main Criteria	Criteria	Policies / Considerations	Exclusionary Zones	Sub-criterion zones	Suitability Classification
	Distance from cultural heritage	The sites shall not be located in or within 250 meters of areas with historical, archaeological, cultural geological, or scientific interests which are more than 100 years old and declared by the traditional Commission for Culture and the Arts National Historical Institute or National Museum.	250 m from cultural heritage sites	250-500 m 500-1000 m 1000-1500 m 1500-2000 m > 2000 m	Low Moderate High Very High Very High
	Distance to Faults (Seismic Conditions)	Avoid areas within 500 meters of active faults or in areas with an average return period between 50 to 100 years for an earthquake of magnitude 6 and above	500 m from active faults	500-1500 m 1500-2500 m 2500-3500 m > 3500 m	Low Moderate High Very High

signs a score to each option according to the decision maker’s pairwise comparisons of the options based on the criterion. The AHP also combines the criteria weights and the options scores that determine a global score for each option and a consequent ranking.

**Table 3** shows the weights assigned for each main criterion with its corresponding consistency ratio (CR). However, this study assumed an equal weight for the sub-criterion zones since some of its categories are not applicable to local conditions. The calculation of the consistency ratio (CR) is an important step because it checks if the estimated weights were already acceptable or needed to be changed. The acceptable value of CR is less than 0.10, otherwise, the

judgments were considered inconsistent and had to be checked and revised. Consistency Ratio (CR) and Consistency Index (CI) were calculated based on the following equations:

$$CR = CI/RI \tag{1}$$

$$CI = ((\lambda_{max}-n))/(n-1) \tag{2}$$

where, CI = Consistency Index; RI = Random Index.

### 2.5 Stepwise spatial analysis

First, eight of the twelve criteria were subjected to the Euclidean distance (ArcGIS toolbox > Spatial Analysis > Distance > Euclidean distance). This tool calculates, for each cell, the Euclidean distance to

**Table 3.** Assigned weights of main criteria and criteria.

Main Criteria	Weight	CR	Criteria	Weight	CR
Economic	0.21	0.016	Distance from urban areas	0.54	0.008
			Distance from roads	0.30	
			Slope	0.16	
Environmental	0.55		Distance from surface waters	0.31	0.007
			Distance from ground waters	0.31	
			Distance from environmentally sensitive areas	0.05	
			Land cover	0.05	
			Flood Susceptibility	0.12	
Physical	0.24		Soil permeability	0.16	0.002
			Distance from settlements	0.68	
		Distance from cultural heritage	0.22		
			Distance to Faults (Seismic Conditions)	0.10	

Source: [17].

the closest source (ArcGIS Help). This tool can be visualized using the illustration provided by ArcGIS Help. For this study, this tool was utilized for creating zones. This zone represents the degree of influence of a specific criterion in a particular zone or distance from the center to the determination of the landfill site. For this step, the software automatically creates the zones. Urban centers, road networks, groundwater point sources, stream networks, critical areas, cultural sites, built-up areas, and active faults

are the criteria wherein this tool was executed for.

### 2.6 Model development

The study utilized ArcGIS™, a licensed model builder to develop the landfill suitability model for landfill site selection in Butuan City, Philippines. The schematic diagram generated from the model builder detailed the general stepwise method implemented to determine the optimized landfill site (Figure 2).

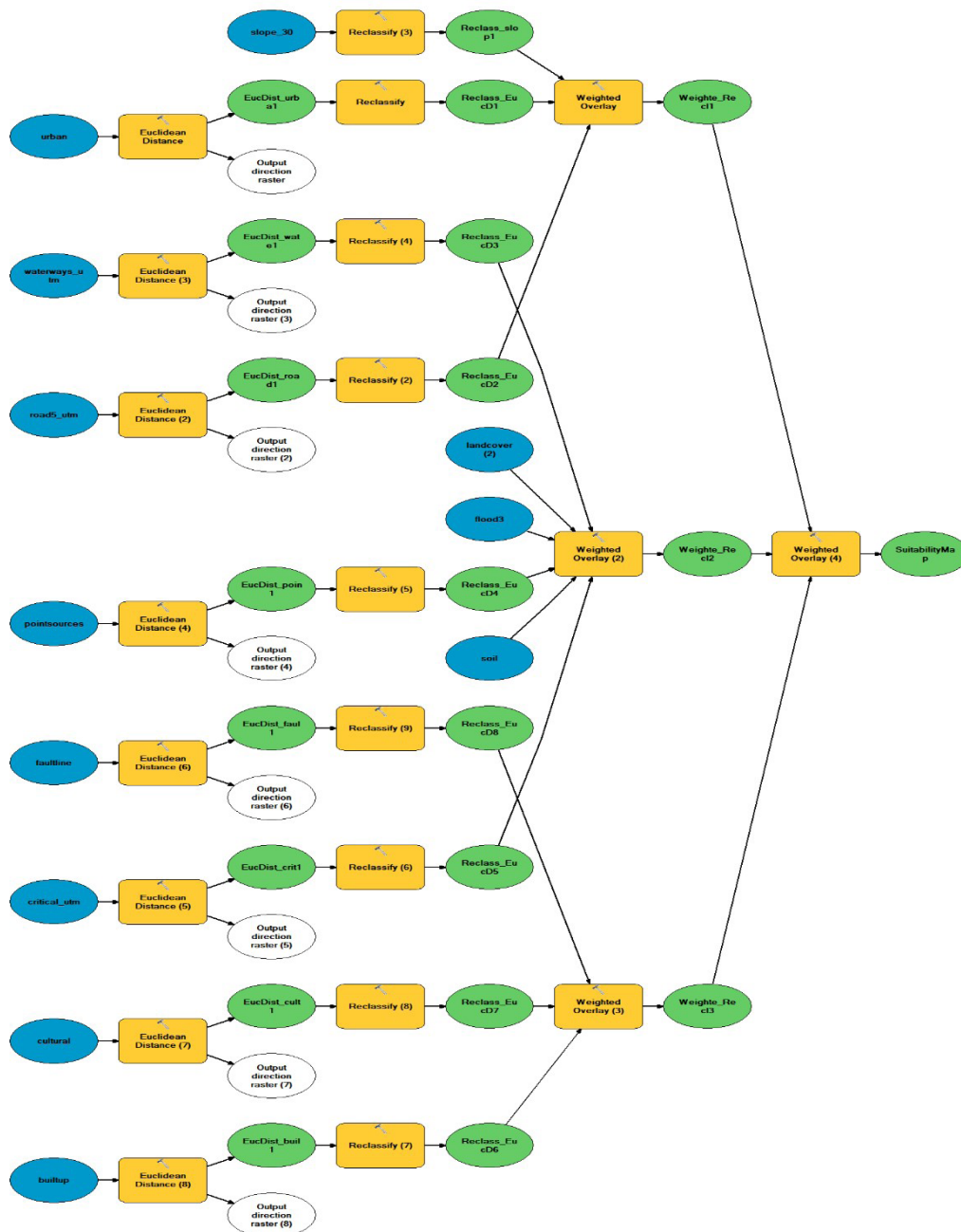


Figure 2. General workflow of the landfill suitability mapping using ArcGIS model builder.

### 3. Results and discussion

To minimize negative long-term environmental impacts, such as groundwater contamination, air and noise pollution, and public health risks, it is crucial to conduct a thorough evaluation of various criteria when siting a landfill. However, economic factors must also be considered, and sometimes it may not be feasible to locate the landfill far from the main roads due to increased transportation and collection costs. In a study conducted by Habiba et al. [19], thirteen criteria maps were developed based on a literature review and Malaysian guidelines for landfill siting to gain a comprehensive understanding of suitable landfill site criteria. A similar approach was taken in Butuan City, Philippines, using the Philippine Guidelines for landfill siting.

After developing a landfill suitability model using ArcGIS model builder, an additional requirement and process were conducted to compute the area needed for landfill site selection in accordance with the Solid Waste Management Guidelines of CLUP Guidebook Volume 2 [20]. The landfill suitability map for Butuan City was produced, and **Tables 4, 5, and 6** discuss the specific areas for low, moderate, high, and very high suitability. **Figure 3** below illustrates the landfill site suitability of Butuan City.

#### 3.1 Very highly suitable areas

**Table 4** and **Figure 3** show the areas (in hectares) of 4 barangays in Butuan City that have very highly suitable sites in Butuan City for building a sanitary landfill. Results show that Barangay Bugsukan has the highest number of areas for building a sanitary landfill with 26.74 hectares of very highly suitable areas. Barangay Nong-Nong has the lowest number of areas for building a sanitary landfill with 0.0956 hectares of a very highly suitable site. However, none of the barangays have met the total land area for building a sanitary landfill.

Land availability is one of the critical factors to consider when selecting a site for a sanitary landfill. According to Ali et al. [16], the size of the site is one of the most important criteria that influence the suitability of a site for landfilling. It is essential to select a site with sufficient land area to accommodate the waste generation of the community for several years to come. However, if the land area is insufficient, the landfill may reach its capacity faster than anticipated, requiring the need to establish additional landfills or expand the existing ones, which can be costly and time-consuming.

Furthermore, the selection of a sanitary landfill site should also consider the distance from residential areas, water bodies, and transportation routes,

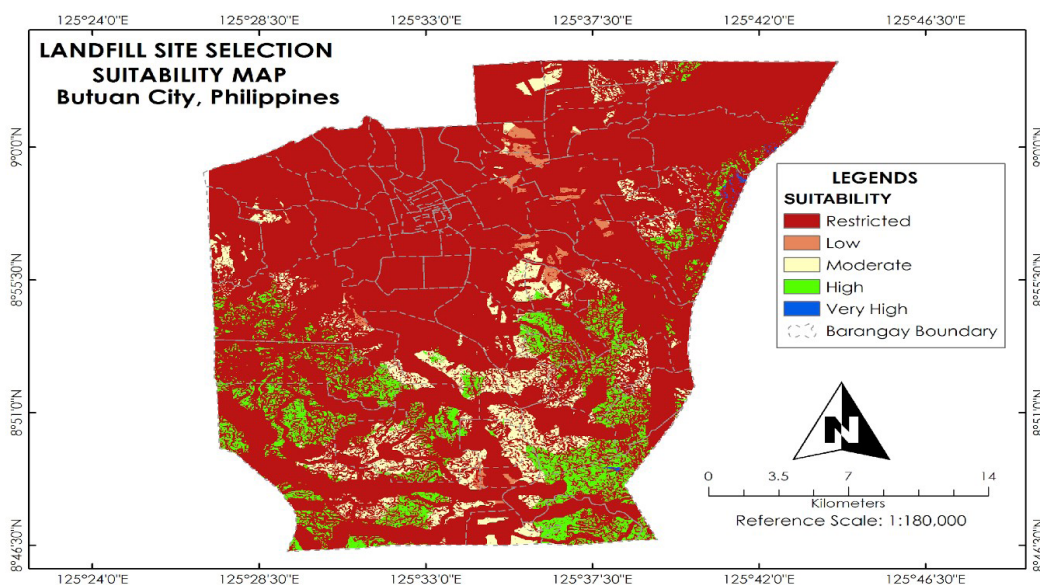


**Figure 3.** Landfill site selection suitability map of Butuan City, Philippines.

among other factors, to prevent adverse environmental and public health impacts. The results of the study by Kara and Doratli <sup>[17]</sup> show that the physical, economic, and environmental criteria are critical in selecting an appropriate site for a sanitary landfill.

In conclusion, while the barangays mentioned in **Table 4** may have very highly suitable sites for building a sanitary landfill, the total land area available in each barangay must also be considered. It is crucial to identify a site with enough land area to accommodate the waste generated by the community for an extended period while considering the necessary criteria to prevent adverse environmental and public health impacts.

**Table 4.** Very highly suitable areas for landfill site selection in Butuan City, Philippines.

BARANGAY	AREA (hectares)
Bugsukan	26.7413283
Florida	10.4310974
Nong-Nong	0.0955391
Pianing	6.9079892
<b>Total Land Area</b>	<b>44.175954</b>

### 3.2 Highly suitable area

The identification of highly suitable areas for constructing a sanitary landfill is an important aspect of solid waste management planning. The results presented in **Table 5** indicate that some barangays in Butuan City have significant areas that are highly suitable for landfill construction. Barangay Florida is one of the barangays that have met the total land area requirement for building a sanitary landfill with 518.48 hectares of the area considered to be highly suitable. Barangay Tungao, having 1131.43 hectares of the area highly suitable for building a sanitary landfill has the highest number of areas as compared to Barangay Tagabaca. It has the lowest number of areas with only 2.73 hectares highly suitable for building a sanitary landfill. This can help decision-makers to identify potential sites for building a landfill that would meet the criteria for proper waste disposal while minimizing negative environmental

and public health impacts.

Furthermore, this finding is consistent with a study conducted by Ali et al. <sup>[16]</sup> which emphasizes the importance of identifying appropriate criteria for landfill suitability analysis. They highlight that the criteria used should vary depending on the scope and objectives of the study and that a review of relevant literature can aid in establishing a hierarchy of criteria and sub-criteria. The use of such criteria can assist in identifying highly suitable areas for landfill construction while minimizing potential negative impacts.

**Table 5.** Highly suitable areas for landfill site selection in Butuan City, Philippines.

BARANGAY	AREA (hectares)
Amparo	72.0874578
Anticala	37.2093499
Aupagan	19.4932393
Basag	3.9174409
Bilay	3.5055031
Bitan-Agan	214.537154
Bit-Os	204.32094
Bugabus	35.1679778
Bugsukan	68.9205218
Camayahan	200.730793
Dankias	34.3457281
De Oro	48.8555106
Don Francisco	105.495956
Dulag	177.908904
Florida	518.478423
Maguinda	291.998449
Maibu	216.915679
Mandamo	378.757613
Manila de Bugabus	166.081443
Nong-Nong	170.753381
Pianing	36.615961
Pigdaulan	25.6876102
Salvacion	161.070872
San Mateo	25.4985378
Sumile	186.126838
Tagabaca	2.7285528
Taligaman	71.5297566
Tungao	1131.42967
<b>TOTAL LAND AREA</b>	<b>4610.16926</b>

### 3.3 Moderately suitable sites

**Table 6** presents the results of the land suitability analysis for potential landfill sites in the study area. It indicates that three barangays, namely Amparo, Tungao, and Manila de Bugabus, have a relatively larger area of land that is moderately suitable for constructing a sanitary landfill, making them potential locations for landfill development. However, it is important to note that the criteria used in the analysis are not the only factors that should be considered when deciding on a landfill site. Other social and economic factors, such as the proximity to population centers and the cost of transportation, should also be considered.

On the other hand, Barangay Basag has the smallest area of moderately suitable land for landfill construction, indicating that it may not be a viable option for landfill development. However, it is important to consider other factors that may impact the suitability of the site, such as its proximity to water bodies, population density, and land use restrictions.

Overall, the results of the land suitability analysis can serve as a useful tool in identifying potential locations for landfill development, but they should be considered in conjunction with other relevant factors and careful consideration of potential environmental and social impacts.

### 3.4 Suitable sites with areas greater than the landfill area requirement of Butuan City

With the addition of landfill area requirements as a factor, no area in the municipality is categorized as a very highly suitable site. Barangay Tungao (1131.42967) and Florida with 518.48 hectares are highly suitable as the landfill site location. Moreover, Barangays Amparo (433.7004 ha), Manila de Bugabus (406.5156 ha), and Tungao (413.0025 ha) are moderately suitable sites. Furthermore, in a study conducted by Zulu et al. <sup>[21]</sup>, an overlay analysis revealed that the current dumpsite in Banket Town Board, Zimbabwe is unsuitable due to various critical parameters, such as roads, hydrological network, and land use. The presence of a power line that runs

**Table 6.** Moderately suitable areas for landfill site selection in Butuan City, Philippines.

<b>BARANGAY</b>	<b>AREA (hectares)</b>
Amparo	433.7004
Ampayon	32.9984
Anticala	19.2062
Antongalon	60.05356
Aupagan	103.6259
Baan Km3	2.192468
Bancasi	59.80117
Baobaoan	80.76925
Basag	1.569937
Bilay	175.169
Bitan-Agan	37.82903
Bit-Os	157.1715
Bobon	0.654652
Bugabus	208.7171
Bugsukan	27.2267
Cabcabon	33.46424
Camayahan	65.06163
Dankias	157.0967
Don Francisco	25.48383
Dulag	48.54295
Dumalagan	121.5627
Florida	53.04027
Los Angeles	57.74676
Maguinda	248.7865
Mahay	35.58821
Maibu	147.8911
Mandamo	20.44589
Manila de Bugabus	406.5156
Nong-Nong	0.147941
Pianing	0.937307
Pigdaulan	183.5733
Pinamanculan	9.355365
Salvacion	6.839699
San Mateo	80.09127
Santo Nino	132.1781
Sumile	44.67656
Sumilihon	18.6711
Tagabaca	129.4023
Taguibo	1.325041
Taligaman	70.08011
Tiniwisan	10.39523
Tungao	413.0025
<b>TOTAL LAND AREA</b>	<b>3922.587</b>

through the dumpsite further complicates the issue. Utilizing key environmental parameters, a map was created, highlighting several alternative sites that are potentially suitable for establishing a well-engineered landfill or dumpsite. This result corresponds with the findings of other studies that have found the existing dumpsites as unsuitable possible suitable sites for establishing a landfill in their respective study areas<sup>[21-23]</sup>.

#### **4. Conclusions and recommendations**

After conducting a spatial determination of an optimal landfill location that ensures proper environmental and social acceptability of the proposed landfill site, several conclusions were reached. First, the researcher identified a set of criteria for Butuan City as per guidelines provided by DENR National Solid Waste Management Commission (NSWMC) on-site identification and suitability assessment procedure for sanitary landfills. These criteria are considered economic, environmental, and physical criteria. The utilization of the Analytical Hierarchy Process (AHP) helped in the identification process of potential sites by considering the most relevant criteria. The relative importance weights for the various criteria were calculated using a pair-wise comparison method that enabled the proper integration of various screening criteria.

Geographical Information System (GIS) was used as a decision-support system to help in finding suitable sites for potential landfill sites. Based on the site area requirement provided by DENR National Solid Waste Management Commission (NSWMC), Barangay Tungao (1131.42967) and Florida with 518.48 hectares were identified as highly suitable for the landfill site location. However, constraints were identified in the proper integration of GIS due to the lack of funds, limited availability of detailed data, and the availability of a technical workforce with adequate knowledge and training in GIS.

Limitations were also identified in terms of evaluation and analysis. The analysis was limited to the availability and accuracy of data, and a careful

field research and evaluation process was required to assess the impact on local communities, the environment, the and ecology of the area. Further geotechnical and hydrogeological analyses were also necessary for the protection of groundwater as well as surface water.

At the end of the analyses, suitable areas for appropriate solid waste landfill sites were identified that generally satisfied the minimum requirements for new landfill site selection and fulfilled the legislative and environmental obligations associated with site selection. The study showed that it provides a tool and methodology for landfill site selection to local authorities.

To ensure proper landfill site selection, several steps must be taken. First, a geotechnical evaluation stage must be conducted, involving rigorous geological and hydrogeological assessment using a combination of site investigation and laboratory techniques. Additionally, more detailed social, ecological, climatic, and economic parameters should be considered, including the impact on humans, flora, fauna, soil, water, air, climate, and landscape. Objective ranking of potential sites in order of suitability and social acceptance is also important. This can be achieved through the use of household surveys or public consultations. The general public must be involved in the selection process from the start, through the dissemination of information, consultation, and public meetings. Moreover, an Advisory Committee on Landfill Site Selection should be in place consisting of various fields of expertise and technical consultants who will oversee the findings and recommendations. They will ensure that the most suitable site is selected, considering all relevant factors.

Lastly, future research should focus on the possibility of GIS with Environmental Impact Assessment in the location of landfills. This will help to further refine the site selection process and ensure that the environmental impact is minimized. By following these steps, the proper selection of landfill sites can be achieved, ensuring the safety and health of both humans and the environment.

## Conflict of Interest

There is no conflict of interest.

## References

- [1] Li, Y., Liu, J., Zhang, X., et al., 2021. Landfill site suitability assessment using GIS and AHP: A case study in a rural area of China. *Journal of Environmental Management*. 288, 112422.
- [2] Mohammadi, M., Yarahmadi, R., Farhadian, M., 2020. Landfill site suitability assessment using GIS and AHP in Iran. *Environmental Earth Sciences*. 79(7), 1-17.
- [3] Abbas, M., Ahamad, S., 2018. Landfill site suitability analysis using AHP and GIS techniques: A case study of district Ghaziabad, India. *Applied Water Science*. 8(3), 70.
- [4] Villanueva, J.A., Chua, P.J.P., Torres, E.L., et al., 2021. Landfill site selection using multi-criteria decision-making (MCDM) approach: A case study in San Nicolas, Pangasinan, Philippines. *Environmental Science and Pollution Research*. 28(8), 9679-9691.
- [5] Congress of the Philippines, 2001. Republic Act No. 9003 [Internet]. Available from: <https://www.officialgazette.gov.ph/2001/01/26/republic-act-no-9003-s-2001/>
- [6] Philippine Statistics Authority (PSA). Population Data 2010 [Internet]. Available from: [www.psa.gov.ph](http://www.psa.gov.ph)
- [7] United States Geological Survey, 2019. Earth Explorer [Internet] [cited 2019 Apr 18]. Available from: <https://earthexplorer.usgs.gov/>
- [8] OpenStreetMap Contributors, 2020. OpenStreetMap [Internet] [cited 2020 Jun]. Available from: <https://www.openstreetmap.org/>
- [9] National Mapping and Resource Information Authority [Internet]. NAMRIA Official Website [cited 2018 Apr 18]. Available from: <https://www.namria.gov.ph/>
- [10] Philippine Groundwater Data Bank [Internet]. Available from: <http://210.213.82.217/Home.asp>
- [11] Google Earth, 2018. Available from: <https://earth.google.com/web/search/historical+places+near+Butuan,+Agusan+Del+Norte>
- [12] Geoportal Philippines [Internet]. Available from: <https://www.geoportal.gov.ph/>
- [13] LiPAD: LiDAR Portal for Archiving and Distribution System [Internet]. Available from: <https://lipad-tst.dream.upd.edu.ph/>
- [14] Department of Agriculture-Bureau of Soil and Water Management, 2019. Available from: <http://bswm.da.gov.ph/>
- [15] Department of Science and Technology (DOST)-Philippine Institute of Volcanology and Seismology (PHIVOLCS). About PHIVOLCS [Internet] [cited 2018 Apr 18]. Available from: <https://www.phivolcs.dost.gov.ph/index.php/about-us/about-phivolcs>
- [16] Ali, K., Islam, K., Khan, A., et al., 2020. A systematic review on land suitability analysis for different land use. *Journal of Environmental Management*. 271, 111020.
- [17] Kara, M., Doratli, N., 2012. GIS-based land suitability analysis for grape production in Turkey. *Environmental Monitoring and Assessment*. 184(2), 1125-1138.
- [18] Sarı, F., Ceylan, D.A., Özcan, M.M., et al., 2020. A comparison of multicriteria decision analysis techniques for determining beekeeping suitability. *Apidologie*. 51(4), 481-498.
- [19] Habiba, M.I., Majid, Z., Yamusa, Y.B., 2019. GIS-based sanitary landfill suitability analysis for sustainable solid waste disposal. *IOP Conference Series: Earth and Environmental Science*. 220, 012056. DOI: <https://doi.org/10.1088/1755-1315/220/1/012056>
- [20] Housing and Land Use Regulatory Board, 2014. A guide to comprehensive land use plan preparation, vol. 2—Sectoral analysis and tools for situational analysis manila, philippines. pp. 260-261.
- [21] Zulu, S., Jerie, S., 2017. Site suitability analysis for solid waste landfill site location using geographic information systems and remote sensing: A case study of Banket Town Board, Zimbabwe. *Review of Social Sciences*. 2(4), 19-31.
- [22] Ebistu, T.A., Minale, A.S., 2013. Solid waste

dumping site suitability analysis using geographic information system and remote sensing for Bahir Dar Town, North Western Ethiopia. *African Journal of Environmental Science and Technology*. 7(11), 976989.

[23] Krčmar, D., Tenodi, S., Grba, N., et al., 2018.

Premedical assessment of the municipal landfill pollution impact on soil and shallow groundwater in Subotica, Serbia. *Science of the Total Environment*. 615, 1341-1354.

DOI: <https://doi.org/10.1016/j.scitotenv.2017.09.283>

ARTICLE

## Domestic Wastewater Treatment through the Application of *Corchuros olitorius L.* as Bio-Coagulant in Cagayan de Oro City, Philippines

Gina C. Lacang<sup>1\*</sup>, Corazon V. Ligaray<sup>2</sup>

<sup>1</sup> Department of Environmental Science and Technology, College of Science and Mathematics, University of Science and Technology of Southern Philippines, Cagayan de Oro, 9000, Philippines

<sup>2</sup> Department of Chemical Engineering and Technology, College of Engineering and Technology, Mindanao State University-Iligan Institute of Technology, Iligan, 9200, Philippines

### ABSTRACT

This research paper presented the potential of *Corchuros olitorius L.* as a natural coagulant in the removal of turbidity, total suspended solids, and biochemical oxygen demand from the domestic wastewater of the University of Science and Technology of Southern Philippines. Optimization of the natural coagulant and synthetic coagulant was employed prior to the treatment design. The jar test method was used in the optimization and lab analysis including the gravimetric method, dilution technique, and digital measurements. The optimization results of *Corchuros olitorius L.* using the jar test method revealed better removal at a lower dosage of 50 mg/L and a higher settling time of 90 minutes. The characterization using FTIR analysis also suggests a functional group that influences coagulation activity. Using the optimum dose and optimum settling time, results with the different treatment designs showed the highest removal at pH 7 showed % BOD removal of 89.78% (A<sub>75</sub>C<sub>25</sub>); 85.98% (A<sub>25</sub>C<sub>75</sub>); 88.76% (A<sub>50</sub>C<sub>50</sub>). TSS removal measured values of 88.50% (A<sub>75</sub>C<sub>25</sub>), 85.56% (A<sub>25</sub>C<sub>75</sub>), and 87.16% (A<sub>50</sub>C<sub>50</sub>), while turbidity removal of 83.47% (A<sub>75</sub>C<sub>25</sub>), 80.27% (A<sub>25</sub>C<sub>75</sub>), and 80.27% (A<sub>50</sub>C<sub>50</sub>). Statistically, measured values differ between treatment designs. It is suggested to investigate removal efficiency in more varied pH conditions, different settling times, stirring speed, and other variables for future studies.

**Keywords:** *Corchorus olitorius L.*; Jar test; Optimization; Removal efficiency; Wastewater

#### \*CORRESPONDING AUTHOR:

Gina C. Lacang, Department of Environmental Science and Technology, College of Science and Mathematics, University of Science and Technology of Southern Philippines, Cagayan de Oro, 9000, Philippines; Email: [gina.lacang@ustp.edu.ph](mailto:gina.lacang@ustp.edu.ph)

#### ARTICLE INFO

Received: 24 March 2023 | Revised: 18 April 2023 | Accepted: 20 April 2023 | Published Online: 27 April 2023

DOI: <https://doi.org/10.30564/jees.v5i1.5593>

#### CITATION

Lacang, G.C., Ligaray, C.V., 2023. Domestic Wastewater Treatment through the Application of *Corchuros olitorius L.* as Bio-Coagulant in Cagayan de Oro City, Philippines. *Journal of Environmental & Earth Sciences*. 5(1): 108-120. DOI: <https://doi.org/10.30564/jees.v5i1.5593>

#### COPYRIGHT

Copyright © 2023 by the author(s). Published by Bilingual Publishing Group. This is an open access article under the Creative Commons Attribution-NonCommercial 4.0 International (CC BY-NC 4.0) License. (<https://creativecommons.org/licenses/by-nc/4.0/>).

## 1. Introduction

Wastewater treatment is employed as an action to protect the quality of limited freshwater resources and therefore make it more acceptable for beneficial reuse <sup>[1]</sup>. Various traditional and advanced technologies have been utilized to remove colloidal particles from wastewater; such as ion exchange, membrane filtration, precipitation, flotation, solvent extraction, adsorption, coagulation, flocculation, and biological and electrolytic methods <sup>[2]</sup>. Among those methods, coagulation/flocculation is one of the most widely used solid-liquid separation processes for the removal of suspended and dissolved solids, colloids, and organic matter present in industrial wastewater <sup>[3]</sup>. Coagulation/flocculation is a commonly used process in water and wastewater treatment in which compounds such as aluminum sulfate, ferric chloride, and/or polymer are added to the wastewater to destabilize the colloidal materials and cause the small particles to agglomerate into larger settleable flocs <sup>[4]</sup>.

Alum (aluminum sulfate), has been the most popular for the treatment of water and is widely used in treatment plants <sup>[5]</sup> but it has been found to pose some health, economic, and environmental problems upon usage, among which are neurological diseases such as percentile dementia and induction of Alzheimer's disease <sup>[6]</sup>. The use of synthetic flocculants like alum and iron can cause health hazards. Alzheimer's disease and dementia are associated with the use of aluminum ions in treated waters <sup>[7]</sup>. As a result, several studies have explored the use of natural coagulants as alternatives or an aid to chemical coagulants to eliminate or if not lessen their harmful effects. Bio-coagulants (plant materials) are considered a good substitute. Presently there is no study about *Corchuros olitorius L.* as a bio-coagulant in the treatment of domestic wastewater at the University of Science and Technology of Southern Philippines. Specifically, the study aims to: i.) Characterize *Corchuros olitorius L.*; ii.) Optimize pure *Corchuros olitorius L.* mucilage powder ( $C_{100}$ ) using various coagulant dosages (50 mg/L, 100 mg/L, 150 mg/L), and settling time (30 min, 60 min, and 90 min) at pH 5, pH 7, and pH 9; iii.) Assess the

removal efficiency of turbidity, total suspended solids (TSS), and biochemical oxygen demand (BOD) at different treatment designs.

## 2. Materials and methods

The methods used in this study are descriptive and experimental. One-way analysis of variance (ANOVA) using Microsoft Excel version 2016 at a 5% level of significance is used to determine the significant difference between the different treatments.

### 2.1 Research setting

**Figure 1** shows the study area. The wastewater sample is collected at the sump pit of the University of Science and Technology of Southern Philippines, Cagayan de Oro Campus, and brought to the laboratory for coagulation treatment.

### 2.2 Collection of water sample

A wastewater sample is collected from the sump pit of the University of Science and Technology of Southern Philippines, Cagayan de Oro Campus. It is characterized as grey water, which is generated from the buildings of the school campus. The sample water is taken and brought to the school laboratory for its analysis using the coagulation process.

### 2.3 Preparation and characterization of *Corchuros olitorius L.* (Saluyot)

#### *Powder preparation*

Saluyot was harvested from the vacant lots of Barangay Iponan, Cagayan de Oro City, leaves were separated from the stalks, washed with distilled water, and boiled for 30 minutes. After boiling, the liquid is allowed to cool, and disintegrated and leaves were separated using a strainer followed by a cotton cloth to fully separate the slimy liquid. The extract that contains the viscous substance was separated from the leaf residue after filtration. Saluyot leaf extract was treated with 2-propanol in a 1:1 ratio to separate the viscous sediments known as the mucilage. It was then dried in an oven at 40 °C for 30

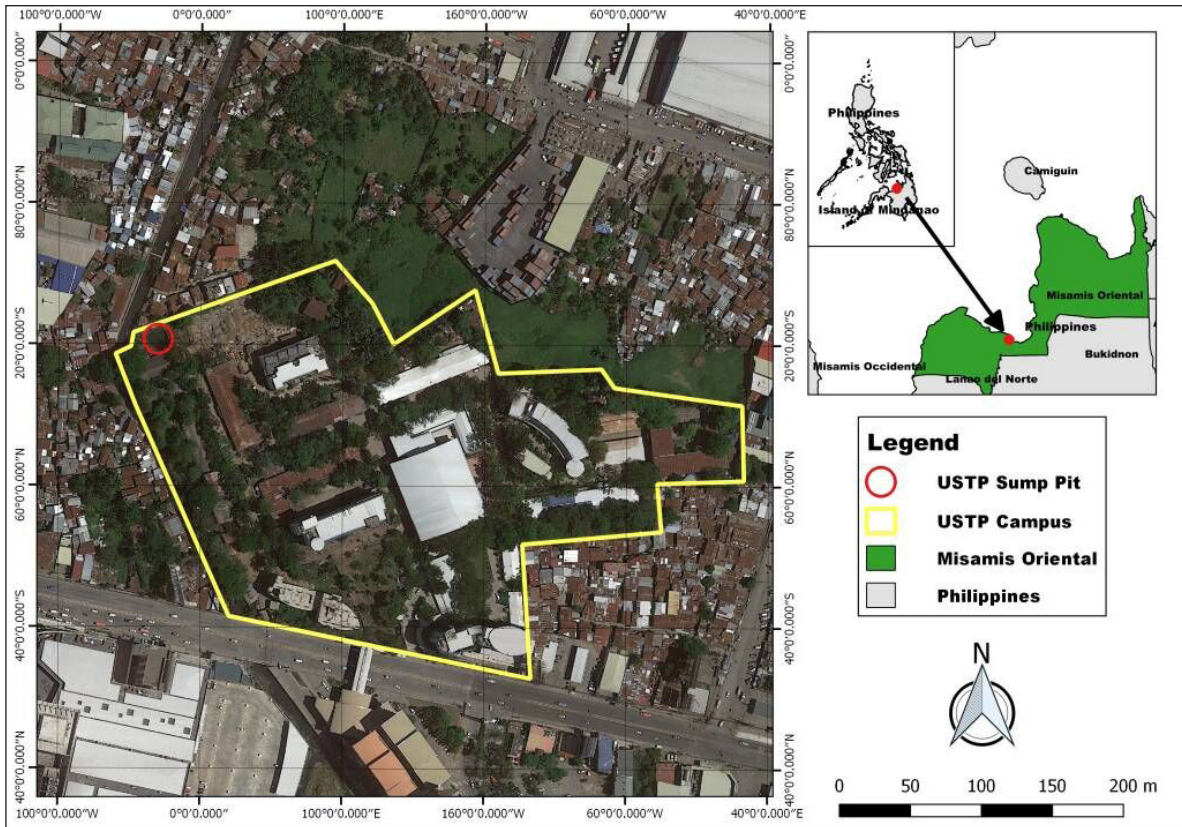


Figure 1. The layout of the study area.

minutes. Finally, it was ground by using a mortar and pestle and sieved to a size between 90-125  $\mu\text{m}$ . The powder from the Saluyot leaf was kept in a tight container ready for use. **Figure 2** showed the exper-

imental setup in the preparation of saluyot powder, and the final product is shown in **Figure 3**.

$$\text{Yield of polysaccharide (\%)} = \frac{\text{Weight of polysaccharides (g)}}{\text{Weight of raw material (g)}} \times 100$$

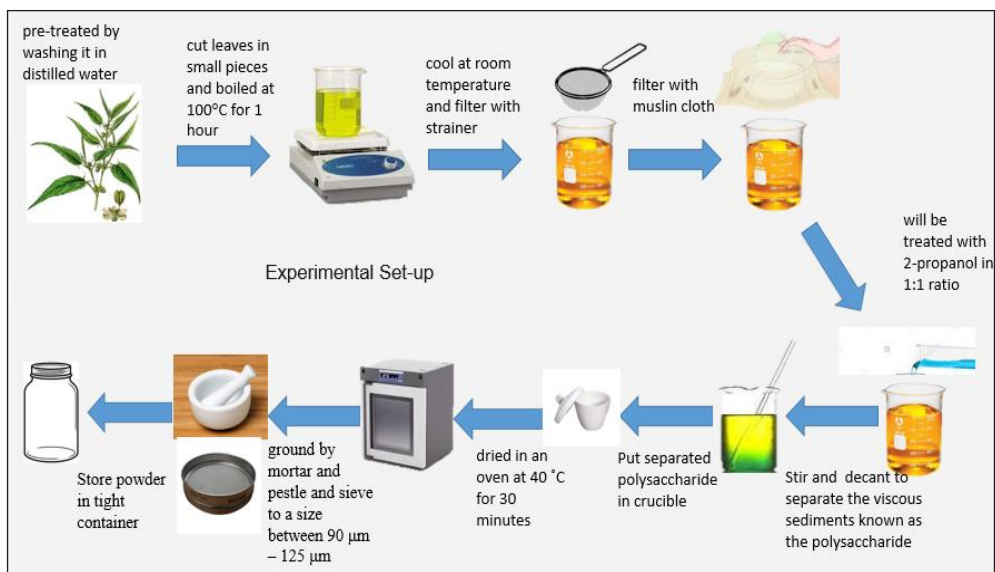


Figure 2. Flow chart diagram of saluyot powder preparation.

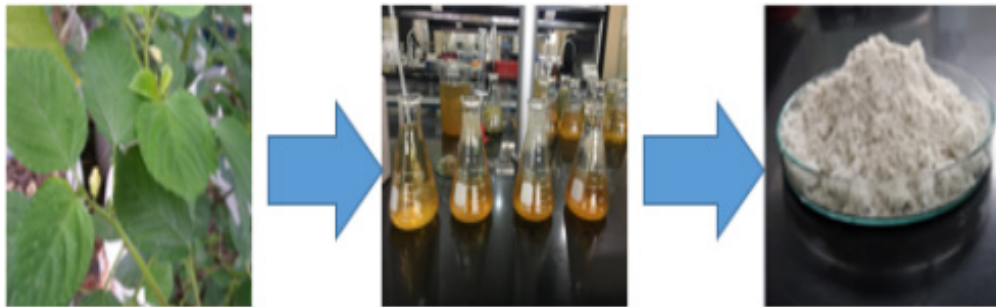


Figure 3. Chart showing the final product after the preparation.

Table 1 showed the characteristics of *Corchorus olitorius L.* (Saluyot), according to total carbohydrate, crude protein, crude fiber, crude lipid, and ash in mg/g, in both leaves and stems, as adapted from Ndovu and Afolayan 2008 [8].

The physical characteristics of *Corchorus olitorius L.* (Saluyot) mucilage powder (Table 1) are determined by its color, odor, texture, and solubility. Chemical characteristics are analyzed using Fourier-transform infrared spectroscopy (FTIR).

**Characterization of *Corchuros olitorius L. mucilage***

Fourier-transform infrared spectroscopy (FTIR) is an analytical technique used to identify organic or inorganic materials. The method of analysis involving FTIR used infrared light to scan test samples and observe chemical properties. The FTIR instrument sends infrared radiation of about 10,000 cm<sup>-1</sup> to 100 cm<sup>-1</sup>. Some radiation is absorbed and some are passed through, in which absorbed radiation is converted into vibrational energy by the sample molecules [9-11]. The resulting signal presents a spectrum that represents the molecular fingerprint of the sample. This technique is useful in analyzing the chemical composition of substances. In this study, the powder sample of *Corchorus olitorius L.* (saluyot) mucilage was subjected to FTIR analysis to determine a functional group of these substances that influenced the coagulation property.

**2.4 Jar test and optimization of synthetic and bio-coagulant**

Analysis of the optimum dosage of synthetic and bio-coagulant was done using a jar test. Figure 4 below showed the flow chart diagram of the jar test design with different treatment combinations using the bio-coagulant *Corchuros olitorius L.* and synthetic coagulant, aluminum sulfate. The purpose of the jar test is to determine the optimum dosage/concentration of each coagulant to be used for the treatment design as shown in Table 2. The jar test for each coagulant (Alum and *Corchuros olitorius L.*) was done separately. Each coagulant dose varies at 50 mg/L, 100 mg/L, and 150 mg/L while stirring speed was also varied at 550 rpm at a 3-minute contact time followed by 200 rpm at 7 minutes for each dose. After the jar test, the optimum dose for each coagulant was used in the treatment design experiment using the same volume of wastewater sample. The aluminum salt and *Corchuros* mucilage were treated separately at various pH conditions namely: pH = 5, pH = 7, pH = 9; while contact time and varying stirring speed at 550 rpm for 3 minutes followed by 200 rpm at 7 minutes. It was then allowed to settle separately at different settling times, between 30 minutes, 60 minutes, and 90 minutes. The same process was applied to the control during the actual treatment (Table 2) using different percent coagulant mix. Af-

Table 1. Characteristics of *Corchorus Olitorius L.* (Ndovu and Afolayan 2008).

	Total carbohydrate, mg/g	Crude Protein, mg/g	Crude Fiber, mg/g	Crude Lipid, mg/g	Ash, mg/g
Leaves	695.0 ± 32.4	162 ± 3.4	20.3 ± 1.0	17.2 ± 2.9	105.2 ± 1.0
Stems	802.0 ± 18.2	51.0 ± 1.8	88.2 ± 4.8	69.0 ± 1.3	51.9 ± 1.2

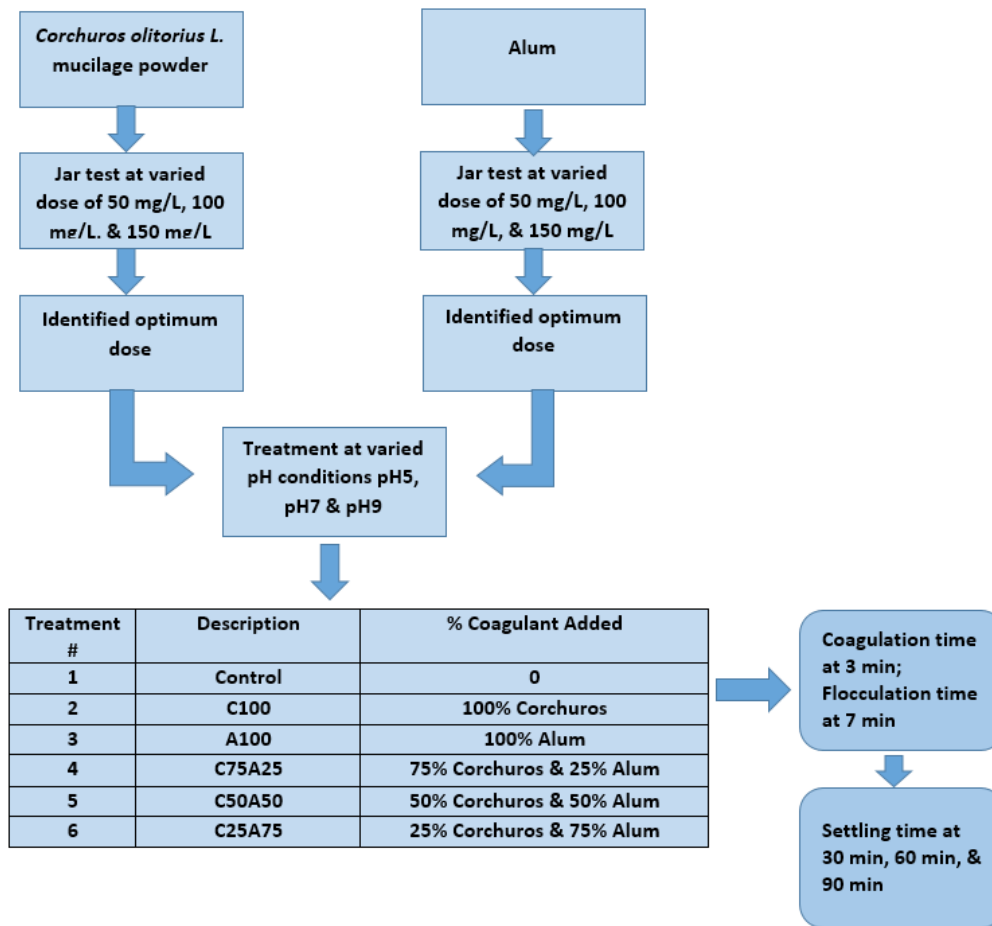


Figure 4. Flowchart diagram of jar test optimization and treatment design.

Table 2. Field layout of various coagulant optimum doses.

Treatment #	Description	% Coagulant added
1	Control	0
2	C <sub>100</sub>	100% Corchuros
3	A <sub>100</sub>	100% Alum
4	C <sub>75</sub> A <sub>25</sub>	75% Corchuros & 25% Alum
5	C <sub>50</sub> A <sub>50</sub>	50% Corchuros & 50% Alum
6	C <sub>25</sub> A <sub>75</sub>	25% Corchuros & 75% Alum

ter sedimentation, following various settling times, the supernatant liquid was collected by decantation and analyzed for turbidity, TSS, and BOD. The coagulant dose that gives the best results in the reduction of the selected water quality parameters, was the optimum dose. All experiments were performed at room temperature ( $22 \pm 1 \text{ }^\circ\text{C}$ ) and the pH of the samples was tested before and after the addition of the coagulant to adjust it to its desired pH. After the jar test, the optimum dose for each coagulant was used to conduct the experiment applying the described

treatment design as shown in **Table 2**.

### 2.5 Analysis of treated effluent

After the treatment of water samples using the coagulation-flocculation procedures, the supernatant liquid was subjected to analysis for the determination of final turbidity, total suspended solids (TSS), and biochemical oxygen demand (BOD). Turbidity was measured using a digital turbidity meter which was calibrated prior to the test. Total suspended solids

were analyzed by the use of the gravimetric method. Filtration of the treated effluent with TSS filtration apparatus followed by a series of heating and weighing until the constant mass is achieved. While BOD was measured using the dilution technique.

### 3. Results and discussions

#### 3.1 Characterization of *Corchuros olitorius L.*

*Corchuros olitorius L.* is characterized according to its physical and chemical characteristics. Chemical characteristics involve the FTIR analysis in determining the possible functional group which is the reason for its coagulative property.

##### **Physical & chemical characteristics of *Corchuros olitorius L.***

**Table 3** showed the physical and chemical characteristics of saluyot mucilage powder. It is grayish-white in color, odorless and fibrous, and is insoluble with alcohol. *Corchorus olitorius L.* (Saluyot) waste can be considered a natural polymer. When used as a coagulant or coagulant aid, it enables the formation of chemical bridges, through hydrogen bonds or van der Waals forces, with the suspended solids in the treated water. This will enhance the flocculation process<sup>[12]</sup>.

**Table 3.** Identification test results of *Corchuros* mucilage.

Identification Test	Characteristics
Color	grayish white
Odor	Odorless
Texture	Fibrous
Alcohol precipitation test *	Gelatinous precipitate
Thorium Nitrate test *	Cloudy gel
Sodium hydroxide test *	Translucent soft gel
Without Heating *	Voluminous precipitate
With Heating *	Floating turbid mass
% degree of esterification *	49.44
% total anhydrogalacturonides *	74.31
Computed molecular weight (g/mole) *	1700
Solubility	Insoluble with alcohol

\*Adapted from Montano et al., 1997.

The high carbohydrate content of saluyot, presenting the carboxyl and hydroxyl groups, increases the clotting ability. Though it is not extensively reported in the open literature, it is highly possible that galacturonic acid [a major constituent of pectin in plants] exists predominantly in the polymeric form [polygalacturonic acid] that provides a ‘bridge’ for particles to adsorb on. The polygalacturonic acid structure evidently indicates that it is anionic due to partial deprotonation of carboxylic functional group in an aqueous solution. The existence of such functional groups along the chain of polygalacturonic acid implies that chemisorption between charged particles and  $-\text{COO}-$  may occur although this requires further empirical substantiation<sup>[12]</sup>. The presence of  $-\text{OH}$  groups along its polymeric chain also infers possible intramolecular interactions which may distort the relative linearity of the chain<sup>[13]</sup>. It is believed that the presence of hydroxyl groups along the polymer chain provides abundant adsorption sites for the removal of suspended particles in water<sup>[14]</sup>. Previous studies revealed that the physical and chemical properties of natural substances have contributed to the effect of their coagulation characteristics.

##### **FTIR analysis of *Corchuros olitorius L.* (Saluyot) mucilage powder**

The potential active functional groups in saluyot powder were characterized using Fourier-transform Infrared Spectroscopy (FTIR). It was found that saluyot powder possibly contained  $-\text{OH}$ ,  $-\text{NH}$ , and  $\text{C}=\text{O}$  functional groups that indicate good potential as a natural coagulant<sup>[15]</sup>. Although the fingerprint region did not show two peaks somewhere  $1050\text{ cm}^{-1}$ , there are studies<sup>[15-19]</sup> that reveal the presence of hydroxyl as a functional group in saluyot mucilage powder. The FTIR spectra of saluyot mucilage is shown in **Figure 5**. Small but sharp peaks were visible between  $1600\text{-}1000\text{ cm}^{-1}$  and low peaks at  $3400\text{-}2900\text{ cm}^{-1}$  which are indicative of phenols and carbonyl stretching. The active groups are a boost to bind and react to form flocs. In the spectrum, it shows adsorption bands between  $1550\text{ cm}^{-1}$  to  $1050\text{ cm}^{-1}$  indicative of N-O stretching and C-O-C stretching.

Other observations showed a medium peak from  $1650\text{ cm}^{-1}$  to  $1550\text{ cm}^{-1}$  signifying that the compound could be C = N and C = C bond at 1600 to 1680 wavenumber. There is a somewhat weaker peak at  $3050\text{ cm}^{-1}$  to  $3200\text{ cm}^{-1}$  indicative of OH stretching. It signifies that a compound could possibly have alcohol content, however, the peak is so weak may be due to the absence of a homogeneous powder sample during preparation. However, studies revealed that the major functional group associated with *Corchorus olitorius L.* mucilage is attributed to the presence of phenolic content<sup>[16,17,20,21]</sup>.

These bands are quite similar to other natural coagulant aid used in the coagulation process<sup>[18]</sup>. Saluyot mucilage powder has a higher molecular weight which explains its viscosity<sup>[19]</sup>. **Figure 5** showed the FTIR results with the characterization of the *Corchuros olitorius L.* mucilage powder.

It has been stated from works of literature that the presence of esters or hydroxyl groups could be the reason for boosting the coagulant capability of saluyot. A study by Baang et al.<sup>[16]</sup> indicated that among the five vegetables being sampled for total phenolics, *C. olitorius L.* (saluyot) ranks the highest phenolic content with an amount of 6.15 mg/gram of dried sample. Additionally, with the DPPH free radical scavenging activity, *C. olitorius L.* ranks second with

a value of 63.76% among the five (5) plants being studied.

Plant-based natural coagulants could be a worthwhile alternative in addressing the environmental and ecological concerns raised over the usage of chemical coagulants in water clarification<sup>[17]</sup>. It is likely that synergistic effects between the polypeptides and polysaccharides in natural coagulants have resulted in the observed coagulation activities.

### 3.2 Optimization of *Corchuros olitorius L.* (C<sub>100</sub>)

Coagulant optimization using *Corchorus olitorius L.* is done in the same process as other coagulants. A stock solution of *Corchorus olitorios L.* is freshly prepared before the experiment. A 100% *Corchorus olitorios L.* stock solution (C<sub>100</sub>) at different alum dosages of 50 mg/L, 100 mg/L, and 150 mg/L was also used to treat a 50 mL wastewater sample at a similar ratio.

As shown in **Figure 6**, the percentage of turbidity removal was found to be optimum with a lower dosage level of 50 mg/L for the settling time of 90 minutes for all pH conditions of pH 5, pH 7, and pH 9. The maximum amount of removal percentage obtained for turbidity was 70.21%, 68.99%, and 62.31% at turbidity of 9.8 NTU, 10.2 NTU, and 12.4

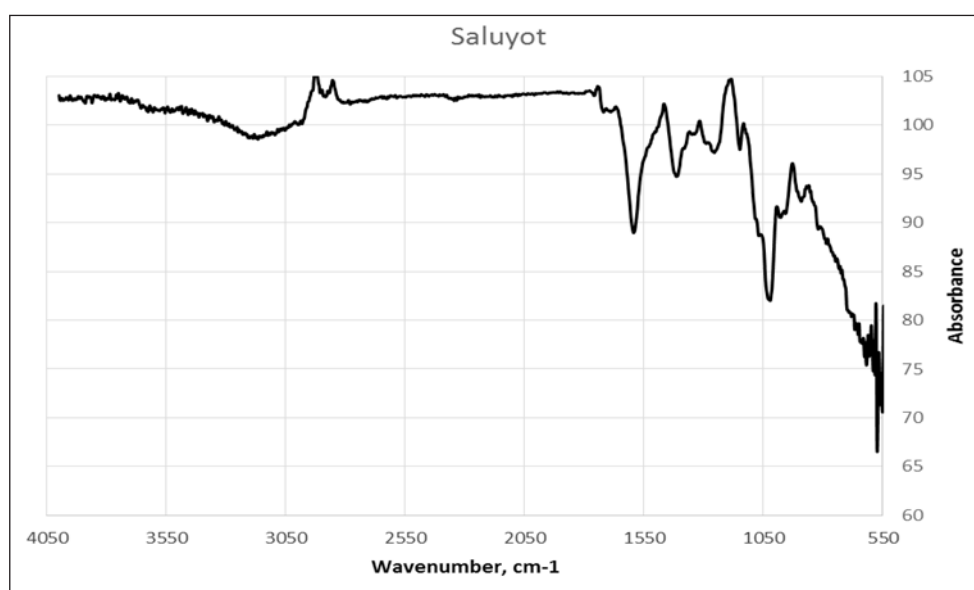


**Figure 5.** FTIR spectra of *Corchuros* mucilage powder.

NTU at pH 5, pH 7 & pH 9 with a turbidity of control at 32.9 NTU. The results of turbidity removal, when saluyot coagulant dosage was increased to 100 mg/L, showed a lower removal at values of 50.15% (pH 5, 30 min), 58.87% (pH 5, 60 min), 60.47% (pH 5, 90 min); 48.94% (pH 7, 30 min), 51.06% (pH 7, 60 min), 55.62% (pH 7, 90 min); 39.21% (pH 9, 30 min), 42.86% (pH 9, 60 min), and 49.24% (pH 9, 90 min).

Further increase of saluyot coagulant dosage to 150 mg/L further reduced the turbidity removal with measured values of 47.42% (pH 5, 30 min), 48.63%

(pH 5, 60 min), 51.38% (pH 5, 90 min); 36.78% (pH 7, 30 min), 40.73% (pH 7, 60 min), 48.02% (pH 7, 90 min); 30.69% (pH 9, 30 min), 35.56% (pH 9, 60 min), & 38.29% (pH 9, 90 min). It is observed from the results that changing the coagulant dosage and settling time had an effect on the turbidity removal from wastewater.

**Figure 7** showed the results of the optimization of coagulant *Corchorus olitorius L.* when total suspended solid (TSS) is used as a water quality parameter to determine the maximum removal. When at first, the coagulant dosage was 150 mg/L, TSS results were 50.64%

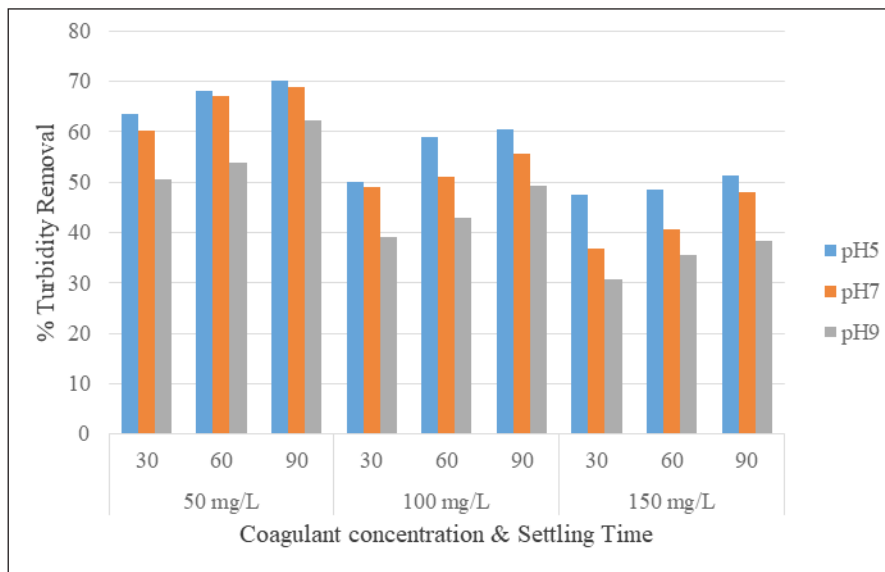


**Figure 6.** Optimization of coagulant *Corchorus olitorius L.* with turbidity.

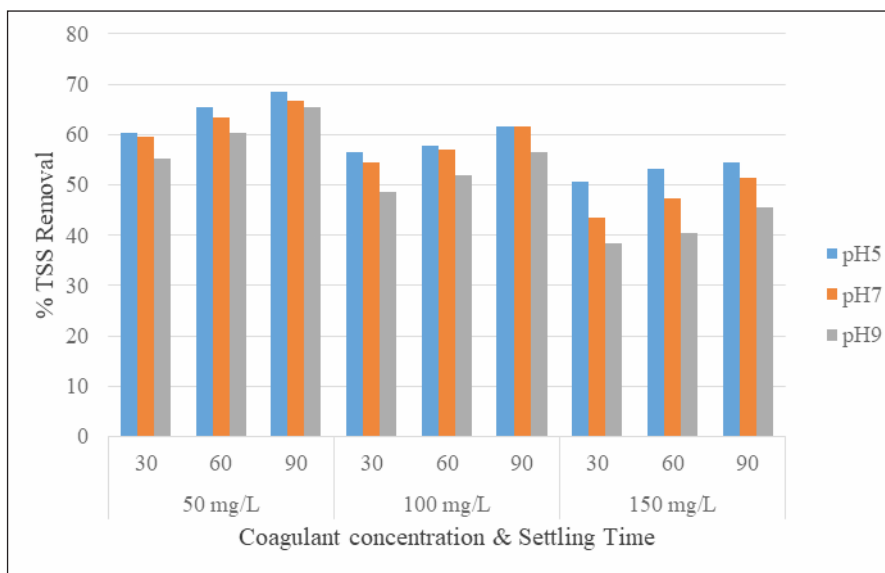


**Figure 7.** Optimization of coagulant *Corchorus olitorius L.* with TSS.

(pH 5, 30 min), 53.21% (pH 5, 60 min), 54.48% (pH 5, 90 min); 43.59% (pH 7, 30 min), 47.44% (pH 7, 60 min), 51.28% (pH 7, 90 min); 38.46% (pH 9, 30 min), 40.38% (pH 9, 60 min), and 45.51% (pH 9, 90 min). When saluyot coagulant dosage was decreased to 100 mg/L, results were 56.41% (pH 5, 30 min), 57.69% (pH 5, 60 min), 61.54% (pH 5, 90 min); 54.49% (pH 7, 30 min), 57.05% (pH 7, 60 min), 61.54% (pH 7, 90 min); 48.72% (pH 9, 30 min), 51.92% (pH 9, 60 min), 56.41% (pH 9, 90 min). There is an increase in the TSS removal when coagulant dose was lowered.

Further decrease of saluyot coagulant dose to 50 mg/L resulted to TSS removal of 60.25% (pH 5, 30 min), 65.38% (pH 5, 60 min), 68.59% (pH 5, 90 min); 59.62% (pH 7, 30 min), 62.46% (pH 7, 60 min), 66.67% (pH 7, 90 min); 55.13% (pH 9, 30 min), 60.26% (pH 9, 60 min) and 65.38% (pH 9, 90 min). It showed from the results that as the saluyot coagulant dose was reduced, there is an increase in the TSS removal.

**Figure 8** showed the results of *Corchorus olitorius L.* optimization when biochemical oxygen demand (BOD) was used as the parameter to evaluate. It revealed that the lowest coagulant dose of 50 mg/L and settling time of 90 minutes attained the highest BOD removal of 72.12%, 70.22% & 67.74% at pH 5, pH 7 & pH 9 respectively.

Statistical analysis using two-way analysis of variance indicated with p-values less than 0.05 ( $p < 0.05$ ) that the means of observations between coagulant dosage and settling time significantly differ. The percentage removal of the five (5) parameters varies with coagulant dose and time of particle settling.

When *Corchorus olitorius L.*, was tried as the primary coagulant it also removed pollutants successfully. The parameters TSS, turbidity, nitrogen, phosphorus, and BOD were observed significantly less after the treatment of water. For 50 mg/L, 100 mg/L, and 150 mg/L doses of 100% *Corchorus olitorius L.* stock solution ( $C_{100}$ ), the measured values of the parameters were reduced as compared to its control, and removal of pollutants is evident and highest at a lower concentration of 50 mg/L and with higher settling time of 90 minutes. Percent removal showed that as the dosage is increased from 50 to 100 and 150 mg/L, measured values increase and percent removal diminishes with increased dosage and shorter settling time respectively. Settling time at 90 minutes resulted in a higher reduction of turbidity, TSS, nitrogen, phosphorus, and BOD. This is attributed to the presence of high concentrations of both carbohydrates and lipids in the stems which can increase the content of organic matter in the treated water and represents a disadvantage due to the increase in turbidity in certain situations if the dose of the primary

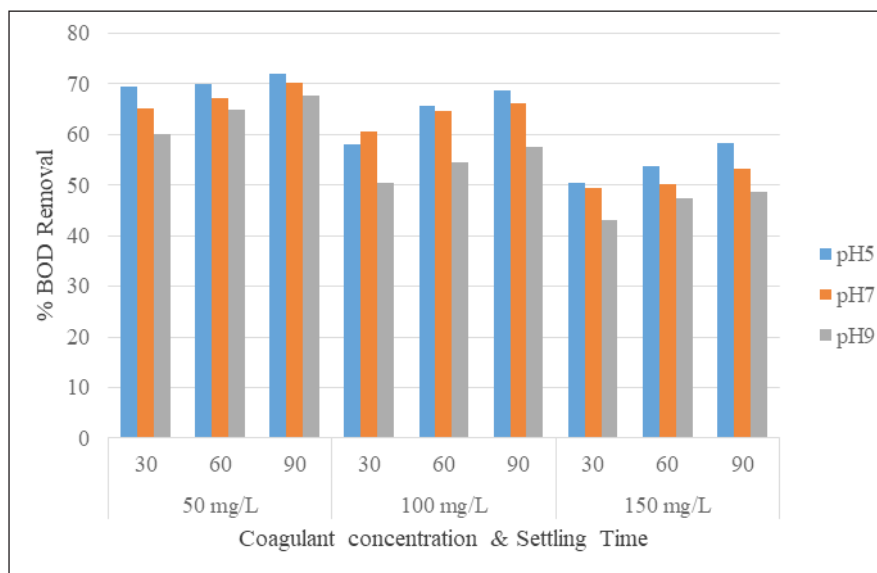


**Figure 8.** Optimization of coagulant *Corchorus olitorius L.* with BOD.

coagulant is not well adjusted [20]. When *Corchorus olitorius L.* was tried as a sole coagulant, removal of turbidity was poor as compared to alum [21]. An explanation is a steric hindrance that takes place between polymer molecules at high concentrations [22].

### 3.3 Removal efficiency of turbidity, TSS & BOD

#### Turbidity

Table 4 showed the results of turbidity removal when wastewater was treated with a coagulation-flocculation process under three (3) pH conditions (pH 5, pH 7 & pH 9).

Table 4. Percent removal efficiency of turbidity.

Treatment	pH 5	pH 7	pH 9
A <sub>100</sub>	97.81	98.14	98.31
C <sub>100</sub>	70.48	67.62	62.23
A <sub>50</sub> C <sub>50</sub>	84.49	84.15	85.33
A <sub>25</sub> C <sub>75</sub>	82.12	80.27	82.97
A <sub>75</sub> C <sub>25</sub>	85.16	83.47	85.67

Data revealed that with the use of 100% alum (A<sub>100</sub>) solution, turbidity removal was highest at pH 9 with a removal percentage of 98.31%. A study also reported that when Alum was used to treat wastewater containing Acid Red 398 dye solution by coagulation/flocculation process, it also removed 80% of turbidity at 140 mg/L of alum [23].

On the other hand, a 100% *Corchorus* solution (C<sub>100</sub>) at an optimum dose of 50 mg/L operating at an optimum settling time of 90 minutes obtained removal efficiency of 70.48%, 67.62%, and 62.23% at pH 5, pH 7, and pH 9. When treatment was done involving coagulant aid mixing; 50% *Corchorus* with 50% alum (A<sub>50</sub>C<sub>50</sub>) treatment at the optimum dose and optimum settling time obtained removal efficiency of 84.5%, 84.2%, and 85.3% at pH 5, pH 7, and pH 9. Additionally, a 75% *Corchorus olitorius L.* and 25% alum stock solution (A<sub>25</sub>C<sub>75</sub>) treatment at an optimum dosage level of 50 mg/L and optimum settling time of 90 minutes obtained a maximum amount of removal percentage of 82.1%, 80.3%, and 82.9%. Similarly, 25% *Corchorus olitorius* and 75% alum

stock solution (A<sub>75</sub>C<sub>25</sub>) treatment at an optimum dosage level of 50 mg/L and optimum settling time of 90 minutes obtained a maximum amount of removal percentage 85.2%, 83.5% and 85.7% for pH level 5, 7 and 9 respectively. It showed that with *Corchorus* as the coagulant aid highest removal was observed at A<sub>75</sub>C<sub>25</sub> at pH 9.

Results, as shown, indicated that removal efficiency varies with treatment designs under optimum coagulant dose and settling time. The magnitude differs for a particular coagulant and pH conditions [24,25]. The other natural coagulants have minimal effect on changes in pH conditions [26].

#### Total suspended solids (TSS)

Table 5 presented results for the removal efficiency of total suspended solids after wastewater has been treated with coagulant and coagulant aids with different treatment designs. As shown in the results, a treatment combination containing 50% *Corchorus olitorius L.* and 50% alum (A<sub>50</sub>C<sub>50</sub>) obtained removal efficiency of 88.8%, 87.2%, and 86.6% for pH 5, pH 7, and pH 9 treatment conditions.

Table 5. Percent removal efficiency of TSS.

Treatment	pH 5	pH 7	pH 9
A <sub>100</sub>	95.9	96.8	98.4
C <sub>100</sub>	68.45	67.65	65.51
A <sub>50</sub> C <sub>50</sub>	88.77	87.16	86.63
A <sub>25</sub> C <sub>75</sub>	86.7	85.56	85.56
A <sub>75</sub> C <sub>25</sub>	89.57	88.5	87.43

Furthermore, a treatment containing 75% *Corchorus* and 25% alum (A<sub>25</sub>C<sub>75</sub>) resulted in removal percentage of 86.7% for pH 5 and 85.6% for pH 7 & pH 9; whilst treatment combination with 25% *Corchorus* and 75% alum (A<sub>75</sub>C<sub>25</sub>) obtained removal efficiency at 89.6%, 88.5% & 87.4%.

#### Biochemical oxygen demand (BOD)

Table 6 has shown results of the removal efficiency of the biological water quality parameter, BOD when wastewater was subjected to a coagulation-flocculation process using treatment designs.

When alum was mixed with *Corchorus olitorius L.* as a coagulant aid, BOD removal efficiency

was observed at 89.70% at pH 5, 88.76% at pH 7 & 86.28% at pH 9 with A<sub>50</sub>C<sub>50</sub>. Similarly, with a treatment design containing 75% *Corchorus* (A<sub>25</sub>C<sub>75</sub>) removal efficiency attained was 86.72% at pH 5, 85.98% at pH 7 & 83.50% at pH 9; whilst at 25% *Corchorus* (A<sub>75</sub>C<sub>25</sub>) BOD removal was obtained was 90.23% at pH 5, 89.78% at pH 7 and 87.44% at pH 9.

**Table 6.** Percent removal efficiency of BOD.

Treatment	pH 5	pH 7	pH 9
A <sub>100</sub>	94.89	95.62	97.81
C <sub>100</sub>	71.97	70.51	68.61
A <sub>50</sub> C <sub>50</sub>	89.78	88.76	86.28
A <sub>25</sub> C <sub>75</sub>	86.72	85.98	83.5
A <sub>75</sub> C <sub>25</sub>	90.23	89.78	87.44

Lastly, results also revealed that BOD removal efficiency decreases with pH when the coagulant used was *Corchorus*. Like any other bio-coagulant, *Corchorus* showed potential in the removal of contaminants in water. By using a natural coagulant, there was substantial removal of BOD<sup>[27]</sup> at more than 50% as compared to the conventional treatment process<sup>[28]</sup>.

#### 4. Conclusions and recommendations

The results of the characterization of *Corchuros olitorius L.* (Saluyot) showed that the mucilage composition of saluyot powder has influenced the coagulation activity. Furthermore, the results of the study proved that optimum doses of coagulant aid *Corchorus olitorius L.* reduced contaminants. Coagulation experiments with this bio-coagulant indicated that the coagulation-flocculation process effectively removed turbidity, TSS & BOD from the wastewater using the optimum dosage. In general removal efficiency of most contaminants in water was highest at pH 5 for *Corchorus olitorius L.* and decreases with the increase in pH. Statistical evidence showed significant differences in the measured values among treatment designs with optimum dose and the effect between pH in removal efficiency in all treatment designs is insignificant. As a whole, it can be concluded that the usage of bio-coagulant *Corchuros olitori-*

*us L.* would considerably save the use of chemicals and reduced impacts associated with health risks. Additionally, it is recommended that further efforts could be made to improve the removal efficiency of the contaminants under study by enhancing other variables such as mixing intensity and contact time between the water and coagulant, as well as other factors.

#### Conflict of Interests

The authors declare no conflict of interest.

#### References

- [1] Shon, H.K., Vigneswaran, S., Snyder, S.A., 2006. Effluent organic matter (EfOM) in wastewater: Constituents, effects, and treatment. *Critical Reviews in Environmental Science and Technology*. 36(4), 327-374.  
DOI: <https://doi.org/10.1080/10643380600580011>
- [2] Radoiu, M.T., Martin, D.I., Calinescu, I., et al., 2004. Preparation of polyelectrolytes for wastewater treatment. *Journal of Hazardous Materials*. 106, 27-37.
- [3] Renault, F., Sancey, B., Charles, J., et al., 2009. Chitosan flocculation of cardboard-mill secondary biological wastewater. *Chemical Engineering Journal*. 155, 775-783.
- [4] Amuda, O.S., Amoo, I.A., 2006. Coagulation/flocculation process and sludge conditioning in beverage industrial wastewater treatment. *Journal of Hazardous Materials*. 141(3), 778-783.
- [5] Ugwu1, S.N., Umuokoro, A.F., Echiegu, E.A., et al., 2017. Comparative study of the use of natural and artificial coagulants for the treatment of sullage (domestic wastewater). *Cogent Engineering*. 4, 1365676.
- [6] Gandiwa, B.I., Moyo, L.B., Ncube, S., et al., 2020. Optimisation of using a blend of plant based natural and synthetic coagulants for water treatment: (Moringa Oleifera-Cactus Opuntia-alum blend). *South African Journal of Chemical*

- Engineering. 34, 158-164.
- [7] Anastasakis, K., Kalderis, D., Diamadopoulou, E., 2009. Flocculation behavior of mallow and okra mucilage in treating wastewater. *Desalination*. 249(2), 786-791.
- [8] Ndovu, L.J., Afolayan, A.J., 2008. Nutritional analysis of the South African wild vegetable *Corchorus Olitorius L.* *Asian Journal of Plant Sciences*. 7(6), 615-618.
- [9] D'Andrea, C., Bochterle, J., Toma, A., et al., 2013. Optical nanoantennas for multiband surface-enhanced infrared and Raman spectroscopy. *ACS Nano*. 7(4), 3522-3531.
- [10] Wathoni, N., Shan, C.Y., Shan, W.Y., et al., 2019. Characterization and antioxidant activity of pectin from Indonesian mangosteen (*Garcinia mangostana L.*) rind. *Heliyon*. 5(8), e02299.
- [11] Sriyanti, I., Dhewa Edikresnha, A.R., Munir, M.M., et al., 2018. Mangosteen pericarp extract embedded in electrospun PVP nanofiber mats: Physicochemical properties and release mechanism of  $\alpha$ -mangosteen. *International Journal of Nanomedicine*. 13, 4927.
- [12] Theodoro, J.P., Lenz, G.F., Zara, R.F., et al., 2013. Coagulants and natural polymers: Perspectives for the treatment of water. *Plastic and Polymer Technology*. 2(3), 55-62.
- [13] Jayag, E.P., Acabal, A.D., 2014. In vitro free radical scavenging activity of Bago (*Gnetum gnemon Linn.*), Pako (*Diplazium esculentum (Retz.) Sw.*) and Saluyot (*Corchorus olitorius Linn.*) Leaf Extracts. *Journal of Society and Technology*. 4(1), 17-24.
- [14] Yin, C.Y., 2010. Emerging usage of plant-based coagulants for water and wastewater treatment. *Process Biochemistry*. 45, 1437-1444.
- [15] Asasutjarit, R., Larpmahawong, P., Fuongfuchat, A., et al., 2014. Physicochemical properties and anti-propionibacterium acnes activity of film-forming solutions containing alpha-mangostin-rich extract. *Aaps Pharmscitech*. 15(2), 306-316.
- [16] Baang, R.P., Del Rosario, R.M., Palmes, N.D., 2015. Phytochemical profiles and antioxidant activity of selected indigenous vegetables in Northern Mindanao, Philippines. *International Journal of Bioengineering and Life Sciences*. 9(8), 870-875.
- [17] Wu, T.Y., Mohammad, A.W., Jahim, J.M., et al., 2010. Pollution control technologies for the treatment of palm oil mill effluent (POME) through end-of-pipe processes. *Journal of Environmental Management*. 91(7), 1467-1490.
- [18] Ali, E.N., Alfarra, S.R., Yusoff, M.M., et al., 2015. Environmentally friendly biosorbent from *Moringa oleifera* leaves for water treatment. *International Journal of Environmental Science and Development*. 6(3), 165-169.
- [19] Montaña, N.E., De Leon, J.F., Loquias, M.M., 1997. Extraction and partial characterization of the water-soluble mucilage from *Corchorus olitorius Linn.* (Fam. Tiliaceae). *KIMIKA*. 13(1), 23-25.
- [20] Altaher, H., Khalil, T., Abubeah, R., 2016. An agricultural waste as a novel coagulant aid to treat high turbid water containing humic acids. *Global Nest Journal*. 18(2), 279-290.
- [21] Asrafuzzaman, M., Fakhruddin, A., Alamgir Hossain, M., 2011. Reduction of turbidity of water using locally available natural coagulants. *International Scholarly Research Network*. 632189, 1-6.
- [22] Hu, C.Y., Lo, S.L., Chang, C.L., et al., 2013. Treatment of highly turbid water using chitosan and aluminum salts. *Separation and Purification Technology*. 104, 322-326.
- [23] Zonoozi, M.H., Moghaddam, M.R.A., Arami, M., 2008. Removal of acid red 398 dye from aqueous solutions by coagulation/flocculation process. *Environmental Engineering and Management Journal*. 7(6), 695-699.
- [24] Ugonabo, V.I., Menkiti, M.C., Onukwuli, O.D., 2012. Coagulation kinetics and performance evaluation of corchorus olitorus seed in pharmaceutical effluent. *International Journal of Multidisciplinary Science and Engineering*. 3(7), 20-32.

- [25] Metcalf, E.A.T., Burton, F.L., Leverenz, H.L., et al., 2006. *Water reuse: Issues technologies, and applications*, 1st edition. McGraw-Hill: New York.
- [26] Effendi, H., Sari, R.D., Hasibuan, S. (editors), 2015. *Moringa oleifera as coagulant for batik effluent treatment*. 35th Annual Conference of the International Association for Impact Assessment; 2015 Apr 20-23; Florence.
- [27] Folkard, G., Sutherland, J., Mtawali, M. (editors), et al., 1994. *Moringa oleifera as a natural coagulant*. 20th WEDC Conference Affordable Water Supply and Sanitation; Colombo, Sri Lanka.
- [28] Kumar, V., Othman, N., Asharuddin, S. (editors), (2017). *Applications of natural coagulants to treat wastewater—a review*. MATEC Web of Conferences. EDP Sciences. 103, 06016.



**B** BILINGUAL  
PUBLISHING  
GROUP

Tel: +65 65881289

E-mail: [contact@bilpublishing.com](mailto:contact@bilpublishing.com)

Website: <https://journals.bilpubgroup.com>

ISSN 2661-3190



9 772661 319234